Carotid atherosclerotic plaque characterisation by measurement of ultrasound sound speed in vitro at high frequency, 20 MHz

Brewin, Mark Paul

Carotid atherosclerotic plaque characterisation by measurement of ultrasound sound speed *in vitro* at high frequency, 20 MHz

A thesis submitted to Queen Mary University of London
for the degree of
Doctor of Philosophy

By

Mark Paul Brewin

June 2010

ACKNOWLEDGEMENTS

I would like to acknowledge a number of people within my department at the Royal London Hospital who helped me with my research through both their knowledge and support. Firstly my supervisor, Dr. Malcolm Birch, was helpful, inspiring and instrumental in devising and developing both the project and the experimental design. Paul Barry was a key person in developing and producing the apparatus and tools to carry out the work. Dr. Jonathan Reeves provided continual support and insight as my mentor. I also would like to thank all my colleagues in the Clinical Physics department at the Royal London Hospital for helping me along the way. Outside my department, I would also like to acknowledge the help I received from Professor Steve Greenwald who wrote the code for the automated segmentation. This work would also not have been possible without the skill and work of both the histologists, Ms. Pauline Levey and Mr. Chris Evagora.

I also would like to acknowledge the enthusiasm, drive and push shown by several members of my family; my sister, mother, father and stepfather. A big 'thank you' goes to my close friends who helped me through the last days and to the submission of this thesis. Finally I want to thank my future wife, Georgette Reed, for encouraging me through to the end of this work and for being my angel.

ABSTRACT

The first part of the study was to characterise the acoustic properties of an IEC agar-based tissue mimicking material (TMM) at ultrasound frequencies centred around 20 MHz. The TMM acoustic properties measured were the amplitude attenuation coefficient (dB $cm^{-1}MHz^{-1}$), the sound speed (ms^{-1}) and the backscattered power spectral density characteristics of spectral slope (dB MHz^{-1}), y-axis intercept (dB) and reflected power (dB). The acoustic properties were measured over a temperature range of 22 - 37^{o}C.

Both the attenuation coefficient and sound speed, both group and phase, showed good agreement with the expected values of 0.5 dB cm^{-1} MHz^{-1} and 1540 ms^{-1} respectively with average values of 0.49 dB $cm^{-1}MHz^{-1}$ (st.dev. ± 0.03) and 1541.9 ms^{-1} (st.dev. ± 8.5). Overall, this non-commercial agar-based TMM was shown to perform as expected at the higher frequency range of 17-23 MHz and was seen to retain its acoustic properties of attenuation and speed of sound over a three year period.

For the second part of the study, composite sound speed was measured in carotid plaque embedded in TMM. The IEC TMM was adapted to a clear agar gel. The contour maps from the attenuation plots were used to match the composite sound speed data to the photographic mask of plaque outline and thus the histological data. By solution of sets of simultaneous equations using a matrix inversion, the individual speed values for five plaque components were derived; TMM, elastin, fibrous/collagen, calcification and lipid.

The results for derived sound speed in the adapted TMM were consistently close to the expected value of soft tissue, 1540 ms^{-1}. The fibrous tissue showed a mean value of 1584 ms^{-1} at body temperature, 37^{o}C. The derived sound speeds for elastic and lipid exhibited large inter-quartile ranges. The calcification had a significantly higher sound speed than the other plaque components at 1760 - 2000 ms^{-1}.

Table of Contents

List of Tables and Figures

Chapter 1:

Chapter 2:

Chapter 3:

Chapter 4:

Chapter 1 INTRODUCTION

1.1 Clinical Context

There is currently a lack of effective non-invasive diagnostic tools for *in vivo* assessment of vulnerable carotid plaques. Vulnerable plaques in the carotid artery are likely to rupture or thrombose and cause an ishaemic attack or stroke. Current treatment for these patients depends foremost on the clinical history of the patient and assessment of the symptoms. However, carotid disease is detected and assessed using Duplex ultrasound and the determination of the degree of stenosis provides a strong indicator as to the need for intervention. Other modalities are used to follow up the assessment but ultrasound is the most commonly used tool.

Currently the number needed to treat, NNT, is fifteen for one to benefit. Therefore there is a clinical need to find a diagnostic tool to reduce this number. In other words, there is a necessity to identify high-risk patients who may benefit from surgical intervention from low-risk patients with stable plaques. It is also evident that surgery can lead to complications and has an implicit risk. This new diagnostic technique ideally needs to cover three criteria. It not only needs to be an accurate predictor of stroke but is also required to be a predictor of benefit to the patient. Thirdly, this technique needs to be readily re-applicable.

Scope was identified in this study for an improvement or enhancement in plaque tissue characterisation. The primary aim of this work was to characterise the components of carotid plaque. This data may be further used to assess plaque vulnerability and therefore stroke risk. It is known what features of plaque structure possibly contribute to its instability but there is still no clear diagnostic technique that can be applied to confirming the likelihood of rupture for carotid plaque.

Tissue characterisation by determination of ultrasound propagation speed through the components of atherosclerotic plaque may provide further knowledge of its vulnerability or risk of thrombosis. It was proposed that the sound speed information of each plaque component may provide a link to identify the plaque vulnerability.

Sound speed data may then be used to work up a predictive diagnostic ultrasound tool for vascular surgery. Some modern ultrasound scanners such as the Zonare (ZONARE Medical Systems Inc., Mountain View, CA, USA) instigate the variation of assumed sound speed within image processing in order to optimise the image. This innovative principle may be utilised in reverse in order to identify the various components of plaque by the determination of their sound speed. Hence knowledge of the individual components within a plaque may help assess the structural integrity and its associated risk of emboli.

Ultrasound pressure wave propagation speed is also widely accepted for determining material properties in engineering and non-destructive testing (NDT), but has not yet been adapted to use in medical diagnostics. As the sound speed is closely related with the elasticity or compressibility of a material, this data may also be used as a parameter for finite element analysis (FEA) modelling of plaque strength and durability. This information may also be used, in conjunction with their density data, to evaluate the bulk modulus of each component.

Finally this tissue characterisation data could be used to improve both knowledge on this subject and the current data ranges for sound speeds in plaque components.

1.2 Method Summary

In the Clinical Physics Department at the Barts and the London NHS Trust hospital, an ultrasound acoustic property measurement system has been developed for the calibration and measurement of tissue mimicking materials and the assessment of human tissue.

The initial task was to produce a consistent, calibrated agar tissue mimicking material, TMM, in our laboratory. The chosen material was developed for the International Electrotechnical Commission (IEC) in a project funded by the European Commission (EC) (Teirlinck et al. 1998). The first part of this thesis presents the work carried out to verify and extensively calibrate the acoustic properties of this tissue mimicking material at around 20 MHz. This high frequency was selected as ultrasound image resolution improves with frequency. The current

transducers for imaging superficial vessels work in the 7-15 MHz range. The carotid lies close to the surface of the neck and therefore the low penetration at this high frequency should not be an issue. Continuing development of high frequency transducers also means that there will be a trend towards higher frequency probes in the pursuit of improved resolution.

The second part of the project was to measure ultrasonic propagation speed through atherosclerotic carotid plaque tissue embedded in this TMM. With full Research Ethics Committee approval (P/03/158, Redbridge and Waltham Forest LREC, UK), carotid plaque was harvested from endarterectomy from consenting patients and was then embedded in an agar-based gel. The composite sound speed through the plaque in TMM was measured using an insertion, or substitution, technique (AIUM 1995). The plaque specimen was plotted in a raster fashion and a 2D sound speed plot was produced. The embedded plaque specimen was then sent to histology where it was sectioned across and through the plane of the speed plot data. Once the proportion of plaque components through the specimen had been determined by histology, the sound speed of each component could be derived by the solution of simultaneous equations. By solution of a matrix inversion of the composite sound speed data and the histological data of the corresponding plaque component percentages, it was possible to calculate a value of sound speed for each component.

1.3 Summary of Chapters

Chapter 1 provides a literature review of both ultrasound TMMs and carotid plaque research. It outlines the past and current materials that have been researched and used as ultrasound tissue mimicking materials. It describes the uses of TMM and details why the agar-based TMM was chosen for our study. Tissue characterisation is discussed; in particular the research into carotid arterial and atherosclerotic tissue. The structure of arteries and the progression of atherosclerosis are detailed. This leads on to a description of carotid disease, stroke and its consequences. Evidence for the vulnerability of plaques is collated along with the various diagnostic techniques that have been studied to characterise this vulnerability or stroke risk.

Chapter 2 details the methods used to measure the acoustic properties of the TMM; namely sound speed, attenuation coefficient and relative backscatter. It outlines the principles of the substitution or insertion method and the apparatus used in the ultrasound measurement system used in this study. Both the reflection and transmission substitution techniques are introduced. It then describes all the experiments that were carried out on the TMM.

Chapter 3 presents the results from the measurements of the acoustic properties of the TMM. The calibration of the measurement system is also detailed. The discussion of these results is also included here.

Chapter 4 begins by outlining the principal and summary of the plotting of composite sound speed and its correlation with the histological data. It introduces the method for derivation of the sound speed of the carotid plaque components. Firstly it explains the necessity for the TMM to be adapted to a clear agar TMM. It details how the plaque is embedded in this TMM. The plotting protocol and system calibration are then described. The process of matching the sound speed data to the histological data is then qualified and the uncertainties are detailed. The tissue segmentation procedure is explained and inter- and intra- observer tests on segmentation are disserted. Finally the matrix inversion or solution of the simultaneous equations is introduced along with the criteria for solution values.

Chapter 5 presents the results from the plaque component speed derivations. Firstly the calibration of the adapted clear gel TMM is outlined. The constancy of the sound speed for embedded tissue within the TMM is determined over a 72 hour period. Any uncertainties for each technique are discussed. The chapter continues by discussion of uncertainty within the plot-photo-histology matching process. The sequence of outcomes for the matching of plot data to histological data is outlined. The automated segmentation process is selected based on the inter- and intra-observer tests. The matrix inversion is tested by adding levels of noise to each plaque component percentage in the derivation of sound speed. The sound speed derived data for both techniques and temperature measurements are tabulated. The derived speed values for the TMM are compared against the QA measured values in order to validate the technique. The influences of temperature and technique on the

derived results for sound speed are quantified. Finally the inter-quartile ranges of sound speed at room and body temperature are compared to those quoted in literature.

Chapter 6 provides a summary of the results of the calibration of the IEC TMM at the higher diagnostic frequencies around 20 MHz and of the derived sound speeds from the plaque components. It then discusses the results for derived sound speed for the TMM and plaque components from the plaque characterisation method. It then draws conclusions on the findings of the plaque study and recommends future work.

1.4 Literature survey and background

1.4.1 Tissue mimicking material

Tissue-mimicking materials (TMMs) have been extensively researched and developed for use in ultrasound (Bude & Adler 1995; Bush & Hill 1983; Madsen et al. 1978; Madsen, Zagzebski, & Frank 1982). They have been specifically designed as a calibrated material with ultrasonic properties similar to human soft tissue for the purposes of assessing the performance of ultrasound imaging systems. They are commonly used in the production of imaging, Doppler and thermal test objects. Anthropomorphic phantoms have also been designed and constructed using TMM for the evaluation of ultrasound techniques used in scanning of the abdomen and breast (ICRU 1998). Some of these phantoms include sample representations of structures within the material that produce beam distortion and varying degrees of attenuation (Lu et al. 1995).

Phantoms or test objects containing agar-based TMMs have been produced for a number of years based on the material developed at the University of Wisconsin (Burlew et al. 1980). A contemporary agar-based TMM has been designed and established as part of an International Electrotechnical Commission project (IEC 2001; Teirlinck, Bezemer, Kollmann, Lubbers, Hoskins, Fish, Fredfeldt, & Schaarschmidt 1998). This has found uses in a range of medical ultrasound research projects (Madsen et al. 2005; Meagher et al. 2007; Poepping et al. 2002; Ramnarine, Anderson, & Hoskins 2001; Ramnarine, Kanber, & Panerai 2004). It has also been utilised at the Barts and the London NHS Trust to develop test objects investigating the feasibility of high frequency ultrasound transducers (Carey et al. 2004) based on the fluoropolymer PVdF (polyvinylidene difluoride, also known as KYNAR®).

The acoustic properties of TMMs are well documented in the present diagnostic ultrasound range, 2 - 15 MHz (Browne et al. 2002; ICRU 1998). However there is now a growing use of higher frequency transducers in medical ultrasound diagnostic techniques such as vascular and muscular skeletal studies. A significant aim of this study has been to characterise the behaviour of this agar-based TMM at the ultrasound frequency bandwidth of 17 - 23 MHz.

1.4.2 Quality assurance and calibration

The assumed values of sound speed and attenuation coefficient of the mimic for soft tissue are 1540 ms^{-1} and 0.5 dB cm^{-1} MHz^{-1}, respectively. The stability of these ultrasonic or acoustic properties of TMM is of paramount importance to these applications, particularly in extended temperature and frequency ranges and over long periods of time.

Two extensive inter-laboratory comparisons of acoustic parameters have been carried out for a standard, calibrated material (Madsen 1999; Wear et al. 2005). Results for each ultrasonic property, propagation speed, attenuation coefficient & backscatter coefficient, were measured in ten different physics laboratories and then compared. However these results only cover the frequency range 2 – 9 MHz. Though good agreement existed for the attenuation coefficient, there were less satisfactory results for speed of sound. Here, there was an unexpectedly large range of 1.7% between laboratories in 1999 compared to their earlier study in 1986 that showed an inter laboratory range of 0.3%. Indeed, in the 2005 comparison, there was disparity in speed of sound between 30 and 60 ms^{-1}. The Madsen (1999) paper also surmised that measurements of backscatter coefficient are often underestimated. The authors postulated that they would have benefited from the use of a common reference material. Wear et al. (2005) observed a large range of variation, of up to two orders, in absolute magnitude of backscatter coefficient measured at the different centres. Measurements of the frequency dependence of backscatter showed better agreement and were found to be more consistent.

Other authors (Browne et al. 2003) have recently assessed the properties of commercially available test objects based on three different TMMs in comparison to the IEC agar-based gel. The first is Zerdine^{TM}, which is a solid elastic water-based polymer (CIRS Inc., Norfolk, VA, USA). The others were a urethane-rubber-based material and a condensed-milk-based gel. These results showed that the speed of sound was frequency independent in the range 2.25 – 15 MHz for all the different materials utilised as TMM**.**

The work highlighted a need for more extensive data on the acoustic properties of TMMs with changes in both frequency and temperature. It also showed that some TMMs, such as urethane-rubber and Zerdine^{TM}, do not demonstrate a linear response with frequency for the amplitude attenuation coefficient. This would lead to a deterioration of results in quality assurance testing due to the decrease in penetration depth performance for higher frequencies above 7 MHz (Browne, Ramnarine, Hoskins, & Watson 2002; Goldstein 2000). The dependence of the ultrasonic characteristics on temperature were measured and showed that the variation of the speed of sound with temperature was within the limits (IEC 1996) of 3 m s^{-1} $^{o}C^{-1}$. Measurements of the variation of the TMM attenuation coefficient with temperature showed no significant change with the important exception of urethane rubber. This showed a change of 0.08 dB cm^{-1} MHz^{-1} $^{o}C^{-1}$ at 15 MHz. This does not comply with the IEC limit of 0.02 dB cm^{-1} MHz^{-1} $^{o}C^{-1}$. The latter may significantly affect ultrasound quality assurance measurements of axial resolution and penetration depth based on urethane test objects, which in turn may lead to unreliable conclusions relating to the performance an ultrasound scanner.

1.4.3 Selection of TMM

There are a number of gel-based TMMs that include agar, polyvinyl alcohol (PVA) and polyacrylamide (PAA). PVA gels have been investigated for use in both MR and ultrasound phantoms (Surry et al. 2004). The mechanical properties of PVA have also been researched for its utility in intravascular elastography (Fromageau et al. 2007). Indeed the PVA cryogel has been moulded for use as a vessel mimicking material (Dineley et al. 2006). PAA gels containing egg white have been used as a research tool for irradiation experiments with high-intensity focussed ultrasound

HIFU (Takegami et al. 2004). Silicone polymers have been considered for TMM but they have a lower sound speed and higher attenuation coefficient than water or human tissue. Polyether-urethane and oil based gel have also been proposed (Kondo & Kitatuji 2005). The former is complex to manufacture and the latter has similar properties to agar gels but is less well documented.

The agar TMM was chosen for this study for the following reasons. It is well documented, relatively cheap to manufacture and can be made easily in our laboratory. It is also a mouldable substance, which is safe to prepare and handle. However, once it is set, it must be handled carefully as it is relatively soft and fragile. One of the main disadvantages of agar is that it is a hydrophilic, organic material that may be prone to propagation of bacteria. It is important that the TMM is kept hydrated. The bacterial degradation is countered by the use of the anti-bacterial, anti-fungal agent Rodalon^{TM} in its manufacture.

1.5 Tissue characterisation

1.5.1 Speed of sound

A great deal of work has been carried out over the last few decades to characterise mammalian tissue using ultrasound. Data from early work on ultrasonic propagation speeds in human and animal tissues have been summarized in a number of papers (Chivers & Parry 1978; Goss, Johnston, & Dunn 1978; Goss, Johnston, & Dunn 1980). The acoustic properties of speed and attenuation have also been documented in relation to their temperature dependence (Bamber & Hill 1979; Clarke, Bush, & Ter Haar 2003; Techavipoo et al. 2004; Towa et al. 2002; Worthington & Sherar 2001) and their frequency dependence (Akashi et al. 1995; Bhagat et al. 1977). Indeed acoustic velocity of eye tissue has already been measured at this relatively high frequency of 20 MHz (De Korte, Van der Steen, & Thijssen 1994) as this is a frequency commonly used in ophthalmology. Indeed most of this work, in addition to other research into tissue properties, has been summarised in two key reference books (Bamber 1997; Duck 1990).

Over the last twenty years, a large body of work has been carried out at Tohoku University in Japan in the development of a scanning acoustic microscope (SAM). This work aimed to provide data for development and understanding of intravascular ultrasound (IVUS) imaging of atherosclerosis. The high frequency range of 100 – 200 MHz limits its use to the characterisation of thinly sectioned tissues or to the assessment of cell biomechanics. Early work was carried out to characterise atherosclerosis in the aorta (Saijo et al. 1998) and aortic aneurysm (Saijo et al. 2004). Later studies investigated the acoustic properties of both normal and atherosclerotic coronary artery (Saijo et al. 2006; Saijo et al. 2007). The results from this work is summarised in table 1.

Tissue Component	**Aortic Aneurysm (2004)** n = 21	**Aortic Atherosclerosis (1998)** n = 12		**Coronary Artery (2006)** n = 6		**Coronary Artery (2007)** n = 2
	Aneurysm	Normal	Athero	Normal	Athero	Athero
Intima		1568 ± 18		1600		
Fibrosis	1561± 34		1677 ± 18		1720	1680 ± 30
Media	1583 ± 32	1614 ± 30		1560		
Adventitia	1641 ± 33	1640 ± 25		1590		
Calcification			1760 ± 14		1830	1810 ± 25
Lipid			1526 ± 6		1520	1520 ± 8

Table 1: This table summarises the speed of sound values for the tissue components found within normal, aneurysmal and atherosclerotic arteries as measured by Saijo et al. All values are measured in ms^{-1}. n specifies the number of plaque specimens in each study.

The SAM is capable of distinguishing six kinds of tissue elements from normal and atherosclerotic artery. They argued that the lower value of sound speed of the fibrotic intima in the aneurysmal aorta (2004) in comparison to atherosclerotic aorta (1998) is related to its change in elasticity or mechanical weakening. Elasticity is directly related to sound speed, refer to equation 1. The trend of change in speed values here agrees with previous values of Young's modulus for lipid and calcified plaque (Richardson, Davies, & Born 1989).

$$c \doteq \frac{K}{\rho}$$

Equation 1

where c, K and ρ are the sound speed, elastic modulus and density, respectively

In the studies of atherosclerotic tissue in both the coronary artery and aorta, the speed is highest for calcified plaque and lowest in the fatty plaque. In the 1998 study, the atherosclerotic fibrosis in the intima of the aorta caused an increase in sound speed that may be due to the hardening of the tissue. It is difficult to compare the absolute values on the coronary artery atherosclerosis as no uncertainties are detailed in the 2006 paper. However the table of data provides a comparison for our study.

An interim project used the SAM to study the stress distribution in atherosclerotic plaque (Saijo et al. 2001). The sound speed was found to correlate with the elasticity distribution in the coronary arterial wall. In atherosclerotic plaques, high stress was concentrated to lesions with a lipid pool with an overlying fibrous cap.

The acoustic properties of atherosclerotic lesions from the aorta have also been compared to normal aortic wall tissue in earlier work (Greenleaf et al. 1974). This experiment used a 10 MHz focused transducer. The normal tissue had a velocity of 1501 ms^{-1} (range 1492 - 1534); the fatty lesion 1532 ms^{-1} (1504 - 1558); the fibrous lesion 1514 ms^{-1} (1492 - 1548) and the ruptured lesion 1518 ms^{-1} (1504 - 1537). The samples have been categorised into five lesion types but there is no indication of the total number of samples. Therefore it is hard to comment on the results or their evident overlap in speed values. Here, the calcified lesion was not measurable. These values are generally lower than those of Saijo et al. (1998). In addition, the

speed for fat or lipid is comparable or higher to normal or fibrous tissue. This is a counterintuitive result in that ultrasound travels faster in a fatty plaque. However it surmises that the lipid may be in a solid phase at the measured temperature of 20^{o}C.

In a compilation of literature (Duck 1990), the velocity of human carotid artery at 20 ^{o}C is quoted as 1575 ± 9.8 ms^{-1}; human fat shows a range of 1412-1462 ms^{-1} at 37 ^{o}C; and collagen, one of the fibrous elements found in plaque, is measured at 1570 ms^{-1}. It is noted that the degree of calcification within plaque is variable. Plaques will therefore be inhomogeneous and this will cause a variation in measured sound speeds. In addition, measurement of sound speed in significantly calcified regions will be difficult as the ultrasound pulse may not be able to traverse the highly attenuative material.

In one study, the calcified lesion of an arterial wall was measured at a higher velocity range of 1900-2000 ms^{-1} at 37 ^{o}C (Rooney et al. 1982). The paper specifies that this is a highly calcified lesion, though does not comment on the degree. This paper also concluded that increased sound speed may be related to an increase in collagen content.

1.5.2 Attenuation

The acoustic property of attenuation can be inherently measured using the same transmission substitution technique. Attenuation data has been collated for human tissue. Most attenuation in soft tissue is caused by absorption as opposed to scatter (Lyons, Chivers, & Parker 1986). This will have relevance in the consideration of tissue heating due to ultrasound.

There is little data in early studies of attenuation. Greenleaf (1974) measured the attenuation coefficient of human aorta at 0.56 – 0.67 dB cm^{-1} MHz^{-1} at 20^{o}C. Pig fat was measured at 1.5 and 1.72 dB cm^{-1} MHz^{-1} using 2 MHz and 10 MHz transducers respectively at 37^{o}C (Gammell, Le Croisette, & Heyser 1979).

Saijo (1998) measured attenuation in addition to sound speed. Intima was measured with an attenuation coefficient of 0.61 dB mm^{-1} MHz^{-1}, calcified lesion as 2.5 dB mm^{-1} MHz^{-1}, fibrosis as 1.7 dB mm^{-1} MHz^{-1} and fatty material as 0.34 dB mm^{-1} MHz^{-1}. As expected, the calcification shows the highest attenuation and the fat the lowest.

Another group measured the integrated attenuation and slope of attenuation in the aorta using backscattered radiofrequency signals at 30 - 50 MHz (Bridal et al. 1997). Their aim was to achieve *in vitro* characterisation of plaque composition using attenuation measurements. Here tissue types were classified into five groups as normal media, dense collagen, collagen-lipidic, lipidic and calcified. The highest values were again observed in the calcified regions. However the slope of attenuation was seen to be significantly higher in lipidic regions than in normal media ($p = 0.002$), dense collagen ($p = 0.0007$) or collagen-lipidic regions ($p = 0.04$). Again this high value may be related to the measurement temperature of 20^0C. The lipid may be in a solid phase and this would cause higher attenuation.

Earlier work by Picano et al. (1985) also investigated plaque characterisation using the attenuation of ultrasound. This study compared normal aortic tissue to three categories of diseased tissue; fibrous, fibrofatty and calcific. They ultrasonically analysed 400 sites, 4 mm in diameter, in the frequency range 7 - 11 MHz. The results showed that while the fibrous sites showed lower attenuation slope or coefficient (per cm per MHz), both the fibrofatty and calcific sites had significantly higher values. Two alternative explanations were detailed to explain the higher attenuation in fibrofatty tissue other than sample temperature. Firstly, the increased in lipid component is accompanied by the presence of cholesterol crystals that have high reflectivity. Secondly, lipidic cores are contained by a fibrous cap. This incurs an increased impedance step that would also cause greater degrees of reflection.

1.5.3 Backscatter

The backscattered ultrasonic features of spectral slope, y-axis intercept and power from plaque have been extensively theoretically studied (Lizzi et al. 1997; Lizzi et al. 2006). They have found application in clinical intravascular studies (Waters et al. 2003; Watson et al. 2000). Integrated backscatter (IB) intravascular ultrasound uses a measure of the average power of the backscattered signal. IB-IVUS has been tested *in vivo* on carotid, femoral and coronary atherosclerotic arteries and has identified five categories of tissue type; thrombus, intimal hyperplasia or lipid pool, fibrous tissue, mixed lesion and calcification (Kawasaki et al. 2001; Kawasaki et al. 2002; Sano et al. 2006).

1.6 Carotid artery, atherosclerosis and plaque

1.6.1 Arterial structure

The common artery or vessel is composed of several layers as shown in figure 1. The multilayer structure of the artery is anisotropic and its elasticity is non-linear. The blood flows through the lumen of the vessel. The endothelium is a thin layer of cells that reduces the friction of blood flow. The intima itself consists of two layers. The inner layer is areolar connective tissue. This holds the endothelium in place and includes both collagen and elastin. The outer intimal layer is composed of elastic fibres. The media is made up of smooth muscle cells and elastic tissue. The adventitia is composed of collagen which serves to anchor the blood vessel to give it stability. Both the intima and the adventitia have a high content of collagen fibre.

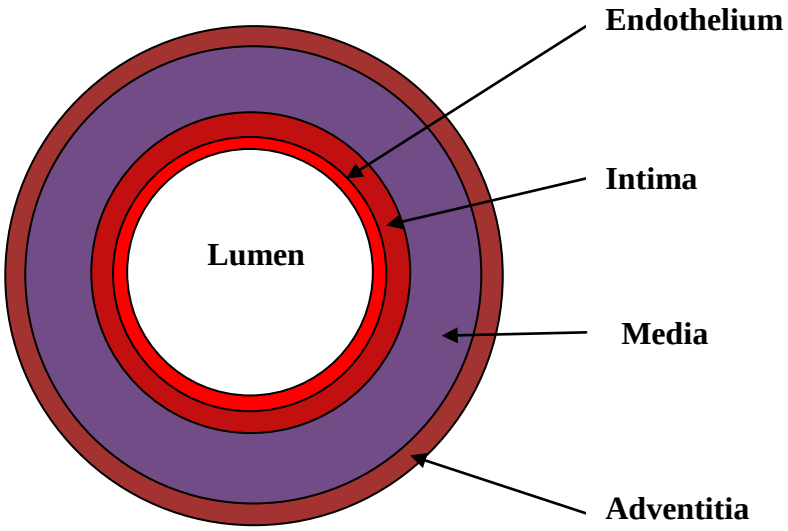

Figure 1: A simple schematic of the layers within an artery

It is well recognised that collagen has major significance in the stiffness of tissue as it has high values of elastic modulus. It follows that it plays an important role in the acoustic properties of arterial tissue.

1.6.2 Atherosclerosis

Atherosclerosis (ATH) and its thrombotic complications are the principal cause of mortality and morbidity in first world countries (Kavey et al. 2003; Petersen et al. 2005). Globally it contributes to approximately half of all deaths. Extracranial carotid atherosclerotic disease is responsible for half of all ischemic strokes, which can result in long-term disability or death.

Department of Health (UK) statistics show that cerebrovascular and other arterial disease accounted for 162,000 hospital admissions and 2.7 million bed-days in England for 2008 - 2009 (HES online, DoH). Cerebrovascular disease and its related complications are also on the increase and are expected to rise to fourth in the rank order of disability-adjusted life-years by 2020 in Europe (Olesen & Leonardi 2003). Medical management, carotid surgery and carotid angioplasty are used to prevent stroke in these patients, yet in spite of many randomised trials and meta-analyses, the

ideal treatment for an individual cannot be reliably selected (Meschia, Brott, & Hobson 2007).

Atherosclerosis is a progressive, systemic disease and is characterised by intimal lesions called plaques. Atherosclerotic plaques develop in elastic arteries and medium to large sized muscular arteries. Atherogenesis, or the development of atheroma or plaque, is precipitated by chronic endothelial injury. The lesion starts with fatty streaks, which are composed of lipid-filled foam cells. These streaks can appear at a very young age and their connection to atherosclerotic plaques is complex. However although the streaks are related to the risk factors of atherosclerosis in adults and are probably a precursor to plaques, they do not necessarily lead to their development. The regression from fatty streaks to normal artery is possible (Stary 2000).

1.6.3 Carotid disease and Stroke

In carotid atherosclerosis, the plaque deposits develop commonly at the bifurcation of the common carotid artery (CCA) into the internal (ICA) and external (ECA) carotid arteries. This can lead to a number of clinical complications. Transient ischemic attacks (TIAs), due to small emboli causing down-stream occlusion in small cerebral vessels, result in a neurological deficit that lasts less than 24 hours. These can be a precursor to stroke. They may be characterised by temporary difficulty in speaking, numbness, loss of sensation, partial paralysis or weakness in one side of the body. Amaurosis fugax results from similar embolic processes affecting the retinal blood supply and is characterised by temporary partial or complete loss of sight to one eye. Complete occlusion of the main retinal artery can cause permanent loss of sight to one eye. A permanent restriction to blood flow leading to neurological deficiency is the thromboembolic stroke. This may lead to permanent disability through hemiplegia or, in approximately 20% of occurrences, can cause death.

A stroke is an acute cerebrovascular attack. This results in a loss of brain function due to ischaemia, which is a decrease in blood supply. A stroke can either occur directly as a result of ischaemia, which is caused by thrombosis or embolism, or can arise through a haemorrhage in the brain. Approximately 80% of all known strokes are a result of ischaemia.

1.6.4 Atherosclerotic Lesions or Plaques

Lesions become fibrofatty plaques through endothelial disfunction, lipid accumulation, monocyte adhesion, macrophage activation, smooth muscle cell (SMC) proliferation and extracellular matrix (ECM) elaboration. They progress and alter through inflammation, calcification, cell death and degeneration to become vulnerable plaques and thus enter the clinical phase, where they may start to present symptoms. This will occur when they go on to thrombose, stenose, occlude, embolise or rupture. Atherosclerosis can lead to myocardial infarction (heart attack), cerebral infarction (stroke), some cases of aortic aneurysm and peripheral vascular disease.

The lesion is commonly called atheroma, fibroatheroma or fibrofatty plaque. The plaque is generally classified into four categories: normal, fibrous, fibrofatty and calcified. An advanced or vulnerable lesion is typically composed of a lipid core with an overlying fibrous cap. It protrudes into and obstructs the vessel lumen while weakening the underlying media. It can occlude the lumen by a critical stenosis and thus compromise the blood flow. This restriction is known as an ischaemic attack or injury. Secondly they can undergo disruption that precipitates a thrombus that adheres to the plaque and obstructs the blood flow. Plaques are also susceptible to haemorrhage either through rupture of small blood vessels within the media of an affected vessel or from blood flowing into the plaque from the lumen after a breakdown of the plaque itself. Lastly plaques can be friable or prone to rupture or erosion. This event may shed emboli that will disrupt blood supply distal to the occlusion.

The atherosclerotic carotid artery can therefore exist in a number of stages of plaque progression or vulnerability:

- Rupture-prone with a thin fibrous cap.
- Ruptured through fissure.
- Severely or critically stenosed (>60%)
- Erosion-prone
- Intraplaque haemorrhage

1.6.5 Plaque Components and Classification

There are many components in atherosclerotic plaques. These include cells such as SMCs, macrophages and other leukocytes. Secondly there is the ECM, which includes collagen and elastic fibres. Lastly there is the lipid, calcified deposits, areas of intraplaque haemorrhage and thrombosis. These components occur in varying proportions and this gives rise to a broad range of stability within the plaques. This stability can also depend on the location of the lesion i.e. carotid artery, coronary artery or aorta.

The classification of plaques divides ATH lesions into six types according to the American Heart Association (AHA) classification (Stary et al. 1995). Types I – III are generally stable or clinically silent. Plaques become unstable or clinically overt from type IV. These are detailed in the table 2:

Histological Classification	Description	Progression Mechanism	Clinical Correlation
Type I	Isolated macrophage foam cells	By lipid accumulation	SILENT
Type II	Intracellular lipid accumulation		
Type III	Type II changes and formation of small extracellular lipid pools		
Type IV	Type II changes and formation of extracellular lipid core		SILENT or OVERT
Type V	Lipid core and fibrous cap, or multi cap/core, or mainly calcific, or mainly fibrotic	Accelerated Smooth muscle and collagen increase	
Type VI	Surface defect, ulceration, haemorrhage, thrombus	Thrombosis, haematoma	

Table 2: The American Heart Association classification of human atherosclerotic lesions (Modified from HC Stary et al. 1995).

1.6.6 Plaque vulnerability or risk

Vulnerable plaques are characterised by many features. Histologically, vulnerability or high-risk is defined as a plaque with a thin (< 250 μm) fibrous cap with moderate to heavy macrophage infiltration and at least 40% atheroma. Risk is related to symptoms and it has been reported that asymptomatic plaques contain significantly more fibrous material, 88%, than symptomatic, 66% (Feeley et al. 1991).

It is known that plaque composition is a factor in determining patients suitable for endarterectomy. Studies have shown that carotid plaque vulnerability may be related to plaque composition (Axisa et al. 2002; Seeger et al. 1995) rather than the degree of stenosis, which is the present indicator for surgery. Although there have been great advances in the understanding of atherosclerosis and its risks, it is important that further work is carried out in the investigation of patients who have lesions or plaques that are liable to rupture, erode or thrombose.

Pathological markers of unstable carotid plaque detectable by imaging techniques include carotid artery intima/media thickness (c-IMT), ulceration, thrombus, intraplaque haemorrhage, calcification, thin fibrous cap, large lipid-rich necrotic core, inflammation, neovasculature growth and microembolic signals in Transcranial Doppler ultrasound (TCD). Hypertension is also a risk factor for stroke. The management of hypertension reduces stroke risk and, in turn, it is possible that it may contribute to plaque rupture. It has been shown that pulse pressure is associated with plaque ulceration and so may be an important cause of eventual rupture (Lovett, Howard, & Rothwell 2003). The morphologic classification of plaque vulnerability is summarised in table 3.

Vulnerable Plaque	Stable Plaque
Soft	Hard
Thin fibrous cap	Thick fibrous cap
Large lipid pool	Small or no lipid pool
High collagen content	Low collagen content
Intraplaque haemorrhage	Minimum or no erythrocytes
Positive remodelling	Concentric vessel
Disrupted cap	Intact cap
Thrombosis	No thrombosis
Endothelial damage	Intact endothelium
Sparse or no calcification	Extensive calcification
>75% stenosed	<60% Stenosed
High strain or low stiffness	Low strain

Table 3: A summary of plaque vulnerability or risk of ischaemic attack, modified from Naghavi et al. (2001).

As is the case with most forms of disease, early identification of vulnerable atherosclerotic lesions may prevent ischaemic events by medical treatment or surgical intervention. Hence an imaging technique that can identify or characterise plaque *in vivo* would greatly improve both diagnosis and the effectiveness of surgical management.

1.6.7 Treatment of Carotid Disease

Carotid endarterectomy (CEA), which is the removal of material from the inside of the artery, is the common choice of surgical procedure used to treat carotid stenosis. European (ECST 1998) and North American (NASCET 1991) carotid surgery trials have proved CEA to be highly beneficial to patients with symptomatic internal carotid artery stenosis≥ 70%. It has been suggested that patients with 50% to 69% stenosis may also expect some benefit from CEA. These findings were found consistent in the reanalysis of the data (Rothwell, Gutnikov, & Warlow 2003) and have been corroborated by an evidence-based review (Chaturvedi et al. 2005). This

latter report adds that asymptomatic patients with 60 - 99% stenosis may benefit, if treated in this way, with peri-operative morbidity and mortality less than 3%. NASCET also showed that luminal stenosis enables the prediction of one in four strokes for symptomatic patients. However, this ratio is reduced to one in ten for asymptomatic patients (Executive Committee for the Asymptomatic Carotid Atherosclerosis Study 1995).

The current methods for assessment of carotid atherosclerosis do not reliably identify those at risk of stroke. The Cochrane review for symptomatic patients with significant carotid stenosis, found that at least 15 patients must undergo this surgery for one to benefit (Cina, Clase, & Haynes 1999). A later study found that the number needed to treat to prevent stroke in the subsequent 5 years is 9 for men and 36 for women (Rothwell et al. 2004).

Carotid angioplasty with stenting (CAS) has been used as an alternative treatment but its benefit has been deemed marginal or similar to CEA (Boules et al. 2005; Coward, Featherstone, & Brown 2005). However, when used in conjunction with an emboli protection device, it proves to be an equally effective intervention (Yadav, Wholey, & Kuntz 2004). Indeed the complication rate for CAS is 6% compared to 8% for CEA. Currently, however, CEA is still used more commonly than CAS.

In addition, the carotid artery can undergo “positive”, “expansive” or “outward” remodelling upon development of a lesion. The vessel will dilate in order to accommodate the plaque without narrowing the lumen (Glagov et al. 1987). It follows that the degree of stenosis is not necessarily connected to plaque progression or disruption. Therefore factors other than stenosis have an effect on plaque vulnerability and risk of stroke. In turn, a better indicator of stroke risk or necessity for treatment would be greatly beneficial in clinical diagnostics. Ideally the solution would be non-invasive, reliable, cheap and safe.

1.6.8 Current diagnosis of carotid disease

Carotid duplex ultrasonography (DUS) is commonly performed to assess extracranial carotid artery disease for patients with TIAs or stroke as it is both practical and cost-effective. In the case of acute or emergency patients, computerised tomography angiography (CTA) may be used as the first exam prior to immediate therapy in the absence of an ultrasound service. Some centres in the UK now have a 7 - day DUS service to cover for this eventuality. DUS is sometimes followed by magnetic resonance angiography (MRA) or CTA when significant disease or inconclusive results are found. MRA and CTA have the added advantage of imaging intracranial circulation, which may further allow the clinician to select appropriate treatment.

DUS is used directly for imaging vessels to perform two major roles. Firstly the severity of the stenosis is assessed by measurement of plaque encroachment into the lumen. This is carried out either by calculation of plaque area, or volume, for less significant stenosis or through the Doppler-derived velocities. The peak systolic velocity (PSV) and end-diastolic velocity (EDV) are recorded in both internal carotid and distal common carotid arteries. Various criteria for relating velocity measurement and calculated velocity ratios derived using DUS have been developed using angiography as the gold standard. Other recommendations have been outlined with a view to the introduction of a standard DUS imaging protocol in the UK (Oates et al. 2008). The second role of DUS imaging is to provide prognostic information of a particular plaque by an assessment of its stability and location. A basic visual evaluation of the B-mode greyscale can determine whether the plaque is homogeneous, heterogeneous or calcified but this can not imply the vulnerability of the plaque.

1.7 Research and future diagnostic techniques

1.7.1 X-ray and Computerised Tomography

X-ray digital subtraction angiography (DSA) was originally used in the diagnosis and quantification of plaques that have caused stenoses. It measures luminal diameter, indicates the degree of stenosis and defines any irregular luminal surface. However DSA is not able to demonstrate plaque morphology or characterise the plaque. Misleading underestimates of stenosis of the degree of stenosis are common and evidence suggests that DUS is more accurate in classifying stenosis (Netuka et al. 2006). The procedure also carries its own risk of stroke and is rarely performed.

Nowadays CTA, MRA and contrast-enhanced MRA (CEMRA) are commonly used in the assessment of carotid stenosis. Indeed a systematic review suggested that MRA is a sensitive and specific test compared to DSA (Nederkoorn, van der Graaf, & Hunink 2003). Many centres find that a combination of Duplex US and CTA is a sufficient method for the quantification of severe stenosis (Herzig et al. 2004). This is beneficial to the patient as their radiation dose is decreased.

Single slice CT is limited in characterising carotid plaque morphology. However multidetector computerised tomography (MDCT) has improved both the slice thickness and spatial resolution and has less volume averaging. (MD)CTA is also both faster and easier to use. It has been found using spiral CT that symptomatic plaques have been shown to be less calcified and more inflamed than asymptomatic ones (Shaalan et al. 2004). These findings are backed up by research using MDCT that showed that calcified plaques are 21 times less likely to be symptomatic (Nandalur et al. 2005).

MDCT is also capable of quantifying plaque area, volume, calcification and fibrous tissue in good correlation with histology (de Weert et al. 2006). This paper also characterised calcification, fibrous tissue and lipid (45 ± 21 st.dev., 79 ± 20 and 960 ± 491 respectively) by assessment of their Hounsfield Values (HV), which is an arbitrary unit of x-ray attenuation. More recent studies comparing MDCT with histology have shown a 72.6 % correlation between the two techniques (Wintermark et al. 2008).

MDCT may also have sufficient sensitivity and specificity for the detection of plaque ulceration (Saba et al. 2007) but cannot currently distinguish haemorrhage and thrombus from lipid. Its use is also limited by the presence of calcifications but this may not be prohibitive as heavily calcified plaques are less likely to be friable and therefore vulnerable. Micro-computed tomography (micro-CT) has also been proposed as an experimental tool in carotid plaque assessment and this work is ongoing. Micro-CT and magnetic resonance imaging (MRI) have been compared to assess the mineral volumes within carotid plaques but micro-CT remains the gold standard (Wolf et al. 2005).

1.7.2 Nuclear Medicine

A number of nuclear imaging techniques have been applied to investigate carotid plaques. Its disadvantages are clear in that detailed anatomic information is limited and the patient is exposed to ionising radiation. Positron emission tomography (PET) with fluorine-18 fluorodeoxyglucose (FDG) is used to assess inflammatory activity and higher uptake has been shown in symptomatic patients (Tawakol et al. 2006). Similarly annexin A5 scintigraphy has been used to detect cell death, which is present in advanced plaques. A pilot study noted an increased uptake in the artery of CEA patients due for surgery (Kietselaer et al. 2004). This and other scintigraphic techniques still need further evaluation in humans but may be simply used to track or monitor either systemic, arterial or local plaque therapy (Rudd et al. 2008). However, with the use of PET, there is also the consideration of an increased radiation dose to the patient and considerable cost in addition to its current lack of availability and the lack of provision of anatomical detail.

1.7.3 Magnetic Resonance Imaging

MRI has very good resolution capability, provides excellent soft tissue contrast and can visualise plaque morphology. As a modality, MRI is becoming more available but it is relatively expensive. In addition, some patients are contraindicated due to the presence of metallic implants or medical devices such as pacemakers.

The identification and characterisation of carotid plaque components (Clarke et al. 2003) and the classification of plaques (Cai et al. 2002) using MRI have proven acceptable. Cross-sectional studies using MRI have shown that there is a correlation between patient symptomatology and plaque composition (Saam et al. 2006; U-King-Im et al. 2008).

Initial *in vivo* imaging has shown that the lipid-necrotic core and intraplaque haemorrhage could be identified with a sensitivity of 85% and a specificity of 92% (Yuan et al. 2001). Indeed using pre- and post-contrast T1-weighted images, measurement of the lipid core as a proportion of the vessel was shown to be similar on MR images and histology (Cai et al. 2005a). Presence of intraplaque haemorrhage was shown to accelerate plaque progression over an 18 month period (Takaya et al. 2005). Further to this, a link was also established to show that intraplaque haemorrhage, thin fibrous cap and a large lipid core may all accelerate plaque progression in a 38 month prospective, longitudinal study (Takaya et al. 2006). The paper went on to highlight the need for further prospective longitudinal studies to be carried out.

Multisequence MRI has also been used to differentiate between intraplaque (IH) and juxtaluminal haemorrhage with an accuracy of 96% (Kampschulte et al. 2004). The study found that there was a higher occurrence of neurologic symptoms for the juxtaluminal haemorrhage with thrombus, whereas IH was found equally in symptomatic and asymptomatic patients. Further MRI research will be required to verify the significance of IH in plaque vulnerability.

An association between fibrous cap rupture and cerebrovascular events has also been identified using standard MR techniques (Yuan et al. 2002b). Patients with a ruptured cap were found to be 23 times more likely to have had a recent TIA or stroke. Other *in vivo* investigations have also found good levels of agreement between the MR findings and the histological state of the cap (Mitsumori et al. 2003; Trivedi et al. 2004).

The use of Gadolinium-based contrast agent in MRI has improved the distinction between the cap and the lipid core (Cai et al. 2005b; Yuan et al. 2002a) through an enhancement of the signal. Dynamic contrast-enhanced MRI has also been used to assess neovascularisation in the plaque (Saam et al. 2007). Other MRI investigations have also shown an association between contrast enhancement and macrophage infiltration which is identified with plaque inflammation (Kerwin et al. 2003; Kerwin et al. 2006).

Conventional Gadolinium enhancement is limited for the purpose of detailed tissue characterisation. Novel contrast agents such as ultrasmall superparamagnetic particles of iron oxide (USPIOs) have been shown to accumulate in the macrophages and reduce the signal (Kooi et al. 2003; Trivedi et al. 2006). Targeted contrast agents such as perfluorocarbon paramagnetic nanoparticles were being developed to identify plaque components such as fibrin (Yu et al. 2000).

MRI has also been used to analyse plaque structure. In major commercial engineering projects, determination of the fatigue and durability of a structure can be achieved with great accuracy by the use of finite element analysis (FEA), where a complex mathematical model of the structure is tested to virtual destruction by computerised manipulation of the forces involved. Geometry is derived from *in vivo* MRI plaque studies and a stress analysis is performed using FEA. The peak stresses of asymptomatic and symptomatic patients have been compared and higher values were shown in the latter (Li et al. 2007). The same group also used a flow-plaque model to show that there is an increase in plaque stress in arteries with a thin fibrous cap (Li et al. 2006), though it has been suggested that reproducibility for fibrous cap identification needs to be improved (Touze et al. 2007). Other computational models have also been researched using geometric and flow data from MRI to study the

relationship between haemodynamics and plaque progression (Steinman et al. 2002; Tang et al. 2004).

There is no single MRI technique that can assess all the criteria of plaque vulnerability and further research is required to verify which method will be most efficacious. It is likely that multi MR sequences will be required for an improved diagnosis. MR will play a major role in plaque characterisation as it is a non-invasive procedure with both high resolution and excellent soft tissue contrast. Serial MRI may also give further insight into plaque progression as histological findings can only capture information from a single time point. Further advances in field strength, coil technology, blood suppression techniques and pulse sequences will have implications in improvement to the characterisation capability.

1.7.4 Other non-ionising techniques

Other non-ionising techniques are under investigation. It has been demonstrated using thermography, both *in vitro* (Casscells et al. 1996) and *in vivo* (Stefanidis et al. 1999; Verheye et al. 2002), that heat is released by active inflammatory cells in atherosclerotic plaques.

Optical coherence tomography (OCT) is being researched (Meissner et al. 2006; Yabushita et al. 2002) in the diagnosis of peripheral arterial diseases but improvements are needed in signal-to-noise ratio (Farooq 2009). As OCT is capable of both high resolution and contrast, the macrophage content can be quantified (Tearney et al. 2003) and therefore may be a good risk indicator. Near Infrared (NIR) spectroscopy has also shown a good correlation between NIR spectra and plaque composition. The components of a vulnerable plaque have been successfully identified in post-mortem atherosclerotic specimens (Moreno et al. 2002).

These various non-ionising techniques are invasive and require another modality to identify the lesion and guide placement of the catheter. They remain research techniques that are unlikely to be used *in vivo* for the assessment of carotid atherosclerosis.

1.7.5 Ultrasound techniques

Ultrasound is the predominant imaging research technique that is being investigated for the assessment of carotid plaque. Vulnerable plaques have been subjectively defined as echolucent or hypoechoic because they contain more soft tissue such as lipid, necrosis and haemorrhage (Grønholdt et al. 1997), whereas echo-rich plaques are composed primarily of fibrous and calcified tissue. However it has also been shown that high risk carotid plaques are not necessarily lipid-rich but can be heterogenous (AbuRahma, Wulu, & Crotty 2002).

A Cardiovascular Health Study showed that asymptomatic elderly patients with hypoechoic plaque have a relative risk (RR) of ischaemic stroke of 2.8 (95% CI, 1.4-5.7) independent of other risk factors (Polak, Shemanski, & O'Leary 1998). This evidence has been buoyed by the Tromsø study which followed up 223 patients with 35-99% stenosis and 215 controls for 3 years. It found that the RRs of ipsilateral cerebrovascular events for the predominantly echolucent and wholly echolucent groups were 3.5 (95% CI, 1.0 – 12.4) and 3.6 (95% CI, 0.8 – 16.8) respectively compared to the echogenic plaques (Mathiesen, Bonaa, & Joakimsen 2001). A further study (Grønholdt et al. 2001) looked at the RR of ischaemic stroke, as opposed to cerebrovascular events, between the two groups and found it to be 3.1 (95% CI, 1.3 – 7.3).

Ultrasound images can be evaluated visually, though assessment has only fair reproducibility (de Bray et al. 1998). Computer assisted analysis has been used to demonstrate that low grey scale median (GSM) values in B-mode imaging are associated with high risk plaques (Biasi et al. 1999; El-Barghouty et al. 1996; Falkowski et al. 2007; Grogan et al. 2005; Mayor et al. 2003b). There has also been suggestion that an inclusion of GSM measurement would allow stratification of risk to patients undergoing CAS (Biasi et al. 2004). In contrast, it has been mooted that the composition of the plaque cannot be visualised with sufficient accuracy by ultrasonographic GSM analysis (Denzel et al. 2003). Haemorrhage can exist within the plaque with a high GSM value and this may be the reason why a sensitive GSM threshold value to distinguish stable from vulnerable has not been established. Adaptations of this technique are being researched and texture analysis has been

shown to identify plaques that are associated with brain infarction (Kakkos et al. 2007). A stratified greyscale measurement of plaque echogenicity has also been devised and this may be an improvement (Sztajzel et al. 2005). This technique shows a high sensitivity of 73% in the measurement of cap thickness and of 84% for the assessment of juxtaluminal position of the necrotic core.

Intraplaque haemorrhage (IH), enlarged lipid cores and their proximity to the vessel lumen are all important determinants of carotid plaque rupture. An image analysis method for B-mode ultrasound, pixel distribution analysis (PDA), has been developed for pre-operative identification of these features (Lal et al. 2006). This method has accurately determined more IH ($p < 0.001$) and higher lipid content ($p = 0.002$), less calcium ($p < 0.001$) and larger lipid cores closer to the lumen in symptomatic patients. However conflicting evidence has been shown in relation to the link between IH and symptomatic patients. IH has been found previously to be equally prevalent in both symptomatic and asymptomatic patients (Montauban van Swijndregt et al. 1999). A systematic review of this correlation found that studies into plaque bleeding and symptoms have been strongly undermined by poor methodological quality and possible publication bias (Gao et al. 2007). A well-designed prospective study into IH in carotid plaques using non-invasive methods needs to be conducted.

Conventional B-mode ultrasound of plaque is compromised by image artifacts. A reduction of reverberation artifacts has been achieved using a new algorithm known as Speckle Reduction Imaging (SRI). Two hundred and twenty two (222) patients were scanned using SRI in addition to conventional B-mode. The reproducibility of plaque echogenicity was higher (kappa value, $\kappa = 0.83$) for SRI than B-mode ($\kappa = 0.68$). The inter-observer agreement for plaque surface characterisation was also improved ($\kappa = 0.8$ vs. $\kappa = 0.61$) in a comparison of the two techniques. This improvement in image quality may allow better visualisation of plaque morphology (Liasis et al. 2008).

The problem of image artifacts may be overcome by the use of modern innovative US imaging techniques such as real-time compound imaging. Here, improvements in the assessment of plaque texture and surface have been observed. Indeed real-

time compound imaging showed good reproducibility in evaluation of morphology and an improvement in inter-observer agreement for classification of plaque echogenicity (Kern et al. 2004; Kofoed et al. 2001).

Other algorithms, such as texture classification imaging (UTCI), have been developed to probe plaque texture. The UTC images have been visually compared with histology and five texture classes were matched with the location of fibrin, elastin, calcium, haemorrhage and lipid. This study was expanded to investigate whether a reliable system could be developed using 3-D *in vivo* data acquisition (Coleman et al. 2005). It is proposed that this system may be useful in detection of changes in tissue type of >2%. This study shows great potential in the capability of ultrasound to monitor change in tissue type *in vivo*. It was noted that the introduction of ECG gating would be beneficial to the system to reduce artifact.

Other studies in 3-D ultrasound have been used for the assessment of carotid plaque volume and progression. Schminke (2000) performed a prospective pilot study on sixteen patients. It was proposed that 3-D US could examine changes in plaque ulceration but limitations were seen in artifacts arising from swallowing and respiration. Landry (2004) showed that reproducibility of plaque volume measurement required an inter-slice distance < 3mm. This study was furthered to show that their 3-D ultrasound analysis tool showed an accuracy of 1.5% - 4.2% in the measurement of plaque volume (Fenster et al. 2006). This may become a more viable tool in clinical studies of carotid plaque regression and progression. However, further work must be carried out on the determination of plaque boundary using a semi-automated segmentation approach.

Colour Doppler imaging (CDI) and B-flow imaging (BFI), which extends B-mode imaging capabilities to blood flow, have more recently been investigated to demonstrate plaque surface as a predictive tool. Both CDI and BFI have exhibited comparable results in the assessment of ICA plaque stability to those in the determination of GSM levels (Reiter et al. 2007). An echolucent plaque may also be highlighted visually to the operator using CDI or BFI.

Further investigation has been achieved by measurement of the carotid intima-media thickness (c-IMT). Three large clinical trials (>3000 subjects) have shown there to be a link between c-IMT and risk of symptomatic disease (Bots et al. 1997; O'Leary et al. 1999). The Rotterdam cohort study (Hollander et al. 2003) showed that the relative risk of stroke is 2.23 (95% CI, 1.48 – 3.36) for an increase in c-IMT. The c-IMT measurement has also been shown to be an independent risk factor that correlates well with the Framingham Stroke Risk Score (FSRS), which is a calculation of 10-year stroke risk (Touboul et al. 2005). This study used five hundred and ten (510) consecutive patients and an equal number of controls. The odds ratio (OR) for the association of c-IMT with stroke was 1.68 (1.25 – 2.26; P = 0.0006). However this OR was smaller than the association of both Framingham Cardiovascular Risk Score (OR = 2.16, 1.57 – 2.98; P < 0.0001) and the simple presence of carotid plaque (OR = 2.73, 1.68 - 4.44; P < 0.0001). This implies that c-IMT measurement is less significant as a marker than the presence of plaque. Indeed, in a cohort study of 1348 randomly selected subjects followed for 12.7 years, its contribution to individual risk prediction has been shown to be limited for the general population but may be useful only in high-risk groups (Prati et al. 2008).

The limitation in the measurement of c-IMT is that the average differences in thickness can be below the axial resolution of the transducer frequency. This may be overcome with continuing improvements to resolution capabilities of ultrasound. The most recent study into the capabilities of US suggest that a combination of Tissue Harmonic Imaging (THI), compound imaging and Adaptive Image Processing (AIP) techniques would optimise the evaluation of c-IMT (Yen et al. 2008). Indeed a number of automated scanner specific software applications now exist on modern US scanners.

Another possible indicator is plaque surface irregularity or ulceration. Studies comparing angiographic surface morphology with detailed histology suggest that it is a highly sensitive marker of plaque instability (Lovett et al. 2004). Ulcerated plaques were shown to be more likely to be ruptured than smooth plaques with an odds ratio of 15.4 (95% CI, 2.7 - 87.3, p < 0.001). A large multiethnic B-mode ultrasound study of 1091 plaques in 1939 stroke-free patients found that the presence of irregularity predicted a relative risk of 3.1 (95% CI, 1.1 - 8.5) for ischaemic stroke

(Prabhakaran et al. 2006). Plaque irregularity may also be a potential source of emboli but more research is required to establish whether it is a useful marker for stroke risk. Studies have been carried out using 3D reconstruction of US images to assess the plaque surface for tracking changes in the lesion. Surface morphology analysis has shown that ulceration of 1mm can be quantified and measured for change with time. This suggests that it may be a tool that is sufficiently sensitive to be used in longitudinal studies of direct measurement of plaque volume (Fenster et al. 2006).

An investigation for fibrous cap thickness (FCT) as a stroke indicator has been shown to be feasible. The discrimination between asymptomatic and symptomatic patients was found to be good with a threshold value for FCT of 0.65 mm proving the best classification rate of 82.8% (Devuyst et al. 2005). A thin fibrous cap in combination with only a moderate (30 - 50%) stenosis has been shown to have a high risk of plaque rupture using a flow-plaque interaction model (Li, Howarth, Tang, & Gillard 2006). The values for minimum cap thickness in these two studies corroborate. However there is the consideration that FCT is variable *in vivo* where the model assumes a constant value.

These values for FCT were validated by the Oxford Plaque Study (Redgrave et al. 2008). This study carried out a histological assessment of consecutive carotid plaques and found that of a combination of minimum cap thickness (<200 μm) and a representative or average cap thickness (<500 μm) identified ruptured plaques reliably. Earlier results from the same study (Redgrave et al. 2006) showed that plaque inflammation through macrophage infiltration had strong correlation with cap rupture (odds ratio 3.39, 95% CI 2.31 - 4.98). More recently it has been seen that fibrous cap inflammation is more likely to occur in non-calcified plaques (Wahlgren et al. 2009). This may imply that plaque calcification is a marker for plaque stability. This conflicts with findings from the North Manhattan Study that claimed that the relative risk of vascular events is 2.5 (95% CI 1.0 - 5.8) for patients with plaque calcification (Prabhakaran et al. 2007).

A recent review paper (Carr & Lindner 2009) outlines a number of current ultrasound research imaging techniques that are under evaluation. It highlights the

development of imaging the molecular mediators of atherosclerosis in addition to current conventional practice. Four techniques are outlined; assessment of histomorphometry using radiofrequency analysis, measurement of arterial elastic properties, inspection of the vasa vasorum using contrast agents and imaging of the molecular phenotype with targeted US contrast agents.

Radiofrequency (RF) spectral analysis has shown promise as a tissue characterisation tool in coronary plaques. Raw RF data has been used as it is not limited by post-processing functions such as compression. RF spectral patterns have been shown to characterise fibrous, fibrofatty, lipid pool and calcified tissue (Nair, Obchowski, & Vince 2001). Lipid-laden plaque has been detected, with a sensitivity and specificity of more than 80%, both *in vitro* and *in vivo* using wavelet analysis of RF intravascular ultrasound (IVUS) signals (Murashige et al. 2005). Later studies show a highly accurate correlation of *in vivo* IVUS RF analysis with histopathology (Nasu et al. 2006). Indeed it has been termed "virtual histology" (Konig & Klauss 2007) and VH IVUS software (Real-Time VH, Volcano Corporation, Rancho Cordova, CA, USA) has been developed.

Arterial pressures from pulsatile forces and their related stresses and strains are also a factor in assessment of tissue deformation. The elastic property of the vessel and lesion will vary with tissue composition. It can be measured from information on vascular dimension derived from ultrasound in combination with the related pulse pressure. IVUS elastography is being researched to investigate this mechanical property. Elastography is a strain or stiffness image of the tissue. In order to form the strain image, two images are acquired at different arterial pressures. The strain is determined from an estimation of the displacement of the RF signals between the images. This displacement is measured for multiple layers using a cross-correlation of the depth-gated RF signals. It is then plotted as a colour-coded 2D image that is superimposed on the IVUS image. In a study of fifty four (54) diseased coronary arteries, it has been shown to have a high sensitivity of 88% and specificity of 89% to detect vulnerable plaques *in vitro* (Schaar et al. 2003). Although elastography can show sites of possible rupture, this sensitive technique is subject to significant artifacts such as caused by catheter angulation or those seen in hyper-echoic calcified regions.

IVUS elastography is unlikely to be applied to the carotid artery despite the fact that the feasibility of non-invasive elastography techniques to characterise carotid plaque has been demonstrated. A problem also arises in that calcified plaques cannot be imaged as the acoustic impedance, z, of calcium is so high. In addition, IVUS is costly, invasive and risky.

IVUS palpography works on the same principle as elastography. However it is a surface-based assessment of the mechanical properties of the first 450 μm of the vessel wall. This may be more applicable to plaques as this is the usual site of rupture. Further studies are currently under way following the finding that a high strain spot surrounded by an area of low strain has a high predictive power to identify an *in vitro* plaque that is prone to rupture (Schaar et al. 2006). In addition, a Young's modulus image has been reconstructed from an elastogram to further investigate plaque vulnerability (Baldewsing et al. 2005).

Plaque progression may be signified by vasa vasorum, or a small network of vessels, in the adventitia. This, in turn, may be associated with neovasculature in the atherosclerotic plaque. They have been probed in the carotid artery using dynamic contrast-enhanced (DCE) MRI to produce a quantitative measurement relating to the extent of the vasa vasorum (Kerwin et al. 2008). Similarly non-invasive contrast-enhanced ultrasound (CEU) has been used to detect this neovascularisation and enhance plaque echolucency (Coli et al. 2008). The use of contrast microbubbles in ultrasound may also improve the assessment of plaque irregularity. Other work has shown that CEU images may be segmented in order for tissue characterisation to be performed and the results are being correlated with histology (Molinari et al. 2007). At present, the benefit of such investigation remains to be proven.

The advance in ultrasound technology and transducer electronics has seen a growth in molecular imaging due to the rapid advances in resolution. It may be increasingly feasible to monitor the cellular processes that initiate and promote atherosclerosis and, in turn, increase the instability of the lesion. Microbubbles can be targeted to image endothelial phenotype. Albumin and lipid shells have been shown to bind with activated leukocytes (Lindner et al. 2000) and therefore CEU may be used to

assess their adhesion to inflammatory sites. More recent studies have investigated microbubbles targeted to VCAM-1 (Vascular Cell Adhesion Molecule-1), which is a protein that mediates the adhesion of certain white blood cells to the vascular endothelium. It was shown that signal enhancement was directly related to severity of inflammation in dissected mice aortas (Kaufmann et al. 2007). The targeted microbubbles were seen to attach to the aorta more readily than the control microbubbles.

Transcranial Doppler (TCD) ultrasound has also been suggested as a potential marker for stroke by detection of microembolic signals (MES) from the middle cerebral artery (Markus & MacKinnon 2005). TCD detects the MES from their characteristic sound of the short, sharp rise in signal intensity. Emboli detection has also been suggested as a method to flag up asymptomatic patients (ACS) for surgical intervention (Spence et al. 2005). For patients with moderate to high grade stenosis, emboli were more prevalent in patients with hypoechoic plaques and this may carry potential clinical relevance (Mayor et al. 2003a). Further study is required as only a low number of patients (71) were used in this study. TCD has the benefits in that it is inexpensive and can be performed bedside. However it is labour intensive and cannot determine the exact origin of the MES. Further to that, TCD is not possible in clinical practice for one in ten patients due to the thickness or texture of the temporal bone window (Kwon et al. 2006).

1.8 Summary

Medical ultrasound appears to be the most researched area in the assessment of stroke and carotid plaques. It may be the most suitable diagnostic tool for the assessment of carotid stenosis for a number of reasons. Duplex is a real-time technique that has the advantage of blood flow measurement through the use of modern Doppler techniques displayed alongside the corresponding B-mode image. It is a safe, non-invasive test which does not make use of ionising radiation. Ultrasound is both relatively cheap and readily available. The drawback though is that it can be operator dependant especially if they are poorly trained. However, ultrasound imaging can be performed bedside or in a clinic and, with the progress in the portability of handheld scanners, it may even become an increasingly mobile method. An ultrasound technique may also provide a convenient serial and mass screening examination.

Advances in transducer technology and electronics continue to improve the resolution of ultrasound. This may mean that the fibrous cap and c-IMT will be measured with greater accuracy. It has been shown that characterisation of plaque components is feasible using very high ultrasound frequency, 100 - 200 MHz. Though this was researched for feasibility in IVUS techniques, an ultrasound technique could be developed at the high diagnostic scanning frequencies around 20 MHz to scan the carotid externally. This technique may be able to perform plaque characterisation and therefore assess its vulnerability or stroke risk.

Historically there have been few studies matching the histology to the ultrasound data other than at the macroscopic level. Most histopathogical comparisons to diagnostic data on carotid plaques draws on either the identification of key features within the plaque, the calculation of total proportions of each plaque component or on the specimen classification according to either Beletsky et al. (1996) or the American Heart Association (Stary et al. 1995). Here, we aim to investigate a novel method of matching ultrasound data to histological data in order to derive the sound speed of carotid plaque components.

1.9 Hypothesis

1.9.1 TMM

It is hypothesised that the acoustic properties of a non-commercial agar tissue mimicking material behave consistently at the higher diagnostic frequencies around 20 MHz, which is beyond the established range of 2-15 MHz (Browne, Ramnarine, Watson, & Hoskins 2003). This tissue mimicking material can thus be used as a calibrated material in which to embed carotid atherosclerotic plaque so that this, in turn, can be investigated ultrasonically.

1.9.2 Carotid Plaque Characterisation

It is hypothesised that wave propagation speed of an ultrasonic pulse centred at 20MHz can be measured through a carotid plaque embedded in tissue mimicking material using the pulse-echo substitution technique. Using this composite speed information, it is further hypothesised that this can be compared with histological component data in order to derive sound speed data for each component of carotid plaque. The components of the plaque may then be characterised *in vitro* by measurement of their ultrasonic sound speed using high frequency ultrasound.

References

AbuRahma, A. F., Wulu, J. T., & Crotty, B. 2002, "Carotid plaque ultrasonic heterogeneity and severity of stenosis", *Stroke*, vol. 33, pp. 1772-1775.

AIUM 1995, *Methods for specifying acoustic properties of tissue mimicking phantoms and objects, Stage I*, American Institute of Ultrasound in Medicine Technical Standards Committee, Laurel, MD.

Akashi, N., Kushibiki, J., Chubchi, N., & Dunn, F. 1995, "Acoustic properties of selected bovine tissues in the frequency range 20-200 MHz", *J Acoust Soc Am*, vol. 98, no. 6, pp. 3035-3039.

Axisa, B., Naylor, A. R., London, N., Bell, P. R. F., & Thompson, M. M. 2002, "The influence of carotid plaque morphology on the development of cerebral symptoms", *Vasc Endovasc Surg*, vol. 34, no. 4, pp. 309-318.

Baldewsing, R. A., Schaar, J. A., Mastik, F., Oomens, C. W. J., & van der Steen, A. F. W. 2005, "Assessment of vulnerable plaque composition by matching the deformation of a parametric plaque model to measured plaque deformation", *IEE Trans Med Imaging*, vol. 24, no. 4, pp. 514-528.

Bamber, J. C. 1997, "Acoustical characteristics of biological media," in *Encyclopedia of Acoustics*, M. J. Crocker, ed., Wiley-Interscience, pp. 1703-1726.

Bamber, J. C. & Hill, C. R. 1979, "Ultrasonic attenuation and propagation speed in mammalian as a function of temperature", *Ultrasound Med Biol*, vol. 5, pp. 149-157.

Beletsky, V. Y., Kelley, R. E., Fowler, M., & Phifer, T. 1996, "Ultrasound densitometric analysis of carotid plaque composition: Pathoanatomic correlation", *Stroke*, vol. 27, pp. 2173-2177.

Bhagat, P., Kadaba, M., Ware, R., & Cockerill, W. 1977, "Frequency dependence of acoustic parameters of freshly excised tissues of Sprague dawley rats", *Ultrasonics*, vol. July, pp. 179-182.

Biasi, G. M., Froio, A., Diethrich, E. B., Deleo, G., Galimberti, S., Mingazzini, P., Nicolaides, A. N., Griffin, M., Raithel, D., Reid, D. B., & Valsecchi, M. G. 2004, "Carotid plaque echolucency increases the risk of stroke in carotid stenting: The Imaging in Carotid Angioplasty and Risk of Stroke (ICAROS) Study ", *Circulation*, vol. 110, pp. 756-762.

Biasi, G. M., Sampaolo, A., Mingazzini, P., De Amicis, P., El-Barghouty, N. M., & Nicolaides, A. N. 1999, "Computer analysis of ultrasonic plaque echolucency in identifying high risk carotid bifurcation lesions", *Eur J Endovasc Surg*, vol. 17, pp. 476-479.

Bots, M. L., Hoes, A. W., Koudstaal, P. J., Hofman, A., & Grobbee, D. E. 1997, "Common carotid intima-media thickness and risk of stroke and myocardial infarction: The Rotterdam study", *Circulation*, vol. 96, pp. 1432-1437.

Boules, T. N., Proctor, M. C., Aref, A., Upchurch, G. R., Stanley, J. C., & Henke, P. K. 2005, "Carotid endarterectomy remains the standard of care, even in high-risk surgical patients", *Annals of Surgery*, vol. 241, no. 2, pp. 356-363.

Bridal, S. L., Fornes, P., Bruneval, P., & Berger, G. 1997, "Correlation of ultrasonic attenuation (30 to 50 MHz) and constituents of atherosclerotic plaque", *Ultrasound Med Biol*, vol. 23, no. 5, pp. 691-703.

Browne, J. E., Ramnarine, K. V., Hoskins, P. R., & Watson, A. J. 2002, "A comparative study of the physical properties of five commonly used ultrasound test phantoms", *J Ultrasound Med*, vol. 21, no. S9.

Browne, J. E., Ramnarine, K. V., Watson, A. J., & Hoskins, P. R. 2003, "Assessment of the acoustic properties of common tissue-mimicking test phantoms", *Ultrasound Med Biol*, vol. 29, no. 7, pp. 1053-1060.

Bude, R. O. & Adler, R. S. 1995, "An easily made, low-cost, tissue-like ultrasound phantom material", *J Clin Ultrasound*, vol. 23, pp. 271-273.

Burlew, M. M., Madsen, E. L., Zagzebski, J. A., Banjavic, R. A., & Sum, S. W. 1980, "A new ultrasound tissue-equivalent material", *Radiology*, vol. 134, pp. 517-520.

Bush, N. L. & Hill, C. R. 1983, "Gelatine-alginate complex gel: A new acoustically tissue-equivalent material", *Ultrasound Med Biol*, vol. 9, no. 5, pp. 479-484.

Cai, J.-M., Hatsukami, T. S., Ferguson, M. S., Kerwin, W. S., Saam, T., Chu, B., Takaya, N., Polissar, N. L., & Yuan, C. 2005a, "*In vivo* quantitative measurement of intact fibrous cap and lipid-rich necrotic core size in atherosclerotic carotid plaque: Comparison of high resolution, contrast-enhanced magnetic resonance imaging and histology", *Circulation*, vol. 112, pp. 3437-3444.

Cai, J.-M., Hatsukami, T. S., Ferguson, M. S., Small, R., Polissar, N. L., & Yuan, C. 2002, "Classification of human carotid atherosclerotic lesions with *in vivo* multicontrast Magnetic Resonance Imaging", *Circulation*, vol. 106, pp. 1368-1373.

Cai, J., Hatsukami, T. S., Ferguson, M. S., Kerwin, W. S., Saam, T., Chu, B., Takaya, N., Polissar, N. L., & Yuan, C. 2005b, "In vivo quantitative measurement of intact fibrous cap and lipid-richnecrotic core size in atherosclerotic carotid plaque: Comparison of high resolution, contrast-enhanced magnetic resonance imaging and histology", *Circulation*, vol. 112, pp. 3437-3444.

Carey, S. J., Gregory, C. M., Brewin, M. P., Birch, M. J., Ng, S., & Hatfield, J. 2004, "PVdF array characterisation for high frequency ultrasonic imaging", *Ultrasonics Symposium*, vol. 3, pp. 1930-1933.

Carr, C. L. & Lindner, J. R. 2009, "Ultrasound imaging of atherosclerotic plaques", *Current Cardiovascular Imaging Reports*, vol. 2, no. 1, pp. 24-32.

Casscells, W., Vaughn, W. K., McAllister, H., Willerson, J. T., Hathorn, B., David, M., Krabach, T., & Bearman, G. 1996, "Thermal detection of cellular infiltrates in living atherosclerotic plaques: possible implications for plaque rupture and thrombosis", *The Lancet*, vol. 347, no. 9013, pp. 1447-1449.

Chaturvedi, S., Bruno, A., Feasby, T., Holloway, R., Benavente, O., Cohen, S. N., Cote, R., Hess, D., Saver, J., Spence, J. D., Stern, B., & Wilterdink, J. 2005, "Carotid

endarterectomy - An evidence-based review: Report of the Therapeutics and Technology Assessment Subcommittee of the American Academy of Neurology", *Neurology*, vol. 65, pp. 794-801.

Chivers, R. C. & Parry, R. J. 1978, "Ultrasonic velocity and attenuation in mammalian tissues", *J Acoust Soc Am*, vol. 63, no. 3, pp. 940-953.

Cina, C. S., Clase, C. M., & Haynes, R. B. 1999, "Carotid endarterectomy for symptomatic carotid stenosis", *Cochrane Database Syst Rev* no. 3, p. CD001081.

Clarke, R. L., Bush, N. L., & Ter Haar, G. 2003, "The changes in acoustic attenuation due to *in vitro* heating", *Ultrasound Med Biol*, vol. 29, no. 1, pp. 127-135.

Clarke, S. E., Hammond, R. R., Mitchell, J. R., & Rutt, B. K. 2003, "Quantitative assessment of carotid plaque composition using multicontrast MRI and registered histology", *Magn Reson Med*, vol. 50, no. 6, pp. 1199-1208.

Coleman, D. P., Rakebrandt, F., Pugh, N. D., Crawford, D. C., & Woodcock, J. P. 2005, "Development and validation of an *in vivo* analysis tool to identify changes in carotid plaque tissue types in serial 3D ultrasound scans", *Ultrasound Med Biol*, vol. 31, no. 3, pp. 329-335.

Coli, S., Magnoni, M., Sangiorgi, G., Marrocco-Trischitta, M. M., Melisurgo, G., Mauriello, A., Spagnoli, L. G., Chiesa, R., Cianflone, D., & Maseri, A. 2008, "Contrast-enhanced ultrasound imaging of intraplaque neovascularization in carotid arteries", *J Am Coll Cardiol*, vol. 52, no. 3, pp. 223-230.

Coward, L. J., Featherstone, R. L., & Brown, M. M. 2005, "Safety and efficacy of endovascular treatment of carotid artery stenosis compared with carotid endarterectomy: A Cochrane systematic review of the randomized evidence", *Stroke*, vol. 36, pp. 905-911.

de Bray, J. M., Baud, J. M., Delanoy, P., Camuzat, J. P., Dehans, V., Descamp-le-Chevoir, J., Launay, J. R., Luizy, F., Sentou, Y., & Cales, P. 1998, "Reproducibility in ultrasonic characterization of carotid plaques", *Cerebrovasc Dis*, vol. 8, no. 5, pp. 273-277.

De Korte, C. L., Van der Steen, A. F. W., & Thijssen, J. M. 1994, "Acoustic velocity and attenuation of eye tissues at 20 MHz", *Ultrasound Med Biol*, vol. 20, no. 5, pp. 471-480.

de Weert, T. T., Ouhlous, M., Meijring, E., Zondervan, P. E., Hendriks, J. M., van Sambeek, M. R. H. M., Dippel, D. W. J., & van der Lugt, A. 2006, "*In vivo* characterization and quantification of atherosclerotic carotid plaque components with multidetector Computed Tomography and histopathological correlation", *Arterioscler Thromb Vasc Biol*, vol. 26, pp. 2366-2372.

Denzel, C., Balzer, K., Muller, K.-M., Fellner, F., Fellner, C., & Lang, W. 2003, "Relative value of normalised sonographic *in vitro* analysis of arteriosclerotic plaques of internal carotid artery", *Stroke*, vol. 34, pp. 1901-1906.

Devuyst, G., Ruchat, P., Karapanayiotides, T., Jonasson, L., Cuisinaire, O., Lobrinus, J.-A., Pusztaszeri, M., Kalangos, A., Despland, P.-A., Thiran, J.-P., & Bogousslavsky, J. 2005, "Ultrasound measurement of the fibrous cap in symptomatic and asymptomatic atheromatous carotid plaques", *Circulation*, vol. 111, pp. 2776-2782.

Dineley, J., Meagher, S., Poepping, T. L., McDicken, W. N., & Hoskins, P. R. 2006, "Design and characterisation of a wall motion phantom", *Ultrasound Med Biol*, vol. 32, no. 9, pp. 1349-1357.

Duck, F. A. 1990, *Physical properties of tissue - A comprehensive reference book* Academic Press.

ECST 1998, "Randomised trial of endarterectomy for recently symptomatic carotid stenosis: final reults of the MRC European Carotid Surgery Trial (ECST)", *Lancet*, vol. 351, pp. 1379-1387.

El-Barghouty, N. M., Nicolaides, A. N., Bahal, V., Geroulakos, G., & Androulakis, A. 1996, "The identification of the high risk carotid plaque", *Eur J Endovasc Surg*, vol. 11, pp. 470-478.

Executive Committee for the Asymptomatic Carotid Atherosclerosis Study 1995, "Endarterectomy for asymptomatic carotid artery stenosis", *JAMA*, vol. 273, no. 18, pp. 1421-1428.

Falkowski, A., Parafiniuk, M., Poncyljusz, W., Kaczmarczyk, M., & Wilk, G. 2007, "Ultrasonographic and histological analysis of atheromatous plaques in carotid arteries and apoplectic complications", *Med Sci Monit*, vol. 13, no. 1, pp. 78-82.

Farooq, M. U. 2009, "The role of optical coherence tomography in vascular medicine", *Vasc Med*, vol. 14, no. 1, pp. 63-71.

Feeley, T. M., Leen, E. J., Colgan, M.-P., Moore, D. J., Hourihane, D. O., & Shanik, G. D. 1991, "Histologic characteristics of carotid artery plaque", *J Vasc Surg*, vol. 13, no. 5, pp. 719-724.

Fenster, A., Blake, C., Gyacskov, I., Landry, A., & Spence, J. D. 2006, "3D ultrasound analysis of carotid plaque volume and surface morphology", *Ultrasonics*, vol. 44, no. Suppl 1, p. e153-e157.

Fromageau, J., Gennisson, J.-L., Schmitt, C., Maurice, R. L., Mongrain, R., & Cloutier, G. 2007, "Estimation of Polyvinyl Alcohol Cryogel mechanical properties with four ultrasound elastography methods and comparison with gold standard testings", *IEEE Trans Ultrason Ferroelectr Freq Control*, vol. 54, no. 3, pp. 498-509.

Gammell, P. M., Le Croisette, D. H., & Heyser, R. C. 1979, "Temperature and frequency dependence of ultrasonic attenuation in selected tissues", *Ultrasound Med Biol*, vol. 5, pp. 269-277.

Gao, P., Chen, Z.-Q., Bao, Y.-H., Jiao, L.-Q., & Ling, F. 2007, "Correlation between carotid intraplaque hemorrhage and clinical symptoms", *Stroke*, vol. 38, pp. 2382-2390.

Glagov, S., Weisenberg, E., Zarins, C. K., Stankunavicius, R., & Kolettis, G. J. 1987, "Compensatory enlargement of human atherosclerotic coronary arteries", *N Engl J Med*, vol. 316, pp. 1371-1375.

Goldstein, A. 2000, "The effect of acoustic velocity on phantom measurements", *Ultrasound Med Biol*, vol. 26, pp. 1133-1143.

Goss, S. A., Johnston, R. L., & Dunn, F. 1978, "Comprehensive compilation of empirical ultrasonic properties of mammalian tissues", *J Acoust Soc Am*, vol. 64, no. 2, pp. 423-457.

Goss, S. A., Johnston, R. L., & Dunn, F. 1980, "Compilation of empirical ultrasonic properties of mammalian tissues. II", *J Acoust Soc Am*, vol. 68, pp. 93-108.

Greenleaf, J. F., Duck, F. A., Samayoa, W. F., & Johnson, S. A. 1974, "Ultrasonic data acquisition and processing system for atherosclerotic tissue characterisation", *Proc IEEE Ultrason Symp* pp. 738-743.

Grogan, J. K., Shaalan, W. E., Cheng, H., Gewertz, B., Desai, T., Schwarze, G., Glagov, S., Lozanski, L., Griffin, A., Castilla, M., & Bassiouny, H. S. 2005, "B-mode ultrasonographic characterization of carotid atherosclerotic plaques in symptomatic and asymptomatic patients", *J Vasc Surg*, vol. 42, no. 3, pp. 435-441.

Grønholdt, M.-L. M., Nordestgaard, B. G., Schroeder, T. V., Vorstrup, S., & Sillesen, H. 2001, "Ultrasonic echolucent carotid plaques predict future strokes", *Circulation*, vol. 104, pp. 68-73.

Grønholdt, M.-L. M., Wiebe, B., Laursen, H., Nielsen, T. G., Schroeder, T. V., & Sillesen, H. 1997, "Lipid-rich carotid artery plaques appear echolucent on ultrasound B-mode images and may be associated with intraplaque haemorrhage", *Eur J Endovasc Surg*, vol. 14, no. 6, pp. 439-445.

Herzig, R., Burval, S., Krupka, B., Vlachova, I., Urbanek, K., & Mares, J. 2004, "Comparison of ultrasonography, CT angiography and digital subtraction angiography in severe carotid stenoses", *Eur J Neurology*, vol. 11, pp. 774-781.

Hollander, M., Hak, A. E., Koudstaal, P. J., Bots, M. L., Grobbee, D. E., Hofman, A., Witteman, J. C. M., & Breteler, M. M. B. 2003, "Comparison between measures of atherosclerosis and risk of stroke: The Rotterdam Study", *Stroke*, vol. 34, pp. 2367-2373.

ICRU 1998, *Report 61: Tissue substitutes, phantoms and computational modelling in medical ultrasound*, International Commission on Radiation Units and Measurements, Bethseda, MD, 61.

IEC 1996, *Ultrasonics - Real-time pulse-echo systems - Guide for test procedures to determine performance specifications, IEC Publication 1390*, International Electrotechnical Commission, Geneva.

IEC 2001, *Ultrasonics - Flow measurement systems - Flow test object, Publication number 61685*, International Electrotechnical Commission, 61685.

Kakkos, S. K., Stevens, J. M., Nicolaides, A. N., Kyriacou, E., Pattichis, C. S., Geroulakos, G., & Thomas, D. 2007, "Texture analysis of ultrasonic images of symptomatic carotid plaques can identify those plaques associated with ipsilateral embolic brain infarction", *Eur J Endovasc Surg*, vol. 33, pp. 422-429.

Kampschulte, A., Ferguson, M. S., Kerwin, W. S., Polissar, N. L., Chu, B., Saam, T., Hatsukami, T. S., & Yuan, C. 2004, "Differentiation of intraplaque versus juxtaluminal hemorrhage/thrombus in advanced human carotid atherosclerotic lesions by *in vivo* magnetic resonance imaging", *Circulation*, vol. 110, pp. 3239-3244.

Kaufmann, B. A., Sanders, J. M., Davis, C., Xie, A., Aldred, P., Sarembock, I. J., & Lindner, J. R. 2007, "Molecular imaging of inflammation in atherosclerosis with targeted ultrasound detection of Vascular Cell Adhesion Molecule-1", *Circulation*, vol. 116, pp. 276-284.

Kavey, R. W., Daniels, S. R., Lauer, R. M., Atkins, D. L., Hayman, L. L., & Taubert, K. 2003, "American heart association guidelines for primary prevention of atherosclerotic cardiovascular disease beginning in childhood", *Circulation*, vol. 107, pp. 1562-1566.

Kawasaki, M., Takatsu, H., Noda, T., Ito, Y., Kunishama, A., Arai, M., Nishigaki, K., Takemura, G., Morita, N., Minatoguchi, S., & Fujiwara, H. 2001, "Noninvasive quantitative tissue characterization and two-dimensional color-coded map of human atherosclerotic lesions using ultrasound integrated backscatter", *J Am Coll Cardiol*, vol. 38, no. 2, pp. 486-492.

Kawasaki, M., Takatsu, H., Noda, T., Sano, K., Ito, Y., Hayakawa, K., Tsuchiya, K., Arai, M., Nishigaki, K., Takemura, G., Minatoguchi, S., Fujiwara, T., & Fujiwara, H. 2002, "*In vivo* quantitative tissue characterisation of human coronary arterial plaques by use of integrated backscatter intravascular ultrasound and comparison with angioscopic findings", *Circulation*, vol. 105, pp. 2487-2492.

Kern, R., Szabo, K., Hennerici, M., & Meairs, S. 2004, "Characterization of carotid artery plaques using real-time compound imaging B-mode ultrasound", *Stroke*, vol. 35, pp. 870-875.

Kerwin, W. S., Hooker, A., Spilker, M., Vicini, P., Ferguson, M. S., Hatsukami, T. S., & Yuan, C. 2003, "Quantitative magnetic resonance imaging analysis of neovasculature volume in carotid atherosclerotic plaque", *Circulation*, vol. 107, pp. 851-856.

Kerwin, W. S., O'Brien, K. D., Ferguson, M. S., Polissar, N. L., Hatsukami, T. S., & Yuan, C. 2006, "Inflammation in carotid atherosclerotic plaque: A dynamic contrast-enhanced MR imaging study", *Radiology*, vol. 241, no. 2, pp. 459-468.

Kerwin, W. S., Oikawa, M., Yuan, C., Jarvik, G. P., & Hatsukami, T. S. 2008, "MR imaging of adventitial vasa vasorum in carotid atherosclerosis", *Magn Reson Med*, vol. 59, pp. 507-514.

Kietselaer, B. L. J. H., Reuteningsperger, C. P. M., Heidendal, G. A. K., Daemen, M. J. A. P., Mess, W. H., Hofstra, L., & Narula, J. 2004, "Noninvasive detection of plaque instability with use of radiolabeled annexin A5 in patients with carotid artery atherosclerosis", *N Engl J Med*, vol. 350, no. 14, pp. 1472-1473.

Kofoed, S. C., Grønholdt, M.-L. M., Wilhjelm, J. E., Bismuth, J., & Sillesen, H. 2001, "Real-time spatial compound imaging improves reproducibility in the evaluation of atherosclerotic carotid plaques", *Ultrasound Med Biol*, vol. 27, no. 10, pp. 1311-1317.

Kondo, T. & Kitatuji, M. 2005, "New tissue mimicking materials for ultrasound phantoms", *IEEE Ultrasonics Symposium* pp. 1664-1667.

Konig, A. & Klauss, V. 2007, "Virtual Histology", *Heart*, vol. 93, pp. 977-982.

Kooi, M. E., Cappendijk, V. C., Cleutjens, K. B. J. M., Kessels, A. G. H., Kitslaar, P. J. E. H. M., Borgers, M., Frederik, P. M., Daemen, M. J. A. P., & van Engelshoven, J. M. A. 2003, "Accumulation of Ultrasmall Superparamagnetic Particles of Iron Oxide in human atherosclerotic plaques can be detected by *in vivo* Magnetic Resonance Imaging", *Circulation*, vol. 107, pp. 2453-2458.

Kwon, J. H., Kim, J. S., Kang, D. W., Bae, K. S., & Kwon, S. U. 2006, "The thickness and texture of temporal bone in brain CT predict acoustic window failure of transcranial Doppler", *J Neuroimaging*, vol. 16, pp. 347-352.

Lal, B. K., Hobson, R. W., Hameed, M., Pappas, P. J., Padberg, F. T., Jamil, Z., & Duran, W. N. 2006, "Noninvasive identification of the unstable carotid plaque", *Ann Vasc Surg*, vol. 20, no. 2, pp. 167-174.

Landry, A., Spence, J. D., & Fenster, A. 2004, "Measurement of carotid plaque volume by 3-dimensional ultrasound", *Stroke*, vol. 35, no. 4, pp. 864-869.

Li, Z.-Y., Howarth, S. P. S., Tang, T., Graves, M. J., U-King-Im, J. M., Trivedi, R. A., Kirkpatrick, P. J., & Gillard, J. H. 2007, "Structural analysis and magnetic resonance imaging predict plaque vulnerability: A study comparing symptomatic and asymptomatic individuals", *J Vasc Surg*, vol. 45, no. 768, p. 775.

Li, Z.-Y., Howarth, S. P. S., Tang, T. Y., & Gillard, J. H. 2006, "How critical is fibrous cap thickness to carotid plaque stability? A flow-plaque interaction model", *Stroke*, vol. 37, pp. 1-5.

Liasis, N., Klonaris, C., Katsargyris, A., Georgopoulos, S., Labropoulos, N., Tsigris, C., Giannopoulos, A., & Bastounis, E. 2008, "The use of Speckle Reduction Imaging (SRI) Ultrasound in the characterization of carotid artery plaques", *Eur J Radiol*, vol. 65, pp. 427-433.

Lindner, J. R., Coggins, M. P., Kaul, S., Klibanov, A. L., Brandenburger, G. H., & Ley, K. 2000, "Microbubble persistence in the microcirculation during ischemia / reperfusion and inflammation is caused by integrin- and complement-mediated adherence to activated leukocytes", *Circulation*, vol. 101, pp. 668-675.

Lizzi, F. L., Alam, S. K., Mikaelian, S., Lee, P., & Feleppa, E. J. 2006, "On the statistics of ultrasonic spectral parameters", *Ultrasound Med Biol*, vol. 32, no. 11, pp. 1671-1685.

Lizzi, F. L., Astor, M., Fellepa, E. J., & Shao, M. 1997, "Statistical framework for ultrasonic spectral parameter imaging", *Ultrasound Med Biol*, vol. 23, no. 9, pp. 1371-1382.

Lovett, J. K., Gallagher, P. J., Hands, L. J., Walton, J., & Rothwell, P. M. 2004, "Histological correlates of carotid plaque surface morphology on lumen contrast imaging", *Circulation*, vol. 110, pp. 2190-2197.

Lu, Z. F., Zagzebski, J. A., Madsen, E. L., & Dong, F. 1995, "A method for estimating an overlying layer correction in quantitative ultrasound imaging", *Ultrason Imaging*, vol. 17, pp. 269-290.

Lyons, M. E., Chivers, R. C., & Parker, K. J. 1986, "Absorption dominates attenuation in soft tissues", *IEEE Ultrasonics Symposium*, vol. 86CH2375-4, pp. 871-873.

Madsen, E. L. 1999, "Interlaboratory comparison of ultrasonic backscatter, attenuation and speed measurements", *J Ultrasound Med*, vol. 18, pp. 615-631.

Madsen, E. L., Frank, G. R., Carson, P. L., Edmonds, P. D., Frizzell, L. A., Herman, B. A., Kremkau, F. K., O'Brien, W. D., Parker, K. J., & Robinson, R. A. 1986, "Interlaboratory comparison of ultrasonic attenuation and speed measurements", *J Ultrasound Med*, vol. 5, no. October, pp. 569-576.

Madsen, E. L., Hobson, M. A., Shi, H., Varghese, T., & Frank, G. R. 2005, "Tissue-mimicking agar/gelatin materials for use in heterogenous elastography phantoms", *Phys Med Biol*, vol. 50, pp. 5597-5618.

Madsen, E. L., Zagzebski, J. A., Banjavic, R. A., & Jutila, R. E. 1978, "Tissue mimicking materials for ultrasound phantoms", *Med Phys*, vol. 5, no. 5, pp. 391-394.

Madsen, E. L., Zagzebski, J. A., & Frank, G. R. 1982, "Oil-in-gelatin dispersions for use as ultrasonically tissue-mimicking materials", *Ultrasound Med Biol*, vol. 8, no. 3, pp. 277-287.

Markus, H. S. & MacKinnon, A. 2005, "Asymptomatic embolization detected by Doppler ultrasound predicts stroke risk in symptomatic carotid artery stenosis", *Stroke*, vol. 36, pp. 971-975.

Mathiesen, E. B., Bonaa, K., & Joakimsen, O. 2001, "Echolucent plaques are associated with high risk of ischemic cerebrovascular events in carotid stenosis: The Tromsø study", *Circulation*, vol. 103, pp. 2171-2175.

Mayor, I., Comelli, M., Vassileva, E., Burkhard, P., & Sztajzel, R. 2003a, "Microembolic signals and carotid plaque morphology: a study of 71 patients with moderate or high grade carotid stenosis", *Acta Neurol Scand*, vol. 108, pp. 114-117.

Mayor, I., Momijan, S., Lalive, P., & Sztajzel, R. 2003b, "Carotid plaque: comparison between visual and grey scale median analysis", *Ultrasound Med Biol*, vol. 29, no. 7, pp. 961-966.

Meagher, S., Poepping, T. L., Ramnarine, K. V., Black, R. A., & Hoskins, P. R. 2007, "Anatomical flow phantoms of the nonplanar carotid bifurcation, Part II: Experimental validation with Doppler ultrasound", *Ultrasound Med Biol*, vol. 33, no. 2, pp. 303-310.

Meissner, O. A., Rieber, J., Babaryka, G., Oswald, M., Reim, S., Siebert, U., Redel, T., Reiser, M., & Mueller-Lisse, U. 2006, "Intravascular optical coherence tomography: comparison with histopathology in atherosclerotic peripheral artery specimens", *J Vasc Interv Radiol*, vol. 17, no. 2pt1, pp. 343-349.

Meschia, J. F., Brott, T. G., & Hobson, R. W. 2007, "Diagnosis and invasive management of carotid atherosclerotic stenosis", *Mayo Clin Proc*, vol. 82, no. 7, pp. 851-858.

Mitsumori, L. M., Hatsukami, T. S., Ferguson, M. S., Kerwin, W. S., Cai, J.-M., & Yuan, C. 2003, "*In vivo* accuracy of multisequence MR imaging for identifying unstable fibrous caps in advanced human carotid plaques", *J Mag Res Imaging*, vol. 17, pp. 410-420.

Molinari, F., Liboni, W., Pavanelli, E., Giustetto, P., Badalamenti, S., & Suri, J. S. 2007, "Accurate and automatic carotid plaque characterization in contrast enhanced 2-D ultrasound images", *Proc IEEE EMBS*, vol. 29th, pp. 335-449.

Montauban van Swijndregt, A. D., Elbers, H. R. J., Moll, F. L., de Letter, J., & Ackerstaff, R. G. A. 1999, "Cerebral ischemic disease and morphometric analyses of carotid plaques", *Ann Vasc Surg*, vol. 13, pp. 468-474.

Moreno, P. R., Lodder, R. A., Purushothaman, K. R., Charash, W. E., O'Connor, W. N., & Muller, J. E. 2002, "Detection of lipid pool, thin fibrous cap, and inflammatory cells in human aortic atherosclerotic plaques by Near-Infrared Spectroscopy", *Circulation*, vol. 105, pp. 923-927.

Murashige, A., Hiro, T., Fujii, T., Imoto, K., Murata, T., Fukumoto, Y., & Matsuzaki, M. 2005, "Detection of lipid-laden atherosclerotic plaque by wavelet analysis of

radiofrequency intravascular ultrasound signals", *J Am Coll Cardiol*, vol. 45, no. 12, pp. 1954-1960.

Naghavi, M., Madjid, M., Khan, M. R., Mohammadi, R. M., Willerson, J. T., & Casscells, S. W. 2001, "New developments in the detection of vulnerable plaque", *Current Atherosclerosis Reports*, vol. 3, pp. 125-135.

Nair, A., Obchowski, N., & Vince, D. G. 2001, "Assessing spectral algorithms to predict atherosclerosis plaque composition with normalized and raw intravascular ultrasound data", *Ultrasound Med Biol*, vol. 27, no. 10, pp. 1319-1331.

Nandalur, K. R., Baskurt, E., Hagspiel, K. D., Phillips, C. D., & Kramer, C. M. 2005, "Calcified carotid atherosclerotic plaque is associated less with ischemic symptoms than is non-calcified plaque on MDCT", *AJR*, vol. 184, pp. 295-298.

NASCET 1991, "Beneficial effect of carotid endarterectomy in symptomatic patients with high grade carotid stenosis", *N Engl J Med*, vol. 325, pp. 445-453.

Nasu, K., Tsuchikane, E., Katoh, O., Vince, D. G., Virmani, R., Surmely, J.-F., Murata, A., Takeda, Y., Ito, T., Ehara, M., Matsubara, T., Terashima, M., & Suzuki, T. 2006, "Accuracy of *in vivo* coronary plaque morphology assessment: A validation study of *in vivo* virtual histology compared with *in vitro* histopathology", *J Am Coll Cardiol*, vol. 47, no. 12, pp. 2405-2412.

Nederkoorn, P. J., van der Graaf, Y., & Hunink, M. 2003, "Duplex ultrasound and magnetic resonance angiography compared with digital subtraction angiography in carotid artery stenosis: A systematic review", *Stroke*, vol. 34, pp. 1324-1332.

Netuka, D., Benes, V., Mandys, V., Hlasenska, J., Burkert, J., & Benes, V. Jr. 2006, "Accuracy of angiography and Doppler ultrasonography in the detection of carotid stenosis: a histopathological study of 123 cases", *Acta Neurchir*, vol. 148, pp. 511-520.

O'Leary, D. H., Polak, J. F., Kronmal, R. A., Manolio, T. A., Burke, G. L., & Wolfson, S. K. Jr. 1999, "Carotid artery initima and media thickness as a risk factor for myocardial infarction and stroke in older adults", *N Engl J Med*, vol. 340, pp. 14-22.

Oates, C. P., Naylor, A. R., Hartshorne, T., Charles, S. M., Fail, T., Humphries, K., Aslam, M., & Khodabaksh, P. 2008, "Joint recommendations for reporting carotid ultrasound investigations in the United Kingdom", *Eur J Endovasc Surg*, vol. 37, no. 3, pp. 251-261.

Olesen, J. & Leonardi, M. 2003, "The burden of brain diseases in Europe", *Eur J Neurology*, vol. 10, pp. 471-477.

Petersen, S., Peto, V., Rayner, M., Leal, J., Luengo-Fernandez, R., & Gray, A. 2005, "European Cardiovascular Disease Statistics", *British Heart Foundation*.

Picano, E., Landini, L., Distante, A., Benassi, A., Sarnelli, R., & L'Abbate, A. 1985, "Fibrosis, lipids, and calcium in human atherosclerotic plaque. *In vitro* differentiation from normal aortic walls by ultrasonic attenuation", *Circ Res*, vol. 56, pp. 556-562.

Poepping, T. L., Nikolov, H. N., Rankin, R. N., Lee, M., & Holdsworth, D. W. 2002, "An in-vitro system for Doppler ultrasound flow studies in the stenosed carotid artery bifurcation", *Ultrasound Med Biol*, vol. 28, no. 4, pp. 495-506.

Polak, J. F., Shemanski, L., & O'Leary, D. H. 1998, "Hypoechoic plaque at US of the carotid artery: An independent risk factor for incident stroke in adults aged 65 years or older", *Radiology*, vol. 208, no. 3, pp. 648-654.

Prabhakaran, S., Rundek, T., Ramas, R., Elkind, M. S., Paik, M. C., Boden-Albala, B., & Sacco, R. L. 2006, "Carotid plaque surface irregularity predicts ischemic stroke: The Northern Manhattan Study", *Stroke*, vol. 37, pp. 2696-2701.

Prabhakaran, S., Singh, R., Zhou, X., Ramas, R., Sacco, R. L., & Rundek, T. 2007, "Presence of calcified carotid plaque predicts vascular events: The Northern Manhattan Study", *Atherosclerosis*, vol. 195, no. 1, p. e197-e201.

Prati, P., Tosetto, A., Vanuzzo, D., Bader, G., Casaroli, M., Canciani, L., Castellani, S., & Touboul, P.-J. 2008, "Carotid intima media thickness and plaques can predict the occurrence of ischemic cerebrovascular events", *Stroke*, vol. 39, pp. 2470-2476.

Ramnarine, K. V., Anderson, T., & Hoskins, P. R. 2001, "Construction and geometric stability of physiological flow rate wall-less stenosis phantoms", *Ultrasound Med Biol*, vol. 27, pp. 245-250.

Ramnarine, K. V., Kanber, B., & Panerai, R. B. 2004, "Assessing the performance of vessel wall tracking algorithms: the importance of the test phantom", *Journal of Physics: Conference Series*, vol. 1, pp. 199-204.

Redgrave, J. N. E., Gallagher, P. J., Lovett, J. K., & Rothwell, P. M. 2008, "Critical cap thickness and rupture in symptomatic carotid plaques: The Oxford Plaque Study", *Stroke*, vol. 39, pp. 1722-1729.

Redgrave, J. N. E., Lovett, J. K., Gallagher, P. J., & Rothwell, P. M. 2006, "Histological assessment of 526 symptomatic carotid plaques in relation to the nature and timing of ischemic symptoms. The Oxford Plaque Study", *Circulation*, vol. 113, pp. 1-9.

Reiter, M., Horvat, R., Puchner, S., Rinner, W., Polterauer, P., Lammer, J., Minar, E., & Bucek, R. A. 2007, "Plaque imaging of the internal carotid artery - Correlation of B-flow imaging with histopathology", *Am J Neuroradiol*, vol. 28, pp. 122-126.

Richardson, P. D., Davies, M. J., & Born, G. V. R. 1989, "Influence of plaque configuration and stress distribution on fissuring of coronary atherosclerotic plaques", *Lancet*, vol. 2, no. 8669, pp. 941-944.

Rooney, J. A., Gammell, P. M., Hestenes, J. D., Chin, H. P., & Blankenhorn, D. H. 1982, "Velocity and attenuation of sound in arterial tissues", *J Acoust Soc Am*, vol. 71, pp. 462-466.

Rothwell, P. M., Eliasziw, M., Gutnikov, S. A., Warlow, C. P., & Barnett, H. J. M. 2004, "Endarterectomy for symptomatic carotid stenosis in relation to clinical subgroups and timing of surgery", *Lancet*, vol. 363, pp. 915-924.

Rothwell, P. M., Gutnikov, S. A., & Warlow, C. P. 2003, "Reanalysis of the final results of the European Carotid Surgery Trial", *Stroke*, vol. 34, pp. 514-523.

Rudd, J. H., Myers, K. S., Bansilal, S., Machac, J., Pinto, C. A., Tong, C., Rafique, A., Hargreaves, R., Faroukh, M., Fuster, V., & Fayad, Z. A. 2008, "Atherosclerosis inflammation imaging with 18F-FDG PET: carotid, iliac, and femoral uptake

reproducibility, quantification methods and recommendations", *J Nucl Med*, vol. 49, pp. 871-878.

Saam, T., Cai, J.-M., Ma, L., Cai, Y.-Q., Ferguson, M. S., Polissar, N. L., Hatsukami, T. S., & Yuan, C. 2006, "Comparison of symptomatic and asymptomatic atherosclerotic carotid plaque features with *in vivo* MR Imaging", *Radiology*, vol. 240, no. 2, pp. 464-472.

Saam, T., Hatsukami, T. S., Takaya, N., Chu, B., Underhill, H. R., Kerwin, W. S., Cai, J.-M., Ferguson, M. S., & Yuan, C. 2007, "The vulnerable, or high-risk, atherosclerotic plaque: Noninvasive MR imaging for characterization and assessment", *Radiology*, vol. 244, no. 1, pp. 64-77.

Saba, L., Caddeo, G., Sanfilippo, R., Montisci, R., & Mallarini, G. 2007, "CT and Ultrasound in the study of ulcerated carotid plaque compared with surgical results: Potentialities and advantages of multidetector row CT angiography", *Am J Neuroradiol*, vol. 28, pp. 1061-1066.

Saijo, Y., dos Santos Filho, E., Sasaki, H., Yambe, T., Tanaka, M., Hozumi, N., Kobayashi, K., & Okada, N. 2007, "Ultrasonic tissue characterization of atherosclerosis by a speed-of-sound microscanning system", *IEEE Trans Ultrason Ferroelectr Freq Control*, vol. 54, no. 8, pp. 1571-1577.

Saijo, Y., Hozumi, N., Lee, C., Nagao, M., Kobayashi, K., Oakada, N., Tanaka, N., dos Santos Filho, E., Sasaki, H., Tanaka, M., & Yambe, T. 2006, "Ultrasonic speed microscopy for imaging of coronary artery", *Ultrasonics*, vol. 44, p. e51-e55.

Saijo, Y., Miyakaya, T., Sasaki, H., Tanaka, M., & Nitta, S.-I. 2004, "Acoustic properties of aortic aneurysm obtained with scanning acoustic microscopy", *Ultrasonics*, vol. 42, pp. 695-698.

Saijo, Y., Ohashi, T., Sasaki, H., Sato, M., Jorgensen, C. S., & Nitta, S.-I. 2001, "Application of scanning acoustic microscopy for assessing stress distribution in atherosclerotic plaque", *Ann Biomed Eng*, vol. 29, pp. 1048-1053.

Saijo, Y., Sasaki, H., Okawai, H., Nitta, S.-I., & Tanaka, M. 1998, "Acoustic properties of atherosclerosis of human aorta obtained with high frequency ultrasound", *Ultrasound Med Biol*.

Sano, K., Kawasaki, M., Ishihara, Y., Okubo, M., Tsuchiya, K., Nishigaki, K., Zhou, X., Minatoguchi, S., Fujita, H., & Fujiwara, H. 2006, "Assessment of vulnerable plaques causing acute coronary syndrome using integrated backscatter intravascular ultrasound", *J Am Coll Cardiol*, vol. 47, no. 6, pp. 734-741.

Schaar, J. A., de Korte, C. L., Mastik, F., Strijder, C., Pasterkamp, G., Boersma, E., Serruys, P. W., & van der Steen, A. F. W. 2003, "Characterising vulnerable plaque features with intravascular elastography", *Circulation*, vol. 108, no. 21, p. 2636.

Schaar, J. A., van der Steen, A. F. W., Mastik, F., Baldewsing, R. A., & Serruys, P. W. 2006, "Intravascular palpography for vulnerable plaque assessment", *J Am Coll Cardiol*, vol. 47, no. 8, p. C86-C91.

Schminke, U., Motsch, L., Hilker, L., & Kessler, C. 2000, "Three-dimensional ultrasound observation of carotid artery plaque ulceration", *Stroke*, vol. 31, pp. 1651-1655.

Seeger, J. M., Barratt, E., LAwson, G., & Klingman, N. 1995, "The relationship between carotid plaque composition, plaque morphology, and neurologic symptoms", *J Surg Res*, vol. 58, pp. 330-336.

Shaalan, W. E., Cheng, H., Gewertz, B., McKinsey, J. F., Schwartz, L. B., Katz, D., Cao, D., Desai, T., Glagov, S., & Bassiouny, H. S. 2004, "Degree of carotid plaque calcification in relation to symptomatic outcome and plaque inflammation", *J Vasc Surg*, vol. 40, pp. 262-269.

Spence, J. D., Tamayo, A., Lownie, S. P., Ng, W. P., & Ferguson, G. G. 2005, "Absence of microemboli on Transcranial Doppler identifies low-risk patients with asymptomatic carotid stenosis", *Stroke*, vol. 36, pp. 2373-2378.

Stary, H. C. 2000, "Lipid and macrophage accumulations in arteries of children and the development of atherosclerosis", *Am J Clin Nutr*, vol. 72(suppl), pp. 1297S-1306S.

Stary, H. C., Chandler, A. B., Dinsmore, R. E., Fuster, V., Glagov, S., Insull, W. Jr., Rosenfeld, M. E., Schwartz, C. J., Wagner, W. D., & Wissler, R. W. 1995, "A definition of advanced types of atherosclerotic lesions and a histological classification of atherosclerosis: a report from the Committee on Vascular Lesions of the Council on Arteriosclerosis", *Arterioscler Thromb Vasc Biol*, vol. 15, pp. 1512-1531.

Stefanidis, C., Diamantopoulos, L., Vlachopoulos, C., Tsiamis, E., Dernellis, J., Toutouzas, K., Stefanadi, E., & Toutouzas, P. 1999, "Thermal heterogeneity within human atherosclerotic coronary arteries detected *in vivo*: a new method of detection of a special thermography catheter", *Circulation*, vol. 99, pp. 1965-1971.

Steinman, D. A., Thomas, J. B., Ladak, H. M., Milner, J. S., Rutt, B. K., & Spence, J. D. 2002, "Reconstruction of carotid bifurcation hemodynamics and wall thickness using computational fluid dynamics and MRI", *Magn Reson Med*, vol. 47, pp. 149-159.

Surry, K. J. M., Austin, H. J. B., Fenster, A., & Peters, T. M. 2004, "Poly(vinyl alcohol) cryogel phantoms for use in ultrasound and MR imaging", *Phys Med Biol*, vol. 49, pp. 5529-5546.

Sztajzel, R., Momijan, S., Momjian-Mayor, I., Murith, N., Djebaili, K., Boissard, G., Comelli, M., & Pizolatto, G. 2005, "Stratified gray-scale median analysis and color mapping of the carotid plaque: Correlation with endarterectomy specimen histology of 28 patients", *Stroke*, vol. 36, pp. 751-755.

Takaya, N., Yuan, C., Chu, B., Saam, T., Polissar, N. L., Jarvik, G. P., Isaac, C., McDonough, J., Natiello, C., Small, R., Ferguson, M. S., & Hatsukami, T. S. 2005, "Presence of intraplaque hemorrhage stimulates progression of carotid atherosclerotic plaques. A high-resolution magnetic resonance imaging study", *Circulation*, vol. 111, pp. 2768-2775.

Takaya, N., Yuan, C., Chu, B., Saam, T., Underhill, H. R., Cai, J.-M., Tran, N., Polissar, N. L., Isaac, C., Ferguson, M. S., Garden, G. A., Cramer, S. C., Maravilla, K. R., Hashimoto, B., & Hatsukami, T. S. 2006, "Association between carotid plaque characteristics and subsequent ischemic cerebrovascular events: A prospective assessment with MRI - Initial results", *Stroke*, vol. 37, pp. 818-823.

Takegami, K., Kaneko, Y., Watanabe, T., Maruyama, T., Matsumoto, Y., & Nagawa, H. 2004, "Polyacrylamide gel containing egg white as new model for irradiation experiments using focused ultrasound", *Ultrasound Med Biol*, vol. 30, no. 10, pp. 1419-1422.

Tang, D., Yang, C., Zheng, J., Woodard, P. K., Sicard, G. A., Saffitz, J. E., & Yuan, C. 2004, "3D MRI-based multicomponent FSI models for atherosclerotic plaques", *Annual Review Biomed Eng.*, vol. 32, no. 7, pp. 947-960.

Tawakol, A., Migrino, R. Q., Bashian, G. G., Bedri, S., Vermylen, D., Cury, R. C., Yates, D., LaMuraglia, G. M., Furie, K., Houser, S., Gerwitz, H., Muller, J. E., Brady, T. J., & Fischman, A. J. 2006, "*In vivo* 18F-Fluorodeoxyglucose Positron Emission Tomography imaging provides a noninvasive measure of carotid plaque inflammation in patients", *J Am Coll Cardiol*, vol. 48, no. 9, pp. 1818-1824.

Tearney, G. J., Yabushita, H., Houser, S. L., Aretz, H. T., Jang, I.-K., Schlendorf, K. H., Kauffman, C. R., Shishkov, M., Halpern, E. F., & Bouma, B. E. 2003, "Quantification of macrophage content in atherosclerotic plaques by optical coherence tomography", *Circulation*, vol. 107, pp. 113-119.

Techavipoo, U., Varghese, T., Chen, Q., Stiles, T. A., & Frank, G. R. 2004, "Temperature dependence of ultrasonic propagation speed and attenuation in excised canine lover tissue measured using transmitted and reflected pulses", *J Acoust Soc Am*, vol. 6, pp. 2859-2865.

Teirlinck, C., Bezemer, R. A., Kollmann, C., Lubbers, J., Hoskins, P. R., Fish, P. J., Fredfeldt, K. E., & Schaarschmidt, U. G. 1998, "Development of an example flow test object and comparison of five of these test objects, constructed in various laboratories", *Ultrasonics*, vol. 36, pp. 653-660.

Touboul, P.-J., Labreuche, J., Vicaut, E., & Amarenco, P. 2005, "Carotid intima-media thickness, plaques, and Framingham risk score as independent determinants of stroke risk", *Stroke*, vol. 36, pp. 1741-1745.

Touze, E., Toussaint, J. F., Coste, J., Schmitt, E., Bonneville, F., Vandermarcq, P., Gauvrit, J.-Y., Douvrin, F., Meder, J.-F., Mas, J.-L., & Oppenheim, C. 2007, "Reproducibility of High-Resolution MRI for the Identification and the Quantification of Carotid Atherosclerotic Plaque Components", *Stroke*, vol. 38, pp. 1812-1819.

Towa, R. T., Miller, R. J., Frizzell, L. A., Zachary, J. F., & O'Brien, W. D. 2002, "Attenuation coefficient and propagation speed estimates of rat and pig intercostal tissue as a function of temperature", *IEEE Trans Ultrason Ferroelectr Freq Control*, vol. 49, no. 10, pp. 1411-1420.

Trivedi, R. A., Mallawarachi, C., U-King-Im, J. M., Graves, M. J., Horsley, J., Goddard, M. J., Brown, A., Wang, L., Kirkpatrick, P. J., Brown, J., & Gillard, J. H. 2006, "Identifying inflamed carotid plaques using *in vivo* USPIO-enhanced MR imaging to label plaque macrophages", *Arterioscler Thromb Vasc Biol*, vol. 26, pp. 1601-1606.

Trivedi, R. A., U-King-Im, J. M., Graves, M. J., Horsley, J., Goddard, M. J., Kirkpatrick, P. J., & Gillard, J. H. 2004, "Multi-sequence *in vivo* MRI can quantify fibrous cap and lipid core components in human carotid atherosclerotic plaques", *J Vasc Endovasc Surg*, vol. 28, pp. 207-213.

U-King-Im, J. M., Tang, T. Y., Patterson, A., Graves, M. J., Howarth, S. P. S., Li, Z.-Y., Trivedi, R. A., Bowden, D., Kirkpatrick, P. J., Gaunt, M. E., Warburton, E. A., Antoun, N. M., & Gillard, J. H. 2008, "Characterisation of carotid atheroma in symptomatic and asymptomatic patients using high resolution MRI", *J Neurol Neurosurg Psychiatry*, vol. 79, pp. 905-912.

Verheye, S., De Meyer, G. R. Y., Van Langenhove, G. V., Knaapen, M. W. M., & Kockx, M. M. 2002, "*In vivo* temperature heterogeneity of atherosclerotic plaques Is determined by plaque composition", *Circulation*, vol. 105, pp. 1596-1601.

Wahlgren, C. M., Zheng, W., Shaalan, W. E., Tang, J., & Bassiouny, H. S. 2009, "Human carotid plaque calcification and vulnerability. Relationship between degree of plaque calcification, fibrous cap inflammatory gene expression and symptomatology", *Cerebrovasc Dis*, vol. 27, no. 2, pp. 193-200.

Waters, K. R., Lori Bridal, S., Cohen-Bacrie, C., Levrier, C., Fornes, P., & Laugier, P. 2003, "Parametric analysis of carotid plaque using a clinical ultrasound imaging system", *Ultrasound Med Biol*, vol. 29, no. 11, pp. 1521-1530.

Watson, R. J., Bridal, S. L., Cohen-Bacrie, C., Levrier, C., Fomes, P., & Laugier, P. 2000, "Classification of arterial plaque by spectral analysis of *in vitro* radio frequency intravascular ultrasound data", *Ultrasound Med Biol*, vol. 26, no. 1, pp. 73-80.

Wear, K. A., Stiles, T. A., Frank, G. R., Madsen, E. L., Cheng, F., Feleppa, E. J., Hall, C. S., Soo Kim, B., Lee, P., O'Brien, W. D., Oelze, M. L., Raju, B., Shung, K. K., Wilson, T. A., & Yuan, J. R. 2005, "Interlaboratory comparison of ultrasonic backscatter coefficient measurements from 2 to 9 MHz", *J Ultrasound Med*, vol. 24, no. 9, pp. 1235-1250.

Wintermark, M., Jawadi, S. S., Rapp, J. H., Tihan, T., Tong, E., Glidden, D. V., Abedin, S., Schaeffer, S., Acevedo-Bolton, G., Bodignon, B., Pan, X., & Saloner, D. 2008, "High-resolution CT imaging of carotid artery atherosclerotic plaques", *Am J Neuroradiol*, vol. 29, pp. 875-882.

Wolf, R. L., Wehrl, S. L., Popescu, A. M., Woo, J. H., Song, H. K., Wright, A. C., Mohler, E. R., Harding, J. D., Zager, E. L., Fairman, R. M., Golden, M. A., Velazquez, O. C., Carpenter, J. P., & Wehrli, F. W. 2005, "Mineral volume and morphology in carotid plaque specimens using High-Resolution MRI and CT", *25* no. 1729, p. 1735.

Worthington, A. E. & Sherar, M. D. 2001, "Changes in ultrasound properties of porcine kidney tissue during heating", *Ultrasound Med Biol*, vol. 27, no. 5, pp. 673-682.

Yabushita, H., Bouma, B. E., Houser, S. L., Aretz, H. T., Jang, I.-K., Schlendorf, K. H., Kauffman, C. R., Shishkov, M., Kang, D.-H., Halpern, E. F., & Tearney, G. J. 2002, "Characterization of human atherosclerosis by Optical Coherence Tomography", *Circulation*, vol. 106, pp. 1640-1645.

Yadav, J. S., Wholey, M. H., & Kuntz, R. E. 2004, "Stenting and angioplasty with protection in patients at high risk for endarterectomy investigators. Protected carotid artery stenting versus endarterectomy in high risk patients", *N Engl J Med*, vol. 351, no. 15, pp. 1493-1501.

Yen, C.-L., Chang, H.-Y., Huang, S.-Y., Huang, Y.-C., & Jeng, C.-M. 2008, "Combination of tissue harmonic sonography, real-time spatial compound sonography and adaptive image processing technique for the detection of carotid plaques and intima-medial thickness", *Eur J Radiol*.

Yu, X., Song, S.-K., Chen, J., Scott, M. J., Fuhrhop, R. J., Hall, C. S., Gaffney, P. J., Wickline, S. A., & Lanza, G. M. 2000, "High-resolution MRI characterization of human thrombus using a novel fibrin-targeted paramagnetic nanoparticle contrast agent", *Magn Reson Med*, vol. 44, pp. 867-872.

Yuan, C., Kerwin, W. S., Ferguson, M. S., Polissar, N. L., Zhang, S., Cai, J.-M., & Hatsukami, T. S. 2002a, "Contrast-enhanced high resolution MRI for atherosclerotic carotid artery tissue characterization", *J Mag Res Imaging*, vol. 15, pp. 62-67.

Yuan, C., Mitsumori, L. M., Ferguson, M. S., Polissar, N. L., Echelard, D., Ortiz, G., Small, R., Davies, J. W., Kerwin, W. S., & Hatsukami, T. S. 2001, "*In Vivo* accuracy of multispectral Magnetic Resonance Imaging for identifying lipid-rich necrotic cores and intraplaque hemorrhage in advanced human carotid plaques", *Circulation*, vol. 104, pp. 2051-2056.

Yuan, C., Zhang, S.-X., Polissar, N. L., Echelard, D., Ortiz, G., Davis, J. W., Ellington, E., Ferguson, M. S., & Hatsukami, T. S. 2002b, "Identification of fibrous cap rupture with Magnetic Resonance Imaging is highly associated with recent transient ischemic attack or stroke", *Circulation*, vol. 105, pp. 181-185.

Chapter 2 IEC TISSUE MIMICKING MATERIAL

The work in the next two chapters has been published in the journal, Ultrasound in Medicine and Biology:

"The acoustic properties, centered on 20 MHz, of an IEC agar-based tissue-mimicking material and its temperature, frequency and age dependence. MP Brewin, LC Pike, DE Rowland and MJ Birch. *Ultrasound Med Biol. 2008 Aug; 34(8): pp 1292-1306"*

2.1 Rationale

Our centre has fabricated the agar-based TMM detailed below for use in the fabrication of in-house ultrasound imaging test objects. This substance was thus chosen as the TMM for the plaque characterisation. It is a mouldable, relatively inexpensive and consistent substance. It is easily fabricated in the laboratory and its recipe (Teirlinck et al. 1998) has been developed for many research tools and ultrasound test objects. Table 4 shows the component materials:

Component	Weight composition, %
Distilled Water	82.97
Glycerol	11.21
Silicon Carbide (~37 µm)	0.53
Aluminium Oxide (3 µm)	0.94
Aluminium Oxide (0.3 µm)	0.88
Rodalon ™ (Benzalkoniumchloride)	0.46
Agar	3.0

Table 4: Weight composition of the TMM (by %). Approximate particulate sizes are shown in brackets.

In order for the TMM to be used in the plaque assessment, it was first necessary to calibrate the material at the higher frequency range of 17 - 23 MHz. For the complete description of the TMM at this higher frequency, its dependence on temperature, frequency and age was investigated.

The primary purpose of this paper is to characterise the fundamental acoustic properties of this TMM at the higher frequency band. Sound speed and attenuation in the TMM were measured using a substitution or insertion technique (AIUM 1995). A longitudinal study over a period of 3 years is detailed and the effect of water immersion on the speed of sound of the TMM is also measured. The acoustic properties were also monitored over a temperature range of 22 - 37^{o}C. One set of gels was measured for speed and attenuation using the same transducer at two different Medical Physics ultrasound laboratories; Royal London Hospital, Whitechapel and St. George's Hospital, Tooting in order to carry out an inter-laboratory comparison. The backscattered power spectral density (distribution of power per unit frequency normalised to the total received power) characteristics were also investigated within and between sample batches.

2.2 Manufacture

Its manufacture is also described in detail elsewhere (Ramnarine, Anderson, & Hoskins 2001) and the recipe was followed in our laboratory. The ingredients are weighed out on digital scales (± 0.01 g, Libror EB-2800, Shimadzu, Japan) and combined in a glass jar. The mixture was prepared in batches of 1 litre. This gave a sufficient volume that could be agitated to achieve a heterogenous mixture. It is stirred with both a coil and surface stirrer at 125 rpm and heated in a double boiler for an hour at 96^{o}C. The gel is then allowed to cool slowly and is poured out at 46^{o}C, while still molten. The gel sets at approximately 43^{o}C.

In order for the acoustic properties to be measured, the gel was moulded into 8 square slabs. This was achieved using pairs of square moulds (6 x 6 cm) of four different thicknesses, as shown in figure 2. These thicknesses were approximately 12.7 mm (labelled sample A, AA), 10 mm (B, BB), 7.1 mm (C, CC) and 3 mm (D, DD). These thicknesses were chosen at the outset of the project when it was unclear what thickness would attenuate the signal. All four thicknesses were measured throughout the study in order to perform the longitudinal study. The sample thickness was measured using each system and the methods are included in the section below.

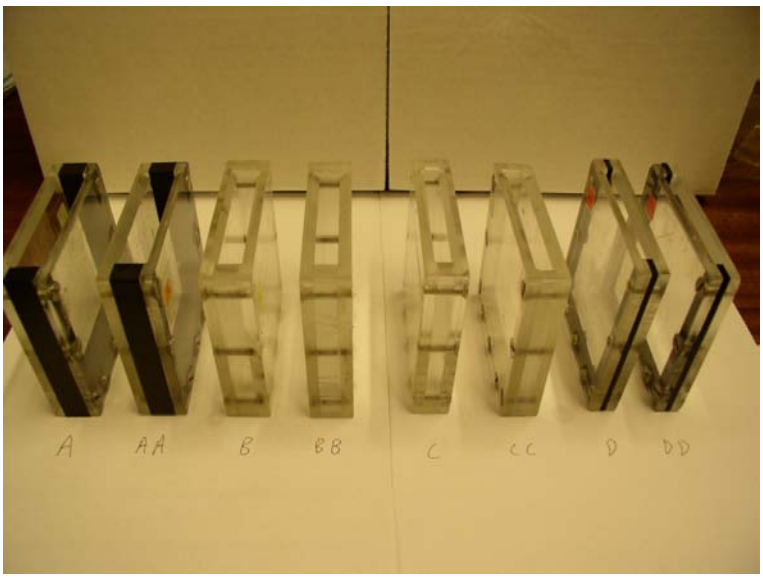

Figure 2: Eight Perspex moulds used to cast the quality assurance samples. The thickest depths are to the left of the picture, and thinnest to the right.

The weight composition of the glycerol component gives rise to the sound speed match within the TMM and the weight composition of the particulates adjusts the attenuation and backscatter characteristics of the TMM. However, the material is prone to degradation through dehydration and is relatively delicate to handle.

The specimens are stored in a high density polyethylene container with airtight lid containing a mixture of glycerol, water and Rodalon^{TM} (Benzalkonium Chloride - an anti-bacterial, anti-fungal agent) to match the proportions within the gel. The percentages by mass in this solution are water 87.67%, glycerol 11.84% and 0.48% Rodalon. The TMM is covered with 500 ml of this mixture. This serves to restore

the concentration of the glycerol component to the TMM and to keep the specimens hydrated.

2.3 Measurement of speed of sound, attenuation and backscatter

Measurements were taken over a period of three years during which an automation of the measurement process was developed. All experiments were carried out in a plotting tank, dimensions 75cm x 30cm x 45 cm, using double distilled water. This had been degassed by leaving to stand for 24 hours. Both the narrowband technique, described below, and an automatic system utilising the broadband technique, described below, were used. The narrowband technique was used at the start of the project before the automated broadband system was developed to integrate the measurement of sample thickness. The systems for both techniques are outlined and described in generic figure 3. The narrowband technique was used at the beginning of the longitudinal study but a broadband technique was used for all other measurements in the TMM and plaque study.

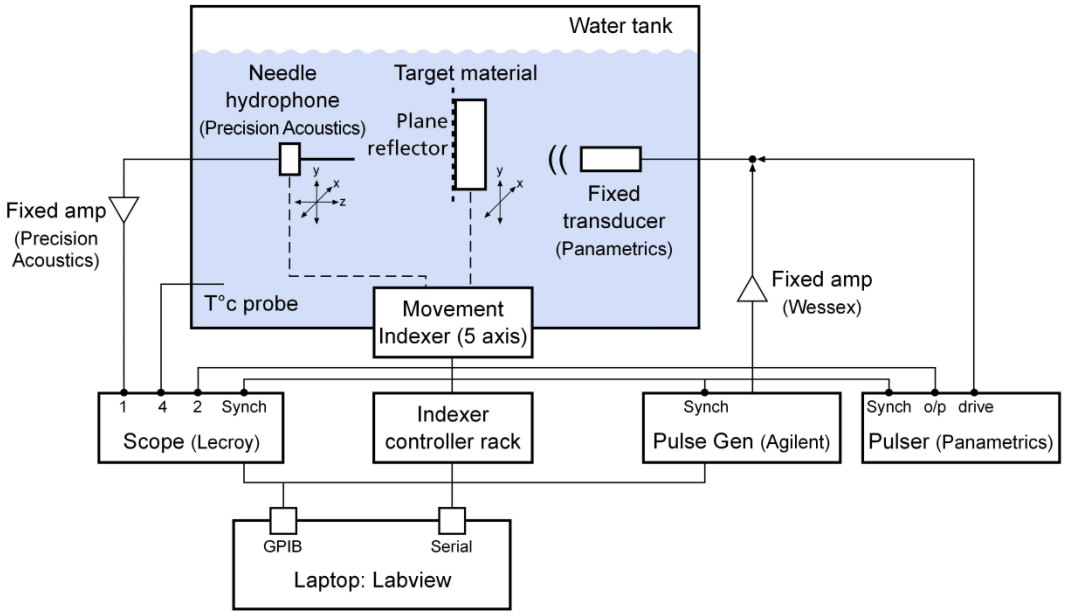

Figure 3: Schematic defining both the narrowband and broadband systems in a generic figure. Narrowband signal is generated at the pulse generator and passes through the target material (with no plane reflector in place) to the hydrophone. The broadband signal is generated by the pulser-receiver and received having been reflected back through the target material by the plane reflector.

2.3.1 Narrowband technique

The phase speed and attenuation coefficient were measured using a narrowband through-transmission substitution technique (AIUM 1995) with a tone burst pulse of 10 cycles (Madsen et al. 1978) that produced a signal centred at 20 MHz.

The ultrasound pulse was produced from a single crystal circular immersible piezoelectric unfocussed transducer (V317-SU, Panametrics-NDT, Waltham, MA, US), which has a nominal 20.0 MHz centre frequency and an element size of 6mm. The tone burst pulse was generated using a signal generator (33250A, Agilent, Santa Clara, CA, US), as shown in figure 3. The signal was then amplified using an RF amplifier with a nominal fixed gain of 42 dB (RC102-12, Wessex Electronics, Bristol, UK). The drive voltage to the transducer was set at a low value of $12.5V_{RMS}$ so that the ultrasound pulse pressure (peak of approx. 40 kPa) remained well beneath 1 MPa in order to ensure that non-linearity effects were not present (Duck 2002; Wu 1996). This was verified experimentally by making measurements at both half the drive voltage and twice the drive voltage. No significant change was observed in the measured value of attenuation coefficient.

A PVdF needle hydrophone (HPM 02/1, Precision Acoustics, Dorchester, Dorset, UK), with a 0.2 mm active element, was employed in reception. This, in turn, was coupled using a DC coupler (DC1, Precision Acoustics, UK) to a submersible pre-amplifier (HP1, Precision Acoustics, UK) and then to a booster amplifier (HA1, Precision Acoustics, UK) with a gain, in combination, of 28.5 dB at 20 MHz. The hydrophone set-up, along with its associated pre-amp and amplifier, was calibrated in the frequency range 2 - 40 MHz giving a sensitivity of 3.04 μV/Pa with a ± 12% uncertainty at 20 MHz by the UK National Physics Laboratory (NPL reference U1930).

The received ultrasound pulse, post-amplification, was acquired using a 1 GHz bandwidth digital oscilloscope (LT264, LeCroy, Chestnut Ridge, NY, US). The time shift was measured using digital callipers on the oscilloscope. A power spectrum of both the signal and the reference medium, with a frequency resolution of 100 kHz, was acquired by the oscilloscope utilising a fast Fourier transform and rectangular window sampling. The data was then downloaded from the oscilloscope using

custom software (ScopeExplorer, LeCroy, US) and analysed on a laptop (Tecra, Toshiba, Tokyo, Japan).

The transducer was in a fixed position and the needle hydrophone was placed at a distance of approximately 12.1 cm from the transducer. This corresponds to the last axial maximum, a^2/λ, where a is the diameter of the aperture, which is 3 mm, and λ is the wavelength of the ultrasound, which is 74 μm. The sample was positioned at half this distance in a frame that is moved in and out of the beam path. The relative positioning of the hydrophone was adjusted in the plane perpendicular to the beam in order to locate the received signal peak. The mounting arm of the hydrophone has two orthogonal metric goniometers (resolution 0.2^o, Edmund Industrial Optics, York, UK) that can tilt the hydrophone respectively around the x and y axes. As the sensitive element may not lie perpendicular to the axis of the needle, this adjustment ensures that the signal is further maximised.

The time shift of the first detectable excursion of the received pulse above the ambient noise is monitored (Greenleaf et al. 1975) as the sample is inserted into the beam path. The phase speed is then calculated using the simple relation:

$$c = \frac{c_w}{\left(1 + c_w\left(\frac{\Delta t}{d}\right)\right)}$$

Equation 2

where c_w is the propagation speed in water, Δt is the time shift of the reflected pulse from inserting the sample into the beam and d is the thickness of the sample.

In all experiments the temperature of the water was measured prior to all measurements using an immersion probe thermocouple (80TK, Fluke, Norwich, Norfolk, UK, accuracy ± 0.2^oC) in order to calculate the speed of sound in the reference medium, water (Marczak 1997).

The thickness of the sample was measured using mechanical callipers with digital readout with a resolution ±0.01 mm (Mitutoyo,Tokyo, Japan). As the TMM is soft, the samples were surrounded by a Perspex ® frame and then sandwiched between

two pieces of Perspex ®, with dimensions 9 cm x 2 cm x 5 mm. Repeated measurements (n = 10 per sample) of a range of sample thicknesses demonstrated a maximum standard deviation of 0.04 mm.

The attenuation was calculated as a relative value from the comparison of the amplitude of the Fourier transform of the signal through the water reference medium with that through the TMM sample. An average of 5 signal spectra was taken along the sample path and was then corrected for the transmission coefficient, $T^2 = 0.998$. This was subtracted from the similarly averaged signal from the water reference path over the frequency range of 19 - 21 MHz at 100 kHz steps. The point measurements at 20 MHz are quoted in table 3. The attenuation (*a (f, x ,y)*) of the TMM was calculated at each point using the following equation:

$$a(f,x,y) = \frac{\left(P_0(f,x,y) - P_1(f,x,y)\right)}{d}$$

Equation 3

where $P_0(f,x,y)$ is the averaged amplitude of the FFT of the pulse in water, measured in dB, $P_1(f,x,y)$ is the corrected averaged amplitude of the FFT of the pulse spectrum with the sample in the beam path, also measured in dB, and *d* is the sample thickness.

2.3.2 Broadband technique

The group speed, attenuation coefficient and backscattered spectral power density were measured using a broadband reflection substitution technique (AIUM 1995). The schematic for the experimental set up can be seen in figure 3. The ultrasound pulse was generated and received using a pulser-receiver (5800, Panametrics-NDT, Waltham, MA, USA) driving an unfocussed 20 MHz immersion transducer (V317-SU, Panametrics-NDT, USA) with a nominal element size of 6 mm. The resultant broadband beam has a 6 dB bandwidth of 54%.

The TMM target material was mounted on a lapped optically flat glass plate in a simple jig. The glass plate was further checked for flatness using an optical flat (19 mm thick, Edmund Industrial Optics, York, UK). The plate was placed at a distance of 6 cm from the transducer which approximates to half a^2/λ.

The target plane was initially adjusted for each sample scan sequence to be perpendicular to the beam. The mounting arm of both the transducer and of the target material each has two orthogonal metric goniometers (resolution 0.2^o, Edmund Industrial Optics, York, UK) that can tilt the transducer and glass respectively around the x and y axes. By a process of minimising the difference in time of flight of pulses from the top/bottom and left/right sides of the plot area, see figure 4, the plane of the target material was set to be orthogonal to the ultrasound beam. Thereafter a fine adjustment to the transducer to achieve a maximum echo would require a further iteration to maintain the orthogonal plane of the glass reflector. Typical maximum time of flight difference was ± 10 ns corresponding to an uncertainty of 0.03% in the path length. This laborious method of flattening the plate was found to be necessary as the initial protocol assumed that the plate was flat in relation to the target arm of the actuator/driver plotting system. The plate was originally calibrated using the four corners of the glass. This resulted in a drift in velocity across the plot area of up to $7ms^{-1}$ in both directions.

The geometry of the drive screw of target arm is not exactly square to the beam at these micrometre tolerances (3 ns ≡ 2 μm) over the range of movement of the target arm. This means that the return time from the reference path and the plot path are not equal. Once the plot area is flattened, the difference between the water reference time, t_1, and plot area (through material transmission) time, t_3, is noted. This time difference has an average of 74.2 ns (s.d. 3.9, n = 25). This value is worked into the speed calculation in the Labview software, see equation 1, by adding it to Δt.

Once the plot area is flattened, the TMM gel sample is positioned in the bottom half of the target plate. The thicker samples are held in held with the adjustable Perspex holding bar. Surface tension holds the thinner gels (thicknesses C & D) in place sufficiently.

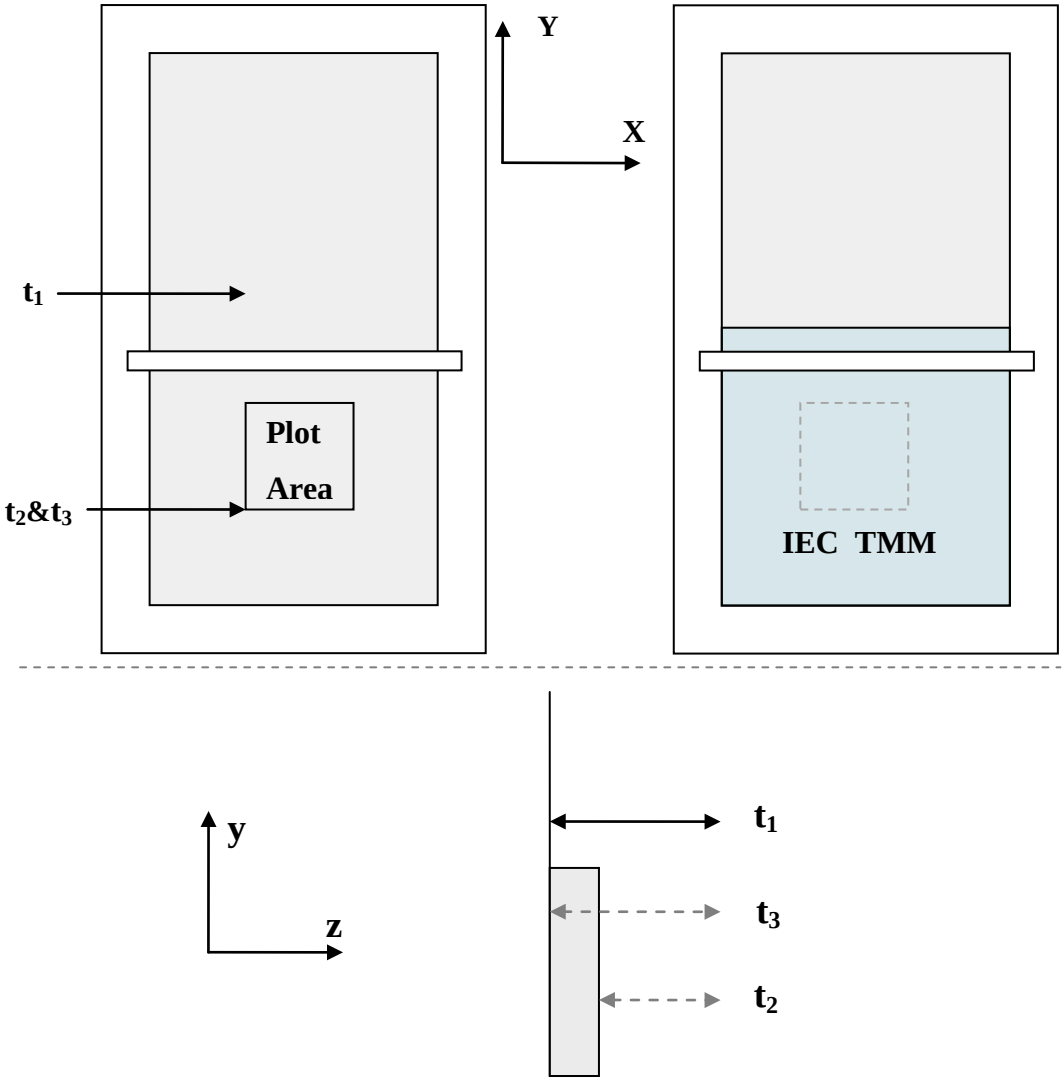

Figure 4: The figure shows the unloaded plate on left and plate loaded with TMM sample on right. The acquisition times are noted as t_1, t_2 and t_3. The horizontal bar is the Perspex sample holding bar.

The mechanical positioning and data acquisition systems are controlled from a laptop (Tecra, Toshiba, Tokyo, Japan) running custom designed code developed using LabView software (National Instruments, version 7.1, Cambridge, Cambridgeshire, UK). The reflected pulse was acquired using a digital oscilloscope (LT584L, 1 GHz

bandwidth, LeCroy, Chestnut Ridge, NY, USA) and the data was continuously transferred via GPIB (General Purpose Interface Bus).

The system software sequences a series of movements and measurements to enable a raster scan of the target material over a 1 cm^2 area. The TMM has been found to be consistently uniform however; raster scanning measures the degree of uniformity and allows spatial averaging of values. An initial reading of the time of flight (t_1) to the glass plate through water was taken, i.e. a reference water path time. The index controller rack then moves the target (step size of 25 μm, accuracy of ± 1 step) so the beam is directed through the TMM. The received signal, t_3, from the back plate was temporally shifted, shorter than t_1, by the change in its path. The system then measured the time of flight, t_2, of the pulse for the reflection from the front face of the TMM and that from the glass plate through the TMM, t_3, as shown in figure 5.

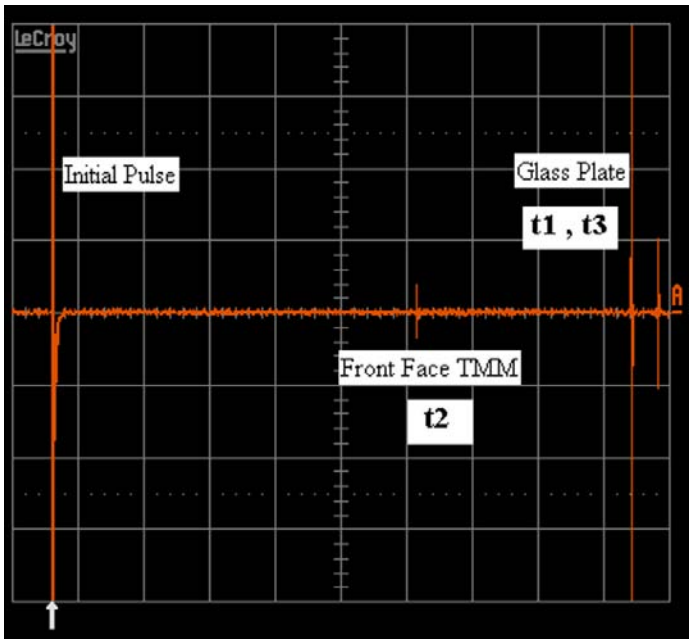

Figure 5: Scope screenshot showing initial pulse and its reflections. t_2 shows the reflection from surface of TMM to quantify TMM thickness. The glass plate reflection will give t_1 as reference water signal and time shifted t_3 when the TMM lies in the ultrasound path.

The time from transmission to reception of the pulse was based upon the time interval between the pulser being triggered and the arrival of the subsequent pulse. The oscilloscope was set up such that the received pulse, v(t), is centred in the data acquisition window. The maths function of the oscilloscope squares the signal

producing a full wave rectified version of the pulse, $v^2(t)$. This signal is then integrated to produce a signal $\int v^2(t)dt$, that continuously increases to a maximum level as shown in figure 6. This signal was acquired by Labview, which the software subsequently interpolates by a factor of four before fitting a sixth order polynomial curve to the data. Thereafter the time at which the curve passes through 2% of the maximum excursion of the curve was detected. This temporal measurement was closely aligned to the first excursion (Greenleaf, Johnson, Samayoa, & Duck 1975) of the pulse signal level from the baseline ($\Delta t = 21.6$ ns, s.d. = 1.5 ns, n = 7).

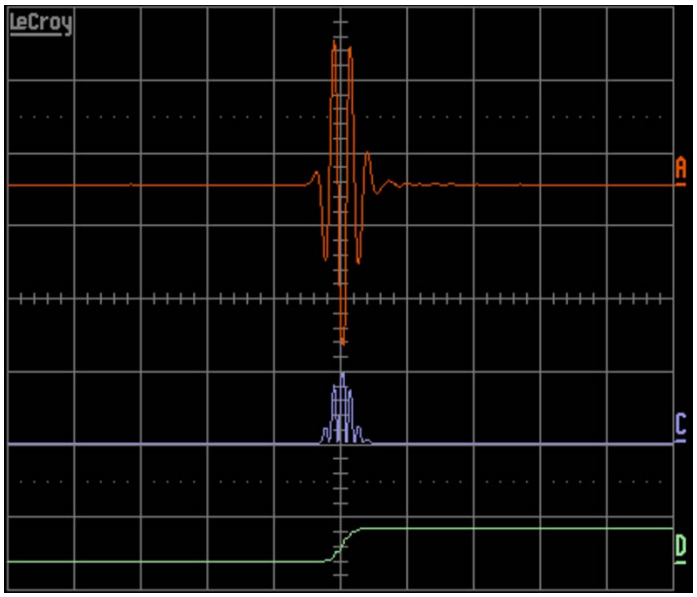

Figure 6: The top signal shows the original reflected pulse. The middle signal is the square of the original. The bottom signal is the squared integral of the original.

The thickness of the TMM was calculated using the time difference between the reflection from the front face of the TMM slab, t_2, and the initial reference time, t_1. This was then multiplied by the speed of sound in water at the measurement temperature to give a distance.

Furthermore the group speed was then calculated, as shown in equation 4 overleaf, using this thickness measurement and the time difference between t_1 and the time reading from the time-shifted signal, t_3, from the glass plate through the TMM.

$$\frac{1}{c_s} = \frac{1}{c_w} - \frac{\Delta t}{2d}$$

Equation 4

where c_s is the speed of sound in the sample, c_w is the speed of sound in the water, d is the sample thickness and Δt is the time shift, t_1-t_3.

The system then moved the target in a raster fashion to obtain a configurable matrix of measurements. In this case, a non-overlapping set of 9 measurements in a 9 mm by 9 mm square with increments of 3 mm, deriving values for thickness and speed of sound at each point. This raster-like process was then repeated for the attenuation coefficient measurement. The initial measurement captured the fast Fourier transform (FFT) power spectrum from the reflected pulse from the glass plate through water alone, i.e. reference water path spectrum. The target is then moved into the beam and at each point in the matrix of the raster; the FFT power spectrum of the pulse reflected from the glass plate through the TMM was captured.

The attenuation was determined by calculating the ratio of the power spectra of the Fourier transforms, see equation 3, with a factor of 2 in the denominator due to the reflected beam passing back through the sample. The data was extracted from the frequency range 17 - 23 MHz and a graph is drawn of attenuation against frequency for both sample and reference.

The backscattered spectral power density of the TMM was measured on the same spatial matrix as the attenuation and speed measurements. In this case, the signal of interest was the backscattered ultrasound RF signal which was captured between the front face of the TMM and the reflecting glass plate as shown in figure 7. The time amplitude reference water path pulse and RF amplitude time data from the TMM were further processed utilising custom software (Matlab version 2006b, Mathworks Inc, Natick, MA, USA) as follows.

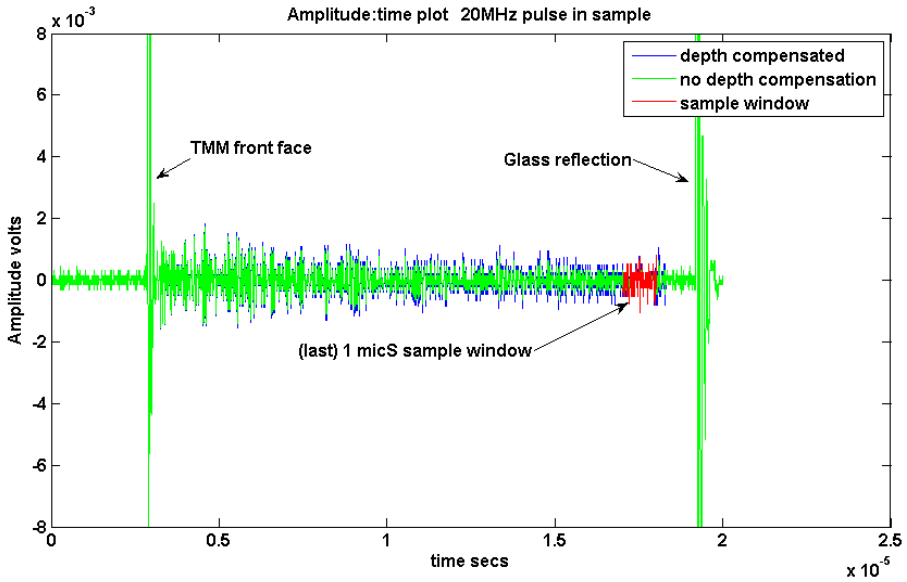

Figure 7: Time amplitude RF signal from one of a 3 x 3 matrix of measurement points. The RF signal is attenuation compensated for thickness and frequency, subdivided into 1µS samples which are then transformed into the frequency domain using a Hamming window and the Welch transform.

Initially the amplitude of each RF line was compensated for the attenuation due to sample depth and frequency dependence by a factor of 0.5 dB MHz^{-1} cm^{-1} or the appropriate factor derived from the preceding attenuation measurement. Each complete RF line was then subdivided into samples of duration 1 µS as shown in figure 7. These 1 µS amplitude-time samples were further divided into 8 equal size segments and each segment windowed using a Hamming function to optimise frequency resolution prior to a spectral analysis of the power density using the Welch transform (Welch 1967). Each segment was transformed utilising the data acquisition sampling frequency from the LeCroy oscilloscope setting and with a 50% data overlap with the prior segment. The Welch transform derives the distribution of power per unit frequency in the backscattered RF signal, normalised to the total received power, by averaging the spectra from all segments.

The backscattering characteristics of the TMM were assessed over a frequency range of 17 MHz to 23 MHz. In order to remove the effect of both the transmitted pulse spectrum and the receiver characteristics from the measurement, the backscattered signal spectrum was normalised to the reference water path spectrum. Normalisation was achieved by the interpolation of the signal and water path spectra to match their frequency range, followed by the logarithmic subtraction of their amplitudes.

2.4 Uncertainties in the measurements

There are a number of uncertainties to be taken into consideration in the determination of speed of sound, attenuation and backscatter (Bamber 1997). For sound speed uncertainties, the systematic errors are due to uncertainties in path length estimation or sample thickness, definition of pulse arrival time and the speed within the reference medium.

For the reflective technique, as the glass is optically flat and both the transducer and glass plate have goniometers to ensure the orthogonality of the TMM surface to the beam, the geometric considerations to overall path length for the reflective method would give rise to a speed of sound error of 0.2 ms^{-1}. The uncertainty is assumed negligible for the transmission method.

For the sample thickness, there is an uncertainty in the mechanical callipers measurement of less than 1% and of 0.1% in the depth measured by time of flight. This results in a 0.05% speed of sound uncertainty in the narrowband system and a negligible error in the broadband system. However, the measurement of the pulse arrival time is affected by change in pulse shape due to beam hardening or dispersion. This is a consideration for the broadband system. Theoretical modelling (Bamber 2004) has demonstrated that changes in pulse shape may lead to overestimations in sound speed of up to 4% in longer sample path lengths with a higher attenuation coefficient relative to our experiment. The specimen path length is a maximum of 24 mm in the reflective technique. Measurements in this material showed a maximum increase in pulse length of 50 ns and this would lead to an uncertainty of 0.1% in pulse arrival time. This would lead to an uncertainty of ±5 ms^{-1} in the sound speed. This effect is not a factor in the narrowband pulse and the

uncertainties due to phase reversal are assumed negligible due to the measurement at earliest time of arrival. Errors in arrival time due to the alignment of the transducer are minimised by the micromanipulation of the goniometers.

The temperature of the water in the plotting tank has an accuracy of ± 0.2^{o}C which leads to an uncertainty of 1 ms^{-1} in the measured speed of sound of the sample. From temperature measurements taken within the TMM using a needle probe thermocouple in conjunction with a handheld thermometer (RS, Corby, Northants., UK), it was shown that the temperature of the sample can differ from the medium by ± 0.5^{o}C. This, in turn, would reflect an added uncertainty of ± 0.75 ms^{-1}. For the longitudinal study, the samples were measured without Saran wrap® and this would contribute an uncertainty of ± 1 ms^{-1}. Combining these errors meant that the narrowband technique has an uncertainty in speed of sound as low as 2.75 ms^{-1}, whereas the broadband technique may have errors as large as 7 ms^{-1}.

The transducer is driven at voltages that produces kPa pressures so non-linearity effects are neglected and diffraction effects are, likewise, neglected for insertion or substitution techniques. The transmission coefficient between water and TMM is calculated at 0.998 and therefore the transmission loss is 0.4%. It is estimated that the uncertainty in attenuation is ± 0.03 dB^{-1} cm^{-1} MHz^{-1}. The uncertainties for both speed and attenuation compare with the uncertainties, ± 1 ms^{-1} and ± 0.03 dB^{-1} cm^{-1} MHz^{-1} from other observers (Browne et al. 2003).

2.5 Experiments

2.5.1 Plate Calibration

The measurements of acoustic properties, in particular the sound speed, rely on a constant path length over the scan area. Any inconsistency will affect the reflected time measurement from the glass plate, t_3. Initially the time difference was minimised between the four corners of the glass. This relied on the assumption that the glass was flat. However it became apparent that there was a kink in the lead screw driving the reflector arm. An inspection of the entire plate was made to determine the 'flattest' area in the centre of the bottom half of the plate. The calibration was repeated so that the time was minimised on the four corners of a 2 cm x 2 cm square area. The time measurements were made using the absolute cursor on the scope screen (time resolution 0.1 ns).

2.5.2 Thermocouple Calibration

The temperature of the water is measured using a thermocouple (type K insulated, RS, UK), which is immersed in the water tank close to measurement area. The sensitive wire is placed behind the transducer so that it does not interfere with the ultrasound beam. Accurate measurement of the water temperature of the bath was integral to the calculation of sound speed. The temperature is read by the oscilloscope and this data is used by the Labview program to calculate the sound speed in the water using the fifth order polynomial Marczak (1997) equation.

The thermocouple was calibrated using a temperature calibrator (Tempcal 140S, Haven Automation Limited, Swansea, UK) over the range 15 - 40^{o}C, as shown in figure 8.

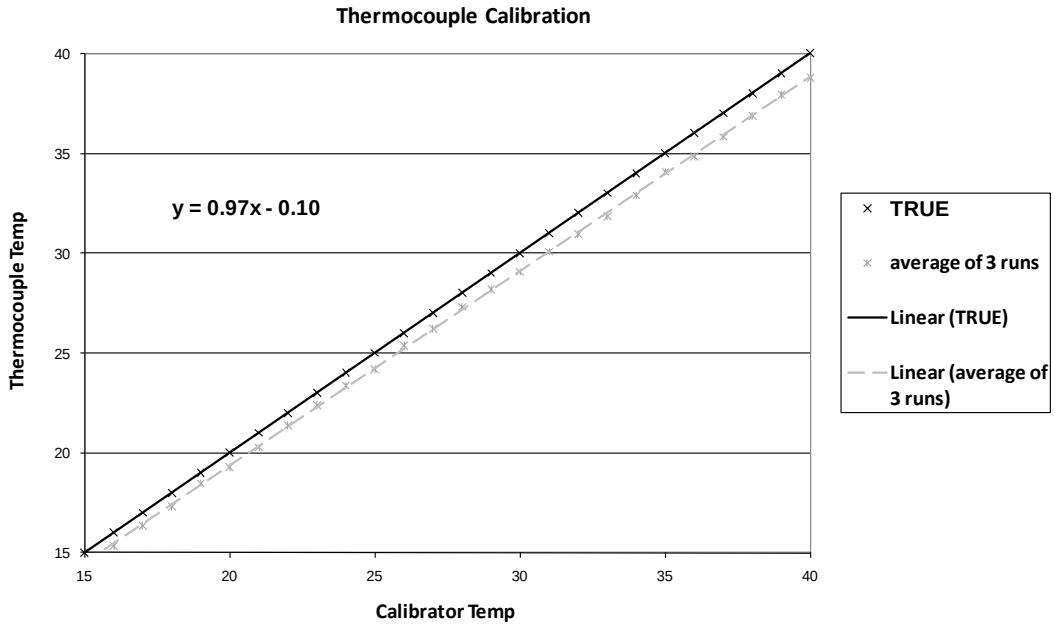

Figure 8: This figure shows the reading of the thermocouple averaged over three runs between 15^{o}C and 40^{o}C. The solid line shows the true reading. The dashed line shows the temperature recorded by the thermocouple averaged over three runs.

The thermocouple showed a drift from the calibrated temperature. The Labview software was altered so that the measured thermocouple temperature was adjusted to record correct temperature.

2.5.3 Longitudinal study

The stability of the TMM parameters for speed of sound (both phase and group) and attenuation were measured with repeated measurements over a 3 year time period. The sample batches are measured immediately when produced (0 years) and then after 1 year and 3 years for the narrowband system and at 0 years, 1 year and 2 years for the broadband system. The batches were not all made at the same time and so the time frame relates to the age of each specific batch of samples.

2.5.4 Glycerol leaching

Broadband experiments were carried out to find the extent and rate of change of the acoustical group speed for the TMM when placed in water at 20^{o}C. As the glycerol diffuses out of an unsealed specimen into the water tank, its concentration in the gel decreases. Therefore the speed of sound of the sample decreases. This decrease is quantified by measuring the speed of sound over a period of 3 hours for all thicknesses of TMM sample.

2.5.5 Cross centre validation

Measurements of group speed and attenuation were carried out on the same set of samples in the Medical Physics Ultrasound Laboratory at St.George's Hospital, London. Speed was measured using a simple in-house pulser-receiver with the same Royal London Hospital 20 MHz unfocussed transducer (6 mm diameter, V317-SU, Panametrics-NDT, Waltham, MA, US). A calibrated test object, see figure 9, of known dimensions was used in which the time of flight principle is used in order to carry out the measurement. The TMM sample was laid on the base of the object with a taut wire stretched between its upright sides. The pulse is then fired perpendicular to this base and wire. The return times from three points along the beam (base of test object/TMM, surface of TMM and a wire above the TMM) are measured using callipers on an oscilloscope (LT584, LeCroy, Santa Clara, CA, US). From the known distance (wire to base) and the time of flight from transducer to surface of the TMM, the thickness of the sample is calculated. The speed of sound within the sample is determined from the shift in time of flight through the TMM relative to the reference water path with the TMM removed.

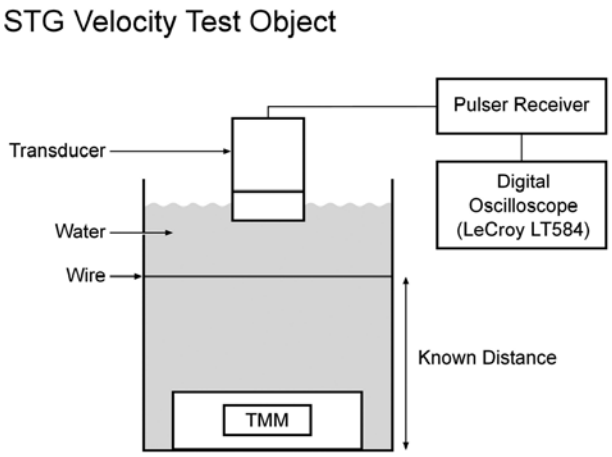

Figure 9: Medical Physics Ultrasound Laboratory St.George's Hospital (STG): Calibrated velocity test object

Attenuation is measured using a Scanning Acoustic Macroscope (SAM). A pulser-receiver (Precision Acoustics, Dorchester, Dorset, UK) is connected to the same transducer as above, the position of which is controlled by actuators and drivers. The system was controlled by a desktop PC. Measurements are taken over a square area in a raster fashion, the FFT of the water reference and sample are compared at each point, as in broadband system detailed above, and the result is averaged over the plot area.

2.5.6 Attenuation and speed of sound against temperature & frequency

The parameters of sound speed and attenuation coefficient of the TMM were measured over a temperatures range of 23 – 37^{o}C. The experiment was repeated twice over the temperature range using the broadband technique. The measurements of speed of sound and attenuation were carried out on spot temperatures as the sample was heated and cooled in water continuously stirred and under thermostat control. The samples were allowed to reach thermal equilibrium at each measurement point. The specimen was sealed using thin clingfilm (Saran wrap®) in order that the speed of sound of the TMM did not change due to glycerol leakage.

For the frequency dependence experiment, measurements were made over the frequency range of 17 – 23 MHz. It was necessary to make a separate set of measurements using the narrowband technique. Measurements were made for one set of samples driving the transducer with the signal generator at 500 kHz steps between 17 – 23 MHz. The attenuation coefficient was calculated as point measurements at each step and the speed was calculated by inspection of the time shift on the oscilloscope.

2.5.7 Mass density, ρ

In order to get a more complete data set for this TMM, the density and specific heat were measured. The density was measured using Archimedes principle (buoyancy method) (Rosin et al. 2002) with digital scales (accuracy ± 0.1 g, Libror EB-2800, Shimadzu Corp., Kyoto, Japan). Five separate samples of TMM of approximate 5 g were measured and an average density was taken.

2.6 References

AIUM 1995, *Methods for specifying acoustic properties of tissue mimicking phantoms and objects, Stage I*, American Institute of Ultrasound in Medicine Technical Standards Committee, Laurel, MD.

Bamber, J. C. 1997, "Acoustical characteristics of biological media," in *Encyclopedia of Acoustics*, M. J. Crocker, ed., Wiley-Interscience, pp. 1703-1726.

Bamber, J. C. 2004, "Speed of sound," in *Physical Principles of Medical Ultrasound*, Second Edition edn, C. R. Hill, J. C. Bamber, & G. R. Ter Haar, eds., Wiley, pp. 167-190.

Browne, J. E., Ramnarine, K. V., Watson, A. J., & Hoskins, P. R. 2003, "Assessment of the acoustic properties of common tissue-mimicking test phantoms", *Ultrasound Med Biol*, vol. 29, no. 7, pp. 1053-1060.

Duck, F. A. 2002, "Nonlinear acoustics in diagnostic ultrasound", *Ultrasound Med Biol*, vol. 28, no. 1, pp. 1-18.

Greenleaf, J. F., Johnson, S. A., Samayoa, W. F., & Duck, F. A. 1975, "Two-dimensional acoustic velocity distributions in tissues using an algebraic reconstruction technique", *Ultrasonics International Conference Proceedings* pp. 190-194.

Madsen, E. L., Zagzebski, J. A., Banjavic, R. A., & Jutila, R. E. 1978, "Tissue mimicking materials for ultrasound phantoms", *Med Phys*, vol. 5, no. 5, pp. 391-394.

Marczak, W. 1997, "Water as a standard in the measurement of speed of sound in liquids", *J Acoust Soc Am*, vol. 102, no. 5, pp. 2776-2779.

Ramnarine, K. V., Anderson, T., & Hoskins, P. R. 2001, "Construction and geometric stability of physiological flow rate wall-less stenosis phantoms", *Ultrasound Med Biol*, vol. 27, pp. 245-250.

Rosin, M., Urban, A. D., Gartner, C., Bernhardt, O., Splieth, C., & Meyer, G. 2002, "Polymerisation shrinkage-strain and microleakage in dentin-bordered cavities of chemically and light-cured restorative materials", *Dental Materials*, vol. 18, pp. 521-528.

Teirlinck, C., Bezemer, R. A., Kollmann, C., Lubbers, J., Hoskins, P. R., Fish, P. J., Fredfeldt, K. E., & Schaarschmidt, U. G. 1998, "Development of an example flow test object and comparison of five of these test objects, constructed in various laboratories", *Ultrasonics*, vol. 36, pp. 653-660.

Welch, P. D. 1967, "The Use of Fast Fourier Transform for the Estimation of Power Spectra: A Method Based on Time Averaging Over Short, Modified Periodograms", *IEEE Trans.Audio Electroacoustics*, vol. AU-15, pp. 70-73.

Wu, J. 1996, "Effects of nonlinear interaction on measurements of frequency-dependent attenuation coefficients", *J Acoust Soc Am*, vol. 99, no. 6, pp. 3380-3385.

Chapter 3 TMM RESULTS AND DISCUSSION

3.1 Sample thickness

The calliper measurement, as shown in table 5, gives a precise measurement and shows a maximum standard deviation of 0.04 mm. The results from time of flight measurements show a maximum standard deviation of 0.01 mm within a single plot but the inter-sample average gave values of up to 0.11 mm for repeated measurements of the same sample over the 2 year period. The values for thickness do not match as well for the sample thicknesses B & C.

Sample	**Calliper Measured** (Narrowband)	**Calliper** St. Dev.	**System Measured** (Broadband)	**System** St.Dev.
A	**12.71**	0.04	**12.71**	0.01
AA	**12.64**	0.04	**12.64**	0.01
B	**9.96**	0.03	**10.05**	0.01
BB	**10.08**	0.03	**10.18**	0.01
C	**7.06**	0.02	**7.21**	0.01
CC	**7.2**	0.02	**7.36**	0.01
D	**3.13**	0.02	**3.12**	0.01
DD	**2.94**	0.02	**2.96**	0.01

Table 5: Thickness measurements in mm of all samples for both broadband and narrowband systems

The results are broadly comparable for sample thickness and the differences between methods are minimal. It is evident that the thickness as measured by the time of flight software shows a smaller standard deviation. The inaccuracy of the inter-sample average for the broadband system may be because the loading of the sample relies on the surface tension of the gel clinging to the plane surface of the glass plate. The gel may therefore not lie flush with the glass for the middle two thicknesses. The thin sample is lighter and therefore adheres well whereas the thicker sample is held in place by a holding bar, which was originally designed for this thickness. It is

evident from the results that the measurement of the thickest and thinnest samples is more precise.

The apparent precision of the electronic calliper measurement arose because the gel was held between two sheets of (5 mm thick) in order for the measurement to be made. This was necessary as the soft material is easily damaged by the callipers. The method of using the Perspex ® sheets may have also compressed the gel which would have lead to a smaller thickness being measured.

3.2 Longitudinal study: speed of sound and attenuation coefficient

All measurements, as displayed in tables 6 & 7, show inter-sample results. The speed of sound measurements centre on the expected value of 1540 ms^{-1} (narrowband 1541 ms^{-1} ± 7.1, broadband 1544 ms^{-1} ± 5.4) with an overall average for all speed of sound measurements of 1540.5 ms^{-1} (± 8.8). For both measurements and systems, the values for the thinnest sample D are more variable with a standard deviation of 13.4 ms^{-1}.

	0 years		**1 year**		**3 years**	
Sample Batch	Speed	Atten^{n}	Speed	Atten^{n}	Speed	Atten^{n}
A	1546	0.49	1541	0.50	1543	0.49
B	1544	0.50	1541	0.49	1539	0.50
C	1542	0.48	1540	0.49	1541	0.49
D	1536	0.48	1538	0.48	1539	0.48
Average	**1542**	**0.49**	**1540**	**0.49**	**1541**	**0.49**
St. dev.	10	0.02	7	0.09	7	0.05
No. of samples	**n = 75**		**n = 49**		**n = 15**	

Table 6: Phase speed (ms^{-1}) and Attenuation Coefficient (dB $cm^{-1}MHz^{-1}$) results: Narrowband system

	0 years		1 year		2 years	
Sample Batch	Speed	Atten^{n}	Speed	Atten^{n}	Speed	Atten^{n}
A	1541	0.49	1546	0.50	1540	0.50
B	1543	0.50	1544	0.49	1542	0.49
C	1544	0.48	1545	0.49	1543	0.48
D	1557	0.48	1551	0.47	1540	0.47
Average	**1546**	**0.49**	**1546**	**0.49**	**1541**	**0.48**
St. dev.	6	0.02	5	0.02	7	0.02
No. of samples	**n = 7**		**n = 37**	**n = 7**	**n = 49**	**n = 7**

Table 7: Group speed (ms^{-1}) and Attenuation Coefficient (dB cm^{-1} MHz^{-1}) results: Broadband system

The 0-year values of attenuation measured by the broadband system were only measured on one set of samples. Again the results are more variable for the thinnest sample, D, with a standard deviation of 0.13. The overall average for attenuation for the narrowband and broadband system was 0.49 dB cm^{-1} MHz^{-1} (±0.08).

The average of both techniques (1541 ms^{-1}) for all samples (n = 271) shows good comparison with the expected value of 1540 ms^{-1} within experimental error, though the results vary more for the thinnest sample, D. This may be because the glycerol leaks out faster from the thinner sample, as the surface area to volume ratio is greater. This would give greater uncertainty for the thinner samples. The speed of sound values, group and phase speed, are comparable for both narrowband and broadband systems. Comparison of results for each system using standard error analysis showed a 95% confidence interval of (-1.6, - 2.6 ms^{-1}).

It is evident that the TMM samples are not degrading or changing significantly within the two year time span of the longitudinal study. The IEC recommends that the speed of sound of test phantoms is constant for the acoustic range 2 - 15 MHz, (IEC 1996) and it appears from these results that this range can be extended to 20 MHz for this TMM.

For measurements that were made at ambient room temperature and pressure, the measured water temperature ranged from 18.1 - 24.5 ^{o}C with an average temperature of 21.0 ^{o}C (st. dev. 1.6 ^{o}C). The room temperature showed seasonal variation and was not controllable as no air conditioning is fitted in our laboratory. The water temperature was measured within ± 0.2 ^{o}C and all measurements were then adjusted, using our measured data, to give a speed of sound at 21 ^{o}C. In the temperature dependence measurements, where water temperature in excess of ambient was required, a thermostatically controlled water heater was used. All measurements were made on unsealed specimens and so the values will be lower due to the leakage of glycerol from the specimen as shown in glycerol leaching results. Therefore as the time in water is limited to 2 minutes for each sample, then the maximum speed of sound loss will have been less than 1 ms^{-1}.

The values for the both systems appear to compare well with the predicted value for the attenuation coefficient. The standard deviation for the narrowband system is 0.07 dB cm^{-1} MHz^{-1} and for the broadband system, it is 0.02 dB cm^{-1} MHz^{-1}. This implies that the broadband system is more precise. Overall, it appears that the value for attenuation remains constant around the expected value of 0.5 dB cm^{-1} MHz^{-1} over the time period of measurements. The overall average for all measurements is 0.49 dB cm^{-1} MHz^{-1} and a standard error analysis shows a 95% confidence interval of 0.46 - 0.51).

3.3 Backscatter

Table 8 shows the backscatter characteristics of spectral slope, y-axis intercept, maximum and average power for 10 TMM samples drawn from 5 batches of material.

				Backscattered power (relative to water reference)			
Sample	**Thickness** mm	**Atten^{n}** dB MHz^{-1}	**Speed** ms^{-1}	**Spectral Slope** dB MHz^{-1}	**Y axis intercept** dB	**Pmax** dB	**Pavg** dB
1A	12.59	0.50	1541	1.53 (0.02)	-72.8 (6.3)	-38.9 (3.5)	-43.0 (3.9)
1AA	12.56	0.51	1541	1.46 (0.02)	-70.9 (6.6)	-38.5 (3.8)	-42.5 (4.1)
2A	12.62	0.55	1541	1.47 (0.02)	-70.4 (6.9)	-37.6 (3.8)	-41.7 (4.2)
2AA	12.58	0.54	1541	1.51 (0.02)	-71.4 (6.3)	-37.8 (3.9)	-41.9 (4.3)
3A	12.62	0.49	1545	1.49 (0.02)	-72.2 (7.0)	-39.1 (3.7)	-43.2 (4.2)
3AA	12.54	0.49	1545	1.50 (0.03)	-72.5 (8.1)	-39.2 (3.6)	-43.3 (4.2)
4A	12.63	0.44	1545	1.50 (0.02)	-72.9 (6.1)	-39.4 (3.7)	-43.6 (4.2)
4AA	12.56	0.42	1532	1.42 (0.03)	-71.6 (7.9)	-40.2 (3.6)	-43.9 (4.0)
5A	12.64	0.44	1542	1.37 (0.03)	-70.2 (7.8)	-39.7 (3.1)	-43.5 (3.7)
5AA	12.59	0.44	1541	1.54 (0.03)	-74.6 (7.0)	-40.1 (3.3)	-44.6 (3.7)
AVERAGE	**12.59**	**0.49**	**1543**	**1.48** (0.05)	**-71.9** (1.3)	**-39.0** (0.8)	**-43.1** (0.8)

Table 8: Backscattered power characteristics from 10 samples drawn from 5 production batches (1 – 5). A & AA denotes two samples from same batch. Figures in brackets denote standard deviation of all samples measured on a 3 x 3 spatial grid, 9mm square by noted thickness of d mms, 1µs sampling window with a bandwidth 17 - 23MHz. P_{max} and P_{avg} are power measurements. All measurements were taken at room temperature (20^{o}C). This table is adapted from Brewin et al. (2008).

Results in table 8 demonstrate that the spectral slope of the material increases with frequency at typically 1.5 dB MHz^{-1}. This compares favourably with theoretical spectral slope values, reproduced in figure 10, calculated for a variety of scatterer sizes albeit at a lower frequency range (Feleppa & Lizzi 1993). It is also apparent that, on extrapolation back to lower frequencies, the backscatter is comparable to that measured in an earlier study by Browne (2003) as shown by the asterisk.

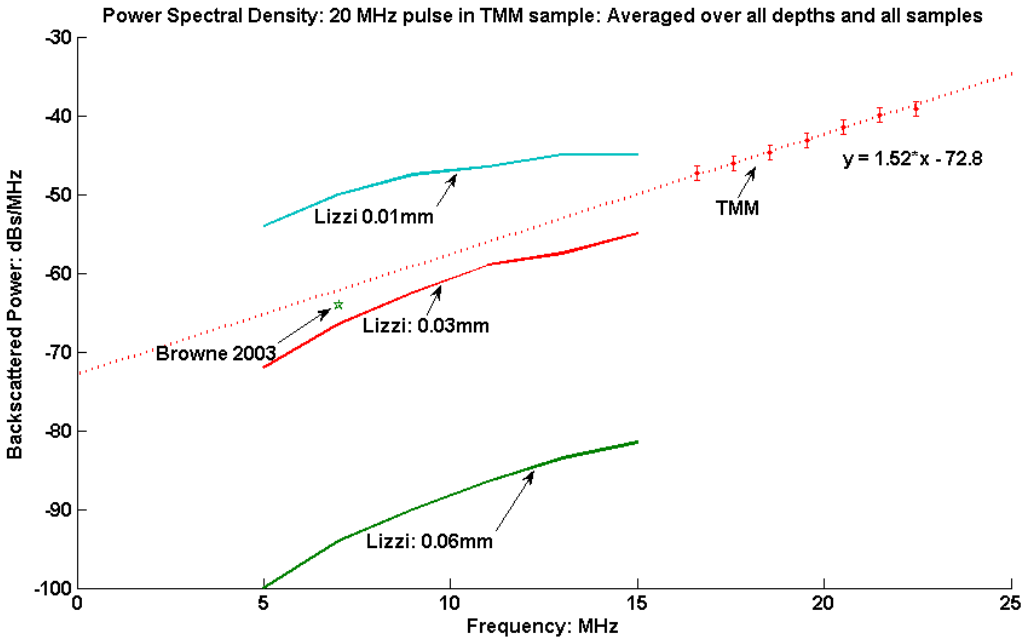

Figure 10: The backscattered power relative to water for all TMM samples (•) measured in the frequency range 17 – 23 MHz compared to theoretical spectral data derived by Lizzi (10 MHz bandwidth centred on 10 MHz and 3 different scatterer sizes) . The straight line fit (—) to the data has a spectral slope of 1.52 dB MHz^{-1} and a Y axis intercept at -72.8 dB. Error bars depict standard deviation. Lizzi data appears with the permission of the CRC press (Florida, USA).

Figure 11 shows the backscattered power, normalised to the reference water path, for all 10 samples. The straight line is derived from a least squares fit to the data.

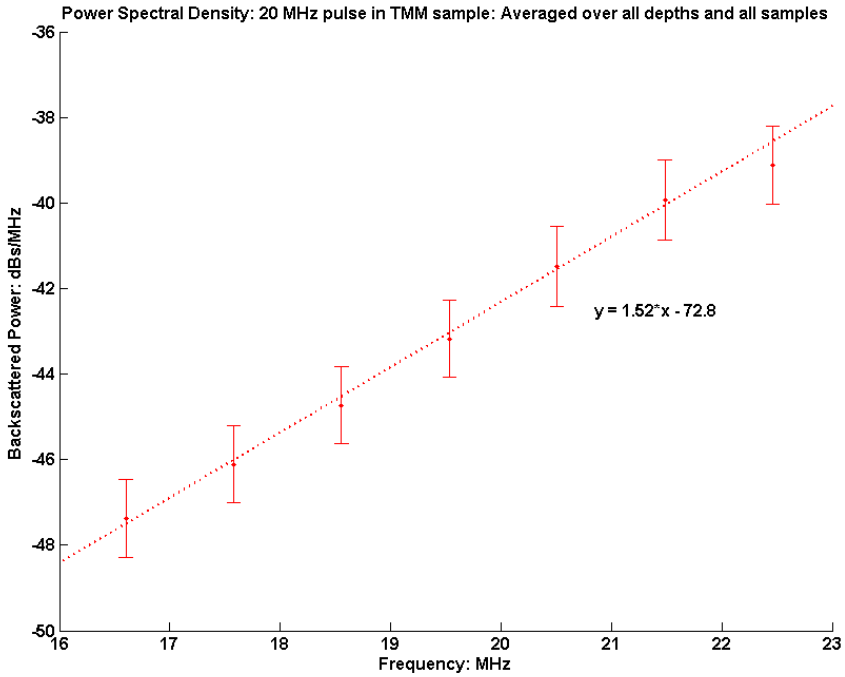

Figure 11: The backscattered power relative to water for 10 samples (•) drawn from 5 batches of TMM. Nominal centre frequency of measurement system was 20 MHz with a bandwidth 17-23 MHz. The straight line fit (—) to the data has a spectral slope of 1.52 dBs MHz^{-1} and a Y axis intercept at -72.8 dB. Error bars depict standard deviation.

The intra-sample standard deviations for the spectral slope parameter are typically 0.03 dB MHz^{-1} which indicates that for any one batch the material is behaving consistently across all sampling points within the 3 x 3 sampling matrix and at all sample thicknesses. The standard deviation for the inter sample comparison of spectral slope is slightly higher at 0.05 dB MHz^{-1} but nevertheless demonstrates consistency between batches of TMM.

The intra sample standard deviations for the Y-axis intercept parameter lay typically between 6 – 8 dBs (8% - 11%) and the closely associated backscattered average power and peak power have typical standard deviations of 3 – 5 dBs (7% - 11%). The inter sample standard deviations for the Y-axis intercept is lower at 1.3 dBs as is the average and peak power standard deviations of 0.8 dBs.

The broader spread of results in the backscatter parameters is to be expected given the known difficulty of measuring this parameter. The result is nonetheless comparable to other authors, for example the large inter-centre study conducted in USA (Madsen 1999). The study measured backscatter in two comparable TMMs but at a lower frequency range between 2.5 MHz and 6.5 MHz. The standard deviation of the mean of back scatter coefficient in the case of 10 samples (type B, attenuation coefficient of 0.61 dB cm^{-1} MHz^{-1}) measured at the reference centre were in the range 7% - 11%.

3.3.1 Glycerol leaching

It is apparent from the experiments, as shown in figure 12, that the speed of sound of the TMM does fall when the samples are kept unsealed in the water tank. The decrease in speed was found to decrease with time (from an initial 0.3 $ms^{-1}min^{-1}$ down to 0.1 ms^{-1} min^{-1} after 40 minutes). This effect was nullified once the specimens were encased in clingfilm (Saran wrap®) as demonstrated by the change in speed of sound over the three hour period was less than 1 ms^{-1}. The thicker specimen loses less speed of sound (19 ms^{-1}) over the time period than the other two (25 ms^{-1} & 20 ms^{-1}).

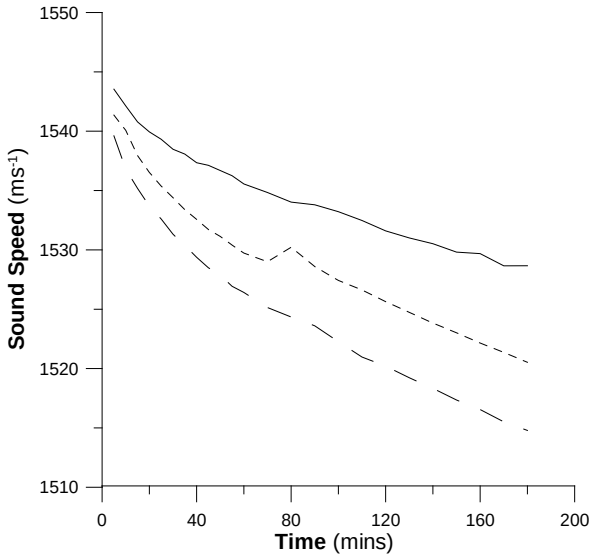

Figure 12: Change in sound speed (ms^{-1}) with time for three sample thicknesses (solid 12 mm, short dash 10 mm, long dash 7 mm) for unsealed samples over a three hour period using the broadband system.

For the purpose of the longitudinal study, the specimens were measured unsealed. However the measurements in the broadband system were carried out within a minute and this source of error is taken into account. The narrowband system took slightly longer to carry out measurements and this may be reflected by the lower average measurement (1539.6 ms^{-1}compared to 1543.5 ms^{-1} in the broadband system).

3.3.2 Cross centre validation

There is an overall agreement, see table 9, between the two in-house techniques (1539 & 1545 ms^{-1}) for speed of sound measurement and St.George's laboratory average (1555 ms^{-1}). The speed of sound results from the St.George's laboratory show a consistently higher value. For the attenuation results, the narrowband technique gives a higher value of 0.5 dB cm^{-1} MHz^{-1} in comparison to the other techniques (0.45 & 0.46 dB cm^{-1} MHz^{-1}), though the standard deviation is larger. The thinnest sample, D, gives the largest standard deviation for the speed of sound result for all measurements.

	Manual		Automatic		St.George's	
Sample	**Velocity**	**Atten^{n}**	**Velocity**	**Atten^{n}**	**Velocity**	**Atten^{n}**
A	**1542** (7)	**0.50** (0.06)	**1542** (6)	**0.47** (0.04)	**1556** (7)	**0.45** (0.03)
B	**1541** (7)	**0.49** (0.08)	**1543** (6)	**0.47** (0.04)	**1559** (6)	**0.46** (0.02)
C	**1540** (7)	**0.50** (0.10)	**1544** (6)	**0.45** (0.04)	**1548** (7)	**0.47** (0.02)
D	**1533** (13)	**0.49** (0.13)	**1549** (9)	**0.43** (0.06)	**1556** (10)	**0.45** (0.04)
Average	**1539**	**0.50**	**1545**	**0.45**	**1555**	**0.46**
St. dev.	(9)	(0.09)	(7)	(0.04)	(10)	(0.03)

Table 9: Cross centre comparison of attenuation coefficient (dB cm^{-1} MHz^{-1}) and sound speed (ms^{-1}). Inter sample standard deviation is quoted in brackets.

The average temperature for the measurements was 4^{o}C higher in the St.George's laboratory. As this result was non-temperature corrected, this would incur an increase of 4.5 ms^{-1} in the speed of sound of the TMM. This would partly explain the higher result. Therefore, there is a good comparison for the speed of sound measurements. For the attenuation, the increase in temperature would correspond to a decrease in attenuation coefficient of 0.02 dB cm^{-1} MHz^{-1}. The results for the broadband system would then match well with the results for the St. George's SAM. These systems share the same measurement method.

3.3.3 Temperature dependence

The speed of sound increases and attenuation decreases as the temperature of the TMM increases, as shown in figure 13. Each has a linear fit with an R^2 value of 0.99 and 0.98 respectively. It is evident that speed of sound increases with temperature at a rate of 2.1 m s^{-1} $^{o}C^{-1}$. Attenuation decreases with temperature at a rate of 0.005 dB cm^{-1} MHz^{-1} $^{o}C^{-1}$.

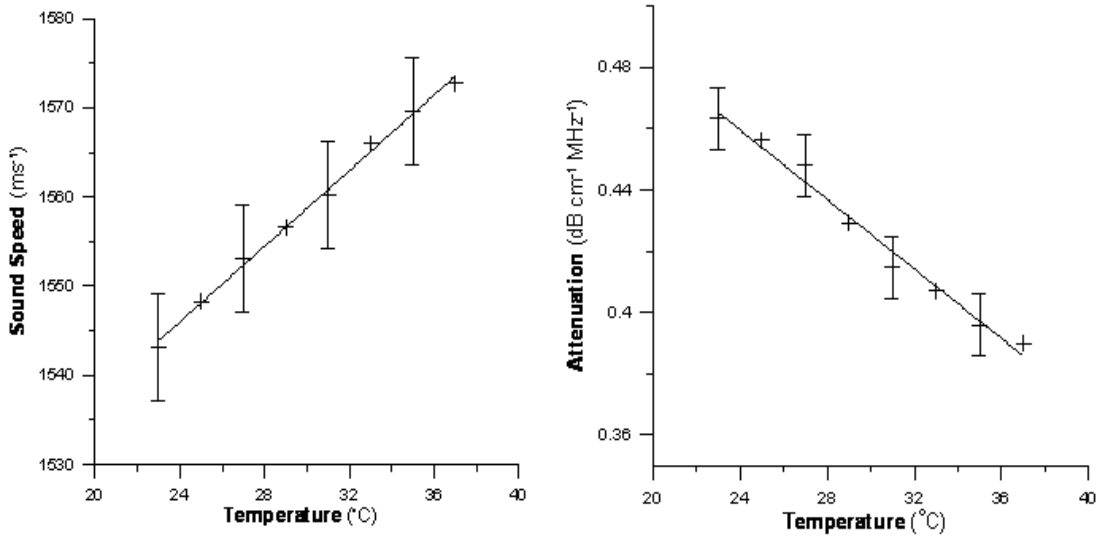

Figure 13: Change in sound speed (left) and attenuation (right) with increase in temperature. + is averaged data, - is linear fit and error bars show 1 standard deviation.

IEC 1390 (1996) states that the change in speed of sound due to temperature should be less than 3 m s^{-1} $^{o}C^{-1}$ and therefore this TMM (+2.1 ms^{-1} $^{o}C^{-1}$) complies at this high frequency of 20 MHz. It also states that the attenuation change (0.005 dB cm^{-1} MHz^{-1} $^{o}C^{-1}$) due to temperature should be less than 0.02 dB cm^{-1} MHz^{-1} $^{o}C^{-1}$ and again this TMM complies at this high frequency. The rise in speed of sound is slightly higher than other measured value of 1.5 ms^{-1} $^{o}C^{-1}$ (Browne et al. 2003).

3.3.4 Frequency dependence

The speed of sound of the TMM remains constant, as shown figure 14, with increasing frequency with a range of measured values of 1533 - 1539 ms^{-1}. The attenuation coefficient of the TMM increases with frequency (see fig.11) at a rate of 0.48 dB cm^{-1} MHz^{-1}. This value comes from the linear fit, which has an R^2 value of 0.99.

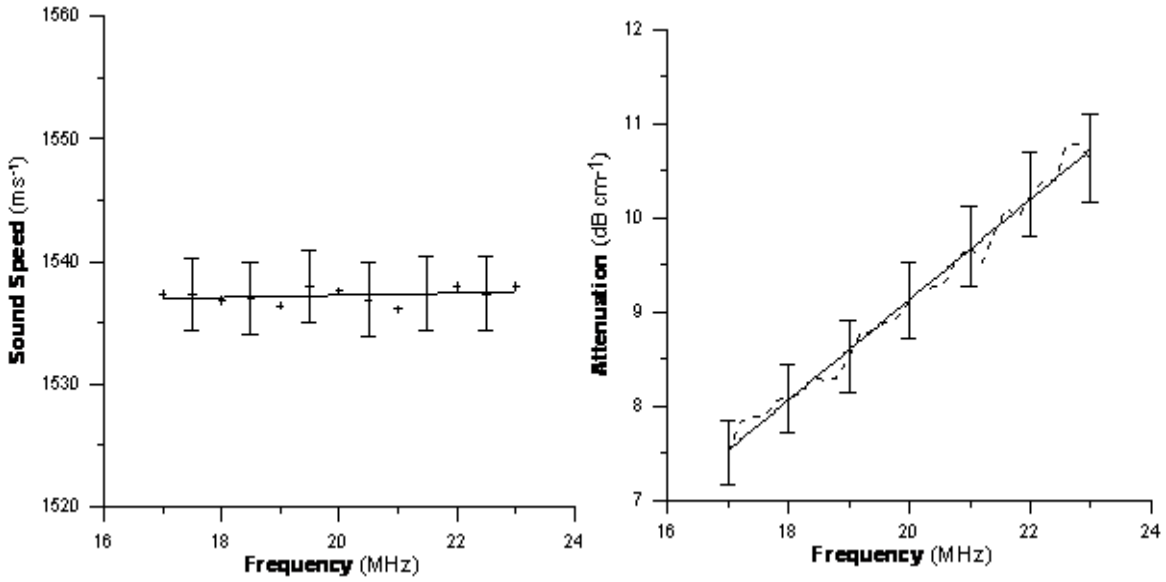

Figure 14: Change in sound speed (left) and attenuation (right) for the frequency range 17-23 MHz. + is averaged data and - is linear fit. Error bars show 1 standard deviation.

The mean value of 1537.1 ms^{-1} lies just below the expected value of 1540 ms^{-1}. Speed of sound shows no change over the higher frequency range which concurs with lower frequency results for the same agar TMM (Browne et al. 2003). The TMM attenuation coefficient shows a linear dependence with frequency and this compares well with that quoted in previous measurement of this characteristic (Browne et al. 2003), where the dependence was shown to be proportional to $f^{1.01}$.

3.3.5 Mass density, ρ

The mass density was calculated as 1.06 (± 0.03) x 10^3 kg m^{-3}. This compares with the value of 1.054 x 10^3 kg m^{-3} measured by Ramnarine et al. (2001).

3.4 References

Brewin, M. P., Pike, L. C., Rowland, D. E., & Birch, M. J. 2008, "The acoustic properties, centered on 20 MHz, of an agar-based tissue-mimicking material and its temperature, frequency and age dependence", *Ultrasound Med Biol*, vol. 34, no. 8, pp. 1292-1306.

Browne, J. E., Ramnarine, K. V., Watson, A. J., & Hoskins, P. R. 2003, "Assessment of the acoustic properties of common tissue-mimicking test phantoms", *Ultrasound Med Biol*, vol. 29, no. 7, pp. 1053-1060.

Feleppa, E. J. & Lizzi, F. L. 1993, "Opthalmological Tissue Characterisation by Scattering," in *Ultrasonic Scattering in Biological Tissues*, K. K. Shung & G. A. Thieme, eds., CRC Press, Boca Raton, pp. 393-408.

IEC 1996, *Ultrasonics - Real-time pulse-echo systems - Guide for test procedures to determine performance specifications, IEC Publication 1390*, International Electrotechnical Commission, Geneva.

Ramnarine, K. V., Anderson, T., & Hoskins, P. R. 2001, "Construction and geometric stability of physiological flow rate wall-less stenosis phantoms", *Ultrasound Med Biol*, vol. 27, pp. 245-250.

Chapter 4 PLAQUE CHARACTERISATION METHOD

4.1 Principle

The composite plaque sound speed was measured and plotted for each specimen using the substitution method. The plaque component percentage was calculated from segmentation of the histological data from the specimen. The plaque component speed was then derived by a matrix inversion of equation 5 below.

$$\begin{bmatrix} V1 \\ V2 \\ .... \\ Vn \end{bmatrix} = \begin{bmatrix} C11 & C12 & ... & Cn \\ C21 & C22 & ... & Cn \\ C31 & C32 & ... & Cn \\ C41 & C42 & ... & Cn \end{bmatrix} \begin{bmatrix} Vc1 \\ Vc2 \\ .... \\ Vcn \end{bmatrix}$$

Equation 5

where V is the composite plotline speed, C is the plaque component proportion and Vc is the speed within an individual plaque component.

The matrix inversion was performed using code written by my supervisor, Dr.Malcolm Birch, in Matlab (Matlab R2009b, MathWorks, Natick, MA, USA). The solution was performed using the biconjugate gradients stabilized method. Component percentage matrices were excluded when they contained either zero or negative coefficients. Similarly, composite speed matrices were excluded when they contained coefficients that were either negative or greater than 3×10^4.

Two different analyses were used to solve for the plaque component speed. A five component analysis (TMM, fibrous, lipid, elastic and calcification) was performed using a 5 x 5 matrix for histological sections where all five components were present, whereas a three component analysis using a 3 x 3 matrix was used where little or no elastic tissue and calcification was seen in the histological section. In the three component analysis, the coefficients were normalised for the component percentages.

4.2 Outline

In order to characterise the sound speed of the plaque components, the plaque specimen was first embedded in tissue mimicking material. The ultrasonic data for the plaque specimen was captured using a raster plot, which created a two dimensional plot of speed data through the plaque, shown in the contour map or surface plot in figure 15. The colour contour or the third dimension is the sound speed data. The ultrasound plotting beam is directed, into the page, in the z direction.

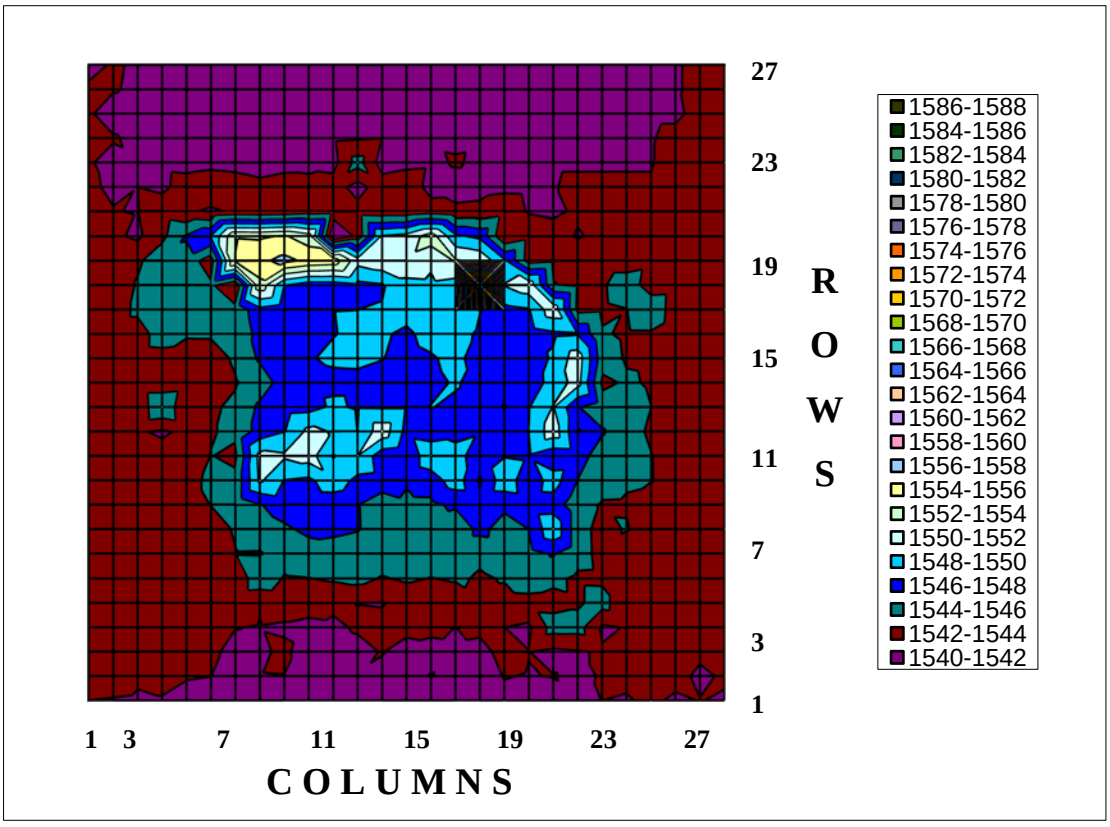

Figure 15: This figure shows a typical speed contour map or surface plot of a plaque specimen. Plot rows are defined in the x direction and plot columns in the y direction. The plot step size (0.66 mm) and plot line centres are marked by the gridlines of the figure. The colour bar to the right of the plot indicates the sound speed in ms^{-1}.

The plot starts in the bottom left corner of the grid at row 1, column 1. It steps along the row and captures data at each plotline, represented here by the gridlines, until it reaches the end column, 27. The transducer then moves up to the next row, 2. It then captures data at each plotline as it "rasters" back along the row to the left to

column 1. The raster is repeated until it reaches the top right corner of the grid at row 27, column 27.

The outline of the plaque specimen can be seen defined by the green contour in the centre of the plot. This outline was observed as a result of the increase in sound speed through the plaque in comparison to the relatively uniform background TMM sound speed.

This plot data outline was then compared against the physical outline of a digital photograph of the embedded plaque specimen. This photograph was captured in the same x-y plane as the plot shown in figure 15.

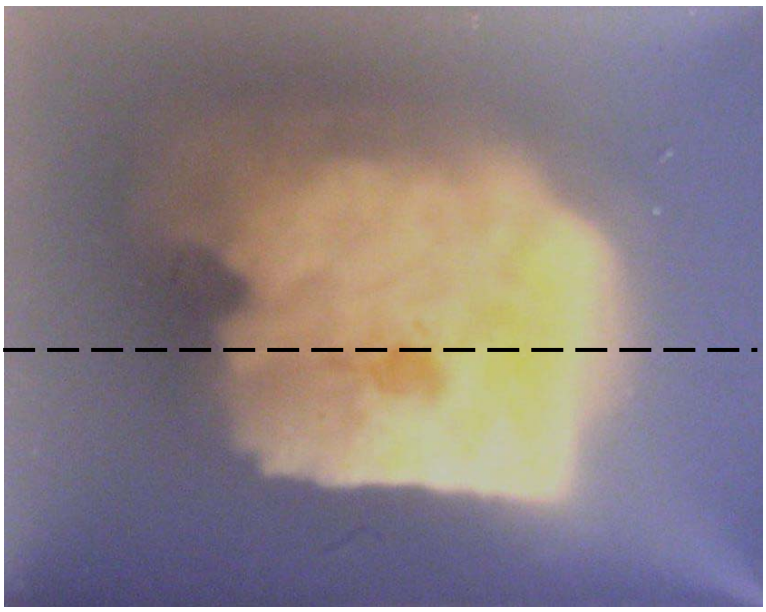

Figure 16: This figure shows the digital image of the plaque specimen embedded in TMM gel. The dashed black line shows the position of the histological section relevant to figure 17.

Once the outlines of the digital photograph and speed plot were matched, the coordinates of the location of the plaque within the speed plot could be determined. The photograph was then matched to the plaque component data from the histological sections. The y dimensions of the photo were first matched to the y dimension of its resultant histology as determined by the sectioning protocol. Each section was then assigned to a plot row. These sections were produced in the x-z plane or, as shown in figure 16, horizontally into the page. This plane was selected as the histological section gave plaque component percentages along the beam axis. It was also histologically easier to section in this plane due to the physical constraints of the plaque specimen size.

The histology was performed by a senior biomedical scientist in the histopathology department in the Blizard Institute of Cell and Molecular Science at the Barts and the London School of Medicine and Dentistry. This x-z plane section can be seen in figure 17, which shows a schematic representation of how the plot was performed and the way in which the histological section was compared to the plot data.

$$\begin{bmatrix} V1 \\ V2 \\ .... \\ Vn \end{bmatrix} = \begin{bmatrix} C11 & C12 & ... & Cn \\ C21 & C22 & ... & Cn \\ C31 & C32 & ... & Cn \\ C41 & C42 & ... & Cn \end{bmatrix} \begin{bmatrix} Vc1 \\ Vc2 \\ .... \\ Vcn \end{bmatrix}$$

Equation 5

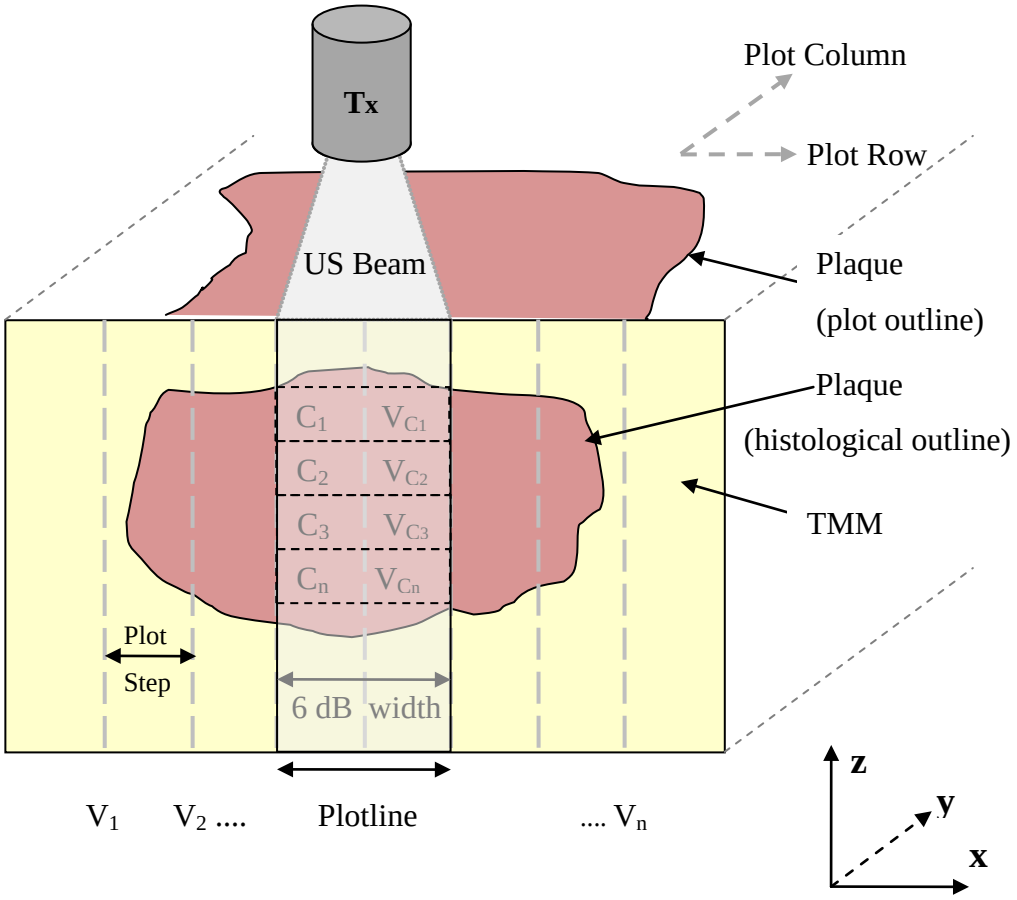

Figure 17: This figure shows a schematic representation of how the speed data was acquired and how the plaque component data was deduced. It shows the direction of the plot rows, x, and columns, y, top right. The plot plane is on the top side of the cube in the x-y plane. The histological slicing plane is the front face of the cube in the x-z plane. The plotline is spanned by the extent of the 6dB beamwidth of 1.33mm. C_1...C_n signify the plaque component percentages, which are measured from the histological section. V_1...V_n signify the composite sound speed along each plotline, which are measured using the sound speed plot. Vc1... V_{Cn} signify the sound speed of each plaque component, which are derived from the solution of the simultaneous equations, top left. The plotline centre and the ultrasound beam axis are shown by the dashed grey lines and are defined in the z direction.

The 6dB beamwidth was the assumed width for the calculation of the tissue components down each plotline. However, it was noted here that the beam is circular in nature. The composite sound speed along a plotline was represented by V_n. The percentage of each plaque component was defined by C_n and its component speed was given by V_{Cn}.

The ultrasound beam was transmitted through the embedded plaque specimen. A composite sound speed, V_n, was recorded for each plotline. The plaque component percentages, C_n, were calculated for each plotline by segmentation of the histological section. The plaque component speed was then derived from the composite speed and the component percentages using the solution of sets of simultaneous equations, as shown in equation 5. The entire plotting and matching procedure is explained in greater detail in this chapter.

4.3 Clear tissue mimicking material

The TMM serves to maintain the spatial alignment and position of the specimen during both measurement and histology. It also mimics, in part, the beam path of the clinical situation. This method of embedding tissue has been adopted in previous carotid plaque work to compare 3D ultrasound spatial compounding with histological analysis (Lind et al. 2007). It has also been used to create reference maps between ultrasound images and histological maps (Jensen et al. 2002; Rakebrandt et al. 2000; Wilhjelm et al. 2004; Wilhjelm et al. 2006).

It was apparent that in order to measure the sound speed of any tissue, it was necessary to hold the material in a fixed position. This was especially true for when repeat or consecutive measurements are to be made. Tissue mimicking material was chosen as it has a sound speed comparable to soft tissue, 1540 ms^{-1}.

After initial experiments, where the carotid plaque specimen was embedded in the IEC tissue mimicking gel, it became apparent that the TMM recipe would need to be altered. Firstly, the IEC gel is opaque. This meant that the outline of the plaque could not be visualised once the gel had set. This would make it impossible to match the speed plot to the digital photograph and, in turn, to the histology with any

certainty. Secondly, the particulates caused the microtome blade in histology to become blunt very quickly. This meant that the gel sample could not be sliced easily and the blade had to be replaced regularly at some expense.

An adaptation of the TMM was therefore required. The silicon carbide and aluminium oxide were removed. The recipe was then adjusted so that the glycerol concentration was kept constant, as shown in table 10.

The aim was to ensure that the sound speed remained matched to 1540 ms^{-1} and the resultant recipe gave a clear gel. This was rigorously tested to determine its acoustic properties of sound speed and attenuation.

Component	Weight composition (%)
Distilled Water	84.98
Glycerol	11.48
Agar	3.07
Rodalon	0.47

Table 10: This table details the weight by composition of the components of the clear agar gel.

It was important that the sound speed of the TMM was maintained at 1540 ms^{-1} in order to match as best as possible to that of the plaque tissue. This ensured that the diffraction effects on the measurements were reduced. The uncertainty due to the diffraction effect in the insertion or substitution method was shown to be very low when the sound speed of reference material is matched to the sample material (Verhoef, Cloostermans, & Thijssen 1985).

4.4 Beam profile

For the ultrasonic plotting of the plaque specimen, a weakly focussed 20MHz transducer (1 inch PTF, V316SU, Panametrics, Waltham, MA, USA) was used. The focussed beam was necessary in order to investigate the acoustic properties of the plaque components. The lipid pools are in the order of magnitude of around 1mm in diameter. The lipid components are of particular interest in this study as they are commonly associated with plaque vulnerability. In addition, in order to match the ultrasonic data to the histological data, it was necessary to optimise the resolution of the beam. The focussed beam improved the definition of the plot outline of the plaque specimen against the uniform background of TMM acoustic property values.

The beam characteristics of the transducer were assessed in order to determine the optimal positioning of the embedded specimen in the beam. In order to measure both the lateral resolution and the z-axis profile of the beam, a detailed inspection of the beam profile of the focussed beam was made. The lateral resolution was determined from the beam width calculated from the beam profile. This would provide an indication of the plot resolution and the physical accuracy of the plot outline. The z-axis beam profile showed the position of the last axial maximum.

The xyz scanning capability of the hydrophone arm of plotting tank, as shown in figure 3, was employed to carry out the beam profiling. The hydrophone set up is described previously in chapter 3. Both a z-axis beam profile plot and a succession of x-y plane profile plots were obtained. Firstly, the signal maximum was located at three arbitrary axial distances from the transducer element. By a process of iterations of the goniometers on both the transducer and the hydrophone arms, the emitted beam axis was aligned with the z axis of, and perpendicular to, the active tip of the hydrophone.

Firstly, a beam pressure intensity plot along the z-axis was obtained. Both positive and negative pressures were recorded at distances of 2 mm to 75 mm from the transducer face at 0.2 mm intervals. This plot is depicted in figure 17. N x N (N=10) matrices in 1mm steps of acoustic pressure in the x-y plane were obtained centred on the beam axis. A succession of plots was obtained in steps of 1 mm along the z-axis of the beam from near to the transducer face, 2 mm, to a distance of 75 mm.

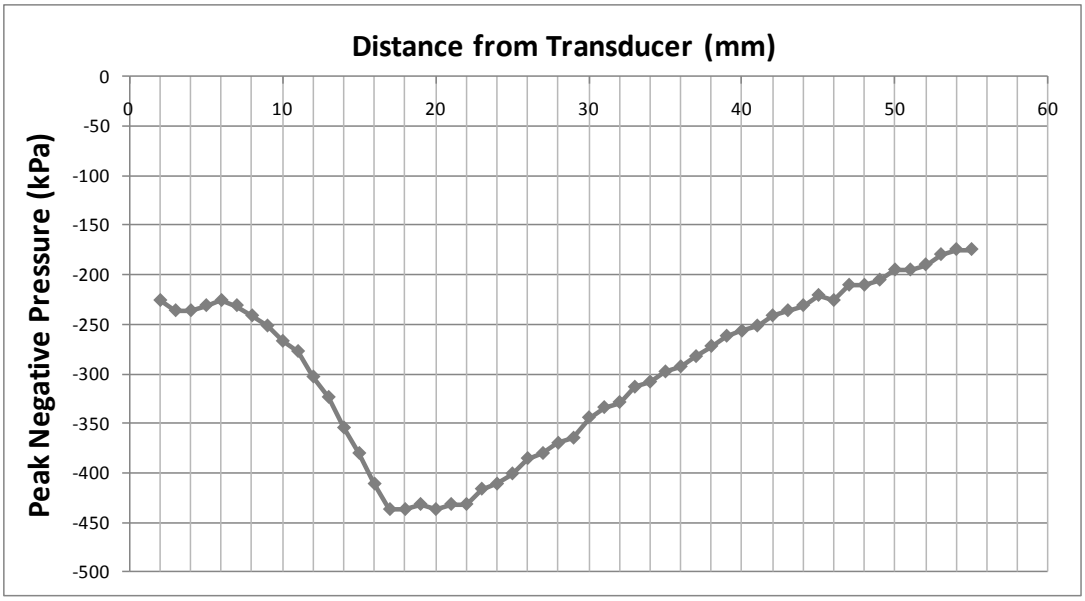

Figure 18: A graph to show the peak negative pressure of the beam along its axis produced by the focussed transducer.

Figure 18 shows that the last axial maximum lies at approximately 20 mm from the transducer face. On inspection of figure 19, it is apparent that the beam focus lies at around 19 mm from the transducer face. This distance did not agree with the technical specification (Panametrics-NDT, Waltham, MA, USA) of a focal length of 1.037 inches or 26.3 mm.

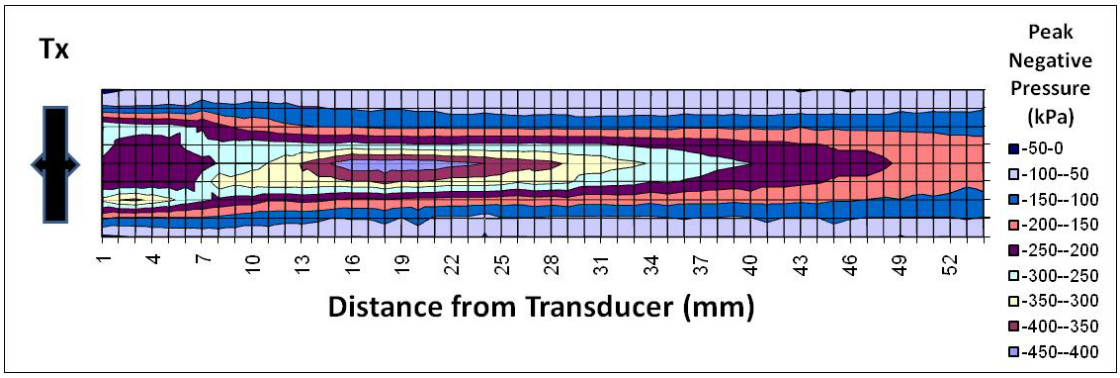

Figure 19: A contour map to show the peak negative pressure x-z beam profile for the focussed transducer for a range of 2 – 55 mm from the transducer face. The vertical axis of the plot represents 5 mm and the transducer aperture of 3mm is depicted to the left of the plot. A similar map was seen for the y-z beam profile.

It can be seen in figure 19 that the beam is laterally uniform from approximately 16 mm to 24 mm. Again, this region spans just short of the quoted technical specification of the focus. Over this range, it was calculated that the 6dB beam width is approximately 1.3 mm.

The transducer and plate were arranged so that the centre of the plaque specimen gel lay at a distance of approximately 23 mm at just short of the quoted focus. This was chosen as the beam profile along the z-axis was uniform here and it lies just past the last axial maximum. The axial centre of the gel also approximates the axial centre of the plaque and this was the inspection plane of interest.

4.5 Physical Validation Phantom

4.5.1 Step Phantom

In order to test that the measurement system is able to distinguish change in sound speed within the investigated subject or gel, step phantoms were designed and constructed. Three sets of gels of different sound speeds were made and the moulds of interlocking steps, see figure 20, were filled. Two steps of different sound speeds were then fitted together to form two different phantoms. Each phantom had a combination of two steps of different sound speed. One combination had sound speeds of 1540 ms^{-1} and 1590 ms^{-1} and the other had a combination of 1540 ms^{-1} and 1500 ms^{-1}. Sound speed profiles across these step phantoms were then plotted.

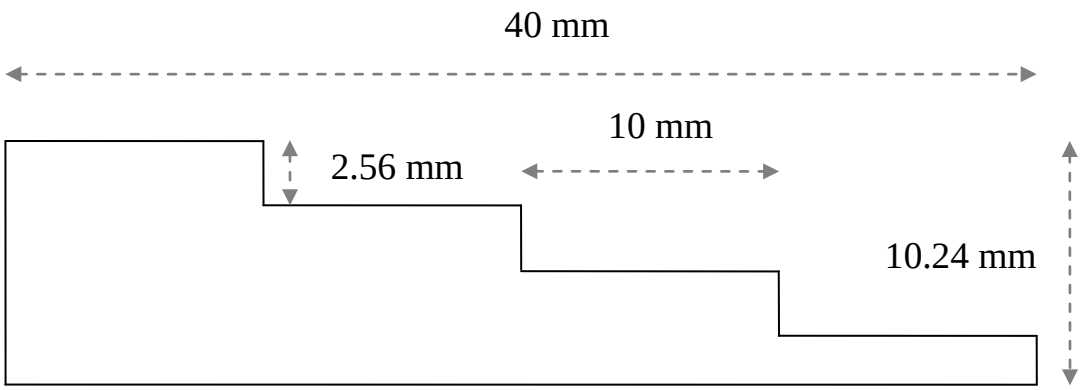

Figure 20: The cross section of the step phantom mould. The mould was 100 mm in length so that two steps could be cut for each gel set. The resultant step phantom of two interlocking steps had a with width and lnegth of 50 mm and height of 12.8 mm.

4.5.2 Grid phantom

In addition to the step phantom, a grid phantom was also constructed, see figure 21. A grid was cut out of a sheet of low density polyethylene (LDPE). This grid was embedded in a clear gel of 1540 ms^{-1}. Line profiles of sound speed were plotted for this grid in order to inspect the resolution of the sound speed plots for a variation of grid spine widths from 5 mm to 1 mm.

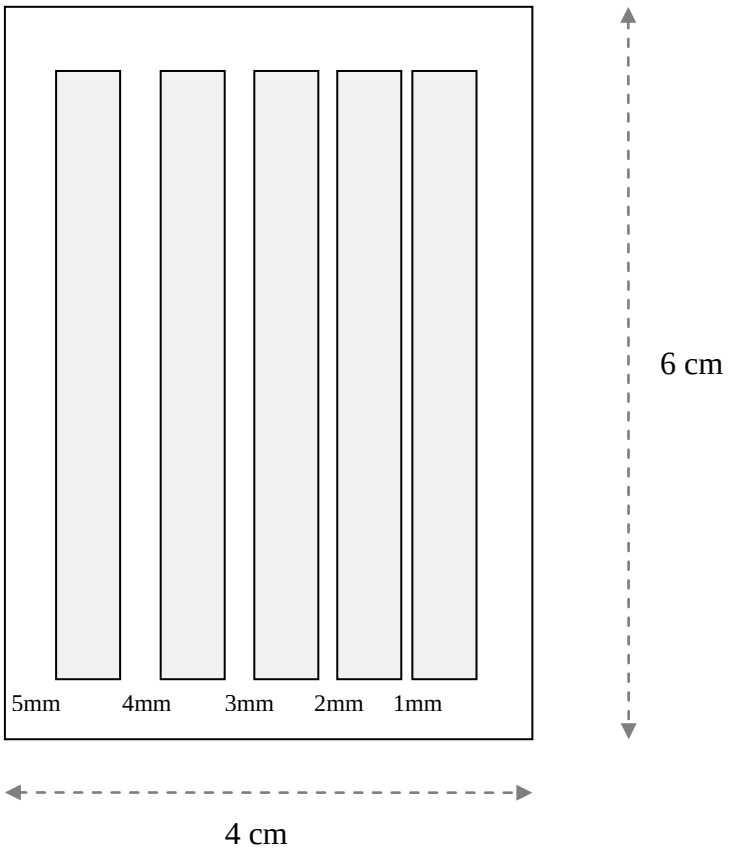

Figure 21: The x-y cut out of LDPE used to embed in the clear gel. The grey sections are cut out. This leaves four vertical bars of 5, 4, 3, 2 and 1 mm from left to right. This grid is then embedded in the bottom of a 60 x 60 mm clear gel block.

4.6 Plaque handling and embedding

4.6.1 Reception and preparation

As part of an ethically approved study (P/03/158, Redbridge and Waltham Forest LREC, UK), human carotid atherosclerotic plaque was obtained from patients undergoing carotid endarterectomy from whom informed consent was taken. On reception of the material from surgery, it was signed into the log book for storage in a dedicated tissue materials refrigerator (ZR 66/4 SI, Zanussi-Electrolux, Stockholm, Sweden).

The plaque specimens were received as intact excisions from the intimal wall of the carotid artery, see figure 1. The tissue was obtained within 1-2 hours post surgery and was stored in sterile saline. Upon reception, the plaque was laid out on a glass plate dedicated for cutting. It was trimmed with a scalpel in order to define and neaten its physical outline. The vessel was then opened out along the longitudinal division to enable the specimen to be spread out flat within the gel. This ensured that air bubbles did not become trapped within the luminal cavity when the specimen was set in the gel. In order to prepare the plaque for embedding in the TMM, the excess blood was washed from the specimen using sterile saline. This chemically active blood would otherwise leach out into the gel when being moulded and obscure the definition of the physical outline in the digital photograph.

The specimen was cut down to fit within a plot area of a certain size. The aim was to reduce the time for each plot to approximately two hours. This meant that the required number of plots can be performed in one day. This size has been determined as less than 20 x 20 mm. This sometimes necessitated dissecting the specimen into two pieces, in which case each piece was embedded into gel in a separate mould.

4.6.2 Tissue Preservation

The tissue was not fixed because the tissue was to be imaged while it was fresh. Formalin-fixation has been shown to increase the ultrasonic velocity by approximately 12 ms^{-1} in ovine and bovine myocardial tissue (Baldwin et al. 2005). However it decreased propagation speed in human brain by 10 ms^{-1} (Kremkau, Barnes, & McGraw 1981), though this was deemed an unexpected result. Fixed tissues are known to have an increased bulk modulus and this would cause an increase in measured speed. Early research also found that, while scattering properties shows appreciable change with time after excision, attenuation is relatively insensitive to autolytic processes for up to five days (Bamber et al. 1977).

The formalin fixing process is also known to reduce the lipid content of tissue and indeed may alter acoustic properties (Sasaki et al. 1996). They concluded that lipid-rich areas of tissue should be histologically assessed only in frozen sections. However this is not feasible for our study as the specimen would be frozen and sectioned before ultrasonic tests could be carried out.

Lipid is a significant component in atherosclerotic plaque in that large lipid pools are associated with vulnerability. In order that the sound speed of lipid may be assessed, the specimen was therefore not fixed. An investigation of the possible change in sound speed at different temperatures due to change in lipid state was also devised. It has been shown that fatty tissue has a negative dependence of sound speed on temperature (Bamber & Hill 1979) and this study aimed to investigate this dependency.

The moulding of the specimen in gel prevents air from making contact with the specimen and will thereby help to delay the decay process. The anti-bacterial agent, Rodalon, in the TMM may also slow autolysis. As the specimen is unfixed, it is desirable to complete the ultrasonic investigation as quickly as possible. All plaque specimens were embedded, plotted and then fixed within 48 hours.

The change in sound speed with time from excision for unfixed tissue was investigated. Two plaque specimens embedded in gel were measured on three consecutive days to assess the change in sound speed with time after excision.

4.6.3 Plaque Embedding

The ingredients for one litre of the clear agar gel (TMM) were measured, as detailed above, and mixed in a glass jar. It was determined that this was a sufficient volume to ensure that the gel could be mixed homogenously during the heating process. A double heated water bath was used to manufacture the gel using a digital immersion thermo-regulator (TE-10D Tempunit, Techne, Burlington, NJ, USA). The ingredients were heated to 96^{o}C (± 3^{o}C) for 1 hour to activate the agar. The mixture was stirred continuously at a rate of 150 rpm, which did not allow the particulates to settle but was not sufficient to promote the production of air bubbles (Ramnarine, Anderson, & Hoskins 2001). Once the gel cooled to a temperature of 45^{o}C, it was poured out as it sets at 42^{o}C. Approximately 200ml of TMM gel was poured off from the top as it may contain bubbles produced by the surfactant property of Rodalon^{TM}, the anti-bacterial agent.

Plaque was then embedded into the gel in a 60 mm x 60 mm x 12.7 mm mould, see figure 22. Approximately a 3 mm layer of TMM was first poured into the bottom of the mould. This layer was allowed to congeal for a short period. The plaque was then placed, lumen up, within the plot area square marked on the lid of the mould. At this stage, the gel surface was strong enough to support the specimen so that it did not sink. The mould was then topped up with the gel to cover the plaque specimen. On visual inspection, it was ensured that any remaining air bubbles were not trapped in and around the plaque. The lid was then slowly lowered over the gel and care was taken to force out all air bubbles from the moulded gel. The lid was then secured with screws and the gel was left to set.

Figure 22: This figure shows the plaque embedding mould. Top plate shows the open mould. The three sets of six holes on the cover (top right) are air release holes that also mark the position of the plot area where the plaque must sit during moulding. The sets of two channels on each edge of the lid allow any air bubbles on the surface to escape when the lid is attached. The lower plate shows the closed mould.

Meanwhile, the rest of the gel was then poured into the quality assurance (QA) moulds marked A - D as detailed in figure 2. Once the gel had set, the gel with embedded plaque was removed from the mould. It was then stored in the hydrating solution in the fridge overnight. Research has shown that the acoustic properties of plaque do not change significantly when specimens are frozen or refrigerated (Lockwood et al. 1991). The QA TMM samples were also stored in hydrating solution in a separate container. These samples were measured for sound speed and attenuation in order to calibrate the TMM batch for the corresponding plaque plots.

4.7 Ultrasonic measurements

4.7.1 Broadband Reflection technique

4.7.1.1 Target Plate Calibration

A new target plate was constructed for the measurement of plaque specimen gels. This was constructed using an aluminium frame that holds the lapped glass. Initial experiments were performed to inspect the flatness of the plate. The perpendicularity of the plate to the beam axis was measured by assessment of the return times of the reflected pulse. This assumed that the sound speed in water is constant over the measurement period of thirty minutes.

A plot area of approximately 20 x 20 mm was identified as the location to perform the plaque plots. The best area for flatness in the bottom section of the plate was selected where the time difference range for the reflected signal was less than 10 ns. This translates to an error of 2 ms^{-1} in the speed determination. This area is shown in figure 23 below.

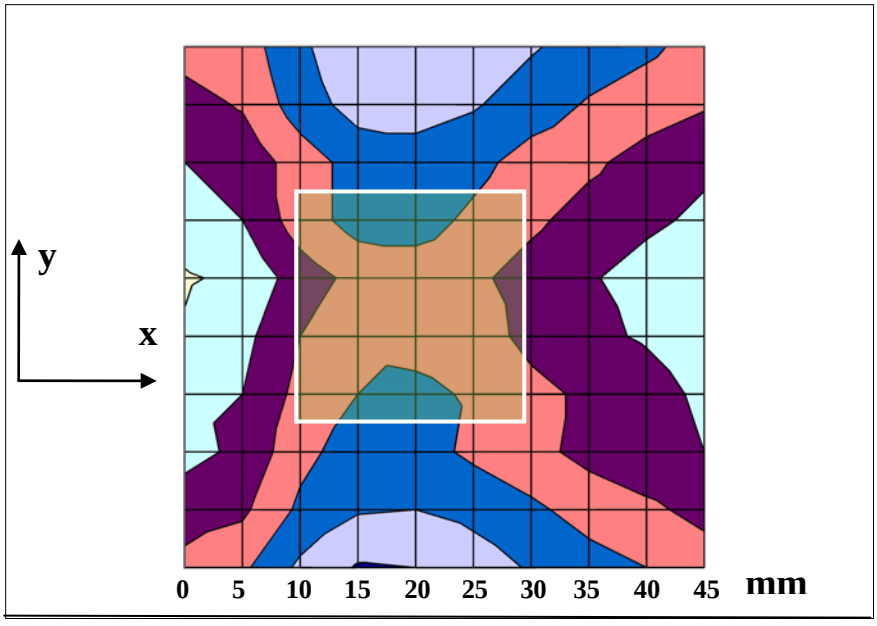

Figure 23: A contour map to show the return times from the central 45 x 45 mm square in the bottom section of the target plate. The contours represent time bandings of 5 ns. The central highlighted square shows the selected 20 x 20 mm plot area.

4.7.1.2 Plotting protocol

Pulse (group) speed, plaque attenuation and backscattered radiofrequency data were plotted for the plaque specimen using the broadband reflection method as outlined in chapter 2.

The specimen gel was removed from the fridge and allowed to reach the temperature of the plotting tank water. This was achieved by submerging the container in the plotting tank. The temperature equilibrium of the gel was measured by using an insertion probe thermocouple (± 1.5^{o}C, type K, RS components, Corby, UK). One hour was afforded for the gel to reach ambient temperature of the water in the tank.

The specimen gel was mounted onto a different target plate where the sample holding bar was replaced with a sample holding frame. As the specimen gel must be sealed to prevent the glycerol leaching as discussed in chapter 2, an alternative method of loading the specimen gel onto the plate was devised. No sufficient method of sealing the gel for extended periods of submersion in water was found so that a sealed specimen gel could be simply slotted onto the target plate while it was *in situ*.

Rigorous calibration of the return times from the time measurement points in the plot area was carried out. The unloaded plate was positioned so that the beam is directed at the centre of the plot area as depicted in figure 24.

The goniometers on both the transducer and target arms were adjusted in turn so that the reflected signal was maximised. The plot area where the plaque will be positioned for the plot was then inspected as to its flatness and perpendicularity to the beam. The return time of the signal from each of the four corners of the plot area were equalised so that the time difference was minimised. Flatness here therefore refers to the calibration of a plotting area over which the return time difference is less than 5ns. This relates to a return distance difference of less than 10 µm.

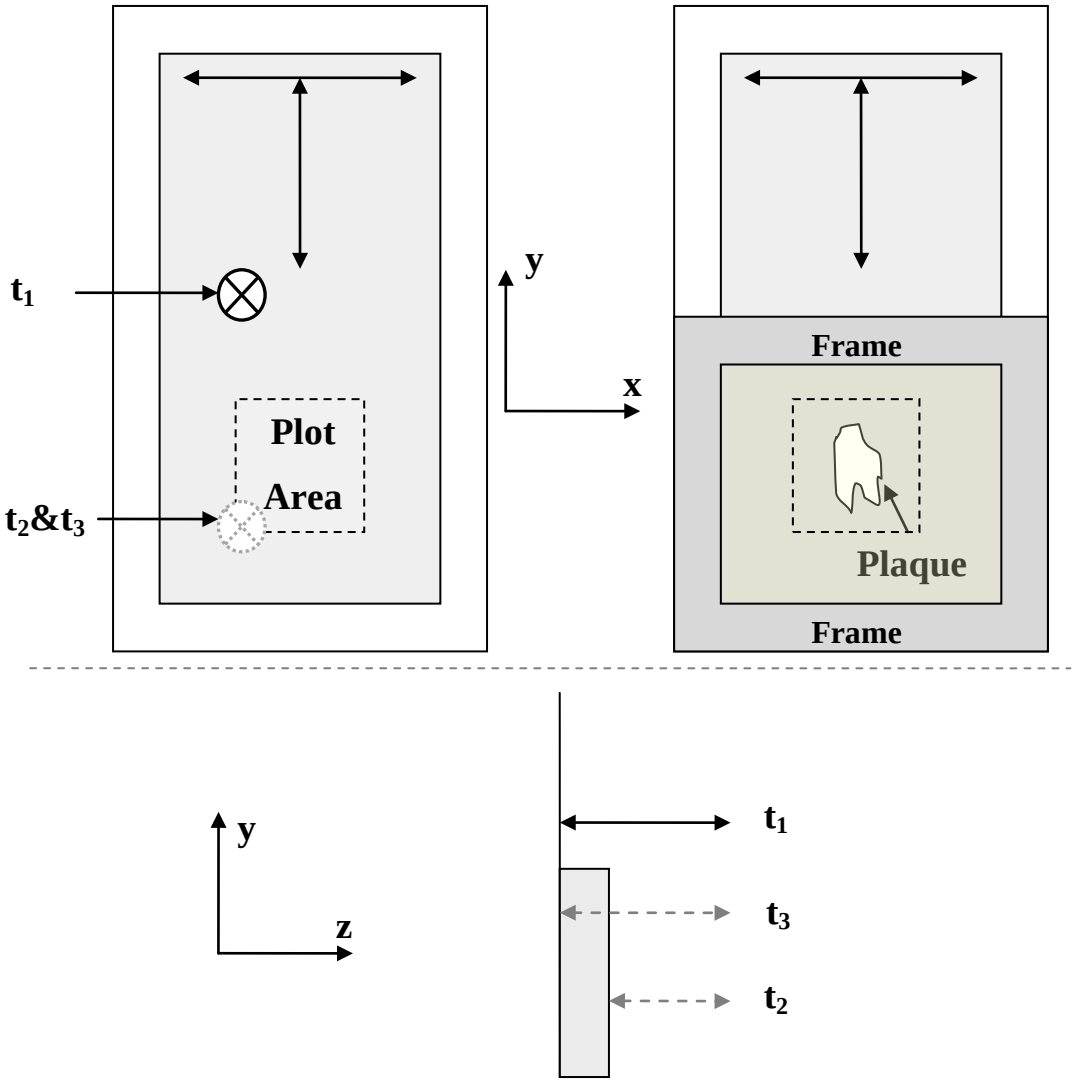

Figure 24: This figure is a schematic of the target plate and return times for the reflection technique. The top part of this figure shows the glass plate, unloaded on left and loaded with plaque gel on right, in the x-y plane. The left figure shows the square plot area where its corners were used to equate the return times. The signal was maximised at the centre of the plot area. The two double headed arrows in the top section of the plate show the position of the measurement extents for the calibration time differences. The circled crosses signify the measurement positions of the transducer directed at the plate in the z-direction, into the page. The transducer sweeps from bottom left to top right of the plot area in a raster fashion to complete the plot. The right figure shows the Perspex™ frame holding the plaque in gel against the glass plate over the plot area. The bottom part of the figure shows the target plate from the side, in the y-z plane, to illustrate the beam paths for each time measurement.

Each time the specimen gel was loaded onto the plate, the plate had to be removed from the target arm. When the target plate was removed and then reattached, it could not be assured that the plot area is flat to this tolerance without this calibration check. Once the plaque gel was loaded, the plot area could not be checked directly for flatness. The signal must now pass through the gel.

Before the plate was removed for the plaque gel to be loaded, two time differences for flatness calibration are recorded. These are measured between two points in both the horizontal and vertical direction on the top section of the plate. This lies above where the gel mounting frame will be attached, see figure 24. The correction time, as discussed in chapter 2, between the water reference time point, t_1, and sample point, t_2 & t_3, was also recorded here. This was entered as a manual input into the software at the start of the plot. The time difference was then simply subtracted from the measured value of t_1 within the software calculation.

Once the three times were recorded, the target plate is removed by releasing its two hold screws at the top of the plate. The specimen gel was placed in the bottom section of the plate as in figure 24. The gel adheres through surface tension to the glass plate. Manual manipulation ensured that no air bubbles are trapped between the gel and the glass. Cling film was then wrapped over the gel and round the back of the target plate. The surface of the cling film was carefully smoothed across the surface of the gel with a sharp edge. The Perspex™ frame was then mounted over the gel. The frame served to secure the cling film to prevent glycerol leakage from the gel. It also tightened the surface of the clingfilm across the gel.

The frame was attached to the aluminium frame of the glass plate using adhesive tape. A single layer of cling film extended up to the top of the plate. This ensured that the reference water beam path also has one layer of clingfilm to traverse. The target plate, loaded with plaque gel, was then re-attached to the target arm. The calibration time differences were checked in both horizontal and vertical directions in the top section of the plate. The goniometers were adjusted so that the recorded calibration time differences are matched. This assured that the plot area was flat and perpendicular to the beam.

The approximate position of the plaque in the gel was known from the moulding position. An initial rough (n x n) plot with a 2mm step size was first carried out to discern where the plaque sits within the plot area. This was visualised on the LabView output screen on completion of the plot. The plot origin was adjusted to ensure that the plaque outline lies centrally within the plot area. The reading of sound speed for the TMM background was checked to be constant at the four corners of the plot. The tolerance in flatness calibration meant that this constancy is to within 2 ms^{-1}. The size of the plot square was also determined from both the rough plot and the known dimensions of the plaque.

The final accurate plots were then performed. A square raster plot was made with a step size of 0.66 mm. This size was chosen for several reasons. Firstly it was determined as approximately half the 6 dB beam width of 1.3 mm, which indicates the lateral resolution of the beam. At this step size, the resulting 2-D plot of speed gave an adequate indication of the size and shape of the plaque being plotted. The step size also influenced the time taken for each plot. Typically, the plot would be 20 mm x 20 mm (30 x 30 steps) and this would take 90 minutes. Total plot time was important so that the plaque specimen can be processed within the 48 hour limit.

Two consecutive "cold" plots of sound speed were made at tank water temperature of 21^{o}C (± 2^{o}C). The ambient temperature of the water was recorded by the thermocouple at each plotline. The temperature was seen to remain constant over the duration of each plot to within 0.5^{o}C. The speed plots were followed by an attenuation plot and a radiofrequency (RF) backscatter plot made in succession on the same raster matrix. The water was then heated to body temperature, 37^{o}C. Two consecutive "hot" plots of sound speed were made, followed by another attenuation plot and an RF plot. The plotting was then finished for the day and the specimen was returned to its container in the fridge overnight.

For the purpose of this study, the speed data was the primary line of investigation but the attenuation and RF were measured and plotted in order to investigate any anomalies or to be used for further studies.

4.7.1.3 Alteration to Labview software

Initial broadband reflection speed plots showed a range of 1520 - 1670 ms^{-1} across the plaque. This was considered reasonable as the hard calcium deposits would indeed cause the observed increase in speed. Conversely, the soft lipid pools would shift the speed down. However, on inspection of the histology, the measured proportions of calcium were deemed not significant enough to cause this increase. The plotting was observed and it was seen that in the more attenuative sections of the samples, the signal was almost totally diminished. This meant that it used only the time delay to the scope window as the measured time and thus a short, inaccurate time measurement of t_3 was recorded. This resulted in a large shift in speed being calculated.

The software was changed so that if no pulse was detected then the gain was ramped up by one step at a time. At each gain step, the time at which the pulse was detected was measured as described in chapter 2. If there was still no signal detected at highest gain, the automation stops and the observer must manually search for the received pulse and input the time shift as measured using the scope callipers. The latter was rarely the case though when a heavily calcified plaque is plotted, insufficient signal was seen through those areas of calcification due to the high signal attenuation. If there was significant calcification, then large areas of no data were seen on the plot. On one occasion, the plotting of the specimen was discontinued and this specimen was processed no further.

4.7.2 Broadband Transmission technique

4.7.2.1 Plotting protocol

On the following day, the plaque was then plotted using a broadband transmission technique. A different target plate was designed for this technique. This target plate was also made with lapped glass in an aluminium frame. In order for the transmission measurements to be made, the glass plate had two circular holes cut into it, see figure 25. Two transmitted signals were now received by the needle hydrophone, see figure 3 in chapter 2. These are the through sample signal, t_3, and an additional water reference signal, t_4. The two existing reflected signals, t_1 and t_2,

were received by the transducer and used to calculate the depth. The time shift, Δt, was now derived from the difference between t_3 and t_4.

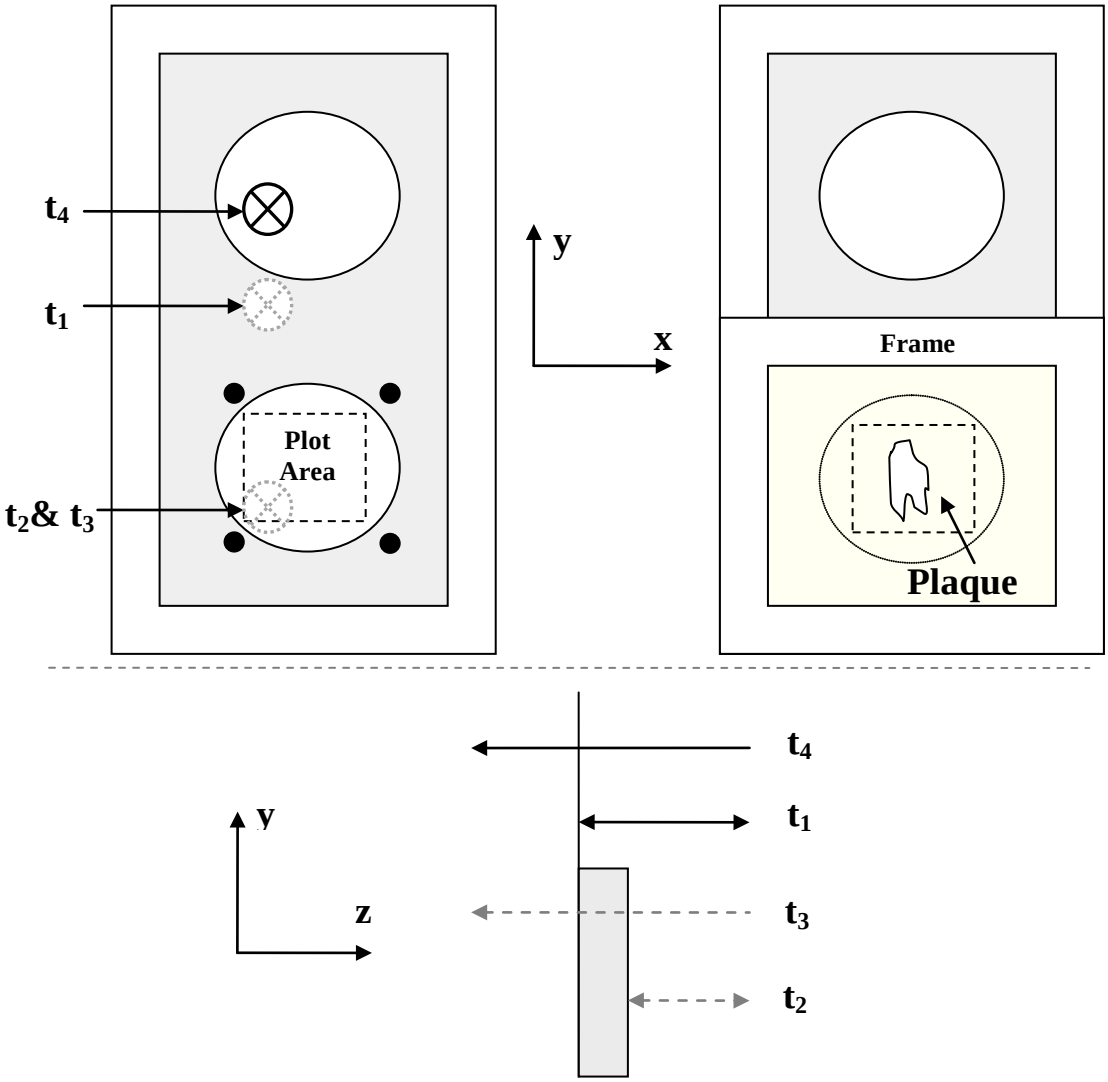

Figure 25: This figure is a schematic of the target plate and return/transmit times for the transmission technique. The top part of this figure shows the unloaded and loaded transmission target plate, in the x-y plane, with two circular holes in the glass. The left figure shows the sample (t_2 & t_3) and reference time (t_4 & t_1) measurement points. The four black dots around the bottom hole represent the time measurement points for plot area flattening. The circled crosses (black solid and grey dotted) signify the measurement positions of the transducer. It is directed at the plate into the page in the z-direction. The right figure shows the position of the plaque in the gel once it has been loaded to the glass plate. The bottom part of the figure shows the target plate from the side, in the y-z plane, to illustrate the beam paths for each time measurement.

Before the plaque gel was loaded to the plate, the plot area was now flattened by equalising the reflected time measurements from the four points around the bottom hole. The flatness of the plate could not be calibrated over the plot area as there is no reflected signal so the nearest points on the glass are used. Again the average values of these four equalised time measurements were different to that found at t_1. This time difference was entered as a manual input into the software at the start of the plot and subtracted from the measured value of t_1.

On the commencement of the plot, the additional time measurement, t_4, was made. This was the reference water path signal, t_4, through the top hole. The target plate was moved and the glass reflected water reference time measurement, t_1, was recorded. The target was then moved over the plot area. The reflection time, t_2, from the gel surface continued to provide data for the gel depth calculation as in the reflection technique. Time t_3 became the through sample transmitted time measurement.

The speed equation, see equation 2, was amended. The factor of 2 was removed from the denominator as the beam only passes through the sample once. The time shift, Δt, and hence the speed was now derived from the difference between t_4 and t_3. The depth calculation remained unchanged. It was calculated by multiplication of the temperature corrected sound speed in water, c_w, and the time difference between t_2 and t_3 at each point. For the attenuation factor, the denominator was similarly reduced by two and the FFTs were derived from the transmitted water reference signal and the through sample signal.

Once the plot origin had been determined from the rough plot, the accurate plots were made. Two plots of speed were made to check for repeatability. These were followed by an attenuation plot. The water was then heated to 37^0C and these three plots were then repeated. No RF backscatter plots were made as no reflected reference signal was measured.

4.7.3 Ultrasonic data output

The LabVIEW speed plot stored ASCII spreadsheet data for both the speed and depth at each plot point. The LabVIEW attenuation plot stored a spreadsheet of the Fourier transform data of the signal at each data point. This was acquired from the oscilloscope maths channel. The same spreadsheet also stored the water reference data that is captured at the start of the plot at reference point, t_2. Depth data was recorded in spreadsheet format for the attenuation plot. The LabVIEW RF backscatter data was stored in similar spreadsheet format to the attenuation data. The speed and attenuation plots were visualised using an Excel surface plot or contour map.

4.7.4 Further data acquisition

Once both the reflection and transmission plots were made, the plaque was then imaged using an ultrasound scanner (HDI 5000, Philips ATL, MA, USA). Transverse B-mode image sections were obtained in the same plane as the speed plot rows. The plaque was scanned with a high frequency "hockey stick" probe (CL 15-7, Philips ATL, MA, USA). The plotting tank system was used to drive the probe in the same matrix of 0.66mm steps that are used in the plots. At each scan plane, the raw RF data was also recorded using a data acquisition board (Raven, Philips ATL, MA, USA). This data was surplus to requirement of the study but may be used later to inspect the RF backscatter. The US images may be used for assessment of grey scale median, GSM, or for registration to make a comparison to our results if they were found to be significant. The raw RF data could also be analysed to compliment the speed data.

4.8 Specimen preparation for histology

4.8.1 Reduction of specimen gel size

Before the plaque specimen gel was sent to histology, the specimen gel was cut down to a smaller size of approximately 25 x 25 mm. This was carried out using a sharp surgical blade in a guillotine set-up. This was done at the request of the histologist in order to make the specimen gel a more manageable size. This made it possible for the sections to be laid out onto the glass slides with more ease. The size reduction also shortened the time taken to fix the embedded specimen. This apparatus, see figure 26, has been engineered in-house so that the guide is perpendicular to the blade. In this way, the geometry of the plot was retained so that the histological sections matched that of the plot row, x-z plane.

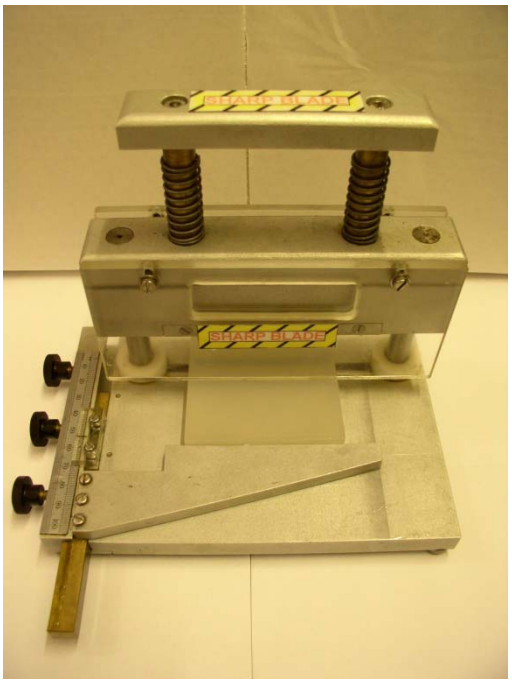

Figure 26: This photograph shows the guillotine used to cut the plaque gel samples down in size for histology. The specimen gel is moved under the blade using the perpendicular guide.

Once the specimen gel was cut down to size, digital photographic images were taken of the plaque specimen with a metric scale or metal ruler along side, as shown in figure 27. This photo was used to indicate the size of the plaque in each dimension, x and y. It also provided a digital image of the physical outline of the specimen to be matched up to that of the speed plot contour map. Only the plaques with good visual comparison of physical outline from the photograph versus speed plot were sent to histology to be processed. A diagonal notch was cut from the top right corner of the specimen gel to signify orientation of the specimen to the histologist.

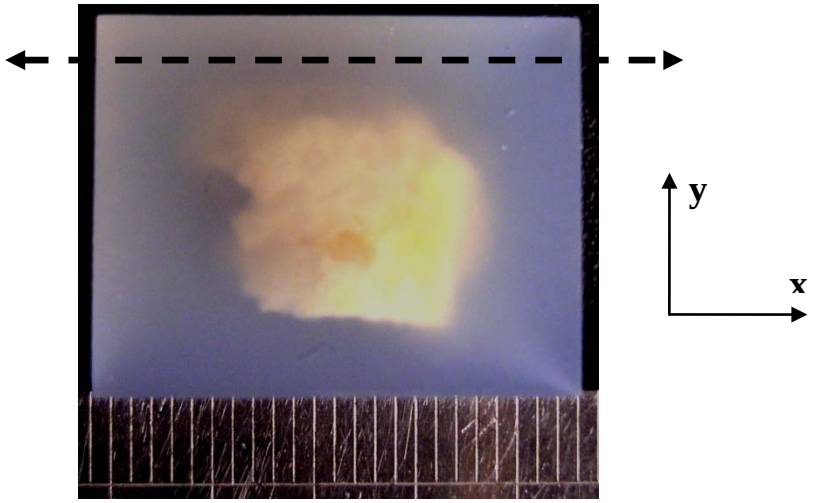

Figure 27: This figure is a schematic to show the direction/plane of histological sectioning. The dashed line shows the direction of the histological slicing. This section direction will match the row direction of the speed plot. The section is a cross-section of the gel into the page. The x dimension of the plaque is defined horizontally, the y dimension vertically and the depth, z, of the plaque into the page.

4.8.2 Specimen gel dimension and orientation - uncertainty

There is a small uncertainty involved on the cutting down of the specimen gel. The accuracy of the scale on the guillotine means that the cut has an uncertainty of ± 0.25 mm. The dimensions of the cut down specimen gel are measured with the digital callipers. The uncertainty in size measurement does not directly affect the outcome of component sound speed.

A small uncertainty may also arise for the specimen orientation in the angle of the slice of the guillotine. It is important that the orientation of the histological sectioning matches that of the plot (x-z) plane down or through the specimen gel. This orientation uncertainty may not be important when the histological section lies in the middle of a plot row. It was observed that there was little variation in the shape or dimension of the plaque over the five sections on one histological slide. In the main, there was little change from one slide to the next. This implied that angle uncertainty in cutting down the block had a tolerance of approximately 1^0. This uncertainty would also be nullified when the percentage components entered into the simultaneous solution are averaged out over three consecutive plotlines.

Further uncertainty in orientation was also inherent in the mounting of the specimen block into the paraffin wax in the histological procedure. Care was taken to level the block on the molten wax and thus retain the geometry. However, this was a difficult process. The uncertainty here was hard to determine but the block may be mounted at an angle of up to 2^0 off the perpendicular.

4.8.3 Histology protocol

The embedded plaque was fixed in 10% formalin solution prior to staining, washing and processing. It was then orientated and embedded in fresh paraffin wax. The blocks were allowed to cool before cutting on a precision rotary microtome (Shandon Finesse E+, Thermo Scientific, Waltham, MA, USA). The block was trimmed down until tissue was just visible then five serial sections at five micrometres (µm) thickness were cut and picked up, in order, onto a coated glass slide labelled '1'. The sectioning direction was indicated in figure 25. A further 250 µm of the block was trimmed away and sections discarded before the next five serial sections were cut and picked up on slide '2'. This sequence was repeated until the tissue was cut through to the bottom of the plaque specimen. The full detail of the histological protocol devised in the histology department at the Barts and the London School of Medicine and Dentistry is included as appendix A.

4.9 Matching histology to speed plot

4.9.1 Principle

In order for the sound speeds of each plaque component, V_{Cn}, to be deduced, it was necessary to match the histological data to the speed plot data. The quantitative plot contains the composite speed data, V_n, through the plaque specimen for each plotline. The histological section contains the information of the percentage of each component, C_n, through the plaque. A plotline and its speed value correspond to a beamwidth band of plaque components down, or through, the histological section. The plot data is matched to the histological data through the physical reference of the digital photograph. The plot gridlines are superimposed on the photograph by matching the photographic mask to the speed plot contour outline. The plotlines are then transferred onto the corresponding histological section.

4.9.2 Plot to Photograph match

The histology was matched to the surface plot (Excel) through the physical size data from the digital photograph. Both the surface plot of speed and the photograph have a physical two dimensional, x-y, outline. These were first scaled against each other. Using a graphics editor (GIMP 2.6.8 freeware, www.gimp.org), the photograph was scaled to the size of the Excel plot in order to perform the comparison. The scale of the photograph was first determined using the metal ruler, as seen in figure 27. Each photo was captured with the ruler both in the horizontal and vertical position to ensure accurate measurement of the plaque specimen dimensions. The plot size was derived from the 0.66mm interval or step size per row or column. The aspect ratio of the plot figure was locked and scaled accordingly. The overall size of the plot was then scaled to the dimension of the ruler in the digital photograph.

A physical mask of the plaque outline was drawn on the photograph as shown in figure 28. This mask of the photograph outline was best positioned visually to the attenuation map. This mask translated directly to its position on the speed plot as the speed and attenuation were plotted consecutively on the same coordinates.

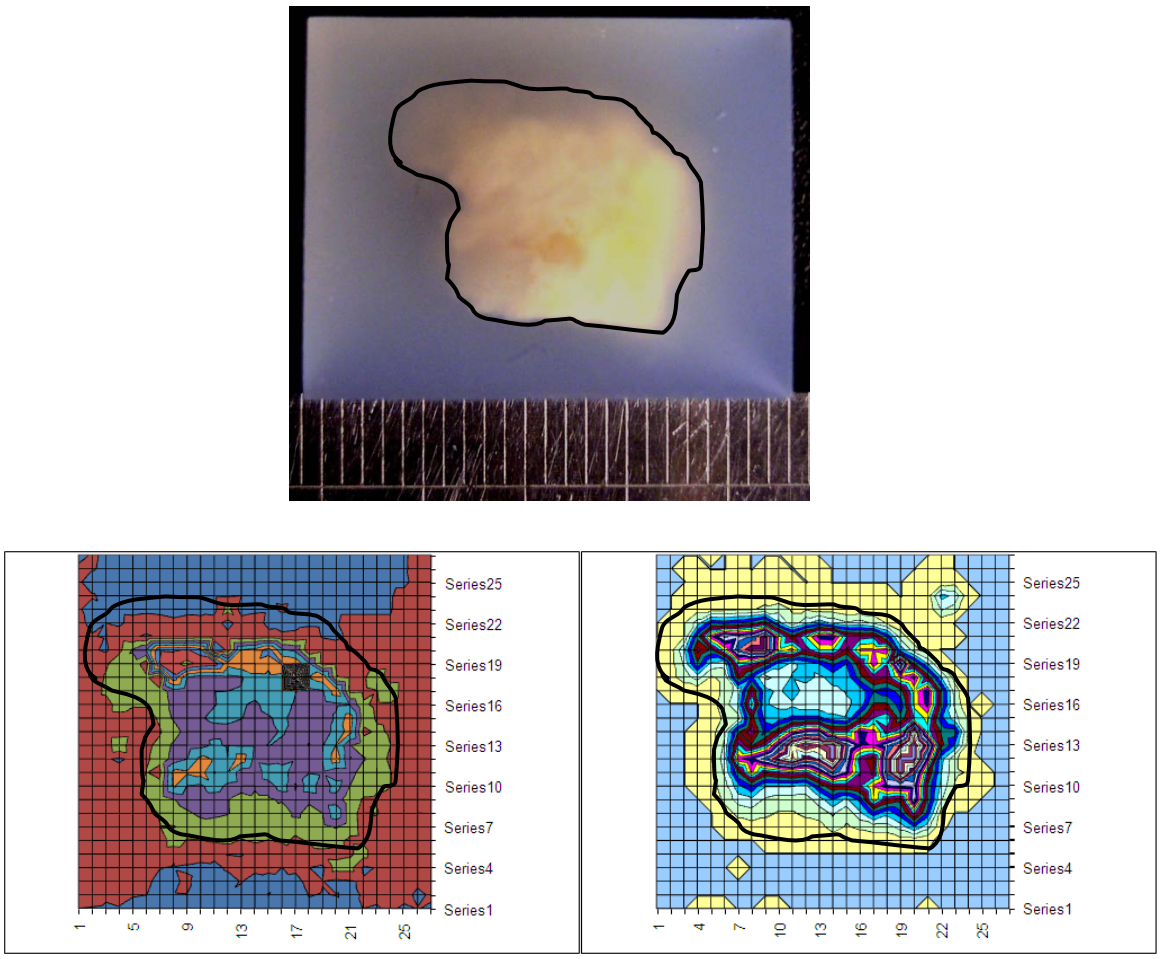

Figure 28: This figure shows how the photographic mask is mapped to the speed and attenuation contour maps. Examples of the speed and attenuation plot are shown bottom left and right respectively. Here, plot rows are horizontal and plot columns are vertical. The lines in the plot are spaced at 0.66 mm and each line signifies the plotline centre. The digital photograph of the corresponding plaque is shown above. A ruler with millimetre intervals can be seen beneath the gel. Once the plots and photograph were scaled, an outline mask was drawn on the photograph. This mask was then superimposed on the plots. The grid lines correspond to the centre of each data point or plotline.

For matching purposes, it was found that the attenuation plot was a better match to the outline of the photograph, see figure 28. This was because the outline of the attenuation plot was better defined than that of the speed plot. The adapted clear gel TMM maintained the speed match at 1540 ms^{-1} but had a much lower attenuation at 0.15 dB cm^{-1} MHz^{-1}. The comparative difference in ranges for attenuation was therefore greater than for speed and thus the contrast resolution was improved. This accentuated the clarity of the plaque outline against the background.

For the purpose of matching the histology to the plot, the mask of the physical outline from the photograph served to show where the plaque sits within the plot data. In other words, the matching of photographic mask to the plot determined where the plot grid lies over the plaque embedded in the gel. The start and end of each row of where the physical plaque lies within the plot was recorded.

4.9.3 Photograph to Histology match

Once the outline of the photograph was physically masked on the plot, the histology was then matched to the photograph. The physical outline of the plaque histology could not be constructed accurately from the sections as the specimen was not sectioned continuously. The approximate y dimension of the histology was determined from the total number of slides (each slide has five sections) and the histological sectioning protocol. It was assumed here that the first and last histological slide corresponds to the top and bottom of the plaque, respectively. The histological x dimension was measured from a section on each slide using digital callipers (Digimatic, Mitutoyo, Kawasaki, Japan). This information was recorded on a worksheet for each specimen.

In order to match the histology to the photograph, the number of histological slides was divided into the photographic y dimension. This assumed that the first slide was at the top of the photograph and the last slide was at the bottom. There is some uncertainty that the last slide matches the bottom of the photograph. As the last sections are sectioned from the gel block, the last part of the plaque specimen was sometimes dislodged. Therefore, in some cases, the plaque specimen was not entirely sectioned.

4.9.4 Histology to Plot match

The histology was then mapped to the plot. The total number of histology slides was compared to the number of plot rows within the physical mask. The number of slides and number of plot rows also correspond directly to the plaque y dimension from the photograph. Histology is known to cause shrinkage of any tissue specimen and therefore the histology is effectively scaled to the physical dimension of the plot.

An assumption is made that the first slide lies in the plot row at the top extent of the mask and the last slide similarly lies in the plot row at the bottom of the mask. By division of number of slides by number of plot rows, the separation of the histological slides down the plot grid was determined. Each histological slide was therefore assigned to a plot row. As the plot step size is 0.66 mm and the separation of the histological slides is approximately 0.25 mm, each plot line has at least two slides of corresponding histological data.

For each plot row within the mask, both its left and right extent and number of plot columns within the mask was measured. This information was then mapped onto each histological slide, as shown in figure 29.

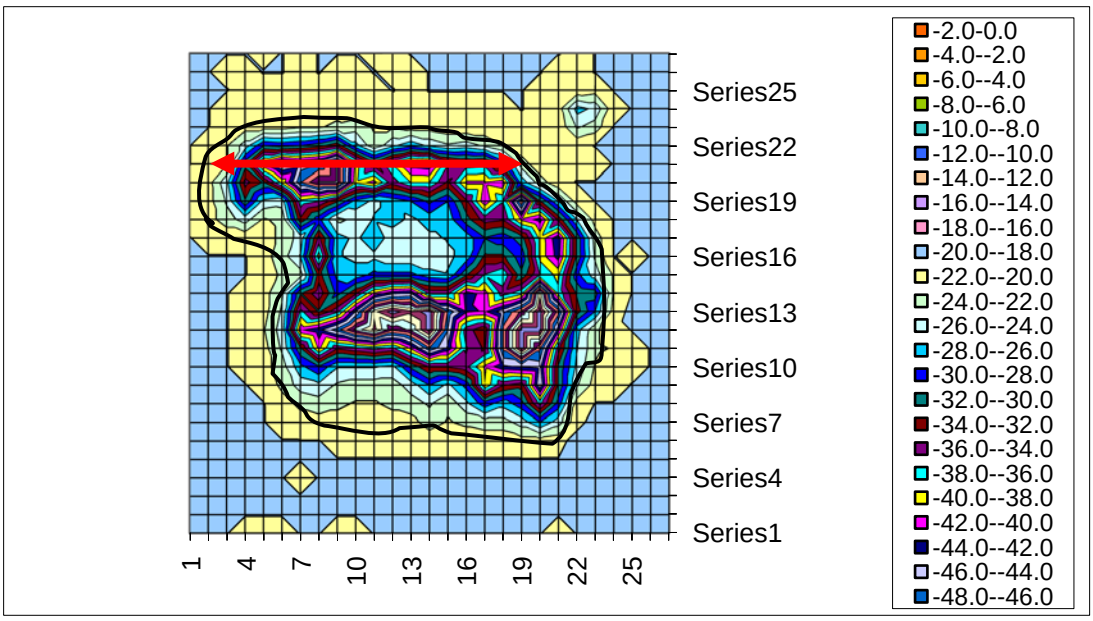

(a)

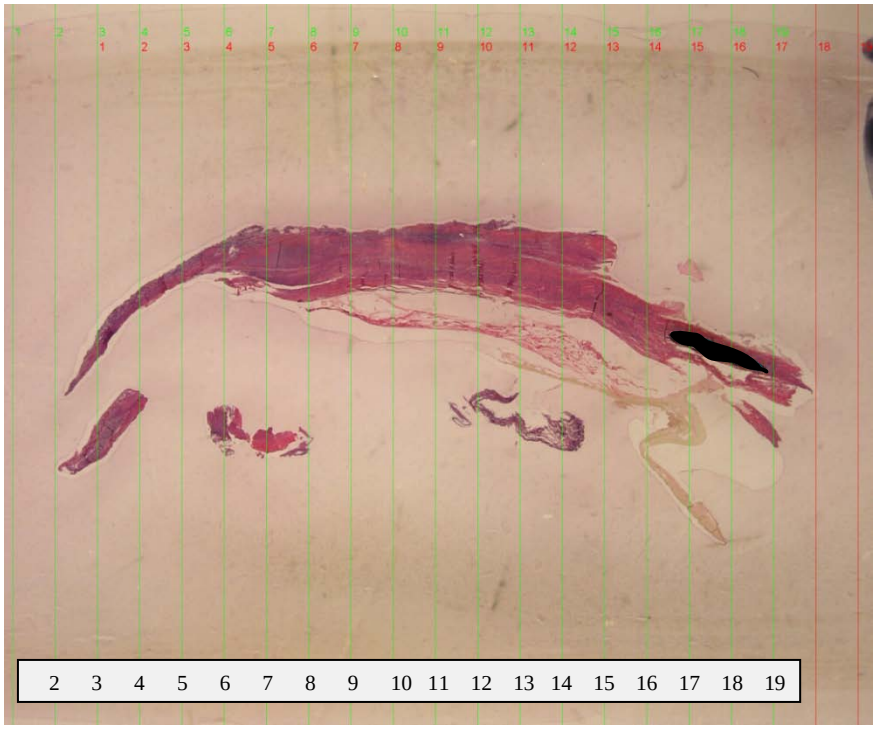

(b)

Figure 29: This figure is a schematic to show how the plotlines are mapped from the attenuation plot to the histological section. The top panel (a) shows the attenuation plot with the photographic mask (solid black line). The legend for (a) shows the attenuation values in dB. The red arrow marks plot row (series) 21 which spans from plot column 2 to plot column 20. The bottom panel (b) shows the histological slide that corresponds to plot row 21. Each plotline is marked by the boxed numbers at bottom of the histological slide. These lines correspond to the plotline centres from the plot grid. The black area to the right of the tissue mass corresponds to calcification within the plaque. The tramlines are numbered by the green numbers. The red numbers represent the right hand edge of the plotline of that number.

The red arrow in figure 29(a) represents the extent of the plot that matched or corresponds to the histological section in figure 29(b). This is plot row (series) 21. This goes from column 2 to column 20. In figure 29(b), the first plotline centre or plot column 2 clips the left hand edge of the histology outline and column 20 clips the right hand edge.

4.9.5 Dimension Measurement

The key to matching the speed plot to the histology was the determination of the dimensions and outlines of the three factors in the match chain; the physical plaque outline from the photograph, the plaque plot outline data and the histological data.

4.9.5.1 Digital Photograph

The digital photograph had the most precise measurement of physical dimension of the plaque specimen. However, there was some uncertainty in the definition of the plaque outline in the photograph. This was due to the similarity in colour of the tissue and TMM.

Small uncertainty in measurement of dimension from the photograph also arose from radial distortion, which is caused by the image magnification of the camera lens. This was minimised by limiting the use of the telephoto lens and the use of the digital camera in super macro mode (C-4000, Olympus, Center Valley, PA, USA). High definition images were cropped rather than any magnification of the image being used. The steel ruler was also placed as near as possible to the specimen in the image. Uncertainty in measurement for the photograph is ± 0.5 mm.

4.9.5.2 Plot

It was shown by plotting the embedded LDPE square that the beam needed to be substantially over the material before a measurable change in sound speed was registered. In addition, the thickness of the sample at the edges of the plaque may be too small to affect a significant change to the ultrasound pulse. The uncertainty was determined as ± 1.3 mm.

4.9.5.3 Histology

As the harvested plaque was cut down to fit into the plot area, the specimens were generally of the size; x dimension 15 - 20 mm and y dimension 10 - 15mm. The measurement uncertainty of specimen x dimension from histology is small, ± 0.2 mm, as each section was measured three times using the digital callipers.

A much larger error was present on the approximation of the plaque specimen y dimension. This was calculated from the number of slides and the sectioning protocol. The number of slides was counted to give an indication of the maximum histological y dimension for each specimen. Each slide was 250 μm apart and each slide contains five sections, which were 5 μm thick. This meant that approximately 40 - 50 slides were produced per specimen. There was a significant uncertainty in this measurement as it was difficult to determine both the exact start and end of the specimen while it was being cut. Greater error arose in the histological slicing. When the last part of the plaque specimen was being sectioned, the small remainder of the plaque was sometimes dislodged from the paraffin embedded block. This was common due to the weak bond between the fixed specimen and gel. The uncertainty in maximum specimen y dimension was assessed to be ± 0.5 mm.

4.10 Histological assessment

4.10.1 Histological Section Selection

Each histological slide contains five contiguous sections. The sections on each slide were first visually inspected for inclusion in the assessment. Due to the rigours of the histological process, the gel did not always keep the rectangular x-z outline and thus the plot geometry. It was important that the outline of the gel was intact so that the geometry of the plotlines through the plaque was maintained. Any section without a clear rectangular outline was discarded from the study. The selected sections to be photographed and segmented should also have no kinks or folds on the slide for the same reason. Any section with minimal bulk of tissue relative to gel size was also discounted. Digital photographs were captured of all selected sections. This was performed using a zoom stereo microscope (SZ-61, Olympus, Center Valley, PA, USA) at x15 magnification and a digital camera (C-5060 wide zoom, Olympus) set-up. These photographs were assessed in order to perform the tissue segmentation.

4.10.2 Segmentation

Initially an assessment of plaque composition was carried out by 3 observers; MPB (myself), PDS (a vascular surgeon) and MJB (chief physicist). All observers were instructed by a consultant histopathologist how to segment the tissue on the histological section from a high resolution digital photograph. Three photographs from randomly chosen sections of one specimen were assessed to compare the inter-observer reproducibility. MJB and PDS performed the manual method (see 5.10.2.1) of segmentation by visual identification and approximation of component areas. MPB carried out the segmentation using automated method (see 5.10.2.2**).**

Microscopically, many plaque components were present in the sections but here, in this more macroscopic study, four categories were established. The plaque sections were thus segmented into five components; TMM, elastic tissue or elastin, fibrous tissue or collagen, calcified or calcification and lipid/intraplaque haemorrhage (IH)/thrombus.

Little thrombus was present as the plaque specimens were washed with sterile saline prior to moulding in gel. Lipid and intraplaque haemorrhage were bundled together as they were considered to be the likely destabilising features of atherosclerotic plaque (de Weert et al. 2005).

4.10.2.1 Manual Method

Each histological slide corresponds to the x-z plane through the plaque of a particular plot row, x, in the speed plot as determined by the plot - photo match. The number of plotlines for that row was known from the superposition of the mask outline of the photograph. The position of the start and end plotline on the plaque was also determined from the physical mask.

Firstly, a best-fit line was drawn along the top of the gel surface. A parallel line was then drawn along the bottom edge of the gel. Perpendicular ‘tramlines’ were drawn down, as seen in figure 29, between these gel surface lines. These ‘tramlines’ represent the plotline centres and plot line extents. These lines directly matched the

centre line of the beam path. Each plotline measured in the segmentation spans two plotline widths centred on these lines. This is equivalent to a beam width of 1.33 mm. The proportions of each plaque component were measured by area within each plotline. A spreadsheet of tissue component by percentage for each plot column was then drawn up.

The elastic material was defined by the purple areas of tissue around the exterior of the tissue sample. This elastic material is from the media of the lumen. The fibrous tissue was defined by the pinkish red material that made up the bulk of the tissue sample. The lipid//IH/thrombus was defined by the pale or yellowish deposits within the sample. The TMM was defined as that outside the tissue sample but within the bounds of the rectangular area of the histological section.

4.10.2.2 Automated method

An automated method was also developed to segment the plaque components on the histological section. The same three images were initially assessed to test the intra-observer reproducibility.

Code was written by Professor Greenwald (Institute of Pathology, QMUL, London) for the digital imaging software (version 3.0, KS400, Karl Zeiss GMBH, Oberköchen, Germany) to perform the automated segmentation. The digital photographic image of the histological section was loaded as the input to the workspace, see figure 30a overleaf.

Figure 30: This figure shows how the histological section is rotated and cropped. Panel (a) shows the raw input image. Panel (b) shows the rotated image, which has been cropped by the rectangular selection. The plotlines are drawn on here as detailed below. The double headed arrow marks the extent of the first plotline. The green numbers show the original positioning of first plotline centre (2), centre of second plotline and the right extent of the first plotline (3) and left hand extent of first plotline (1). The red numbers show the right extent of each plotline. Red (1) is the first plotline extent from green (1) to (3). Each plotline overlaps half of the next plotline.

The image was first rotated so that the outline of the gel on the section was aligned with the workspace geometry. A line was drawn along the top edge of the gel outline between two points selected using the mouse cursor. The image was rotated to zero degrees using the angle determined from the vector of this drawn line. A rectangle was then drawn around the gel outline of the section. This rectangular selection was then used to crop the image and the area lying outside the gel was discarded from component calculation. Only the area within the rectangle, and therefore gel, was included for the segmentation process, see figure 30b.

The operator selected, by clicking on the image with the mouse cursor, where the position of the centre of the first plotline lies. A vertical line was drawn down the rectangular selection by the software to represent the centre of this plotline. In fig. 30b, this is the line midway between the two arrow heads at the bottom left of the image marked by green 2. The centre of the second plotline, marked by green 3 and red 1, was then selected. This represents the right hand extent of the first plotline. It also represents the centre of the second plotline. Finally the left hand extent of the first plotline was marked at an equal distance. The program automatically superimposes the remaining plotlines across the section at equal spacing.

These lines are equivalent to the plot step size and each line therefore represents the centre of a plotline, see figure 30b. The plotline width here has been chosen so that each plotline overlaps half of the next plotline. In other words, the plotline width is twice the plot step size. The code allows for variation in the selection of both plotline width and the degree of plotline overlap. This represents two plot step sizes or the equivalent beam width of 1.33 mm in the original plot.

The operator selected all tissue on the section to be segmented from the TMM as shown in figure 31. This was done by tracing the perimeter of the tissue on the section using the mouse cursor. Multiple areas can be drawn and areas of TMM within the tissue can be removed. When selection of tissue was completed, any area lying outside this tissue selection was deemed to be TMM for the purpose of component calculation.

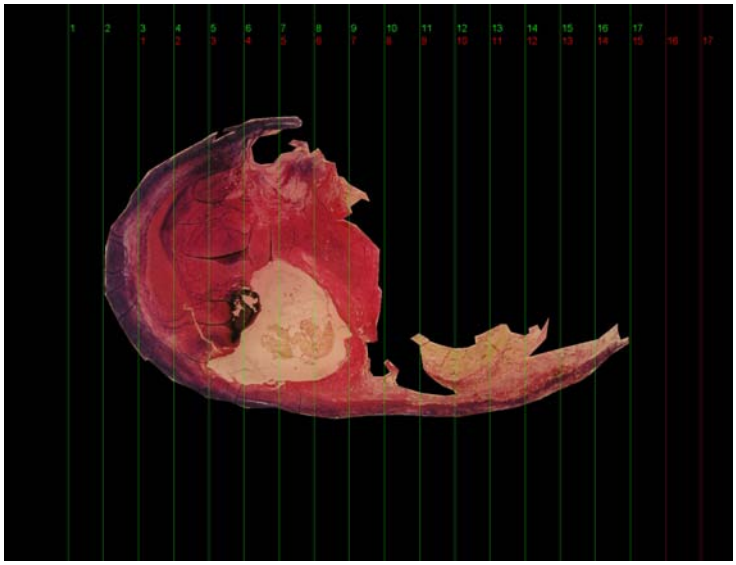

Figure 31: This figure shows the edited image with the TMM segmented and the plotlines drawn on. The black area is now calculated as the TMM.

The tissue was segmented into the four remaining components; calcified, fibrous, elastic and lipid. This was achieved using a true colour segmentation function. The threshold values for each of the three colour components (Red, Green, Blue) determined which of the colour value regions of the image were copied or deleted into the final output image. The threshold areas were determined for each component in turn by circling their regions in the image. The thresholds were set according to the colour values in the surrounded regions, see figure 32.

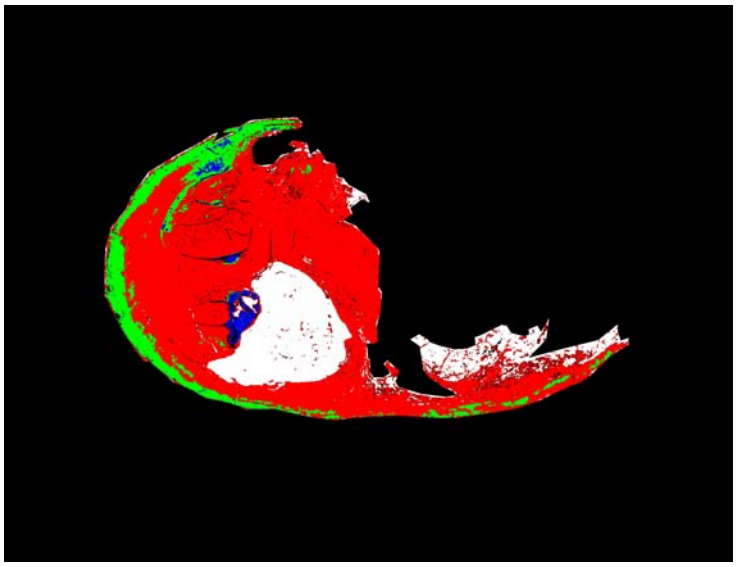

Figure 32: This figure shows the final output colour coded image of the automated tissue segmentation. Green represents the elastin from the media. Red represents the fibrous tissue or collagen. White represents the lipid. Blue represents the calcification. Black areas within the confines of the plaque section outline are defined as unclassified by the segmentation.

Once the segmentation was complete, the percentage of each component was calculated for each plotline across the plaque section. These data were outputted as a spreadsheet file. Any crossovers in the thresholding or areas thresholded as more than one component were outputted in the data. In addition, regions not thresholded were also recorded. Typical output data are included in appendix B.

4.11 Matrix inversion – modelled data

In order to test the robustness of the derivation of the plaque component speed data from the matrix inversion, some modelled data was used. Data values were selected for each plaque component from literature (Duck 1990). These were:

- TMM 1540 ms^{-1}
- Fibrous tissue 1570 ms^{-1}
- Lipid 1500 ms^{-1}
- Elastic tissue 1600 ms^{-1}
- Calcification 2000 ms^{-1}

Typical values were then chosen for the plaque component percentages. These were selected in the following ranges:

- TMM 70 – 90 %
- Fibrous tissue 10 – 20 %
- Lipid 0.5 – 5 %
- Elastic tissue 0.5 – 5 %
- Calcification 0.1 – 2 %

A spreadsheet was created with ten plotlines of 'input' data. This spreadsheet of plaque component percentages and given speed of each plaque component had a known outcome for the plaque composite speed for each plotline. The effect of measurement uncertainty was then tested by addition of noise to a single component. The components were chosen as fibrous tissue and calcified tissue for the 5 component analysis. These two components represented a component where there was a large bulk of component (fibrous) and one where there was a small bulk of component (calcified). The aim was to examine the effect of noise on a large bulk and a small bulk of plaque component in the derivation of speed values. For the 3 component analysis, noise was added separately to fibrous tissue and lipid.

To further test the matrix inversion, increasing levels of noise (1 – 20%) were added simultaneously to all tissue components in our modelled spreadsheet and the derived data was assessed.

4.12 Plaque component: speed calculation

4.12.1 Single section calculation

The spreadsheet of plaque component percentages for each plotline was used to calculate the speed of each component. The percentages of plaque component for each plotline were correlated with the composite speed value for that plotline. A set of simultaneous equations was drawn up for each plotline along the plot row across each segmented histological section. Sets of five equations from five consecutive

plotlines were then solved to give the speed value for each plaque component. This was repeated across the plaque section along its associated plot row. The number of plotlines used in the simultaneous equations could be altered.

Firstly a five component analysis was performed. The five component analysis consisted TMM, calcium, lipid/IH, elastic tissue and fibrous tissue. The simultaneous equations for this analysis did not always solve. Many sections had little or no calcium. Other sections contained little elastic tissue or lipid. In order to perform more simple analysis, the elastic and fibrous tissues were assimilated and the calcium removed from the calculation. The three component analysis consisted TMM, elastic/fibrous and lipid/IH. This analysis was performed for all sections that did not contain calcium. The three component analysis also assimilated the elastic and fibrous tissue into one component.

A spreadsheet containing the component percentages and the speed value for each section was entered into custom written Matlab code. The component speeds were derived using a simple matrices calculation, see equation 5. A value of sound speed for each plaque component was then derived. This is repeated for all selected slides and a bank of data is obtained for each plaque. The value for TMM has been measured from independent QA calibrated measurements. These calibrated values were compared to the derived sound speed value from the calculation and acted as a quality indication for the measurement.

When the equation solved for a plotline, it often resulted in the outcome of NaN (not a number) for one or two of the components for both the 3 and 5 component analyses. For the 5 component analysis, solutions were discarded when NaN was the result for two components where that component was present in the plotline. Solutions were also discarded where NaN was seen as a result for one component in conjunction with a result for another component falling outside the sound speed range for each of the following criteria:

- Lipid 1000 – 2000 ms^{-1}
- Fibrous tissue 1000 – 2000 ms^{-1}
- Elastic tissue 1000 – 2500 ms^{-1}
- Calcified 1000 – 10000 ms^{-1}

For the 3 component analysis, the results were discarded when there was a NaN result for any component solution where that component had been present in the segmentation.

4.12.2 Consecutive section calculation

The calculation of component speed was first calculated using one section. This calculation utilised a beam width of 1.33 mm for each plotline. However the beam is circular and was shown to be symmetric in the beam profile plotting. This implied that it was necessary to average the plaque component percentages in the y direction. This was performed by averaging over sections from three or five contiguous histological slides. This approximated to a 0.55 mm or 1.1 mm beamwidth, respectively. It was often not possible to average over five slides. The reason for this was that good section selection did not commonly occur over this range. The consistency of the sectioning was not always sufficient over five consecutive slides. This meant that the sections did not meet the criteria of retained geometry for inclusion for segmentation.

4.13 Summary

The seven plaque specimens were plotted. The plots of attenuation were displayed as contour maps that could be directly matched to the photographic outline from the photograph. Their speed data was then correlated with their histological data. The known plaque component percentages and composite speed data were then inputted to the matrix inversion in sets of five equations. The results are outlined in chapter 5.

4.14 References

Baldwin, S. L., Yang, M., Marutyan, K. R., Wallace, K. D., Holland, M. R., & Miller, J. G. 2005, "Measurements of the anisotropy of ultrasonic velocity in freshly excised and formalin-fixed myocardial tissue", *J Acoust Soc Am*, vol. 118, no. 1, pp. 505-513.

Bamber, J. C., Fry, M. J., Hill, C. R., & Dunn, F. 1977, "Ultrasonic attenuation and backscattering by mammalian organs as a function of time after excision", *Ultrasound Med Biol*, vol. 3, pp. 15-20.

Bamber, J. C. & Hill, C. R. 1979, "Ultrasonic attenuation and propagation speed in mammalian as a function of temperature", *Ultrasound Med Biol*, vol. 5, pp. 149-157.

de Weert, T. T., Ouhlous, M., Zondervan, P. E., Hendriks, J. M., Dippel, D. W. J., van Sambeek, M. R. H. M., & van der Lugt, A. 2005, "*In vitro* characterization of atherosclerotic carotid plaque with multidetector computed tomography and histopathological correlation", *Eur Radiol*, vol. 15, pp. 1906-1914.

Duck, F. A. 1990, *Physical properties of tissue - A comprehensive reference book* Academic Press.

Jensen, M. S., Wilhjelm, J. E., Sahl, B., Brandt, T., Martinsen, K., Jespersen, S. K., & Falk, E. 2002, "A method to obtain reference images for evaluation of ultrasonic tissue characterization techniques", *Ultrasonics*, vol. 40, pp. 89-94.

Kremkau, F. K., Barnes, R. W., & McGraw, C. P. 1981, "Ultrasonic attenuation and propagation speed in normal human brain", *J Acoust Soc Am*, vol. 70, no. 1, pp. 29-38.

Lind, B. L., Fagertun, J., Wilhjelm, J. E., Jensen, M. S., & Sillesen, H. 2007, "3D reconstruction of carotid atherosclerotic plaque: Comparison between spatial compound models and anatomical models", *Ultrasound Med Biol*, vol. 33, no. 7, pp. 1064-1074.

Lockwood, G. R., Ryan, L. K., Hunt, J. W., & Foster, F. S. 1991, "Measurement of the ultrasonic properties of vascular tissues and blood from 35-65 MHz", *Ultrasound Med Biol*, vol. 17, no. 7, pp. 653-666.

Rakebrandt, F., Crawford, D. C., Havard, D., Coleman, D. P., & Woodcock, J. P. 2000, "Relationship between ultrasound texture classification images and histology of atherosclerotic plaque", *Ultrasound Med Biol*, vol. 26, no. 9, pp. 1393-1402.

Ramnarine, K. V., Anderson, T., & Hoskins, P. R. 2001, "Construction and geometric stability of physiological flow rate wall-less stenosis phantoms", *Ultrasound Med Biol*, vol. 27, pp. 245-250.

Sasaki, H., Saijo, Y., Tanaka, M., Okawai, H., & Nitta, S.-I. 1996, "Influence of tissue preparation on the high frequency acoustic properties of normal kidney tissue", *Ultrasound Med Biol*, vol. 22, no. 9, pp. 1261-1265.

Verhoef, W., Cloostermans, M. J. T. M., & Thijssen, J. M. 1985, "Diffraction and dispersion effects on the estimation of ultrasound attenuation and velocity in biological tissues", *IEEE Trans Biomed Eng*, vol. 32, no. 7, pp. 521-529.

Wilhjelm, J. E., Jensen, M. S., Jespersen, S. K., Sahl, B., & Falk, E. 2004, "Visual and quantitative evaluation of selected image combination schemes in ultrasound spatial compound scanning", *IEE Trans Med Imaging*, vol. 23, no. 2, pp. 181-190.

Wilhjelm, J. E., Jespersen, S. K., Falk, E., & Sillesen, H. 2006, "The challenges in creating reference maps for verification of ultrasound images", *Ultrasonics*, vol. 44, p. e141-e146.

Chapter 5 PLAQUE CHARACTERISATION RESULTS

5.1 Clear TMM: Acoustic property data

Each of the seven plaque specimens had an associated QA batch of six gels which are measured for calibration purposes. Only gel samples from moulds A-C were measured. Mould D was not used is it was shown to be too thin to give accurate results in chapter 4. The sound speed and the attenuation of each QA batch of gels were verified by independent measurement of these sets of six moulded gels. This ensured that the correct speed was used for the background material in the plaque specimen measurement.

Measurements of sound speed and attenuation were again made on an N x N matrix (N = 3) for each specimen QA batch. Results for all seven clear gel batches manufactured over the study period were measured. An average sound speed of 1543.1 ms^{-1} (st.dev. = 3.2, n = 378) and an attenuation coefficient of 0.15 dB cm^{-1} MHz^{-1} (st.dev. = 0.01, n = 378) were recorded at 21^{o}C. The results associated with each plaque gel are detailed here and compared to the derived sound speed values for TMM later in this chapter.

A longitudinal study was not carried out for this clear TMM gel as the plaque specimens are processed and measured within two days. There was assumed to be no measurable change in acoustic properties over this time period. In the plaque characterisation study, the acoustic properties of the specimen were measured at both 21^{o}C and 37^{o}C. Therefore the temperature dependence of both sound speed and attenuation coefficient for the clear gel were measured independently over a range of 17 - 37^{o}C, see figures 31 and 32.

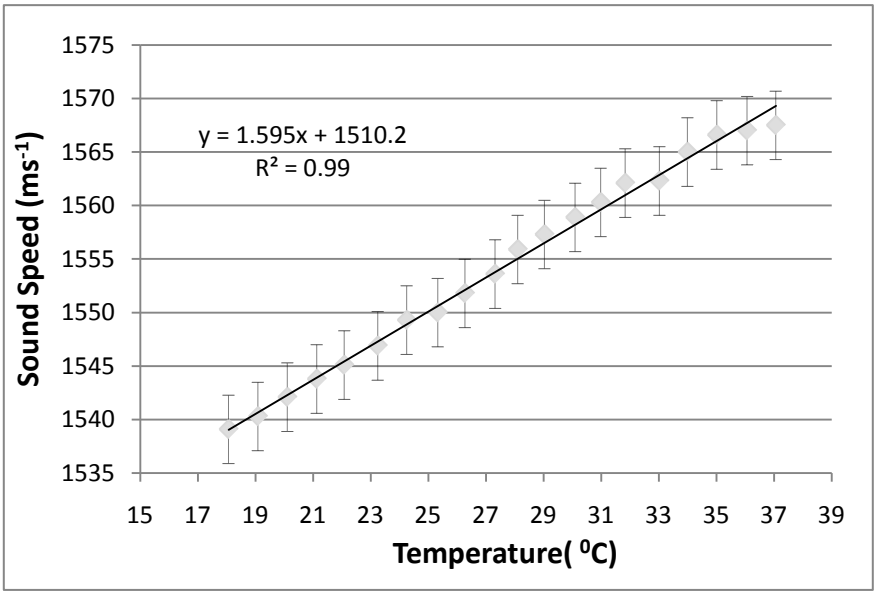

Figure 33: This figure shows the temperature dependence of sound speed (ms^{-1}) for the adapted clear gel TMM. The error bars show ± 2 st. dev.

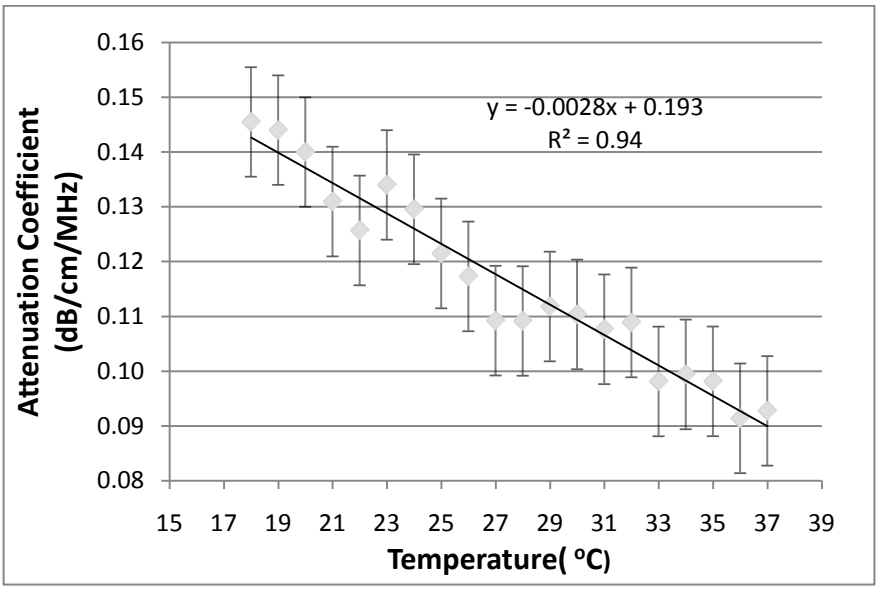

Figure 34: This figure shows the temperature dependence of attenuation coefficient (dB $cm^{-1}MHz^{-1}$) for the adapted clear gel TMM. The error bars show ± 2 st. dev.

Both the sound speed and attenuation showed a linear dependence to temperature. The sound speed increased at 1.6 $ms^{-1}\ {}^{0}C^{-1}$ as shown in figure 31. The attenuation coefficient decreased at 0.003 dB $cm^{-1}\ MHz^{-1}\ {}^{0}C^{-1}$ as shown in figure 32.

The frequency dependence showed no change in sound speed over the frequency range of 17 - 23 MHz. There was no discernible slope in the comparison of sound speed with frequency over this higher frequency range. This concurred with the results for the standard EC TMM and the lower frequency results for that agar TMM (Browne et al. 2003).

The attenuation over the frequency range 15 - 25 MHz was measured for the adapted clear TMM, as shown in figure 33 below.

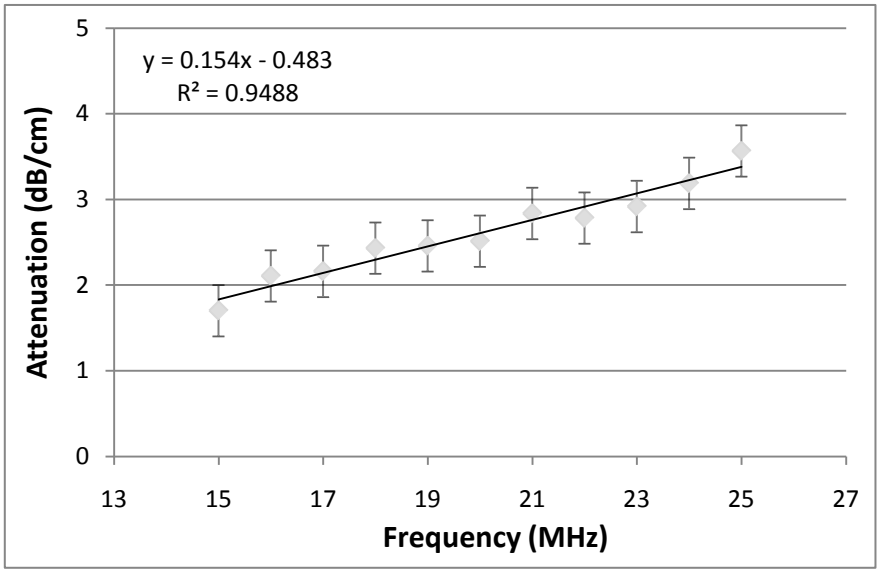

Figure 35: This figure shows the frequency dependence of attenuation (dB/cm) for the adapted clear gel TMM over the frequency range 15 - 25 MHz. The error bars show ± 2 st. dev.

The slope of the attenuation plot against frequency shows that the attenuation coefficient for the clear TMM is 0.15 dB cm^{-1} MHz^{-1}. This is lower than the value for the EC TMM gel of 0.5 dB cm^{-1} MHz^{-1}. This was expected as the particulates have been removed. These were originally added to the EC TMM to match both the attenuation and backscatter to that of soft tissue.

5.2 Physical Validation Phantom

5.2.1 Step Phantom

The three gel sets had independently measure sound speeds of 1483.1 (±0.6) ms^{-1}, 1536.7 (±0.2) ms^{-1} and 1593.8 (±0.5) ms^{-1}. The two measured phantoms had a combination of these gels. Both contained a 1540 ms^{-1} step. One was in combination with the higher speed gel and one in combination with the lower speed gel.

Each step phantom was measured consecutively in time. The higher speed combination sound speed profile can be seen in figure 34.

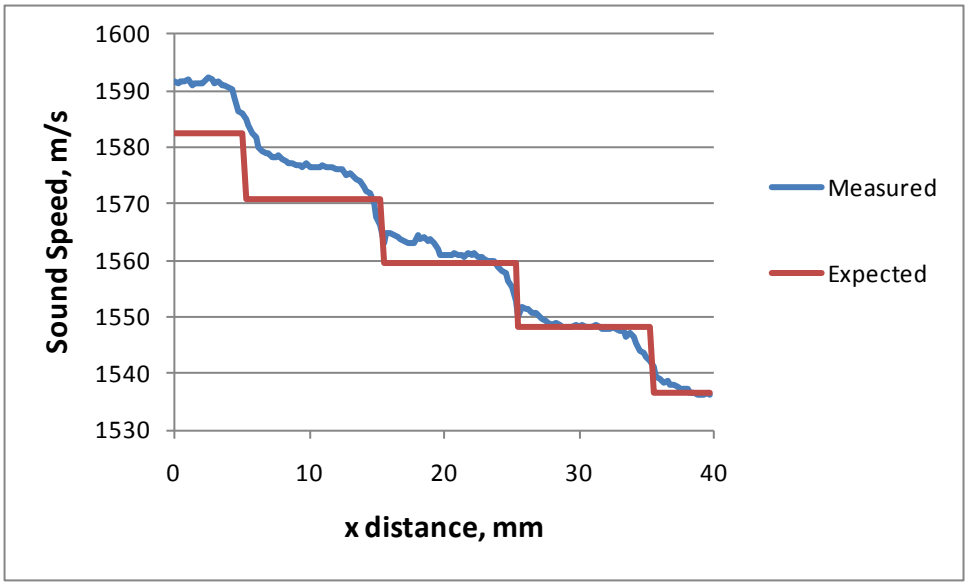

a)

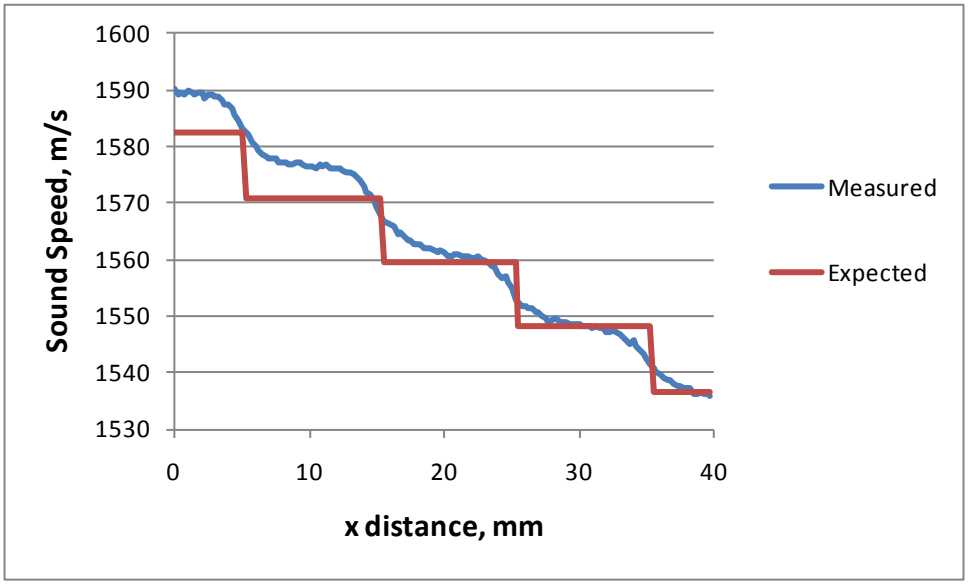

b)

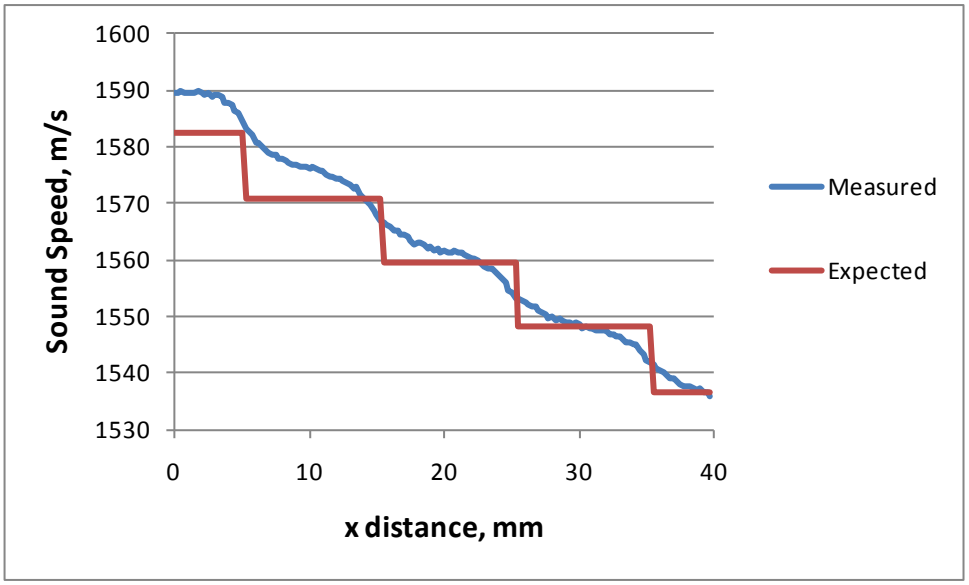

c)

Figure 36: The measured sound speed profiles (in blue) of the higher speed step phantom are shown here plotted against teh expected profile (in red). Each speed profile is taken consecutively in time. Panel a) is taken after 10 minutes of construction of the interlocking steps. Panel b) is taken after 30 minutes and panel c) is taken after 50 minutes. Each sound speed profile took 20 minutes to plot.

The lower speed combination sound speed profile can be seen in figure 35.

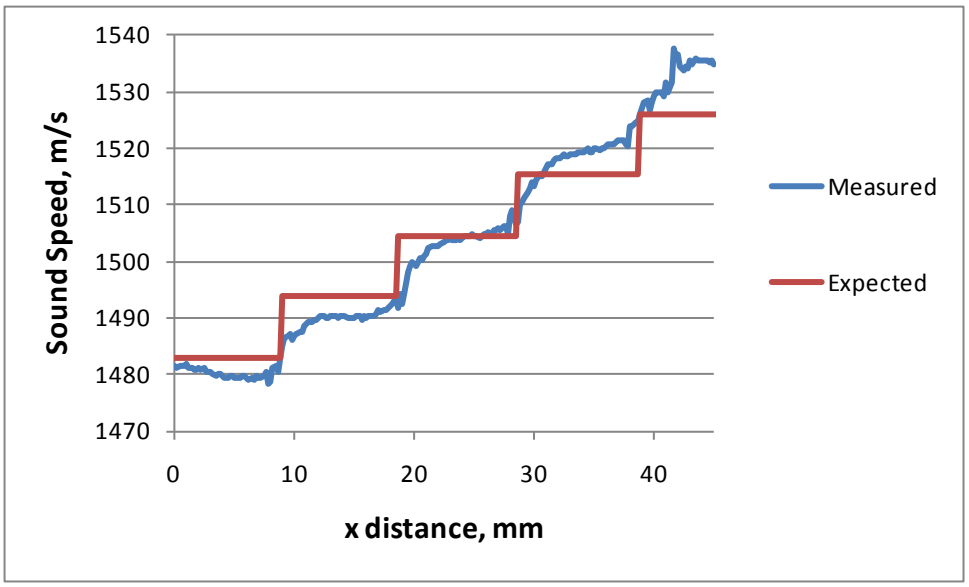

a)

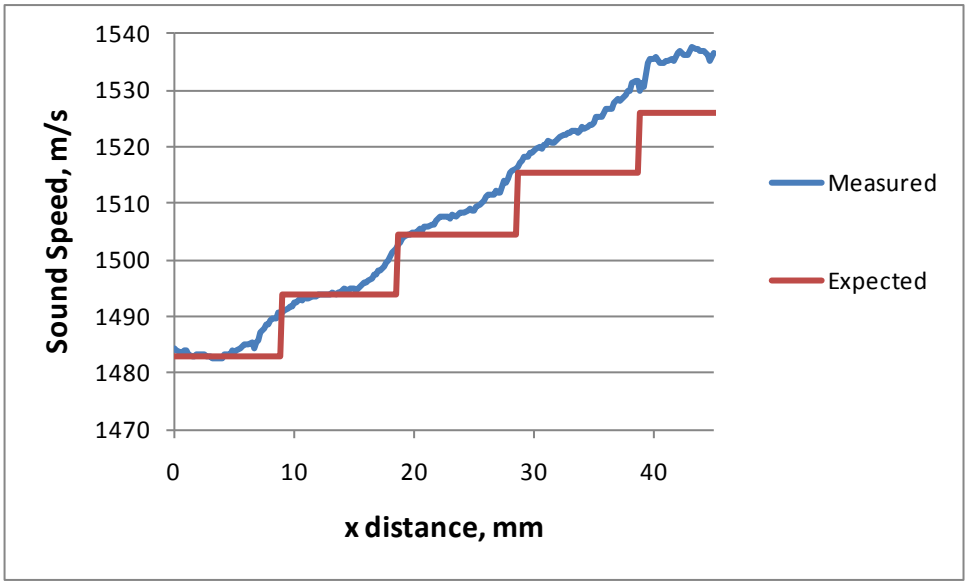

b)

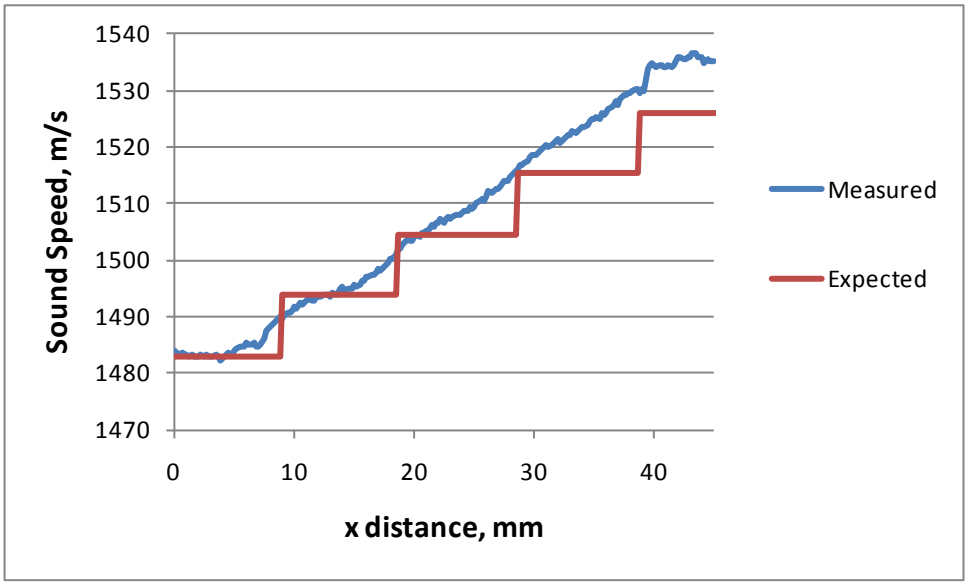

c)

Figure 37: The measured sound speed profiles (in blue) of the higher speed step phantom are shown here plotted against the expected profile (in red). Each speed profile is taken consecutively in time. Panel a) is taken after 10 minutes of construction of the interlocking steps. Panel b) is taken after 30 minutes and panel c) is taken after 50 minutes. Each sound speed profile took 20 minutes to plot.

It is apparent in both figure 36 and 37 that the definition of the steps within the phantom are evened out so that the steps in sound speed are no longer clear. This occurs due to the diffusion of glycerol across the boundary. There is also a drift away from the expected in figure 37 a) to c) as the greater bulk of TMM at the higher sound speed makes greater effect on the increase of sound speed. This is also evident in figure 36 a) to c) with the drift towards the expected value of sound speed as the greater bulk of lower sound speed TMM lowers the composite speed on the left side

of the graph. At each bulk end (right for figure 36 and left for figure 37) of each set of speed profiles, the sound speed matches well with the independently measured values. The low TMM sound speed of 1536.7 ms^{-1} is due to the measurements being made at 18^0C.

5.2.2 Grid Phantom

In order to clarify that the measurement system correctly defines the sound speed steps of a subject embedded with the clear gel, the grid phantom was also made.

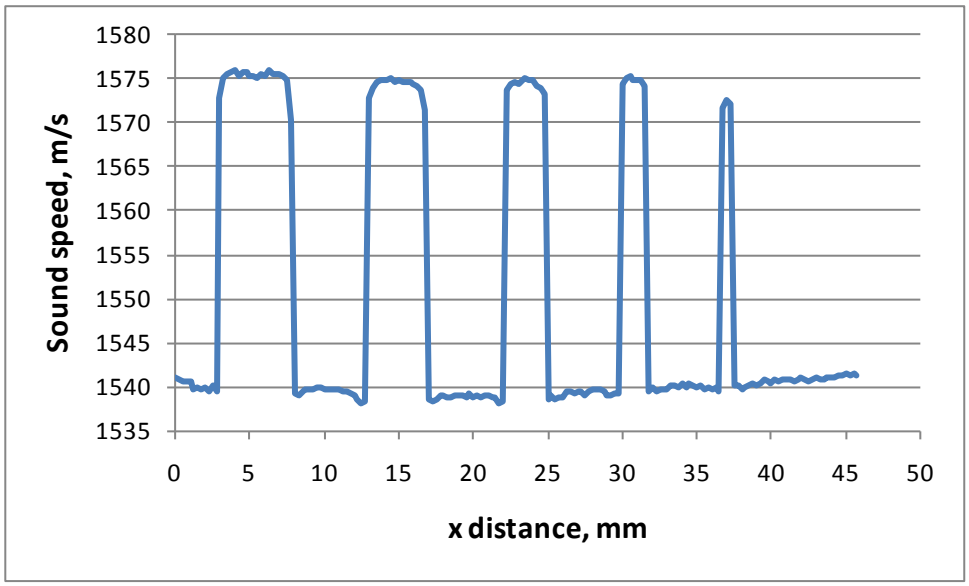

Figure 38: This figure depicts the sound speed profile along the x-axis through the grid phantom.

The LDPE is 1mm thick and the phantom block was 12.85mm overall. The clear gel has a sound speed of 1539.7 (±0.2) ms^{-1}. The LDPE has a measured sound speed of 1998.7 (±0.5) ms^{-1}. Using simple algebra, the expected sound speed at the grid spines should be 1576 ms^{-1}. This expected sound speed is seen to be comparable with that for the 5, 4, 3 and 2 mm spines in the grid phantom. However, the thinner spine shows a lower speed of approximately 1574 ms^{-1}. This is due to the fact that the spine is only 1 mm whereas the 6 dB beam profile is approximately 1.33 mm. The beam therefore does not register the LDPE fully. This is reflected in the slightly lower measured sound speed.

5.3 Plaque handling and embedding

5.3.1 Tissue Preservation

Two unfixed plaque specimens were selected to investigate the change in sound speed within the specimen over a three day period. Both specimens were embedded and measured in accordance with the study protocol. Three sound speed plots were performed on three consecutive days for each specimen. N x N matrices of plotlines of sound speed through the plaque from each plot were matched for the three consecutive days. These three sets of paired data for each specimen were then compared. They are included in their entirety in Appendix C i) and C ii).

The data was statistically analysed using the Kruskal-Wallis test. This is a non-parametric test to assess equality of population medians among groups. This was chosen as the speed data were shown to be not normally distributed using the Anderson-Darling test. The p-values for the plaque specimens over the three days were 0.224 and 0.095, respectively. This shows that there is no significant change in the sound speed of the plaque specimens over the three day measurement period.

5.3.2 Plaque Embedding

Care was taken to allow the TMM to cool as far as possible without it setting. It was important that the TMM was not too hot as it is known that cell kill occurs at a temperature of 45^{o}C. However it was not possible to assess the effect of the TMM temperature on the plaque as it must be embedded in order for it to be measured.

5.4 Ultrasonic measurements

5.4.1 Broadband Reflection and Transmission techniques

Both broadband reflection and broadband transmission techniques were performed on each plaque specimen in order to ensure the consistency of the measurement of sound speed. The purpose of measuring each plaque specimen at both room temperature (cold) and body temperature (hot) was to investigate the hypothesis that the sound speed in lipid showed a decrease with increasing temperature.

For the reflection technique, it was found that the return times through the gel at the four corners of the plot area indicated agreement in plot area flatness with the calibration times calculated for the top of the plate. The return times through the gel therefore provided further assurance to the flatness of the plot area once the gel was loaded. The return times from the four corners were equalised to within 5 ns. The flatness calibration time for the vertical showed an average difference of 63 ns (st.dev. ± 12 ns). For the horizontal calibration, this time difference was 20 ns (st.dev. ± 4 ns). Likewise, the correction time, between reference measurement and plot area measurement, had an average time difference of 96 ns with a standard deviation of 17 ns. This shows that the calibration and correction times plate set-up were highly repeatable. It follows that the target plate set up for the reflection measurement was also repeatable.

Both techniques showed a maximum difference of 2 ms^{-1} in the sound speed data of the TMM background. This arose from the systematic error in the flatness of the plot area. There was an uncertainty of 5ns in the return time from the corners of the plot area. This was equivalent to a 10 µm uncertainty in the return distance. This translated to an uncertainty of 2 ms^{-1} in the speed measurement. There was a systematic drift in sound speed between diagonally opposite corners of the plots. Sound speed was comparable for three corners and a difference of up to 2 ms^{-1} was seen in the remaining corner. That drift was also observed in the return time calibration of the plot area.

The clingfilm was measured as negligibly thin at approximately 10 µm using a micrometer (Moore & Wright, Bradford, Yorks, UK). The measurement was likely to be less than 10 µm but this was the limit of the measurement capability of the micrometer. No measurable change in pulse shape, signal size or time shift was seen when the pulse was reflected through a double sheet of clingfilm. The clingfilm sealed the specimen gel for the duration of plotting. There was no observable change in the sound speed of the TMM with time. Any drift in sound speed of the background TMM was explained by the physical drift in the plot area.

The speed data was highly reproducible for both techniques and at both temperatures. The average difference between plots in composite sound speed for each plaque specimen was less than ±1 ms^{-1}; where the number of plotlines per specimen is typically 200 - 300. The maximum positive difference over all specimens for a single plotline was observed at 12 ms^{-1} and the maximum negative difference was -13 ms^{-1}. These large differences only occur once or twice in a plot.

5.5 Histology to speed plot: spatial match

The physical dimensions from the photograph are compared to those of each plot in table 11. It is apparent from these results that the speed plots for the reflection technique were smaller in both the x dimension and the y dimension than the photograph for certain specimens. The range of difference in dimension lay between 0.2 and 5.9 mm. For specimens 1, 6 and 7, the difference was less than 1.33 mm. Similarly, the transmission plots matched the photographic dimension to within 1.33 mm.

Specimen	Dimension	Rx Plot (mm)	Tx Plot (mm)	Photograph (mm)	Histo (mm)	Shrinkage (%)
1	y	12.7	12.7	12.9	9.9	-24
	x	15.3	15.3	15.6	12.4	-21
2	y	16.7	N/A	18.0	13.5	-25
	x	12.0	N/A	14.5	10.0	-31
3	y	10.7	12.0	12.0	8.9	-28
	x	10.7	14.0	14.6	11.2	-33
4	y	10.7	12.3	12.0	8.9	-29
	x	12.7	16.0	16.7	14.3	-14
5	y	14.0	14.0	15.3	10.5	-42
	x	12.0	15.3	15.4	11.7	-35
6	y	15.3	14.7	15.7	11.3	-28
	x	12.0	12.0	11.8	9.8	-17
7	y	17.3	18.0	18.3	9.9	-46
	x	12.0	12.0	12.0	8.4	-30

Table 11: Table of comparison for maximum y dimension and maximum x dimension of the plots against the physical dimension of the carotid plaque specimen. The histological dimensions and percentage shrinkage, to be discussed later, are detailed on the right of the table and are specific to each linear dimension. No transmission plots were performed on specimen 2.

There was large uncertainty in the calculation of the dimensions of the plot. The measurement accuracy was limited by the plot step size of 0.66 mm. In addition, the beam was not infinitely narrow at the point of measurement. The 6dB beamwidth was calculated at 1.3 mm at the depth of the plaque specimen. It was hypothesised that the uncertainty for each dimension in the speed plots was related to the corresponding step size of 0.66 mm. As the lateral resolution of the beam was larger than the step size, this uncertainty may arise when a plotline at each end of the row or column missed the edge of the plaque. The edge would not register in these cases as the plaque may not lie sufficiently within the beam.

This hypothesis was tested by plotting a square, 10 mm x 10 mm x 1 mm thick, of low density polyethylene (LDPE) embedded in the gel. The plot showed a range of 13 – 15 plotlines in the x dimension and y dimension for the LDPE square. This corresponds to a physical dimension of 8.66 – 10 mm. An uncertainty of up to 1.33 mm can therefore be expected in this plotting protocol.

There is a clear difference in the x dimension of the reflection plots and those of transmission plots with the exception of specimens 1, 6 and 7. For specimens 3, 4 and 5, both the transmission plot dimensions match those of the photograph. However the reflection plots show a considerably smaller value for the x dimension calculation. For the measured x dimensions in the reflection plots in these specimens, there is a difference of 3.5 - 4 mm from the photographic measurement. Similarly the reflection plots for specimen 2, the plot is 2.5 mm smaller than the photograph.

On inspection of the histology for these specimens, it was evident that, for the widest part of the specimen, the tissue had a thin edge. The plaque components in these thin regions composed either of elastic or fibrous tissue. This means that there may well be no increase in speed in these regions due to the match of the gel mimic. This may explain the anomaly for the difference in x dimensions. On inspection of the attenuation plots, the x dimension and y dimension measurements matched the photographic dimensions for all specimens within the 1.3 mm uncertainty. The attenuation of the clear gel is much lower than that of the plaque and therefore any amount of tissue is likely to register on the attenuation plot. As the attenuation

provided a better match to the photographic mask, the superposition of plot gridlines was made using the attenuation data. The speed data was acquired on the same grid and therefore the speed data could be matched physically to the physical photographic data.

This reduction in dimension size was not observed in the y direction. The nature of the surgical resection means that the specimen is scraped from the media concentrically. It is not possible or necessary for the surgeon to resect the plaque with equal thickness around the diameter of the artery due to the morphology of the lesion. The specimen will therefore have varying thickness in the x dimension once it is opened out and flattened prior to being embedded. The plaque specimen often has a thin edge. As the specimen was embedded with the artery in longitudinal section, it follows that the specimen will be equally thick along the line of maximum y dimension measurement.

5.5.1 Histological Shrinkage

The y dimension measurements in table 11 correspond to the length or the artery in longitudinal section. Similarly, the x dimension measurements correspond to the circumference of the artery in the opened and flattened transverse section. The plaque was embedded into the gel in this configuration in order that the histological shrinkage could be tracked. The maximum y dimension and maximum x dimension of the histology were compared directly to the dimensions of the photograph to determine the shrinkage in histology.

It is known that the histological process shrinks the plaque specimen. It has been shown that the shrinkage is 30% in length and 15% in width (Eubank et al. 1998). Other papers have shown the percentage size decrease to be 19-25% (Dobrin 1996). It was evident from the results that there was greater shrinkage in the y dimension and therefore longitudinal section or length of the arterial specimen. Indeed, the majority of the plaque specimens agree with the percentages of shrinkage quoted by Eubank et al. (1998). Specimens 2 and 3 showed similar shrinkage in each dimension. The results for specimens 5 and 7 showed a higher amount of shrinkage for both dimensions. This may have been due to an elongated time period of

formalin soaking. In order to verify this possibility, the histological shrinkage of the gel itself was then measured as seen in table 12. The z depth and x dimension of the histologically processed gel were measured from the histological sections. The z depth dimension was compared to that from the measurement in the plotting and the x dimension to that measured from the photograph.

TMM Sample	**Histo z depth** (mm)	**Shrinkage** (%)	**Histo x dimension** (mm)	**Gel x dimension** (mm)	**Shrinkage** (%)
1	10.8	16	20.6	26	20
2	10.4	19	20.6	26	20
3	10.8	16	20.2	23	12
4	10.3	20	21.1	25	16
5	10.7	17	21.5	25	14
6	10.5	19	19.9	23	13
7	8.5	34	13.3	20	33

Table 12: This table details the histological shrinkage of the clear TMM gel for both its z dimension, depth, and x dimension measurements. The gel depth from the mould is 12.8 ± 0.1 mm. Depth measurements of the histological section have an associated uncertainty of ± 0.2 mm. The histology z depth dimension is the depth / z dimension of the gel on the histological section. The values for depth and the x dimension for the histo gel are an average of 10 measurements.

It is apparent that sample blocks 1 - 6 showed similar degrees of shrinkage for both depth and x dimension. This was expected as the gel is a homogeneous substance. Average shrinkage was 18% for the depth and 16% for the x dimension. These were deemed similar within experimental error. The gel had shrunk equally in each dimension. It was evident that sample block 7 showed more significant shrinkage.

It was suggested by Eubank et al. (1998) that shrinkage varies with tissue composition. The values from the automated tissue segmentation were used to calculate the overall component percentage for each specimen. Not all slides were segmented and therefore the values detailed in table 13 only represent an approximate indication of specimen composition.

Specimen (n)	**Fibrous** (%)	**Elastic** (%)	**Lipid** (%)	**Calcified** (%)	**TMM** (%)	**Unclassified**
1 (25)	10.0 (90)	0.3 (2)	0.9 (8)	0 (0)	88.5	0.3
2 (20)	12.0 (66)	2.0 (11)	4.0 (22)	0.2 (1)	82.8	1.2
3 (13)	8.2 (75)	0.1 (1)	2.2 (20)	0.5 (4)	89.3	0.6
4 (13)	11.2 (65)	1.5 (9)	4.4 (25)	0.2 (1)	81.5	1.6
5 (16)	11.7 (65)	3.9 (22)	1.8 (10)	0.6 (3)	81.9	1.4
6 (12)	12.7 (68)	1.5 (8)	4.4 (23)	0.2 (1)	80.2	1.7
7 (26)	16.7 (88)	1.6 (8)	0.7 (4)	0.0 (0)	79.5	1.7

Table 13: This table details an approximate composition by percentage of the specimen section. The values in bold represent the approximate percentage of each component over the segmented plotlines. The bracketed values represent the approximate percentage of each component within the tissue alone. The unclassified column represents the tissue that was not segmented or identified by or within the colour thresholding. In the specimen column, n represents the number of sections that were averaged.

Specimen 7 showed a high percentage of fibrous tissue within the plaque. It had a similar composition to specimen 1 though the amount of shrinkage for each specimen was different. On consultation with histology, it became apparent that the processing for specimen 7 was carried out by a different histologist who had evidently not adhered to protocol. Meanwhile specimen 5 showed the greatest spread of tissue composition. This implied that it was heterogenous and this may have been the reason for its high amount of shrinkage. It also contained the highest amount of elastic tissue, which may also have caused greater shrinkage.

5.6 Histological assessment

5.6.1 Segmentation

The segmentation process in our studies measured percentage component as continuous variables. The intra-observer and inter-observer reproducibility in each case was therefore compared using Bland-Altman plots. The results of the segmentation for MJB and PDS were compared against my (MPB) automated segmentation. The results can be seen in figures 39a and 39b.

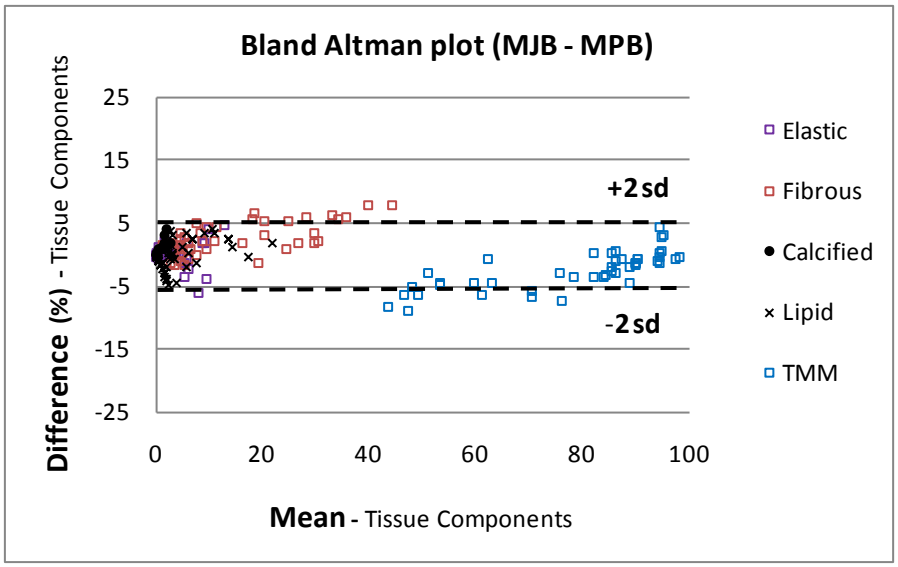

(a)

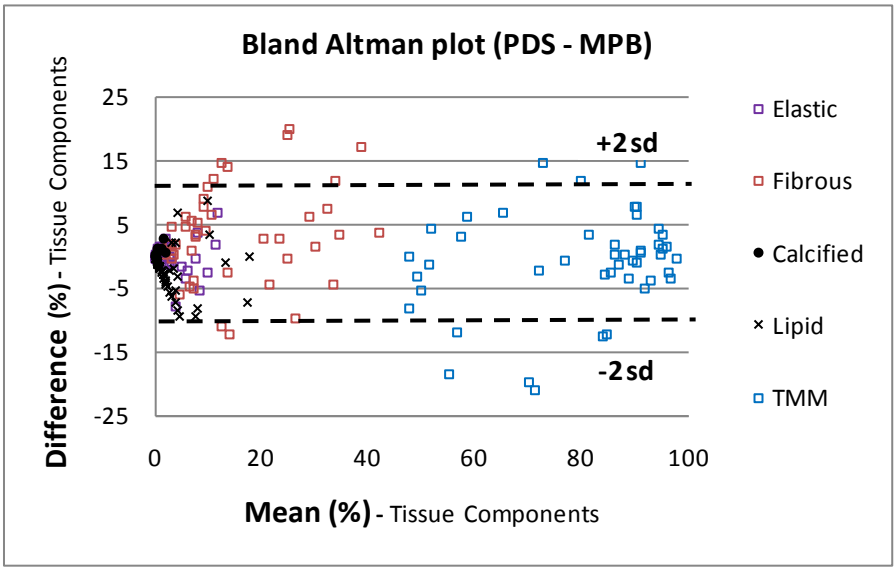

(b)

Figure 39 (a) and (b): This figure shows Bland-Altman plots to compare the manual segmentation for three sections from specimen 2 of two trained observers against an automated segmentation (MPB). The segmentation was for three sections from specimen 2.

The agreement for MJB-MPB was better than PDS-MPB as the spread is much smaller. The standard deviations were 2.7 and 5.4 respectively. The main reason for the difference in results is that an empty hole in one of the photographs was described as TMM by PDS, whereas MJB and MPB segmented it as a lipid pool. The delineation of fibrous and elastic tissue also contributed to the uncertainty.

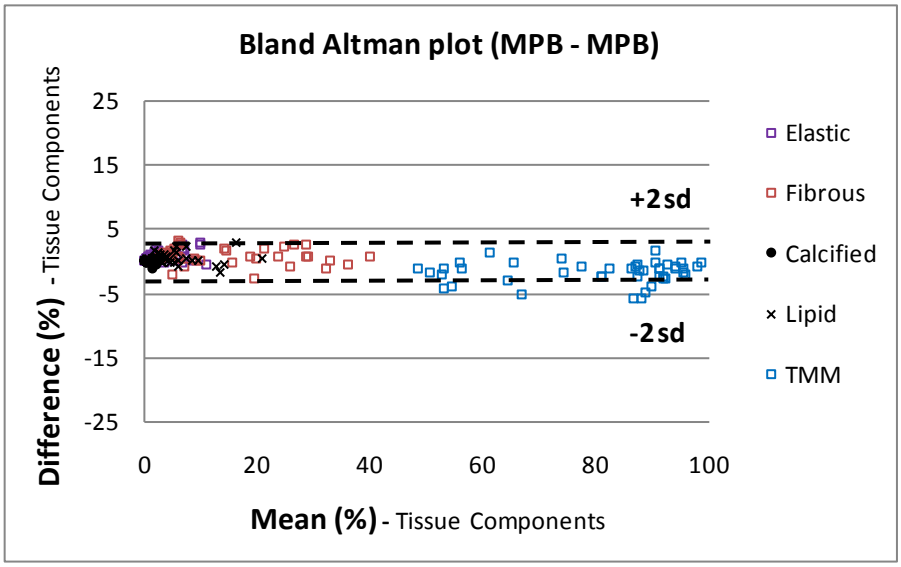

Figure 40: This figure shows the intra-observer reproducibility for the automated segmentation code for three sections from specimen 2.

The results from the intra-observer test, as shown in figure 40, indicated that the segmentation using the automated program was highly reproducible. The standard deviation was 1.4. There again was an amount of overlap between the fibrous and elastic delineation. There was also a small contribution to the uncertainty by the unclassified areas in the histology. It was extremely laborious to minimise the unclassified regions to below 1%. The automated program was used for all tissue segmentation in this study.

5.7 Matrix inversion – modelled data results

When an increasing level of noise (0 – 30%) was added to a single component in the 5 component analysis, the effect became increasingly apparent. The noise was first added to the fibrous tissue. This noise was then removed and the same levels of noise were added to the calcified component in this modelled data. The results are shown in figure 41 below:

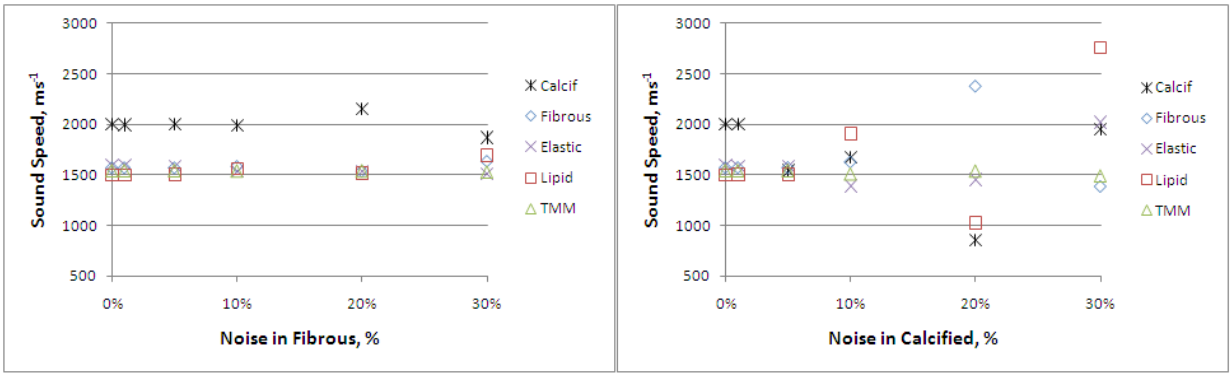

Figure 41: This figure shows that the derived sound speed data when increasing levels of noise were added to the fibrous tissue component, left, and the calcified component, right, in the 5 component analysis with modelled data. The levels of noise tested were 0, 1, 5, 10 and 20%.

It is apparent from figure 41 that the matrices solve to produce the expected result until the noise levels reach 10% in the fibrous component, where the bulk in each plotline is 10 - 20%. However when noise was added to the calcified component, with small bulk of 0.1 – 2%, the derivation began to diverge at the 5% noise level. Once the noise reaches the 20% level, there was an appreciable difference between the two graphs. The range of derived values spanned from 853 – 2760 ms^{-1} in comparison to the true modelled range of 1500 – 2000 ms^{-1}. The maximum difference for the derived values was up to 84% (lipid 2760 ms^{-1}) from the true modelled value (lipid 1500 ms^{-1}) in the calcified 30% noise data. This compared to differences of up to 13% for the derived values (lipid 1692 ms^{-1}) when 30% noise was added to the fibrous tissue.

Similar levels of noise addition (0 – 30%) were then used to test the robustness of the 3 component analysis. The noise was again added to the fibrous tissue. Having been removed from the fibrous tissue, it was then added to the lipid component which again represented the least bulk (0.5 – 5%) within the modelled data. The results are shown in figure 42:

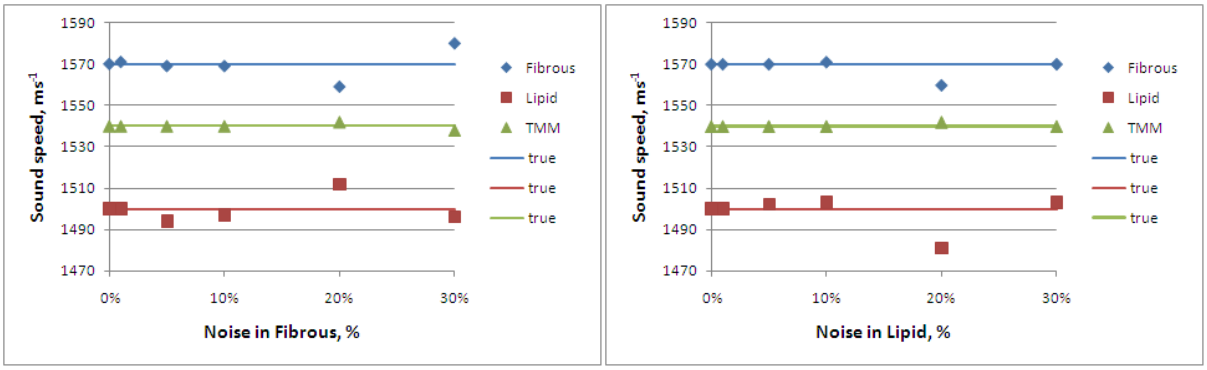

Figure 42: This figure shows that the derived sound speed data when increasing levels of noise were added to the fibrous tissue component, left, and the lipid component, right, in the 3 component analysis with modelled data. The levels of noise tested were 0, 1, 5, 10 and 20%.

In figure 42, it can be seen that the 3 component analysis behaves well with noise levels in each component up to 10%. Indeed the derivation worked with reasonable success up to the 30% noise level. There was a maximum divergence of 1.3% in the sound speed from the true data with the addition of noise to either the fibrous or lipid component.

In the last test of the matrix derivation using the modelled data, increasing levels of noise (0 – 20%) were added to all the components simultaneously. This test was carried out on both the 5 and the 3 component analysis. The results are shown in figure 43:

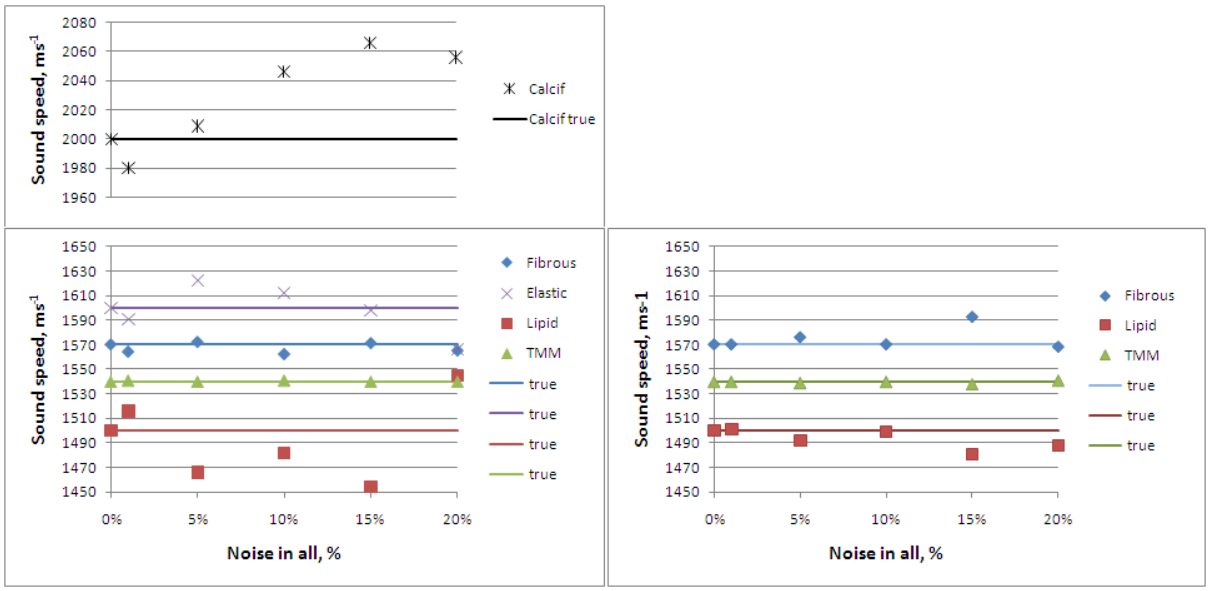

Figure 43: This figure shows that the derived sound speeds from the modelled data when increasing levels of noise were added to all the components in the 5 component analysis, left, and the 3 component analysis, right. The calcified sound speed results are seen top left. The levels of noise tested were 0, 1, 5, 10, 15 and 20%.

It was evident from the 5 component analysis results that the derivation of data is fairly robust up to the 10% noise level. Here, the maximum divergence from the true value was only 2.3%. This increased to 3.3% at the highest level of noise. However the 3 component analysis remained robust with noise levels up to 30%, where the divergence for derived values is less than 1%. It can be seen that the sound speed for both TMM and fibrous remain relatively unaffected by 20% noise levels in both analyses.

5.8 Plaque component: speed data

5.8.1 Single section calculation

The Matlab solution to the simultaneous equations failed to solve for a majority of the plotlines over the seven plaque specimens. Where the simultaneous equation was solved, there were a number of erroneous results.

The proportion of successful solutions for each specimen, technique and analysis are tabulated in table 14.

Mode	Temp	TC	1	2	3	4	5	6	7
Rx	Cold	5		66/189		59/119	82/211	26/73	7/14
		3	185/425	151/173	91/188	141/223	178/316	67/109	181/275
	Hot	5		66/147		68/129	49/217	28/61	
		3	200/427	177/253	86/175	158/232	221/318	88/107	186/271
Tx	Cold	5				49/133	33/107	29/39	
		3	195/398		63/179	128/235	77/192	53/84	179/278
	Hot	5				76/133	66/115	32/50	
		3			94/182	147/237	144/191	69/95	187/287

Table 14: A table to show the proportion of successful solutions for the matrix inversion derivation of plaque component sound speed. The modes Rx and Tx represent reflection and transmission techniques respectively. TC represents the 3 and 5 component analyses used in the Matlab calculation. Cold shows measurements at 21^0C and Hot shows measurements at 37^0C.

The denominators in table 14 represent the total number of solutions from the sets of plotlines for each specimen. In other words, they represent the number of times that the matrix inversion solved. The denominator varied between techniques and measurement temperatures as different speed data was correlated with its respective segmentation data. The specimens were all of a similar size with an equivalent number of associated histological slides. The quality of histological sections from these slides was not always consistent and this affected how many sections were suitable for segmentation. This may also explain the variation in number of successful solutions due to the number of sections that were selected for input. This denominator, or total number of solutions, reflects the overall success of the Matlab calculation for that specimen. The numerator represents the number of solutions that fitted the criteria outlined in section 5.11.1. The proportion of solutions, as detailed in table 14, gave a further indication as to the ease of solution of the simultaneous equations for the sets plotlines for each specimen.

Specimens 1, 4, 6 and 7 showed the highest number of successful solutions and this number was consistent across each technique. Specimen 2 had a lower number of solutions but a high percentage of solutions that fitted the criteria. Specimen 3 had a lower number of solutions and a poor success rate at around 50%. This was the smallest and thinnest specimen. The proportion of successful solutions was consistent showed a range of 38 - 82% over all specimens for the 3 component analysis. There was no evident connection of successful solution with the tissue composition percentages as shown by table 13.

5.8.1.1 Reflection Technique Results – Cold

Table 15 shows the results of sound speed values for the broadband reflection technique at ambient temperature of 21^{o}C. However specimen 5 and 7 were measured at 24^{o}C. The laboratory temperature was not controllable and therefore the tank water temperature was sustained at this elevated temperature for these specimens.

SPEC.	TC (n)	TMM		LIPID		FIBROUS		ELASTIC		CALCIF.	
		Ave	Std	**Ave**	Std	**Ave**	Std	**Ave**	Std	**Ave**	Std
1	5										
	3 (185)	**1543**	8	**1502**	194	**1574**	69				
2	**5** (66)	**1543**	6	**1591**	184	**1555**	73	**1665**	319	**3320**	2302
	3 (151)	**1544**	7	**1535**	122	**1566**	92				
3	5										
	3 (91)	**1544**	8	**1536**	113	**1572**	87				
4	**5** (59)	**1545**	11	**1738**	385	**1585**	93	**1876**	933	**2103**	1147
	3 (141)	**1546**	24	**1570**	150	**1567**	91				
5	**5** (82)	**1546**	11	**1752**	492	**1577**	94	**1815**	914	**2149**	2029
	3 (178)	**1548**	5	**1571**	184	**1563**	67				
6	**5** (26)	**1544**	12	**1669**	410	**1602**	145	**1949**	673	**3492**	2876
	3 (67)	**1542**	15	**1601**	176	**1577**	101				
7	**5** (7)	**1552**	10	**2382**	1032	**1486**	69	**1719**	453	**8367**	4920
	3 (181)	**1546**	15	**1369**	426	**1581**	91				

Table 15: This table shows the sound speed data for the seven specimens from the broadband reflection measurements at 21^{0}C (± 1^{0}C). The means and standard deviations are quoted. Specimen 5 was measured at 24^{0}C. The TC, tissue component, column represents the 3 or 5 component Matlab analysis. The number of specimens, n, is also quoted in the TC column. The inter-quartile ranges are tabulated in Appendix D.

The fibrous tissue values show the lowest range of standard deviations (69 - 145) of the plaque components. The sound speed for fibrous tissue is consistently higher than TMM with a mean value over all specimens of 1566 ms^{-1} (n = 1234, sd = 86 ms^{-1}). In comparison, the results for elastic tissue and lipid show wide inter-quartile ranges. The average for elastic tissue was 1757 ms^{-1} (n = 240, sd = 750 ms^{-1}) and for lipid was 1579 ms^{-1} (n = 1027, sd = 247 ms^{-1}). The calcified tissue showed an appreciably higher value for sound speed of 2655 ms^{-1}, though with a high standard deviation of 1692 ms^{-1} (n = 182).

The overall derived average of the TMM for specimens 1 - 4 and 6 was 1545.1 ms^{-1} (n = 970, sd = 12.7 ms^{-1}). The sound speed for the independently measured QA (quality assurance) was 1542.4 ms^{-1} (n = 270, sd = 1.2 ms^{-1}) at 21^0C. These average values for sound speed differ significantly ($p << 0.05$). The TMM for specimen 5 and 7 had a derived average of 1548.5 ms^{-1} (n = 178, sd = 4.8 ms^{-1}) which also differed (p = 0.04) from the QA measured TMM value of 1547.7 ms^{-1} (n = 108, sd = 0.8 ms^{-1}) at 24^0C.

The QA measured values for each specimen TMM are compared against the derived values in figure 44.

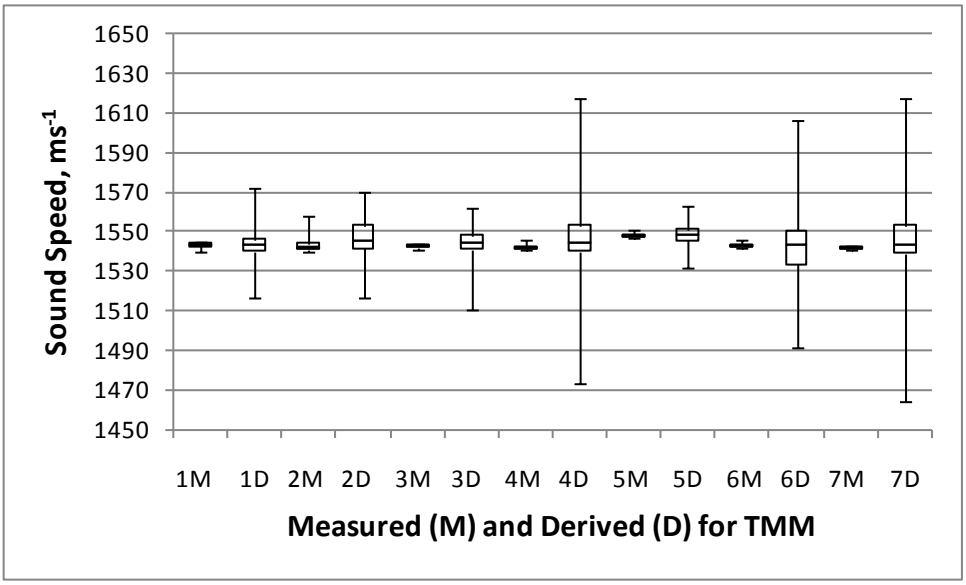

Figure 44: This figure shows the derived values of sound speed from the matrix inversion solution for the TMM in each specimen gel compared to their QA measured values for the 'cold' reflection technique.

The derived values for specimens 2, 4, 6 and 7 show the largest inter-quartile range. The median values for the derived and measured values are comparable for all specimens. The maximum difference between medians was 3.9 ms^{-1} for specimen 2.

5.8.1.2 Reflection Technique Results – Hot

Table 16 shows the results of sound speed values for the broadband reflection technique at tank water temperature of 37^{o}C.

SPEC.	TC	TMM		LIPID		FIBROUS		ELASTIC		CALCIF.	
		Ave	Std	**Ave**	Std	**Ave**	Std	**Ave**	Std	**Ave**	Std
1	5										
	3 (200)	**1565**	8	**1550**	181	**1592**	61				
2	**5** (66)	**1574**	8	**1626**	193	**1550**	97	**1637**	293	**2397**	966
	3 (177)	**1572**	8	**1588**	121	**1575**	93				
3	5										
	3 (86)	**1570**	13	**1556**	124	**1592**	113				
4	**5** (68)	**1570**	14	**1680**	242	**1578**	105	**1656**	387	**2772**	1689
	3 (158)	**1574**	17	**1613**	163	**1600**	85				
5	**5** (49)	**1572**	5	**1709**	412	**1589**	48	**1671**	308	**1864**	593
	3 (221)	**1573**	8	**1546**	280	**1571**	83				
6	**5** (28)	**1564**	23	**1704**	452	**1553**	88	**1770**	751	**3165**	2170
	3 (88)	**1565**	16	**1579**	181	**1589**	112				
7	5										
	3 (186)	**1571**	15	**1423**	390	**1600**	70				

Table 16: This table shows the sound speed data for the seven samples from the broadband reflection measurements at 37^{0}C (± 1^{0}C). The means and standard deviations are quoted. The TC, tissue component, column represents the 3 or 5 component Matlab analysis. The number of specimens, n, is also quoted in the TC column. The inter-quartile ranges are tabulated in Appendix D.

With the temperature rise of 16^{o}C, the sound speed of fibrous tissue across all the specimens was seen to rise to an average of 1579 ms^{-1} (n =1327, sd = 88 ms^{-1}). The lipid tissue also showed an overall increase to 1588 ms^{-1} (n =1031, sd = 210 ms^{-1}). In comparison, the elastic tissue and the calcified tissue showed an average value of 1664 ms^{-1} (n =218, sd = 397 ms^{-1}) and 2463 ms^{-1} (n =1355, sd = 178 ms^{-1}) respectively.

The overall derived average of the TMM for all specimens was 1569.4 ms^{-1} (n = 700, sd = 12.3 ms^{-1}). The derived TMM values of sound speed again differ statistically ($p << 0.01$) from the values of 1567.8 ms^{-1} (n = 378, sd = 2.6 ms^{-1}) measured in the background TMM at 37^{o}C. This difference, 0.1%, is however very small and so the values can be considered comparable within experimental error. For the measurements at 37 ^{o}C, the measured results were taken from the sound speed values for the background TMM. The measured values for each specimen TMM are compared against the derived values in figure 45.

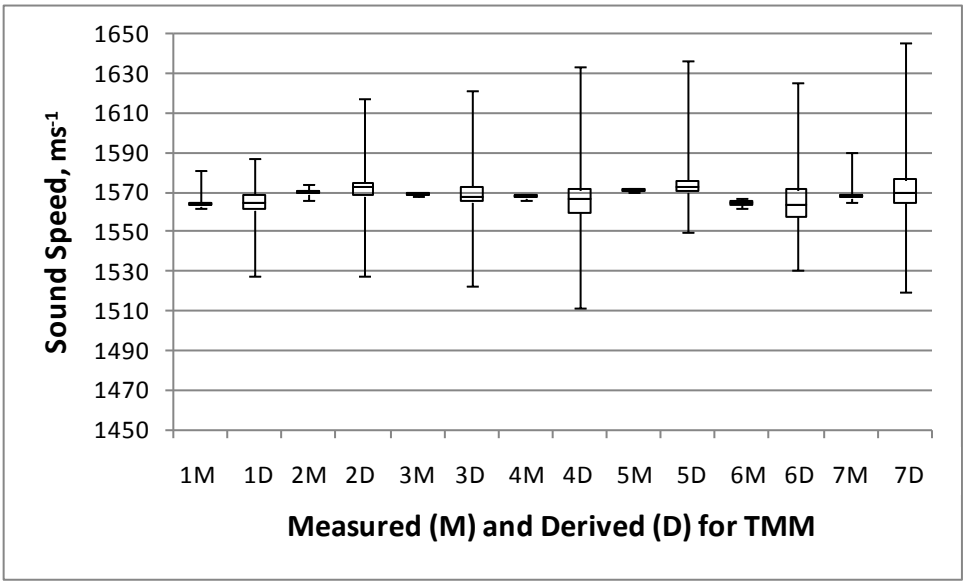

Figure 45: This figure shows the derived values of sound speed from the matrix inversion solution for the TMM in each specimen gel compared to the values measured in the background TMM for the 'hot' reflection technique.

The derived values for specimens 2, 4, 6 and 7 show the largest inter-quartile range. The median values for the derived and measured values are again comparable. The maximum difference between medians was 2.7 ms^{-1} for specimen 2.

5.8.1.3 Transmission Technique Results - Cold

The results for the broadband transmission technique at ambient temperature of 21^{o}C are shown in table 17. However specimens 5 and 7 were measured at 24^{o}C. The laboratory temperature was not controllable and therefore the tank water temperature was sustained at this elevated temperature.

SPEC.	TC (n)	TMM		LIPID		FIBROUS		ELASTIC		CALCIF.	
		Ave	Std	**Ave**	Std	**Ave**	Std	**Ave**	Std	**Ave**	Std
1	5										
	3 (195)	**1547**	8	**1523**	196	**1594**	60				
2	5										
	3										
3	5										
	3 (63)	**1545**	9	**1578**	142	**1568**	89				
4	**5** (49)	**1545**	11	**1678**	442	**1566**	99	**1556**	191	**1779**	1007
	3 (128)	**1551**	18	**1603**	172	**1556**	74				
5	**5** (33)	**1549**	11	**1939**	1013	**1502**	163	**1907**	990	**1588**	772
	3 (77)	**1547**	7	**1499**	388	**1544**	65				
6	**5** (29)	**1549**	10	**1939**	657	**1516**	83	**1894**	556	**6999**	5226
	3 (53)	**1548**	18	**1535**	189	**1568**	68				
7	5										
	3 (179)	**1548**	16	**1519**	287	**1575**	120				

Table 17: This table shows the sound speed data for the seven samples from the broadband transmission measurements at 21^{0}C (± 1^{0}C). The means and standard deviations are quoted. The TC, tissue component, column represents the 3 or 5 component Matlab analysis. The number of specimens, n, is also quoted in the TC column. No transmission measurements were carried out on specimen 2. For specimens 1, 3 and 7, the five component analysis failed. The inter-quartile ranges are tabulated in Appendix D.

The fibrous tissue values again show the lowest range of standard deviations (60 - 163) relative to the TMM at 21^0C. The sound speed for fibrous tissue is consistently higher than TMM with a mean value over all specimens of 1568 ms^{-1} (n = 806, sd = 93 ms^{-1}). Meanwhile the results for elastic tissue and lipid again show a wide range of results. The average for elastic tissue was 1772 ms^{-1} (n = 106, sd = 629 ms^{-1}) and for lipid was 1556 ms^{-1} (n = 629, sd = 208 ms^{-1}). The calcified tissue showed an appreciably higher value for sound speed of 2094 ms^{-1}, though also with a high standard deviation of 1428 ms^{-1} (n = 72).

The overall derived average sound speed of the TMM for specimens 1 - 4, and 6 was 1545.5 ms^{-1} (n = 517, sd 13.3 ms^{-1}). These values differed (p = 0.005) from the QA measured values of 1543.8 ms^{-1} (n = 270, sd = 1.3 ms^{-1}) at 21^0C. The TMM for specimen 5 and 7 had an average of 1547.1 ms^{-1} (n = 311, sd = 14.7 ms^{-1}) which differed (p = 0.007) from the QA measured TMM value of 1544.8 ms^{-1} (n = 108, sd = 1.3 ms^{-1}) at 24^0C. The measured values for each specimen TMM are compared against the derived values in figure 46.

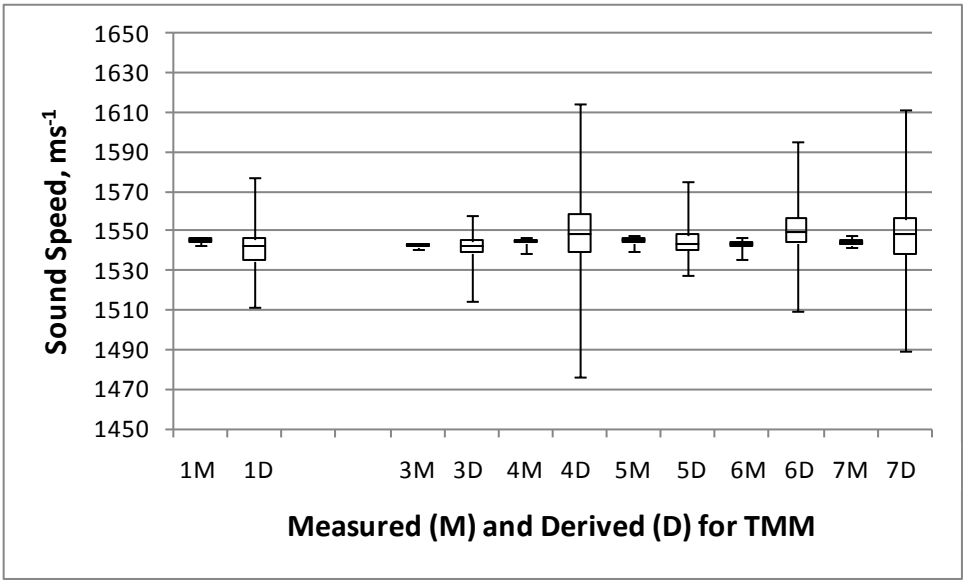

Figure 46: This figure shows the derived values of sound speed from the matrix inversion solution for the TMM in each specimen gel compared to their QA measured values for the 'cold' transmission technique.

The derived values for specimens 4, 6 and 7 show the largest inter-quartile range. In addition, specimens 4, 6, and 7 show some strong outliers. The median values for the derived and measured values are comparable for specimen 3.

5.8.1.4 Transmission Technique Results - Hot

The results for the broadband transmission technique at body temperature of 37^{o}C are shown in table 18.

SPEC.	TC	TMM		LIPID		FIBROUS		ELASTIC		CALCIF.	
		Ave	Std	**Ave**	Std	**Ave**	Std	**Ave**	Std	**Ave**	Std
3	5										
	3 (94)	**1568**	10	**1552**	171	**1599**	86				
4	**5** (76)	**1568**	16	**1792**	684	**1574**	131	**1724**	653	**2359**	1141
	3 (147)	**1575**	19	**1584**	184	**1594**	83				
5	**5** (66)	**1574**	11	**2252**	1713	**1574**	111	**1796**	675	**2643**	2758
	3 (144)	**1578**	10	**1436**	287	**1575**	103				
6	**5** (32)	**1571**	8	**1834**	466	**1604**	76	**1735**	456	**NaN**	NaN
	3 (69)	**1574**	12	**1564**	170	**1594**	77				
7	5										
	3 (187)	**1572**	13	**1467**	379	**1588**	91				

Table 18: This table shows the sound speed data for the seven samples from the broadband transmission measurements at 37^{0}C (± 1^{0}C). The means and standard deviations are quoted. The TC, tissue component, column represents the 3 or 5 component Matlab analysis. The number of specimens, n, is also quoted in the TC column. No transmission measurements were performed on samples 1 or 2 at 37 ^{0}C. The inter-quartile ranges are tabulated in Appendix D.

The fibrous tissue show the smallest range of sound speed values after TMM at 21^{0}C. The sound speed for fibrous tissue is consistently higher than TMM with a mean value over all specimens of 1588 ms^{-1} (n = 815, sd = 93 ms^{-1}). Meanwhile the results for elastic tissue and lipid again show a wide range of results. The average for elastic tissue was 1771 ms^{-1} (n = 170, sd = 622 ms^{-1}) and for lipid was 1564 ms^{-1} (n = 629,

sd = 200 ms^{-1}). The calcified tissue showed an appreciably higher value for sound speed of 2583 ms^{-1}, though also with a high standard deviation of 1749 ms^{-1} (n = 72).

The overall derived average of the TMM for all specimens was 1573.2 ms^{-1} (n = 806, sd = 13.5 ms^{-1}). The derived TMM values of sound speed differ significantly ($p<<0.05$) from the values of 1570 ms^{-1} (n = 378, sd = 4.0 ms^{-1}) measured in the background TMM at 37^{o}C. For the measurements at 37^{o}C, the measured results were taken from the sound speed values for the background TMM. The measured values for each specimen TMM are compared against the derived values in figure 47.

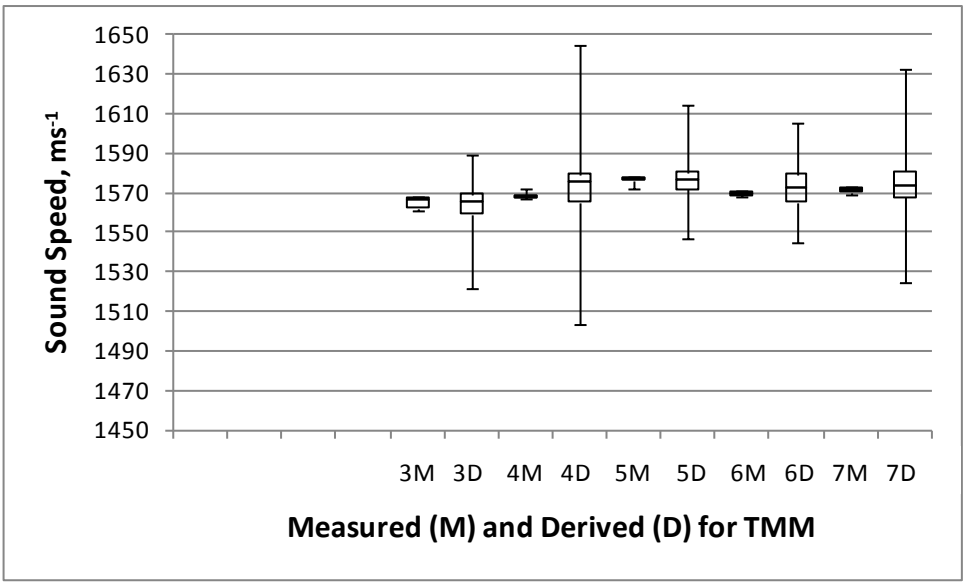

Figure 47: This figure shows the derived values of sound speed from the matrix inversion solution for the TMM in each specimen gel compared to the values measured in the background TMM for the 'hot' transmission technique.

The derived values for specimens 4, 6 and 7 show the largest inter-quartile range while the other specimens show relatively moderate inter-quartile range. In addition, specimens 4 and 7 show some strong outliers. The median values for the derived and measured values are comparable with the exception of specimen 4.

5.8.2 Sound Speed in TMM – Measured vs. Derived

It is apparent from the box plots shown in figures 35 - 38 that the median values for the derived values follow, in general, the measured values for the sound speed. However the unpaired Student t-test values show that the mean values differ significantly between the measured and derived values. The derived value is higher than the measured value for both techniques at both temperatures.

5.9 Consecutive section calculation

Results from the averaging of plaque component percentages from the histological sections over three contiguous slides were obtained for specimens 2 - 7. Results are only displayed for the reflection technique at 21^0C and 37^0C, as shown in table 19 and 20.

SPEC.	TC (n)	TMM		LIPID		FIBROUS		ELASTIC		CALCIF.	
		Ave	Std	Ave	Std	Ave	Std	Ave	Std	Ave	Std
2	5 (7)	1544	2	1629	61	1549	16	1591	375	5915	8770
	3 (11)	1544	8	1628	69	1514	129				
3	5										
	3 (3)	1540	6	1572	19	1597	52				
4	5 (6)	1540	7	1609	105	1574	37	1610	327	4371	3223
	3 (13)	1541	10	1667	112	1581	60				
5	5 (11)	1553	3	1532	137	1579	55	1502	257	2523	620
	3 (14)	1547	12	1554	196	1582	112				
6	5 (6)	1540	8	1751	562	1724	186	2258	777	1991	n/a
	3 (6)	1545	9	1522	256	1640	61				
7	5										
	3 (20)	1546	35	1122	433	1614	94				

Table 19: This table shows the sound speed data for six of the specimens derived from consecutive sections for the broadband reflection measurements at 21^0C ($\pm$ 1^0C). Specimens 5 and 7 were measured at 24^0C ($\pm$ 1^0C). In the TC column, n is the number of solved sets of simultaneous equations that meet the criteria.

SPEC.	TC	TMM		LIPID		FIBROUS		ELASTIC		CALCIFIED	
		Ave	Std	Ave	Std	Ave	Std	Ave	Std	Ave	Std
2	**5** (7)	**1572**	2	**1600**	18	**1577**	13	**1657**	140	**2315**	569
	3 (11)	**1568**	8	**1616**	78	**1593**	139				
3	5										
	3 (3)	**1573**	10	**1596**	32	**1563**	83				
4	**5** (6)	**1574**	1	**1611**	60	**1624**	59	**1444**	265	**5847**	7396
	3 (13)	**1574**	3	**1670**	81	**1581**	22				
5	**5** (11)	**1576**	4	**1462**	287	**1607**	68	**1535**	315	**2426**	946
	3 (14)	**1575**	7	**1558**	90	**1587**	65				
6	**5** (6)	**1548**	6	**1908**	577	**1726**	184	**2417**	661	**NaN**	NaN
	3 (6)	**1570**	26	**1354**	544	**1634**	172				
7	5										
	3 (20)	**1566**	25	**1244**	659	**1609**	60				

Table 20: This table shows the sound speed data for the seven specimens derived from consecutive sections for the broadband reflection measurements at 37^0C ($\pm$ 1^0C).

There was no substantive difference in the results when the plaque component percentages were averaged over contiguous slides. However the number of plotlines used for the matrix inversion was much smaller. For each specimen, there were only one or two instances where it was possible to average over three consecutive slides. For this reason, this analysis was not repeated for the transmission technique. The number of solutions was also too low to compare results or make any conclusion as to the improvement of the method.

5.10 Plaque Specimen inter-comparison

The derived sound speeds for each component were compared between all plaque specimens. For the seven specimens, this meant that there were twenty one inter-specimen comparisons. It was seen that, for both the reflection and transmission techniques, approximately 70% of inter-specimen comparisons were seen to be significantly similar, using the student t-test, for the derived speeds of TMM. For the fat and fibrous tissue components, the reflection technique showed better inter-specimen comparison (where 47% and 29% were similar respectively vs. 32% and 23% for the transmission technique). There were not sufficient results to make valid comparisons for elastic tissue and calcification.

5.11 Effect of Temperature Change

It was expected that a reduction in sound speed for the lipid content would be seen with the rise in temperature. There was also an expected rise in sound speed with temperature for the fibrous and elastic. Due to the solid nature of calcification, no change in sound speed would be expected with an increase in temperature.

5.11.1 Overall unpaired data

The effect of temperature on each component averaged over all the specimens was investigated for both techniques. The comparison of mean and medians are shown in figure 48.

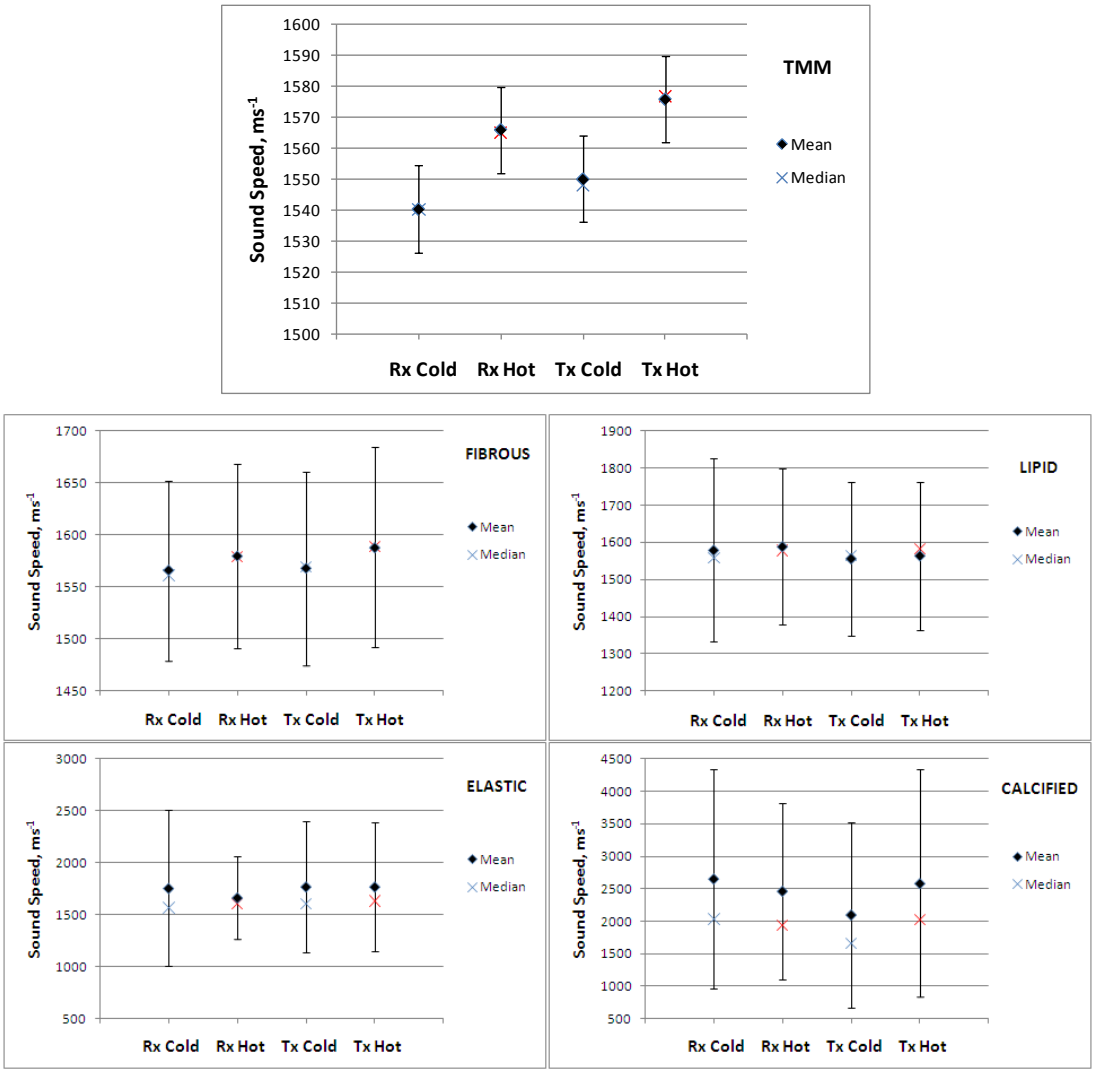

Figure 48: This figure shows the effect of temperature on each plaque component for each technique. Means and medians are shown here. Rx and Tx represent reflection and transmission technique respectively. Cold represents 21^{o}C and hot 37 ^{o}C. The error bars show ± 1 standard deviation.

There was a clear increase in sound speed with the change in temperature of 16^{o}C for both techniques, 24 ms^{-1} for the reflection technique and 20 ms^{-1} for the transmission technique. There was also a clear rise in sound speed for fibrous tissue in both techniques. The unpaired student t-test gave values of p = 0.00006 for the reflection technique and p = 0.00002 for the transmission when the cold and hot speed values are compared. There was no significant difference for the other three components with the temperature change for either technique.

5.11.2 Reflection vs. Transmission Technique comparison

The results shown in figure 48 were also used to compare the techniques at each temperature. The calcium data showed that while the results from the techniques were not significantly different, at the 95% confidence interval, for the 'hot' measurements (p = 0.53), they were significant differences at the 'cold' temperature (p = 0.01). The results showed for the other three components that the techniques were not significantly different at 'cold' temperature (fibrous p = 0.63, lipid p = 0.057, elastic p = 0.86). Moreover, at 'hot' temperature, the speed data for the fibrous and elastic component were not significantly different between the two techniques (fibrous p = 0.058, elastic p = 0.053). However, the result for the lipid component at body temperature (p = 0.02) was significantly different between the reflection and transmission technique.

5.11.3 Specimen Paired data

These results above compared the overall derived averages for each component. The data is therefore unpaired. Two specimens were chosen, 3 and 7, and the paired plotline data for each plaque component was then compared. The results for specimen 3 are shown in figure 49.

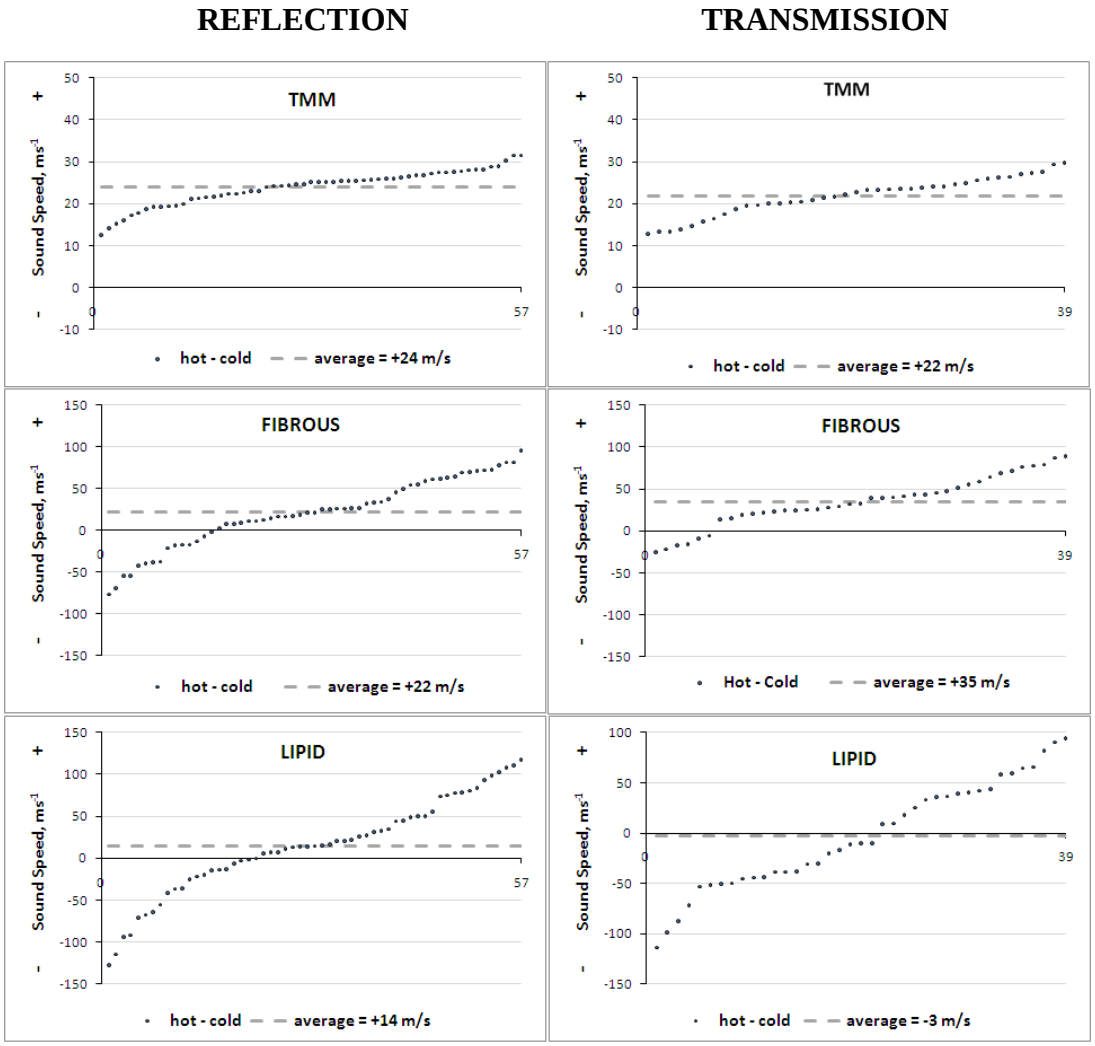

Figure 49: The graphs show the difference in sound speed of paired data for the TMM, fibrous tissue and lipid in specimen 3 for each technique. The reflection technique data (n = 57) is on the left and the transmission technique data (n = 39) is on the right. The data is ordered before it is plotted so that an indication of speed range is seen. This ordering leads the graph to have an apparent trend, which is not the case.

The maximum number of paired data identified for specimen 3 was small (n = 57). The average rise in sound speed for TMM was consistent for each technique at 24 ms^{-1} for the reflection technique and 22 ms^{-1} for the transmission technique. Both plots for TMM gave a reasonably flat curve with a variation of approximately ±10 ms^{-1} from the average. Fibrous tissue gave an average positive temperature dependence for sound speed in each technique, 22ms^{-1} for reflection and 35 ms^{-1} for transmission. However the range of results for the paired data was large for both fibrous tissue and fat. The negative dependence on temperature for sound speed was observed in the transmission technique, - 3 ms^{-1}, but not in the reflection technique, + 14 ms^{-1}.

The results for specimen 7 are shown in figure 50, overleaf.

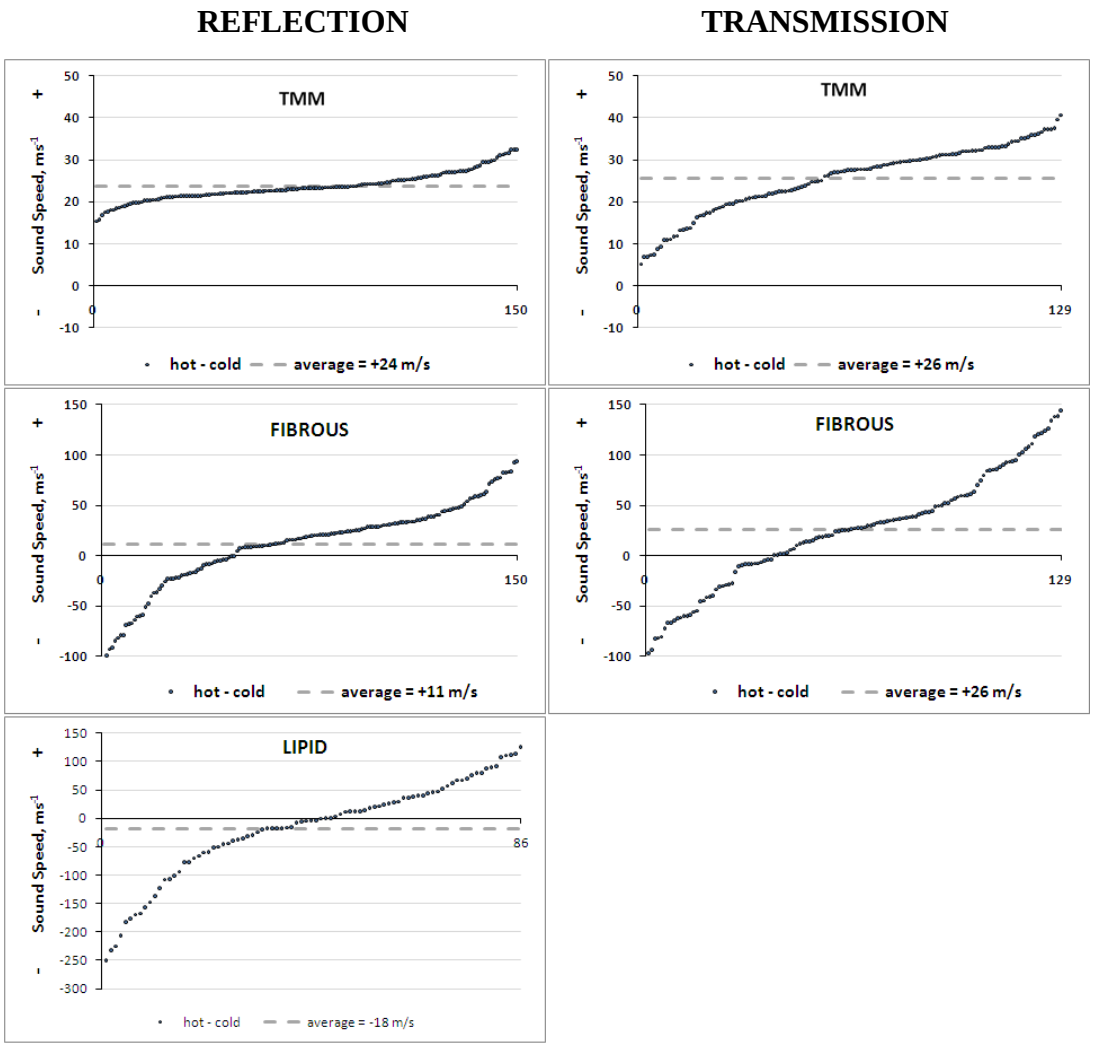

Figure 50: The graphs show the difference in sound speed of paired data for the TMM and fibrous tissue in specimen 7 for each technique. The reflection technique data (n = 150) is on the left and the transmission technique data (n = 129) is on the right. There were no matched pairs for lipid in the transmission technique. The data is ordered before it is plotted so that an indication of speed range is seen. This ordering leads the graph to have an apparent trend, which is not the case.

There was a large number of paired data for specimen 7, as shown in figure 45. However there were significantly less matched pairs for the fat data. For the transmission technique, there were very few solutions for the fat data. The average rise in sound speed for TMM was consistent for each technique at 24 ms^{-1} and 26 ms^{-1}. Both plots for TMM gave a reasonably flat curve with a variation of approximately ±10 ms^{-1} from the average. Fibrous tissue gave positive temperature dependence for sound in each technique. However the range of results for the paired

data was again large for both fibrous tissue and fat. The negative dependence on temperature for sound speed was observed in the reflection technique, -18 ms^{-1}.

5.12 Plaque component sound speed

5.12.1 Room or 'Cold' temperature - 21°C

The plaque component speeds were calculated as inter-quartile ranges for all specimens for each technique. (The inter-quartile ranges for each specimen for each technique are included in Appendix D.) The ranges are compared in table 21 for the measurements at 21°C.

Plaque Component	Technique		Quoted Ranges
	Rx	Tx	
Fibrous / Collagen	1529 -1598	1553 – 1615	1560 – 1720 [a,b]
Lipid / Fat	1478 – 1645	1453 - 1670	1430 – 1526 [c,d]
Elastic / Smooth Muscle	1445 – 1812	1492 – 1603	1530 – 1600 [d]
Calcification	1698 – 2810	1345 - 2205	1760 – 1830 [b,d]

Table 21: This table shows the overall inter-quartile range values for sound speed in ms^{-1} for each of the plaque components. The quoted values for sound speed are defined at 20°C. References: a - Saijo (2004), b - Saijo (2006), c - Duck (1990), d - Saijo (1998).

It is apparent from these results that the sound speed inter-quartile (IQ) ranges all lie in comparable ranges to quoted values. The IQ range for fibrous tissue in each technique is the smallest. The range spans the quoted value for collagen or fibrous tissue of 1570 ms^{-1} (Lees & Rollins 1972) and that of 1561 ms^{-1} (Saijo et al. 2004). However it does not extend to the higher values of 1680 and 1720 ms^{-1} (Saijo et al. 2007; Saijo et al. 2006). The speed values for calcium show a wide range but at

significantly higher speeds than the other components. However the results for both lipid and elastic tissue also show broad IQ ranges, which span both the upper and lower limits of the fibrous tissue range.

5.12.2 Body or 'Hot' temperature - 37°C

The inter-quartile ranges for sound speed of each plaque component measured at 37°C are quoted in table 22.

Plaque Component	Technique		Quoted Ranges
	Rx	Tx	
Fibrous / Collagen	1533 – 1607	1554 -1625	1560 – 1720 [a,b]
Lipid / Fat	1510 – 1669	1464 – 1664	1430 – 1526 [c,d]
Elastic / Smooth Muscle	1460 – 1751	1461 – 1857	1530 – 1600 [d]
Calcification	1687 – 2746	1564 - 2832	1760 – 2000 [e]

Table 22: This table shows the overall inter-quartile range values for sound speed in ms^{-1} for each of the plaque components. The quoted values for sound speed cover the range of temperatures from 20 - 37°C. References: a - Saijo (2004), b - Saijo (2006), c - Duck (1990), d - Saijo (1998), e - Rooney (1982).

There is little difference in the IQ ranges of sound speed for each component at this higher temperature in comparison to the 'cold' temperature. This evidence was also shown in figure 43. Speed values for all plaque components at 37^0C correspond to the quoted ranges but the IQ ranges for lipid, elastic tissue and calcification are broader.

5.13 Summary

The adapted clear TMM gel was shown to retain the property of sound speed of approximately 1540 ms^{-1}. The lower attenuation enabled the matching of the contour plot to the photographic mask to be performed with more certainty. The sound speed of embedded plaque was measured over a 72 hour period to assess decay. Both reflection and transmission substitution techniques were used to obtain sound speed, attenuation and RF backscatter data for each of the specimens. The derived data was compared against the measured data for the 'cold' measurements and against the TMM background for the 'hot' measurement. The improvement of results was probed using plaque component percentage data from consecutive slides. The effect of temperature on each plaque component was studied for both unpaired and paired data. Finally the plaque component sound speed values were tabulated as inter-quartile ranges. The results are further discussed and conclusions are made in chapter 6.

5.14 References

Dobrin, P. B. 1996, "Effect of histologic preparation on the cross-sectional area of arterial rings", *J Surg Res*, vol. 61, pp. 413-415.

Duck, F. A. 1990, *Physical properties of tissue - A comprehensive reference book* Academic Press.

Eubank, W. W., Yuan, C., Fisher, E. R., Luna, J. A., Reichenbach, D. D., Schmiedl, U. P., & Beach, K. W. 1998, "Endarterectomy plaque shrinkage: comparison of T2-weighted MR imaging of *ex vivo* specimens to histologically processed specimens", *J Vasc Invest*, vol. 4, pp. 161-170.

Lees, S. & Rollins, F. R. 1972, "Anisotropy in dental tissues", *J Biomech*, vol. 5, pp. 557-566.

Rooney, J. A., Gammell, P. M., Hestenes, J. D., Chin, H. P., & Blankenhorn, D. H. 1982, "Velocity and attenuation of sound in arterial tissues", *J Acoust Soc Am*, vol. 71, pp. 462-466.

Saijo, Y., dos Santos Filho, E., Sasaki, H., Yambe, T., Tanaka, M., Hozumi, N., Kobayashi, K., & Okada, N. 2007, "Ultrasonic tissue characterization of atherosclerosis by a speed-of-sound microscanning system", *IEEE Trans Ultrason Ferroelectr Freq Control*, vol. 54, no. 8, pp. 1571-1577.

Saijo, Y., Hozumi, N., Lee, C., Nagao, M., Kobayashi, K., Oakada, N., Tanaka, N., dos Santos Filho, E., Sasaki, H., Tanaka, M., & Yambe, T. 2006, "Ultrasonic speed microscopy for imaging of coronary artery", *Ultrasonics*, vol. 44, p. e51-e55.

Saijo, Y., Miyakaya, T., Sasaki, H., Tanaka, M., & Nitta, S.-I. 2004, "Acoustic properties of aortic aneurysm obtained with scanning acoustic microscopy", *Ultrasonics*, vol. 42, pp. 695-698.

Chapter 6 CONCLUSION

6.1 IEC tissue mimicking material

6.1.1 Discussion and Conclusion

This IEC agar-based tissue mimicking material has proven to maintain its relevant values for the acoustic parameters at this extended frequency range of 17 – 23 MHz. It has been shown to retain these values over an extended time period of three years. However, it was noted that the organic nature of the material meant that there was some biological growth within the hydrating fluid. This may affect the imaging when it is used in the construction of test objects as this matter may deposit in the surrounding hydrating fluid within the phantom. If the material is left unhydrated, it shrinks and hardens. It is evident that this material must be kept in a hydrating solution with anti-bacterial, anti-fungal agent in order to retain its form and to prevent both leaching of glycerol out of the gel and the biological growth.

For speed of sound, the results for both systems show good agreement with the expected value of 1540 ms^{-1}. It was shown also that the glycerol leaches out from the sample, which affects the speed of sound, if placed in water. This effect was nullified by sealing the sample in clingfilm, also known as Saran wrap®. For attenuation, the results from both the narrowband and broadband technique show a good agreement with the expected value of 0.5 dB cm^{-1} MHz^{-1}. The results for both properties were affirmed for this higher frequency by good agreement at another ultrasound laboratory using the same transducer.

The gel responds to both a change of temperature and frequency as shown at lower frequencies by previous authors. The speed of sound rises and the attenuation decreases as expected and within the IEC guidelines for the higher frequency range of 17 - 23 MHz. A significant change in temperature of ± 5^{o}C should be avoided when using this material within a test object as the validity of the test may be compromised by the changes in the acoustic parameters.

Improvements in time of flight measurements were proven successful. The software initially measured the time shift by identifying the signal peak however its first excursion from the baseline is now used to minimise phase reversal effects.

Backscatter measurements indicate that the TMM behaves consistently with the theoretical predictions, albeit for lower frequencies, based on commensurate scattering material sizes. The backscattering data measured from within and between TMM batches demonstrates a high degree of consistency but the stability of the material's backscatter performance over an extended period of time is the subject of an ongoing study.

6.2 Plaque characterisation

6.2.1 Summary of Results

The IEC TMM had to be adapted in order for the plaque composite speed data to be matched to the histological plaque component percentage data. The adapted clear tissue mimicking gel was shown to match the sound speed of soft tissue, 1540 ms^{-1}. The attenuation no longer matched that of soft tissue and was significantly diminished to 0.15 dB cm^{-1} MHz^{-1}.

The step phantom showed that the glycerol diffuses across the boundary between two gels of different glycerol concentration. This means that the sound profile of the constructed step phantom is 'blurred' with time to give a steady change of sound speed across the width of the phantom. The grid phantom showed that change in sound speed for a high sound speed object embedded within the clear gel is registered. However the 1mm spine was too narrow to measure the entire range of the sound speed step.

It was shown that the sound speed of the unfixed tissue did not change over a period of 72 hours when it was embedded within this clear TMM. The comparison of the three paired plaque speed plots over the 3 consecutive days showed p-values of 0.224 and 0.095.

It was observed that the speed plots were reproducible for consecutive plots. The average difference was calculated to be less than 1 ms^{-1} over the 400 - 500 plotlines through each plaque specimen. This was true for both techniques. This showed that the reproducibility of this measurement is robust for measuring group speed in plaque specimens.

It was observed that the histological shrinkage varied in each dimension and there was some variation between specimens, as shown in table 11. The variation seen in the histological shrinkage of the specimen may have been related to the time period that was taken to fix the specimen. Specimen 7 was shown to have been processed incorrectly by a trainee histologist. It was suggested that specimen 5 showed greater shrinkage due to its heterogeneity relative to the other specimens.

There was shown to be considerable difference in the comparison between the manual and automated segmentation method. The standard deviations for each test in the inter-observer comparison were 2.7 and 5.4%. These differences were explained by the misinterpretation of some tissue components and the delineation between elastic and fibrous tissue. The automated segmentation method was shown to be reproducible in the intra-observer comparison with a standard deviation of only 1.4%.

The Matlab code was tested by adding up to 30% noise to modelled data. It was seen that, when noise was added to the plaque component with less bulk (0.5 - 5%) in comparison to significant bulk (10 – 20%), the derivation of sound speed began to diverge at a lower level of noise (5%) in the 5 component analysis. The 3-component analysis was shown to be less sensitive to noise in a single component. Indeed the derivation worked with reasonable success up to the 30% noise level where there was a maximum divergence from the true modelled data of 1.3%. The 3-component analysis was shown, in this way, to be more robust. When noise was added to all components, the 3-component analysis was again shown to be more robust than the 5-component analysis. The maximum divergence from the true modelled data was 1.5% in the 3 component analysis and 3.3% in the 5 component analysis. It was also evident in the testing with noise in all components that the

derivation of sound speed for TMM and, to a certain extent the fibrous tissue, was less prone to divergence than the tissues with lower component percentage.

It has been shown that the derived values for sound speed fall into inter-quartile ranges for each component comparable with literature. This was true for both techniques at both temperatures. The results for plaque components showed that the derived sound speed for fibrous tissue exhibited the smallest inter-quartile range (1529 - 1625 ms^{-1}). Fibrous tissue made up the greatest percentage (10 – 20%) of the plaque components, as shown in table 13. It therefore had the most bulk in most plotlines.

The derived results for sound speed in TMM matched very well with those measured independently. Fibrous tissue showed narrowest inter-quartile range, 1529 - 1598 ms^{-1} for the reflection technique and 1533 – 1607 ms^{-1} for the transmission technique, of all the plaque components. Both lipid and elastic tissue had broader inter-quartiles ranges, 1478 - 1670 and 1445 - 1812 ms^{-1} respectively for the reflection technique and 1453 - 1670 and 1492 – 1838 ms^{-1} for the transmission technique, for sound speed than fibrous tissue. However their values were comparable to those quoted in literature. The calcification had consistently higher sound speed values (1700 - 2800 ms^{-1}) than the other plaque components and this was an expected result as the material is more rigid.

Though the derived speed values for TMM were shown statistically to have a significant difference to the QA measured data, it was seen that the derived data for TMM behaved as expected. The derived speed data for the TMM may have been affected by the uncertainties in the other plaque component data. The variation in derived sound speeds results may have been due, in part, to their inherent biological variation. However, it has been shown that low levels of noise can have an effect on the solution of the matrix inversion but it has been suggested that the main inaccuracy lay in plot-histo matching.

6.2.2 Discussion

The alteration to a clear TMM gel was necessary in order for the physical dimensions and outline of the embedded plaque to be measured and mapped. The lower attenuation also meant that the attenuation map showed clearly the outline of the embedded plaque. This plaque attenuation outline then provided a good match to the photographic mask. It was also successful in providing a material in which to embed the tissue. The transparency of the gel allowed the physical outline of the plaque to be mapped from the photograph to the plots and thus to the histological data.

The step phantom showed that a "stepping" of two sound speeds within a phantom was discernible. This showed that the measurement system was capable of measuring changes of sound speed of material embedded within clear TMM. The grid phantom showed that smaller dimension objects within a carotid plaque may not register the true sound speed change. This is due to the width of the beam profile in the focussed ultrasound beam. A thinner beam would be required in future work.

There are several limitations within the matching process that may have affected the results for plaque component speed. Though there was an anomaly in matching the x dimension of the speed plots to the photograph, this did not affect the photo-plot match. It was found that the contour maps from the attenuation plots showed considerable improvement to the match. This arose as the attenuation of the adapted clear TMM was lower than that of the embedded tissue. In this way, the non-mimic of this acoustic property aided the matching process. The attenuation map was therefore used instead of the speed plot map to compare the plot data to the physical data from the photograph. The plotting step size of 0.66 mm enabled sufficient resolution for the attenuation data to provide both a clear and matchable outline on the plot contour map.

The result from the decay experiment for the plaque specimen determined the time period within which our measurements could be carried out. This investigation will require further work to validate these findings as only two specimens were measured in this study.

The histological process was laborious. It was imperative that the outline of the gel remained intact so that the orientation of the plaque in relation to the plotlines could be maintained. This was not always achieved. However the quality of histological sections showed improvement through the duration of the study. The sectioning also gave an inaccurate record of the y dimension of the specimen. This was caused by the dislodgement of the bottom part of the plaque from the gel. This inaccuracy was noted and the histologist was informed to keep a record of this occurrence. The remaining plaque, where possible, will be retained in any future work so that this inaccuracy can be determined.

The causation between the percentage shrinkage and the tissue composition was not established as there were an insufficient number of specimens. This connection was also precluded by the fact that the tissue composition could only be approximated from the histological data. This approximation arose as not all histological sections through each specimen were segmented. An assumption was made in this study that the plaque shrunk uniformly in each dimension. If this was not true then the matching of histological data to its relevant plotline would be both difficult and irregular. An error of only 0.5 mm in the geometry match may have resulted in the histological data being assigned to the wrong plot row. This inaccuracy may have been a significant contributing factor to the mismatch of the speed plot to the component percentage data.

The automated segmentation technique was selected for the project due, in part, to the improvement in reproducibility over the manual segmentation technique. It was specifically designed for this study as a device that had the capability to resize the plotline widths and to move the plotline positions once the segmentation had been performed. The automated segmentation, in this way, was also selected as a labour saving device. Future work may involve the shifting or widening of the plotlines in

order to inspect any improvement in sound speed accuracy resulting from different plaque component percentage data.

On consideration of the sound speed data derived from the matrix inversion, it was observed that the solution occurred more often in the 3-component analysis. This could reflect the fact that the solution was more probable when the tissue in the plotline was more homogeneous. The results also show that the solutions for plaque component speed did not occur with a high success rate. In other words, where the matrices did solve, the plaque component speed data did not meet the criteria set out in section 4.12.1. This lack of success was possibly due to the fact that the input data may have been unsolvable.

As the percentage for fibrous tissue was significant, the matrix indeed solved more often than for less bulky components. In addition, the relatively low amount of attenuation and diffraction in fibrous tissue meant that there was less effect on the timing accuracy. It was also observed that fibrous tissue sound speed increased with a temperature rise of 16^{o}C (21^{o}C - 37^{o}C). This was seen in both techniques; resulting in an increase of 24 ms^{-1} for the reflection technique and 20 ms^{-1} for the transmission technique.

The wide range of results for lipid and elastic tissue may be explained by the small component percentages (0 – 5%) seen within the plaque tissue. The elastic tissue was only present in small amounts as the aim of surgery is to leave the media intact. Similarly the lipid pools do not always make up a significant amount in plaque formation.

The histology for lipid relies on its non-presence for location on the section. The formalin fixing removes the lipid from the lipid pools in the plaque. An assumption is therefore made that it was present in the holes or gaps left behind on the histological section during segmentation. Therefore there was no certainty that the lipid was correctly identified in the segmentation. It follows that the lipid component data entered into the matrix was not always accurate. Uncertainties of 5 - 10% may have been sufficient to affect the derivation of sound speed, particularly in the 5 component analysis. It was not evident from our study that lipid had an

expected lower speed value than fibrous tissue. The results were also inconclusive as to the negative temperature dependence of sound speed in lipid where there were conflicting results for the paired data. There was a decrease in sound speed for lipid in specimen 7 of 18 ms^{-1} over the temperature range. A fall of 3 ms^{-1} was also seen for specimen 3 in the transmission technique but an increase of 14 ms^{-1} was observed in the reflection technique for the same specimen.

The large inter-quartile range of sound speed results for calcification may be explained by the fact that there were not a large number of solutions for this component. This may have been caused by its minimal presence within the plaque. The timing accuracy of the pulse may have been affected by the diffraction and scatter caused by these calcified masses.

Whereas soft tissue and body fluids have been shown to exhibit very little dispersion over lower frequency ranges 0.3 - 10 MHz (Carstensen & Schwan 1959), dispersion evidently may have had an effect on the accuracy of our results. However the spread of values may be caused by the frequency dependent attenuation of the pulse and the resulting distortion of the received waveform. The measurement of phase speed may give a more accurate measure of propagation speed. This problem may be addressed in future work by utilising the phase spectra of the sample and reference RF echo. The broadband phase spectroscopy technique could be incorporated to deduce phase speed by analysis of the Fourier transforms of captured time domain signals (Mobley et al. 1998).

6.2.3 Conclusion and future work

In summary, a reproducible and novel method was established for measuring the group speed in plaque material embedded in a TMM. This method was shown to work equally well working in both transmission and reflection mode. Evidence was produced to show that the sound speed of the embedded carotid plaque tissue did not change over a 72 hour period. It was also shown that the measurement system was capable of measuring and detecting sound speed changes of subjects embedded in TMM, though subjects below 1mm in size may not register true sound speed due to the resolution of the larger beam width.

It is concluded that the overall accuracy of the method was reduced by the difficulty in accurately matching the geometry of the plotting to that of the histology. A methodological improvement was observed in matching the contour maps from the attenuation plots to the photographic mask in the plot-histo matching process. It is suggested that the main reason for the match inaccuracy may be the irregular histological shrinkage of the plaque.

The derived sound speed values for TMM were shown to match those that were independently measured. The sound speed data for each plaque component are in comparable ranges to those quoted in literature. Fibrous tissue has low inter-quartile range and its speed increases with temperature. It is proposed that both the plaque may be too heterogeneous and the beam resolution may be too large to produce accurate results for lipid and calcification.

The inhomogeneity of the tissue may have caused beam dispersion and diffraction which had a consequence on the timing accuracy of the received pulse. This may be probed in future work by the measurement of phase speed in embedded plaque. A significant difference was observed between the measured and derived sound speed for the TMM. This difference may have been due to the uncertainties in the derived data of the plaque components. However the derived sound speed for fibrous tissue compared favourably to values quoted in literature and was seen to increase with temperature. Similarly the calcification showed an expectedly higher value of derived sound. The 5 component analysis was shown to be a fairly robust

method of sound speed derivation up to the 10% noise level but the 3 component analysis was more robust.

Future work may therefore focus on the derivation of sound speeds in the more homogeneous regions of plaque before investigation of more heterogenous specimens. Insufficient accuracy of the sound speed measurements of carotid plaque components in this study meant that no sufficient advance was made in plaque tissue characterisation. Therefore further work must be carried out in order to improve these measurements. The sound speed values may still then be used to predict the stroke risk of patients with carotid disease.

References

Carstensen, E. L. & Schwan, H. P. 1959, "Acoustic properties of hemoglobin solutions", *J Acoust Soc Am*, vol. 31, pp. 185-189.

Mobley, J., Marsh, J. N., Hall, C. S., Hughes, M. S., Bandenburger, G. S., & Miller, J. G. 1998, "Broadband measurements of phase velocity in Albunex suspensions", *J Acoust Soc Am*, vol. 103, no. 4, pp. 2145-2153.

GLOSSARY OF TERMS

ACS - asymptomatic patients

AHA - American Heart Association

AIP - adaptive image processing

ASCII - American Standard Code for Information Interchange

ATH - atherosclerosis

ATL - Advanced Technology Laboratories

BFI - B-flow imaging

CAS - carotid angioplasty with stenting

CCA – common carotid artery

CDI - colour Doppler imaging

CEA - carotid endarterectomy

CEMRA – contrast enhanced MRA

CEU - contrast-enhanced ultrasound

CI – confidence interval

c-IMT - carotid intimal-medial thickness

CTA - computerised tomography angiography

DCE-MRI - dynamic contrast-enhanced MRI

DSA - (X-ray) digital subtraction angiography

DUS – Duplex ultrasonography

EC - European Commission

ECA - external carotid atherosclerosis

ECM - extracellular matrix

ECST - European carotid surgery trials

EDV - end-diastolic velocity

FCT - fibrous cap thickness

FDG – PET - F-18 fluorodeoxyglucose positron emission tomography

FEA - finite element analysis

FFT - fast Fourier transform

GSM - grey scale median

HV – Hounsfield Value

IB - integrated backscatter

IEC – International Electrotechnical Commission

ICA - internal carotid atherosclerosis

ICRU – International Commission on Radiation Units

IQ – inter-quartile

IVUS - intravenous ultrasound

κ value – kappa value

LDPE – low density polyethylene

MDCT - multidetector computerised tomography

MES - microembolic signals

MRA - magnetic resonance angiography

MRI - magnetic resonance imaging

NASCET - North American symptomatic carotid endarterectomy trial

NDT – non-destructive testing

NIR - near infrared

PAA - polyacrylamide

PDA - pixel distribution analysis

PSV - peak systolic velocity

PVA - polyvinyl alcohol

PVDF - polyvinylidene difluoride

RR – relative risk (ratio)

SAM – scanning acoustic microscope

SMC - smooth muscle cell

SRI – speckle reduction imaging

TCD - transcranial Doppler

THI - tissue harmonic imaging

TIA - transient ischemic attacks

TMM - tissue mimicking material

USPIOs - ultrasmall superparamagnetic particles of iron oxide

UTCI - ultrasound texture classification image

VCAM-1 - Vascular Cell Adhesion Molecule-1

APPENDICES

Appendix A

Silver Block impregnation and processing of endarterectomy specimens

(This is a modification of the Tripp and Mackay method for staining undecalcified bone specimens)

Carotid artery specimens, embedded in agar, were fixed in 10% formal saline for 24 hours. A notch was made in the agar to aid orientation prior to staining using a modification of the Tripp and Mackay silver staining technique (Tripp and Mackay, 1972). Briefly, fixed arteries (in agar) were washed in distilled water, changed hourly, for eight hours. Arteries placed in 2% silver nitrate in complete darkness for 48 hours. After thoroughly washing in running tap water for an hour, arteries were transferred to a freshly prepared reducing solution for 48 hours. The reducing solution was washed off with running tap water for an hour prior to fixing the reduced silver with 5% sodium thiosulphate for 24 hours. Arteries were washed as previously described before decalcifying in 5% formic acid solution, the fluid changed every two days. When decalcification was complete (usually after a week), the arteries were washed well, as before, and hand processed through industrial methylated spirits (IMS) at concentrations of 50%, 70%, 90% and 100%, 24 hours per grade. Alcohol clearing was achieved using toluene (24 hours), prior to placing the artery in molten paraffin wax at 60°C for 48 hours. All stages from fixation through staining and decalcification, to toluene clearing were performed on a rocker. Arteries were orientated, embedded in fresh paraffin wax and blocks allowed to cool before cutting on a base sledge microtome. Blocks were trimmed down until tissue was just visible then five serial sections at five micrometres (µm) thickness were cut and picked up (in order) onto a coated glass slide labelled '1'. A further 250µm of the block was trimmed away and sections discarded before the next five serial sections were cut and picked up on slide '2'. This sequence was repeated until the tissue was cut through. Slides were finally dried down overnight in a 60°C oven prior to staining using Elastic Van Gieson technique.

Protocol

1. Tissue blocks fixed in 10% formol saline.
2. Make two notches in agar to enable orientation when embedding.
3. Wash tissue in distilled water 8hrs (minimum 8 changes).
4. Place tissue in 2% silver nitrate for 48 hours in complete darkness.
5. Rinse in three changes of distilled water one minute each.
6. Place in reducer, 48 hours.
7. Wash in running tap water, 1 hour.
8. Place in sodium thiosulphate, 24 hours.
9. Wash in running tap water, 1 hour.
10. Decalcify in 10% formic acid
11. Process to paraffin wax.
12. At intervals of 250 microns, section in ribbons of 5 x 5 microns.
13. Stain sections with elastic and Van Gieson stain.

Modified Reducer:

Hydroquinone	0.5g
Sodium sulphite	2.5g
Distilled water	100ml

Reference:

Silver staining of bone prior to decalcification for quantitative determination of osteoid in sections. EJ Tripp and EM Mackay. (1972). Stain Technol 47129-36.

Appendix B

This table shows typical output data from the automated image segmentation.

PL	Calc	Norm	Elas	Fat	Total	TMM	Ca+Elas	Elas+Fat	Ca+Fat	N+Fat	N+Ca	N+Elas	Not threshld
1	0.0	3.9	4.8	0.2	99.1	90.3	0.0	0.0	0.0	0.0	0.0	0.0	0.8
2	0.0	17.8	7.9	0.4	98.4	72.4	0.0	0.0	0.0	0.1	0.0	0.0	1.6
3	0.1	31.4	6.3	0.5	98.2	60.3	0.0	0.0	0.0	0.2	0.0	0.0	1.8
4	1.3	32.9	7.3	2.9	97.7	53.8	0.3	0.0	0.0	0.2	0.0	0.0	2.4
5	1.7	27.9	5.9	12.3	98.2	51.4	0.3	0.0	0.0	0.8	0.0	0.0	1.9
6	0.4	25.7	2.2	20.8	99.0	51.2	0.0	0.0	0.0	1.4	0.0	0.0	1.1
7	0.0	29.3	0.6	17.7	99.1	52.8	0.0	0.0	0.0	1.2	0.0	0.0	0.9
8	0.0	28.8	0.1	8.4	99.3	63.0	0.0	0.0	0.0	1.0	0.0	0.0	0.7
9	0.0	15.3	0.0	2.9	99.7	82.5	0.0	0.0	0.0	1.0	0.0	0.0	0.3
10	0.0	5.1	0.2	3.9	99.8	91.4	0.0	0.0	0.0	0.8	0.0	0.0	0.3
11	0.0	6.0	0.4	5.9	99.3	88.1	0.0	0.0	0.0	1.0	0.0	0.0	0.7
12	0.0	7.6	0.4	6.7	99.3	86.3	0.0	0.0	0.0	1.7	0.0	0.0	0.7
13	0.0	7.3	0.3	6.3	99.6	87.7	0.0	0.0	0.0	2.0	0.0	0.0	0.4
14	0.0	5.4	0.2	4.0	99.7	91.5	0.0	0.0	0.0	1.3	0.0	0.0	0.3
15	0.0	2.8	0.2	2.4	99.7	94.8	0.0	0.0	0.0	0.4	0.0	0.0	0.3
16	0.0	0.7	0.1	1.0	99.9	98.2	0.0	0.0	0.0	0.0	0.0	0.0	0.2
17	0.0	0.0	0.0	0.0	100.0	100.0	0.0	0.0	0.0	0.0	0.0	0.0	0.0

Appendix C i)

1545	1545	1547	1546	1547	1547	1546	1546	1546	1546	1547	1548	1545	1548	1549	1549	1549	1548	1545
1549	1547	1546	1546	1547	1547	1547	1551	1548	1547	1547	1547	1545	1545	1545	1545	1545	1545	1546
1548	1546	1546	1547	1550	1547	1552	1550	1549	1549	1547	1547	1546	1546	1546	1546	1546	1546	1545
1547	1546	1546	1551	1552	1553	1551	1550	1549	1548	1546	1547	1548	1546	1546	1545	1549	1548	1549
1546	1546	1555	1564	1563	1543	1548	1548	1547	1548	1546	1547	1547	1549	1549	1547	1547	1547	1547
1546	1547	1564	1565	1564	1554	1555	1553	1556	1547	1547	1547	1548	1547	1547	1547	1547	1547	1547
1546	1557	1564	1565	1555	1553	1553	1553	1552	1551	1550	1549	1549	1547	1547	1546	1549	1546	1546
1546	1558	1559	1558	1553	1553	1551	1554	1557	1552	1551	1550	1550	1549	1549	1548	1548	1551	1545
1546	1559	1557	1553	1553	1553	1553	1554	1557	1552	1551	1550	1550	1550	1551	1560	1555	1549	1547
1555	1557	1562	1553	1553	1553	1553	1554	1556	1550	1551	1551	1551	1551	1555	1555	1555	1549	1547
1554	1557	1566	1560	1552	1552	1553	1554	1554	1551	1551	1551	1551	1553	1550	1555	1550	1546	1547
1554	1561	1565	1564	1551	1552	1552	1552	1554	1553	1551	1551	1551	1554	1552	1549	1549	1547	1547
1558	1558	1563	1563	1550	1551	1551	1552	1552	1553	1551	1551	1550	1552	1552	1562	1546	1547	1547
1553	1558	1560	1562	1551	1551	1551	1551	1552	1550	1550	1550	1550	1550	1552	1562	1548	1546	1547
1558	1558	1559	1560	1550	1551	1551	1551	1551	1550	1550	1550	1550	1549	1550	1562	1547	1547	1546
1557	1558	1558	1560	1551	1551	1551	1551	1551	1550	1550	1550	1550	1549	1550	1562	1546	1547	1546
1559	1558	1558	1558	1551	1550	1551	1552	1552	1551	1551	1550	1550	1549	1558	1546	1547	1546	1546
1553	1559	1559	1559	1551	1551	1551	1551	1550	1550	1550	1549	1550	1550	1547	1546	1547	1546	1546
1546	1557	1554	1558	1550	1550	1550	1549	1549	1548	1547	1547	1546	1546	1546	1547	1545	1546	1546
1546	1546	1546	1543	1550	1549	1549	1548	1547	1546	1546	1547	1547	1547	1548	1548	1545	1546	1546

Day 1

1546	1546	1547	1547	1547	1547	1546	1548	1548	1548	1547	1547	1546	1546	1546	1546	1546	1546	1547
1546	1547	1547	1547	1548	1548	1547	1551	1550	1549	1548	1547	1548	1546	1545	1545	1546	1545	1546
1548	1546	1545	1551	1550	1550	1552	1549	1549	1549	1547	1547	1548	1546	1545	1546	1545	1545	1545
1547	1546	1545	1550	1551	1560	1546	1550	1550	1548	1547	1546	1546	1548	1545	1545	1548	1546	1547
1546	1545	1552	1564	1569	1560	1552	1550	1556	1547	1548	1547	1547	1547	1545	1546	1546	1546	1546
1546	1546	1559	1564	1564	1553	1552	1553	1552	1551	1552	1548	1548	1547	1546	1546	1545	1546	1547
1545	1548	1561	1562	1552	1553	1552	1553	1553	1554	1550	1549	1549	1548	1546	1544	1547	1545	1545
1546	1548	1559	1561	1553	1553	1552	1551	1556	1556	1550	1550	1550	1549	1547	1548	1555	1550	1549
1545	1557	1558	1558	1554	1552	1552	1551	1556	1551	1550	1550	1550	1550	1550	1554	1556	1549	1546
1545	1556	1557	1564	1554	1552	1551	1552	1553	1552	1550	1550	1550	1551	1549	1558	1555	1550	1546
1545	1559	1564	1564	1551	1551	1551	1551	1553	1553	1550	1550	1550	1550	1550	1552	1550	1547	1547
1545	1555	1562	1564	1551	1550	1550	1551	1552	1551	1551	1551	1550	1551	1551	1556	1556	1546	1546
1545	1559	1559	1562	1550	1550	1550	1551	1551	1551	1550	1549	1549	1549	1550	1565	1546	1546	1546
1546	1559	1558	1560	1559	1550	1551	1550	1550	1551	1550	1550	1549	1548	1550	1560	1557	1546	1546
1548	1558	1558	1560	1553	1550	1550	1550	1551	1550	1550	1550	1549	1549	1546	1562	1547	1546	1545
1546	1558	1559	1559	1559	1550	1551	1551	1552	1551	1550	1549	1549	1549	1550	1558	1546	1547	1545
1548	1558	1559	1558	1558	1550	1551	1552	1552	1551	1551	1549	1549	1550	1542	1546	1547	1545	1545
1546	1558	1560	1563	1556	1550	1550	1551	1550	1549	1549	1549	1548	1546	1546	1547	1547	1545	1546
1547	1546	1546	1547	1551	1550	1549	1550	1549	1548	1547	1547	1547	1547	1547	1548	1546	1546	1546
1545	1547	1547	1547	1546	1547	1548	1548	1548	1548	1549	1546	1546	1546	1546	1546	1546	1546	1546

Day 2

1546	1545	1547	1547	1547	1547	1547	1549	1549	1547	1547	1547	1546	1546	1546	1546	1546	1546	1546
1546	1547	1547	1547	1551	1548	1551	1551	1550	1550	1547	1547	1546	1546	1546	1546	1547	1546	1547
1547	1546	1547	1551	1551	1555	1552	1551	1550	1549	1547	1547	1546	1546	1546	1546	1546	1546	1546
1547	1546	1547	1562	1552	1553	1550	1551	1546	1547	1547	1547	1547	1546	1546	1546	1547	1547	1547
1546	1546	1558	1566	1564	1555	1552	1551	1556	1548	1548	1547	1547	1548	1549	1547	1546	1547	1547
1547	1549	1560	1565	1563	1552	1552	1553	1553	1552	1550	1548	1548	1548	1547	1547	1547	1549	1547
1546	1548	1564	1559	1553	1551	1552	1554	1555	1551	1551	1550	1550	1548	1547	1547	1547	1546	1546
1546	1559	1564	1557	1553	1552	1552	1553	1556	1552	1550	1551	1550	1549	1549	1549	1555	1549	1546
1545	1558	1560	1554	1553	1553	1553	1554	1557	1552	1550	1550	1550	1549	1555	1555	1555	1549	1547
1545	1556	1559	1559	1553	1552	1553	1552	1554	1551	1550	1550	1550	1550	1549	1557	1554	1545	1547
1547	1560	1564	1564	1551	1551	1552	1554	1554	1552	1551	1550	1551	1553	1551	1551	1549	1547	1547
1546	1557	1563	1564	1551	1551	1551	1552	1552	1552	1551	1551	1551	1551	1552	1557	1546	1547	1546
1547	1560	1560	1562	1550	1551	1551	1551	1552	1551	1549	1549	1549	1550	1551	1563	1547	1546	1547
1548	1558	1559	1560	1551	1551	1551	1551	1552	1551	1550	1550	1550	1549	1549	1563	1552	1546	1547
1555	1559	1559	1560	1551	1551	1551	1552	1551	1551	1550	1550	1549	1549	1550	1559	1547	1547	1545
1555	1559	1559	1559	1554	1551	1552	1553	1552	1552	1550	1550	1550	1549	1551	1547	1546	1548	1546
1555	1558	1560	1560	1552	1551	1552	1553	1552	1552	1551	1550	1550	1551	1547	1547	1548	1546	1546
1547	1559	1563	1562	1551	1551	1551	1551	1551	1550	1549	1548	1548	1546	1547	1547	1546	1546	1546
1548	1547	1547	1546	1550	1550	1549	1550	1548	1548	1547	1547	1547	1547	1548	1546	1546	1546	1546
1546	1546	1547	1547	1547	1547	1548	1548	1548	1546	1546	1546	1546	1546	1546	1546	1546	1546	1546

Day 3

These 3 sets of data represent the paired grids of plot data from consecutive days used to compare the change in sound speed for an unfixed plaque specimen embedded in clear Agar tissue mimicking material.

Appendix C ii)

1542	1542	1541	1541	1543	1541	1541	1541	1541	1541	1542	1541	1542	1541	1540	1541	1541	1541	1541
1542	1542	1544	1544	1546	1546	1541	1541	1542	1541	1542	1544	1548	1541	1542	1540	1541	1542	1542
1542	1543	1544	1544	1545	1546	1540	1541	1541	1541	1542	1542	1554	1548	1541	1543	1541	1541	1541
1541	1543	1545	1545	1546	1545	1544	1541	1541	1542	1542	1543	1548	1553	1544	1541	1540	1541	1541
1543	1549	1546	1546	1546	1546	1545	1541	1542	1542	1542	1542	1557	1560	1556	1541	1542	1541	1541
1543	1548	1547	1547	1547	1548	1549	1543	1542	1542	1542	1542	1557	1560	1563	1561	1541	1542	1541
1542	1548	1547	1547	1548	1548	1549	1543	1541	1541	1542	1543	1559	1561	1562	1561	1542	1541	1540
1543	1547	1548	1548	1548	1548	1548	1544	1539	1542	1542	1545	1557	1561	1562	1561	1556	1541	1542
1542	1544	1548	1549	1549	1549	1547	1546	1546	1546	1546	1551	1556	1560	1562	1558	1550	1542	1540
1544	1542	1552	1551	1550	1549	1548	1548	1546	1546	1545	1554	1556	1556	1559	1564	1545	1541	1540
1544	1542	1555	1559	1546	1548	1548	1547	1545	1552	1553	1553	1556	1558	1559	1564	1542	1542	1540
1542	1542	1560	1564	1563	1558	1559	1555	1555	1553	1552	1554	1556	1559	1559	1551	1550	1542	1541
1541	1542	1560	1566	1565	1560	1557	1557	1556	1550	1551	1557	1556	1556	1555	1550	1546	1542	1540
1542	1543	1551	1561	1562	1559	1556	1556	1558	1563	1562	1557	1555	1556	1554	1549	1551	1542	1541
1541	1542	1556	1558	1559	1558	1555	1555	1556	1563	1563	1558	1558	1562	1550	1547	1548	1541	1540
1542	1543	1543	1555	1556	1558	1557	1554	1555	1553	1563	1564	1563	1563	1558	1547	1547	1547	1540
1541	1542	1542	1557	1557	1559	1561	1556	1552	1550	1546	1559	1562	1560	1557	1546	1546	1546	1540
1542	1540	1543	1556	1559	1561	1561	1561	1552	1550	1549	1549	1563	1561	1548	1545	1545	1547	1542
1541	1541	1541	1552	1559	1564	1562	1554	1553	1553	1549	1549	1558	1553	1545	1545	1545	1544	1542
1541	1542	1542	1550	1559	1563	1563	1555	1552	1554	1552	1551	1550	1540	1544	1545	1544	1544	1542
1541	1541	1542	1542	1557	1561	1562	1555	1552	1554	1551	1547	1548	1541	1542	1544	1544	1543	1540
1541	1541	1541	1542	1550	1558	1563	1553	1552	1553	1550	1548	1542	1543	1541	1543	1543	1543	1540
1541	1541	1541	1542	1549	1556	1559	1556	1553	1551	1541	1542	1541	1541	1540	1542	1543	1542	1540
1541	1541	1541	1540	1542	1541	1554	1548	1542	1541	1542	1540	1541	1541	1541	1542	1543	1542	1540
1541	1541	1541	1541	1542	1542	1542	1542	1542	1540	1540	1541	1540	1540	1540	1540	1541	1540	1540

Day 1

1541	1541	1541	1541	1545	1542	1541	1541	1541	1541	1542	1542	1540	1541	1542	1541	1541	1541	1541
1543	1542	1545	1544	1545	1545	1543	1542	1542	1542	1543	1543	1549	1542	1543	1541	1542	1542	1542
1542	1543	1544	1545	1547	1545	1546	1542	1542	1542	1543	1543	1551	1546	1543	1543	1541	1541	1541
1541	1543	1545	1546	1546	1546	1545	1542	1542	1542	1543	1542	1548	1545	1545	1541	1544	1541	1542
1543	1544	1547	1546	1547	1546	1545	1544	1542	1542	1543	1542	1551	1557	1555	1541	1542	1541	1541
1542	1542	1546	1547	1548	1547	1549	1543	1542	1542	1543	1542	1557	1559	1562	1561	1541	1542	1541
1543	1548	1547	1547	1548	1549	1549	1544	1542	1542	1543	1542	1558	1561	1563	1563	1542	1542	1541
1543	1544	1548	1548	1548	1548	1548	1545	1541	1541	1543	1544	1557	1562	1563	1563	1558	1542	1542
1560	1560	1549	1548	1549	1549	1548	1546	1544	1545	1546	1547	1555	1560	1563	1561	1555	1541	1542
1560	1560	1565	1551	1550	1550	1549	1547	1547	1546	1546	1545	1555	1557	1560	1565	1548	1541	1542
1560	1560	1565	1552	1549	1549	1548	1547	1547	1546	1552	1553	1555	1559	1559	1575	1545	1542	1541
1559	1559	1561	1563	1562	1546	1559	1550	1546	1554	1553	1553	1556	1559	1560	1560	1549	1542	1543
1546	1543	1548	1565	1567	1561	1558	1557	1556	1551	1553	1553	1557	1559	1558	1555	1553	1542	1540
1541	1542	1542	1562	1562	1561	1559	1557	1557	1563	1564	1558	1555	1556	1556	1548	1552	1542	1543
1542	1542	1541	1557	1558	1559	1556	1555	1556	1564	1563	1558	1557	1556	1549	1550	1549	1544	1542
1542	1542	1542	1557	1556	1557	1557	1554	1554	1554	1560	1562	1563	1564	1560	1547	1547	1548	1542
1541	1542	1542	1557	1557	1558	1557	1556	1556	1552	1547	1560	1561	1561	1560	1547	1547	1547	1542
1542	1541	1542	1558	1557	1560	1562	1560	1554	1550	1550	1550	1561	1564	1558	1547	1546	1546	1543
1541	1541	1541	1557	1559	1560	1560	1559	1553	1553	1550	1550	1556	1558	1547	1546	1545	1545	1543
1541	1541	1542	1549	1560	1562	1559	1557	1552	1554	1553	1551	1548	1550	1547	1546	1545	1545	1543
1541	1541	1542	1541	1558	1562	1561	1556	1553	1554	1552	1548	1548	1538	1543	1544	1544	1544	1542
1541	1541	1541	1541	1550	1558	1560	1560	1555	1554	1552	1548	1539	1542	1542	1543	1543	1544	1543
1541	1541	1541	1542	1540	1556	1559	1558	1554	1553	1547	1541	1542	1541	1540	1543	1543	1542	1542
1541	1542	1541	1541	1541	1544	1554	1555	1552	1542	1541	1542	1541	1541	1541	1542	1543	1543	1542
1541	1541	1541	1541	1542	1542	1541	1541	1541	1541	1540	1540	1540	1540	1540	1543	1542	1541	1540

Day 2

1541	1540	1542	1542	1540	1540	1540	1541	1541	1540	1542	1542	1542	1541	1541	1542	1540	1541	1541
1541	1540	1542	1543	1542	1541	1541	1541	1540	1542	1541	1548	1553	1553	1542	1541	1540	1540	1541
1541	1542	1544	1543	1543	1541	1540	1542	1542	1541	1552	1554	1557	1557	1556	1541	1542	1541	1541
1541	1542	1544	1544	1543	1540	1542	1541	1548	1551	1553	1552	1558	1562	1557	1550	1541	1540	1541
1541	1542	1545	1544	1544	1542	1541	1549	1547	1552	1554	1553	1556	1562	1558	1558	1542	1542	1541
1541	1543	1545	1545	1545	1542	1549	1548	1549	1552	1553	1552	1556	1558	1562	1561	1549	1542	1541
1541	1543	1545	1546	1546	1547	1557	1556	1550	1550	1552	1553	1559	1558	1562	1556	1552	1541	1541
1540	1542	1546	1545	1546	1547	1562	1560	1549	1550	1550	1554	1558	1559	1559	1556	1554	1541	1540
1541	1542	1546	1546	1546	1562	1561	1561	1550	1548	1548	1555	1556	1561	1557	1557	1556	1542	1543
1541	1542	1547	1547	1547	1560	1563	1563	1562	1559	1553	1555	1554	1556	1556	1554	1554	1542	1542
1541	1542	1546	1549	1546	1558	1560	1558	1558	1563	1563	1553	1555	1555	1557	1555	1556	1542	1543
1541	1540	1542	1551	1548	1554	1556	1554	1557	1562	1562	1557	1554	1556	1558	1558	1559	1547	1542
1541	1540	1542	1553	1550	1558	1556	1554	1554	1552	1556	1557	1557	1557	1560	1566	1565	1546	1542
1542	1541	1542	1552	1559	1559	1559	1556	1553	1553	1553	1561	1555	1560	1558	1563	1565	1559	1542
1541	1543	1542	1546	1565	1560	1557	1553	1553	1553	1549	1546	1548	1548	1548	1550	1561	1551	1542
1542	1541	1542	1545	1565	1560	1557	1555	1554	1546	1546	1547	1548	1548	1549	1548	1550	1553	1542
1542	1543	1543	1557	1562	1562	1556	1555	1546	1546	1547	1547	1547	1548	1549	1549	1549	1548	1543
1542	1543	1542	1558	1562	1563	1562	1557	1546	1544	1544	1542	1545	1548	1548	1548	1548	1548	1543
1542	1543	1543	1559	1562	1562	1561	1557	1543	1544	1543	1543	1545	1548	1549	1548	1547	1548	1545
1542	1542	1543	1542	1562	1562	1560	1557	1543	1542	1543	1543	1544	1550	1549	1548	1548	1547	1549
1542	1542	1541	1543	1545	1561	1559	1556	1543	1544	1542	1543	1544	1546	1549	1547	1548	1547	1544
1542	1542	1542	1544	1543	1554	1555	1549	1543	1543	1542	1542	1542	1545	1546	1547	1546	1546	1544
1543	1542	1542	1542	1543	1545	1555	1556	1544	1544	1543	1543	1543	1545	1546	1546	1546	1546	1544
1542	1542	1542	1542	1541	1542	1542	1548	1542	1544	1542	1542	1543	1543	1545	1545	1546	1542	1543
1543	1543	1543	1542	1542	1543	1542	1543	1543	1544	1542	1542	1543	1543	1546	1546	1543	1543	1543

Day 3

These 3 sets of data represent the paired grids of plot data from consecutive days used to compare the change in sound speed for an unfixed plaque specimen embedded in clear Agar tissue mimicking material.

Appendix D i)

Reflection – Cold 21^{o}C

This table shows the sound speed data as inter-quartile ranges for each of the seven specimens from the broadband reflection measurements at 37^{0}C (±1^{0}C).

Specimen	TC (n)	TMM		FAT		FIBROUS		ELASTIC		CALCIFIED	
		Q1	Q3	Q1	Q3	Q1	Q3	Q1	Q3	Q1	Q3
1	5										
	3 (185)	1540	1546	1356	1619	1537	1596				
2	5 (66)	1542	1553	1495	1602	1522	1587	1478	1785	1986	3607
	3 (151)										
3	5										
	3 (91)	1541	1548	1494	1576	1533	1609				
4	5 (59)	1540	1554	1550	1665	1535	1571	1400	1588	1800	2486
	3 (141)										
5	5 (82)	1546	1551	1486	1685	1534	1586	1433	1836	1508	2234
	3 (178)										
6	5 (26)	1534	1551	1509	1723	1523	1612	1490	2473	1630	4491
	3 (67)										
7	5 (7)	1539	1553	1211	1644	1538	1622	1415	1883	5004	8576
	3 (181)										

Appendix D ii)

Reflection – Hot 37^{o}C

Specimen	TC	TMM		FAT		FIBROUS		ELASTIC		CALCIFIED	
		Q1	Q3	Q1	Q3	Q1	Q3	Q1	Q3	Q1	Q3
1	5										
	3 (200)	1561	1569	1451	1641	1561	1614				
2	**5** (66)	1568	1575	1495	1602	1522	1587	1478	1785	1986	3607
	3 (177)										
3	5										
	3 (86)	1566	1573	1494	1576	1533	1609				
4	**5** (68)	1570	1576	1550	1665	1535	1571	1400	1588	1800	2486
	3 (158)										
5	**5** (49)	1570	1576	1486	1685	1534	1586	1433	1836	1508	2234
	3 (221)										
6	**5** (28)	1558	1571	1509	1723	1523	1612	1490	2473	1630	4491
	3 (88)										
7	5	1565	1576	1211	1644	1538	1622	1415	1883	5004	8536
	3 (186)										

This table shows the sound speed data as inter-quartile ranges for each of the seven specimens from the broadband reflection measurements at 37^{0}C (±1^{0}C).

Appendix D iii)

Transmission – Cold 21^{o}C

Specimen	TC (n)	TMM		FAT		FIBROUS		ELASTIC		CALCIFIED	
		Q1	Q3	Q1	Q3	Q1	Q3	Q1	Q3	Q1	Q3
1	5										
	3 (195)	1535	1546	1433	1634	1555	1617				
2	5										
	3										
3	5										
	3 (63)	1543	1549	1476	1647	1515	1610				
4	**5** (49)	1540	1558	1505	1683	1532	1595	1479	1630	1277	1712
	3 (128)										
5	**5** (33)	1541	1548	1356	1804	1519	1563	1449	2224	1327	1863
	3 (77)										
6	**5** (29)	1544	1557	1458	1641	1548	1610	1610	1989	2912	8169
	3 (53)										
7	5										
	3 (179)	1539	1557	1257	1745	1510	1631				

This table shows the sound speed data as inter-quartile ranges for the seven specimens from the broadband transmission measurements at 21^{0}C (±1^{0}C). No transmission measurements were carried out on specimen 2. For specimens 1,3 and 7, the five component analysis failed.

Appendix D iv)

Transmission – Hot 37^{o}C

Specimen	TC	TMM		FAT		FIBROUS		ELASTIC		CALCIFIED	
		Q1	Q3	Q1	Q3	Q1	Q3	Q1	Q3	Q1	Q3
3	5										
	3 (94)	1563	1573	1483	1620	1545	1624				
4	**5** (76)	1565	1580	1512	1750	1561	1614	1405	1806	1613	2765
	3 (147)										
5	**5** (66)	1572	1580	1287	1614	1553	1606	1483	1881	1319	2823
	3 (144)										
6	**5** (32)	1566	1580	1513	1664	1547	1644	1505	1793	2376	13954
	3 (69)										
7	5										
	3 (187)	1568	1581	1349	1747	1565	1635				

This table shows the sound speed data as inter-quartile ranges for the seven specimens from the broadband transmission measurements at 37^{0}C (±1^{0}C). No transmission measurements were performed on samples 1 or 2 at 37 ^{0}C.